Structures and dynamics of Poly(ionic liquid)s in bulk and at interfaces

Tiago Outerelo Corvo

université
PARIS-SACLAY

Structures and dynamics of Poly(Ionic liquid) in bulk and at interfaces

Structures et dynamiques de Poly(liquide ionique) en volume et aux interfaces

Thèse de doctorat de l'Université Paris-Saclay

École doctorale n°564 Physique en Île de France (PIF)
Spécialité de doctorat: Physique
Graduate School : Physique. Référent : Faculté des sciences d'Orsay

Thèse préparée dans les unités de recherche **Laboratoire de Physique des Solides (Univ. Paris-Saclay, CNRS)** et **Laboratoire Léon Brillouin (Univ. Paris-Saclay, CEA, CNRS)**, sous la direction de **Frédéric Restagno**, Directeur de Recherche CNRS et la co-direction d'**Alexis Chennevière**, Chargé de Recherche CEA Saclay.

Thèse soutenue à Paris-Saclay, le 08 décembre 2023, par

Tiago OUTERELO CORVO

Composition du jury

Membres du jury avec voix délibérative

Benoît Coasne Directeur de Recherche CNRS, Univ. Grenoble Alpes	Président
Jean-Paul Chapel Directeur de Recherche CNRS, Univ. de Bordeaux	Rapporteur & Examinateur
Ralph H. Colby Professeur, Pennsylvania State Univ. (Etats-Unis)	Rapporteur & Examinateur
Emmanuelle Dubois Directrice de Recherche CNRS, Sorbonne Univ.	Examinatrice
Simone Napolitano Maître de conférences, Univ. Libre de Bruxelles (Belgique)	Examinateur

THESE DE DOCTORAT

NNT : 2023UPASP176

université PARIS-SACLAY

ÉCOLE DOCTORALE
Physique en Île-de-France (PIF)

Titre: Structures et dynamiques de Poly(liquide ionique) en volume et aux interfaces
Mots clés: Liquide Ionique, Poly(Liquide Ionique), Diffusion de neutrons, Réflectivité de rayons X, Viscoélasticité polymère

Résumé: Les poly(liquide ionique)s (PLI) sont des macromolécules composées de liquides ioniques (LI). Ils possèdent donc des propriétés hybrides qui font d'eux des matériaux prometteurs, notamment pour des applications en tant qu'électrolyte solide. Ils héritent des LIs une nanostructure particulière qui repose sur la ségrégation de la phase apolaire qui mène chez les LI imidazolium à une structure globulaire pour les chaînes carbonnées courtes ou bicontinue en éponge pour des chaînes longues. L'ajout de ces interactions locales à un polymère ouvre la voie au développement de nouvelles fonctionnalités reposant à la fois sur leur structure et leur dynamique.

La présente étude est centrée sur une série de PLI imidazolium (PC$_n$VImTFSI) de longueur de chaîne latérale n variable, et par conséquent aux interactions locales ajustables. En utilisant la diffusion de neutrons aux petits angles et celle des rayons X aux grands angles, nous avons étudié la structure en volume de la taille de la chaîne de PLI jusqu'à son diamètre. Le rayon de giration révèle une surprenante évolution non monotone et à l'échelle locale une interpénétration des longues chaînes latérales. Ces résultats suggèrent une variation de la flexibilité de la chaîne, potentiellement affectée par des répulsions électrostatiques qui varient avec n.

Malgré les nombreuses applications qui se jouent aux interfaces et le comportement inhabituel des LIs qui s'y stratifient en couches d'ions, la structure interfaciale des PLIs est peu connue. À ce sujet, nous avons étudié la structure de films fins de PLIs dans les trois directions de l'espace en utilisant à la fois la réflectivité de rayons X et leur diffusion en incidence rasante. Pour des chaînes latérales courtes, les films sont homogènes mais une stratification apparaît pour les chaînes plus longues. La distance interlamellaire et la distance interchaîne dans le plan dépendent de l'épaisseur du film. Nous proposons ici un mécanisme moléculaire impliquant un alignement préférentiel des groupes latéraux avec l'interface.

Ces matériaux sont aussi un rare cas de polyélectrolyte en fondu, malgré leur grande densité ionique. D'autres matériaux comme les ionomères perdent leur processabilité quand leur fraction ionique augmente et pourtant, les PLI ont la totalité de leurs monomères chargés. La longueur de la chaîne latérale est un moyen de changer la polarité des interactions et nous avons, par conséquent, étudié les propriétés viscoélastiques de la même série de (PC$_n$VImTFSI). Ces résultats sont discutés en lien avec leur structure et les polymères associatifs.

Cette approche fondamentale, reposant sur une série de PLI modèle, révèle les propriétés remarquables de ces matériaux. Il reste cependant à démontrer si ces conclusions sont universelles pour fournir les outils nécessaires pour tirer le meilleur parti de la variété de structures chimiques, d'architecture polymère ou encore de conditions de température ou de confinement afin de cibler au mieux leurs applications.

Title: Structures and dynamics of Poly(Ionic liquid) in bulk and at interfaces
Keywords: Ionic Liquid, Poly(ionic liquid), Neutron Scattering, X-ray reflectivity, Polymer viscoelasticity

Abstract: Polymerized ionic liquids (PIL) are macromolecules composed of covalently linked ionic liquid (IL) monomers. As such, they present a unique combination of properties from both polymers and ILs and are promising for potential applications as solid-state electrolytes. They inherit their particular nanostructure from ILs, arising from the segregation of the alkyl moiety leading, in imidazolium-based ILs, to a globular structure for short alkyl chains or a bicontinuous sponge-like one for long chains. The addition of such interactions to macromolecules provides new opportunities to design polymer materials with targeted functionalities, highly related to both structural and dynamic properties of PILs.

The present work focuses on a series of imidazolium-based PILs (PC_nVImTFSI) with varying side-chain length n, thereby finely tuning the local interactions. Using small angle neutron scattering and wide angle X-ray scattering, the bulk structure was probed at length scales ranging from the polymer coil to the chain diameter. The former showed a surprising non-monotonic evolution with n, while at the latter scale, interdigitation of was observed for long side-chains. This suggests the flexibility of the main chain varies with n, with a potential contribution of modulated electrostatic repulsions.

Although numerous applications rely on interfacial behaviours, and ILs themselves are unusual in that regard, arranging in a layered structure, very little is known about PILs at interfaces. To address this, we focused on the structure of spin-coated thin films of the same series of PILs using both specular X-ray reflectivity (XRR) and Grazing Incidence Wide Angle X-Ray Scattering (GIWAXS), so that all directions of space were explored. While short side-chain PC_nVImTFSI form homogenous films, a lamellar structure develops in long side-chain ones. Both the interlayer spacing and the in-plane distance between neighbouring chains in the vicinity of the interface depend on the thickness of the film. We suggest a molecular picture of such confinement effect, involving a preferential orientation of pendant groups close to the interface in thinner films.

Besides deeply interesting structural considerations, these materials are also rare examples of polyelectrolytes presenting a melt state, despite their ionic nature, akin to ionomers. An increase in ionic content, however, leads to the loss of ionomers' processability. PILs, on the other hand, have an ionic fraction of 100% without losing their viscoelastic properties. Changing the length of the alkyl side chain, as it was done in our structural study, is a way to vary the polarity of interactions at fixed ion fraction. Hence, the linear viscoelasticity of the PC_nVImTFSI series with varying side-chain length n was probed. These results are discussed in connection with the structural features mentioned above and similarities with associating polymers such as ionomers.

This fundamental approach of the structure and dynamics of a model PIL series with varying side-chain length brought to light some remarkable properties of these materials. Hopefully this could ultimately be extended to other and more complex PIL chemical structures and provide better guidance to make use of the wide variety of IL ion pairs, polymeric architectures, temperature conditions or confinement design to reach precise targeting of applications.

Contents

Acknowledgements - Remerciements

Avec le recul, ces trois ans de thèse sont passés en un clin d'œil, et c'est grâce à tant de gens avec qui je les ai partagés, de près ou de loin, et que je tiens à remercier ici. Beaucoup ont été mentionnés le jour de la soutenance mais j'en ai bien évidemment oublié, on mettra cela sur le dos de l'émotion.

J'aimerais commencer par mes directeurs, Frédéric Restagno et Alexis Chennevière. Fred, Alexis, je n'aurais pas pu mieux tomber. Déjà lors du stage en confinement puis tout au long de la thèse vous avez toujours fait preuve de soutien et de compréhension, professionnellement mais aussi personnellement. Si je devais résumer votre encadrement en un mot ce serait la confiance. Vous m'avez laissé tant d'autonomie, vous saviez que les résultats viendraient même quand j'en doutais moi-même.

Fred, même si j'étais le plus souvent au LLB tu passais me voir dans mon bureau dès que je passais au LPS. Tu as guidé le projet avec toute ton expérience, tu savais recentrer les idées, poser les bonnes questions, pas seulement en tant que chef de projet mais aussi pour être sûr que cette thèse soit la mienne et qu'elle prenne une direction qui me convienne. Tu m'as tellement appris, scientifiquement, sur le monde de l'académique mais aussi humainement. Merci pour tout.

Alexis, tu étais le chef au plus proche de l'action, au quotidien. C'est toi qui as éveillé ma curiosité pour ce projet le jour où j'ai visité le LPS. Et puis on s'est vus dans un café à Denfert à cause des grèves de la RATP. Cet épisode qui peut paraître anodin résume bien l'attention que tu portes aux autres. Tu m'as tout appris, des techniques expérimentales, de la physique, du code, sur la communauté neutrons et j'en passe. J'ai mentionné la confiance, je me souviens quand tu m'as laissé très rapidement gérer le Xeuss tout seul, j'étais moi-même un peu inquiet mais pas toi. Quand je repense à ce que je savais faire il y a trois ans et maintenant je vois à quel point cette thèse m'a formé et c'est grâce à toi, à ta présence, ton enthousiasme et ta curiosité que tu communiques si bien et avec tant de pédagogie. Je ne peux qu'encourager d'autres étudiants à se lancer dans une thèse avec toi. Merci pour tout.

Je voudrais remercier les membres de mon jury, Jean-Paul Chapel, Ralph Colby, Benoît Coasne, Emmanuelle Dubois et Simone Napolitano, d'avoir pris le temps de lire ce manuscrit en détails et d'évaluer ce travail. Je me souviendrai longtemps du jour de ma soutenance, en bien, et c'est notamment grâce à vous. Les discussions que nous avons eu pendant les questions, toujours de manière bienveillante et avec un intérêt sincère ont rendu ce jour inoubliable. Un remerciement en particulier au Pr. Ralph Colby pour nos discussions à Cargèse puis à Athènes, et ses conseils qui m'ont permis d'aller plus loin dans la compréhension de nos résultats de rhéologie. J'ai hâte de rejoindre votre équipe en postdoc.

Cette thèse a aussi été l'occasion de collaborer avec plusieurs personnes, à commencer par Eric Drockenmuller chez qui les matériaux ont été synthétisés. Merci

Eric d'avoir accompagné ce projet, de m'avoir expliqué toute cette synthèse, de m'avoir accueilli à Lyon et d'avoir fait partie de mon jury. Merci à Antoine Jourdain, Shona O'Brien puis Rania Akacha qui ont successivement pris la main sur la synthèse. Merci à l'équipe à l'IMP, que j'ai pu côtoyer à Lyon mais aussi à l'EPF à Prague. Merci Rania, de m'avoir supporté une semaine à Lyon, un peu démuni dans un labo de chimie.

Puis vient la rhéologie et la collaboration avec Guillaume Miquelard-Garnier et Jorge Peixinho. Merci à tous les deux de m'avoir accueilli au labo pour profiter de votre expertise de rhéologie de fondus de polymère, et pour tous vos conseils et merci à Guillaume d'avoir accepté de faire partie de mon jury. J'aimerais également remercier Cyrille Sollogoub que j'ai croisé à plusieurs reprises ainsi que les thésards du PIMM, de très bonne compagnie à l'EPF à Prague ainsi que pendant mes journées de manips au PIMM. Anna Dmochowska, en particulier, merci pour ta compagnie et ton soutien, notamment à l'ICR à Athènes quand il a fallu se lancer et aller discuter avec certains professeurs.

Merci également à Joshua McGraw de m'avoir accueilli à l'IPGG pour ces expériences d'AFM, après que l'on ait discuté de tes idées sur les films fins à Grenoble.

Un grand merci aux local contacts pendant les manips grands instruments (rayons X et neutrons), Arnaud Hemmerle à SOLEIL, à Viviane Lütz Bueno à PSI en Suisse et Philipp Gutfreund à l'ILL.

Je tiens à remercier également mon comité de suivi de thèse, Patrick Judeinstein et Michel Cloître pour nos discussions, et votre bienveillance.

À mes deux équipes, MMB au LLB et MMOI au LPS, un immense merci pour un quotidien si agréable. Ce n'est pas toujours évident de faire sa place dans deux labos mais vous m'avez toujours si bien accueilli. Merci en particulier à Marie Corpart, sans qui je ne serais peut-être pas venu ici en thèse. Tu m'as convaincu de me lancer, si bien accueilli au labo et accompagné pendant bien deux ans de thèse. Un grand merci à tout le reste de l'équipe MMOI avec ses permanents, ma co-bureau Emmanuelle Rio, Anniina Salonen, François Boulogne, Christophe Poulard, Liliane Léger, Dominique Langevin, Sandrine Mariot et Laura Wallon ; les non-permanents qui m'ont accueilli et sont malheureusement partis avant moi Manon Marchand, Raphaelle Taub, Marina Pasquet, Chiara Guidolin, Aymeric Duigou-Majumdar, Julian Wailliez ; mes trois cothésards Suzanne Lafon, Alexis Commereuc, Elina Gilbert; et celles et ceux qui restent Alice Requier, Alice Etienne-Simonetti, Théophile Gaichies, Marion Berry, Salomée Berland et Victor Ziapkoff.

Du côté du LLB, je tiens à remercier tout le laboratoire et en particulier l'équipe MMB. Merci notamment à Marion Grzelka, pour tous tes conseils, ton aide et ton soutien, déjà depuis Amsterdam puis d'autant plus après ton arrivée au LLB. Merci à tous les permanents de l'équipe et en particulier à Annie Brûlet, Fabrice Cousin, Clémence Le Coeur, Stéphane Longeville, Christiane Alba-Simionesco, Daniel Dudzinski, François Boué, Lay-Theng Lee et Marianne Bombled pour tant de bons moments, nos discussions et vos conseils. Merci à Arnaud Hélary pour cette cellule de préparation de galettes de polymères qui m'a fait gagner un temps fou. Un grand merci à tous les non-permanents également, Maja Napieraj et Oriana Osta qui m'ont accueilli en stage puis en début de thèse avant que l'équipe ne se renforce en thésards que je remercie aussi, notamment Maëva Almeida, Christelle Saade, Manon Pépin, Qiang Zhang. Merci à Émeline Esnouf pour les quelques mois

que tu as passés au labo et qui ont marqué ma thèse.

Entre ces deux labos il y avait, comme moi, Suzanne Lafon, que je remercie pour tant de moments mémorables. On a commencé par déménager une table optique dès notre première semaine de thèse. S'en s'ont suivies des manips grands instruments à SOLEIL et à l'ILL, une coloc en école d'été à Cargèse, une conf à Athènes. Je n'aurais pas pu tomber sur une meilleure cothésarde avec qui partager ces trois ans. Je me dis souvent que tu m'as aidé incroyablement plus que ce que j'ai pu faire pour toi, un immense merci.

Je tiens bien évidemment à remercier les directeurs des laboratoires pour leur accueil, Sylvain Ravy puis Pascale Foury au LPS et Eric Eliot puis récemment Arnaud Desmedt au LLB, ainsi que les équipes de direction. Une thèse ne serait pas possible sans toutes les ressources qui sont mises à notre disposition. Enfin, il reste également les équipes administratives et financières à remercier, indispensables à faire tourner les labos, et notamment Véronique Bellu et Mélanie Décraëne au LPS, pour votre réactivité et votre efficacité, vous nous rendez la vie tellement plus simple au quotidien. AU LLB, c'est Sarah Même et Olivier Sineau que je voudrais remercier tout particulièrement, pour les mêmes raisons mais également pour votre soutien sur le plan humain, et pour faire autant partie de l'équipe. Je venais souvent vous voir pour des sujets un peu pénibles mais c'était toujours un plaisir. Du côté de l'école doctorale je tiens à remercier Véronique Terras qui rend les procédures avec l'ED tellement plus simples.

J'ai eu aussi l'occasion, pendant cette thèse, d'effectuer quelques missions. À ce propos, je voudrais remercier Véronique Meder et toute l'équipe à la Direction de la communication de l'université de m'avoir accueilli, de m'avoir donné le goût du journalisme scientifique et l'opportunité de discuter avec tant de chercheuses et chercheurs de l'université. Merci également à Matthieu Vincendon, Fabien Cailliez et Pierre Morel qui m'ont confié des enseignements.

En sortant de l'université, c'est maintenant mes amis, dont beaucoup sont venus jusqu'à Orsay pour ma soutenance, que je veux remercier. Merci tout particulièrement à Baska, Vincent, Alexandre, j'ai adoré qu'on ait assisté aux soutenances des uns et des autres, que l'on se soit épaulés pendant ces trois ans et pour votre aide, même quand je ne sais pas la demander. Jacques merci pour notre amitié qui n'a pas besoin de beaucoup. Adèle merci d'être toujours là pour moi, dans les bons moments comme dans les plus difficiles. Merci à toutes et à tous pour votre soutien inébranlable depuis maintenant plusieurs années.

Un grand merci à ma famille, et notamment ma sœur qui a vécu cette thèse au plus près. On en a traversé des choses ensemble et s'il y a une personne sur qui je sais que je peux compter c'est bien toi. Un immense merci à ma mère pour m'avoir accompagné et encouragé inconditionnellement pendant tout mon parcours, quelques soient mes choix. Ce qui m'amène à mon père, qui n'est plus avec nous mais qui aurait adoré suivre cette thèse et être là le jour de la soutenance. Je présente souvent ce travail comme je te l'aurais expliqué. Merci pour tout et notamment de m'avoir poussé, parfois trop à mon goût, mais finalement sans quoi je ne serais probablement pas arrivé jusqu'ici aujourd'hui. Cette thèse est pour toi.

General introduction

The point of these introductory remarks is to step into the subject of the present work stripped, for now, of its scientific and fundamental aspects. The term poly(ionic liquid) probably speaks to the reader, if it does, in many ways depending on their background. The etymology of the word already indicates they are polymers in which the repeating unit contains an ionic liquid. With this simple definition, a number of physical and chemical concepts have already surfaced and need some introduction.

Polymers have been used by humankind for centuries before they were effectively called polymers. The prime example of that is natural rubber, which first use traces back to Aztec and Maya cultures, namely to waterproof textiles. By the 19$^{\text{th}}$ century, its properties, and namely its resistance, were better controlled, making it the material of choice for car tires. The first synthetic plastic, Bakelite, came in the early 20$^{\text{th}}$ century. It soon spread to most industrial sectors due to its unmatched availability and processing simplicity. Yet, the understanding of polymers was at the time quite limited. The first picture of large molecules, *i.e.* macromolecules, which today defines polymers was only put forward in the 1920s by H. Staudinger. His idea was met, like all breakthrough discoveries, with a lot of criticism but, once accepted, delivered the basis for substantial advances in the fundamental understanding of polymers. Polymer physics quickly developed in the following decades with mathematical descriptions of a polymer chain, its size and thermodynamics and their subsequent refining into a statistical description that led to complete theories of how chains relax, diffuse and flow. These allowed a better control over the macroscopic properties of polymers and contributed to the surge of performance materials, further widening the range of applications beyond the plastic industry.

At the centre of chemical physics and the understanding of condensed matter, are molecular interactions. How atoms and molecules interact with each other shapes the macroscopic properties of the material. Initially, they were described as discrete interactions between point-like objects, either attracting or repelling each other. A crucial paradigm shift came with the probabilistic concepts of statistical mechanics in the later half of the 19$^{\text{th}}$ century providing continuum thermodynamics and mean field theories which succeeded in describing a large number of molecules, where previous theories failed. Following the advent of quantum physics in the early 20$^{\text{th}}$ century, a variety of intermolecular interactions could be classified under unifying concepts. Excluding quantum interactions which govern interactions at a smaller scale, such classification distinguishes purely electrostatic and entropic interactions. The latter stems from collective motion which, to keep it simple, promotes disorder. They are essential in polymers due to their large size and numerous possible conformations. Among purely electrostatic interactions is the most conspicuous one, that between effective charges. Positive and negative charges attract

each other, whereas same charges repel each other. Other interactions between atoms, hence neutral species, are also electrostatic in origin as revealed by quantum physics, but rely on dipole polarization effects. In other words, their surrounding confers them with temporary polarized states, hence a transient charge-like behaviour although undeniably weaker. Ions, in contrast, have permanent effective charges. The strong Coulomb interactions between them is the reason most ionic compounds are crystals, like table salt NaCl, meaning they form a nicely arranged structure to maximize the close contact between opposite charges. Only when dissolved, in water for instance, can ions actually diffuse and transport charges, hence delivering what is intended for electrolytes in batteries or other energy storage and delivery devices. Charges can also be bonded together to form a polyelectrolyte, an ionic polymer. These are actually widely present in living matter, and DNA itself is a polyelectrolyte. They have deeply contrasting properties in solution compared to their neutral counterparts, and open up additional possibilities by creating complexes with other charged species. However, in the absence of solvent, unlike non-ionic polymers, pure polyelectrolyte is crystalline like the building block salt, and cannot be processed or moulded like other polymers.

Of course, salts also have a melting temperature above which the molten salt is liquid, yet without any water or solvent. However, these temperatures are usually too high for conventional electrolyte applications, let alone for investigation equipment in the early 20^{th} century. The latter is the reason salts with low enough melting temperatures were sought, leading to the first report of an ionic liquid. Such a high density of charges in a liquid at room temperature without any water is quite puzzling, but also tremendously promising to meet the increasing demand for electrolytes in the late 20^{th} century. As we will see, their application go nonetheless far beyond. It is at this point that the topic of the present work steps in. In keeping with these fundamental interests and promising applications, polyelectrolytes formed by ionic liquids as building block, hence termed poly(ionic liquid)s, form hybrid materials. They are processable and can be moulded like neutral polymers and yet preserve the high density of charges of ionic liquids. They initially offered a way to improve the mechanical properties of ionic liquid electrolytes but rapidly became a staggeringly promising polymeric material on their own and in many ways unique, compared to both ionic liquids and polyelectrolytes. As of today, the understanding of poly(ionic liquid)s is still clouded, either because of the still unsettled debates on ionic liquids themselves or their unique character of processable polyelectrolytes.

To understand, let alone predict, the behaviour of materials, a closer look at their structure down at the molecular scale is often required. Just like a civil engineer working up a structure to meet specified requirements, a chemical engineer does not go without observational and measurement techniques. Those are nonetheless quite different in the engineering of the nanoscopically small. A precious magnifying glass is afforded by how light or other radiations behave when going through the material. Atomically precise measurements can be traced back from the study of scattered patterns or reflected intensities. From these nanoscopic observations, the chemical synthesis and all the way to the macroscopic properties, the physical chemist must put everything together to uncover the molecular mechanisms involved.

The ambition of the present work is to provide a few contributions to the ongoing efforts in unravelling the complex interplay between ionic interactions and

polymeric behaviour in poly(ionic liquid)s, or at least one particular class of them. We will use scattering in different setups to go down the rabbit hole into the structure at the molecular scale. We will first travel around the bulk, afterwards moving to the interface with a solid and finally deform the material to see how it behaves. Hopefully these brief introductory considerations sparked some curiosity and, without further due, we will give a more detailed description of ionic liquids and their polymerized form in the following Chapter 1. The unanswered questions we intend to contribute to will be more precisely formulated therein. We will then move on to our specific poly(ionic liquid) series with tunable polarity of interactions which delivered precious results regarding the role of local interactions on their bulk structure in Chapter 3, their interfacial one in Chapter 4, that of nanoparticles in Chapter 5 and finally their viscoelasticity in Chapter 6.

Chapter 1

Introduction

After our introductory considerations, we start the present work with a brief review of the state of the art regarding ionic liquids (ILs) and poly(ionic liquid)s (PILs). A historical perspective on how they became a promising research topic in both materials science and fundamental soft matter physics is given in section 1.1 before moving on to a more scientifically detailed description of the current state of understanding of their structure in bulk and at interfaces respectively in sections 1.2 and 1.3. Dynamics of ILs and PILs are respectively discussed in sections 1.4 and 1.5. A particular emphasis is also put on associating polymers in the latter, as they provide precious insights into the viscoelasticity of PILs.

1.1 Introduction to ionic liquids and their polymerized form

ILs are organic salts namely characterized by an unusual melting point typically below 100 °C, a lot of them being actually liquid at room temperature which confers them with the name Room Temperature Ionic Liquids (RTIL). Contrary to conventional salt solution electrolytes such as table salt NaCl in water, ILs are composed solely of ions, they are molten electrolytes. Their large size, typically five to ten times larger than monoatomic ions, induces weaker electrostatic interactions. Additionally, their asymmetric structure, usually containing alkyl chains, allows for considerable conformational entropy, hence their characteristic low melting point. Examples of such chemical structures are given in Figure 1.1a. This grants them with a wide panel of thermal, physical and electrochemical properties as well as an enhanced ionic conductivity compared to usual electrolytes. They have attracted wide interest for several decades now, but while they are often referred to as novel materials, they have actually been around for over a century.

The emergence of a new class of electrolytes

The earliest report of ILs traces back to P. Walden in 1914 [3]. As mentioned in the introductory remarks, he sought a molten salt with a low enough melting temperature simply for practical reasons and limitations of his equipment. The finding went essentially unnoticed for nearly 40 years until F.H. Hurley and T.P. Weir reported the use of ILs as a medium for electrodepositions of metal coatings [4] which remains to this day an important application of ILs, benefiting from the good solubility of metal ions. Subsequent use of ILs in the following decades was

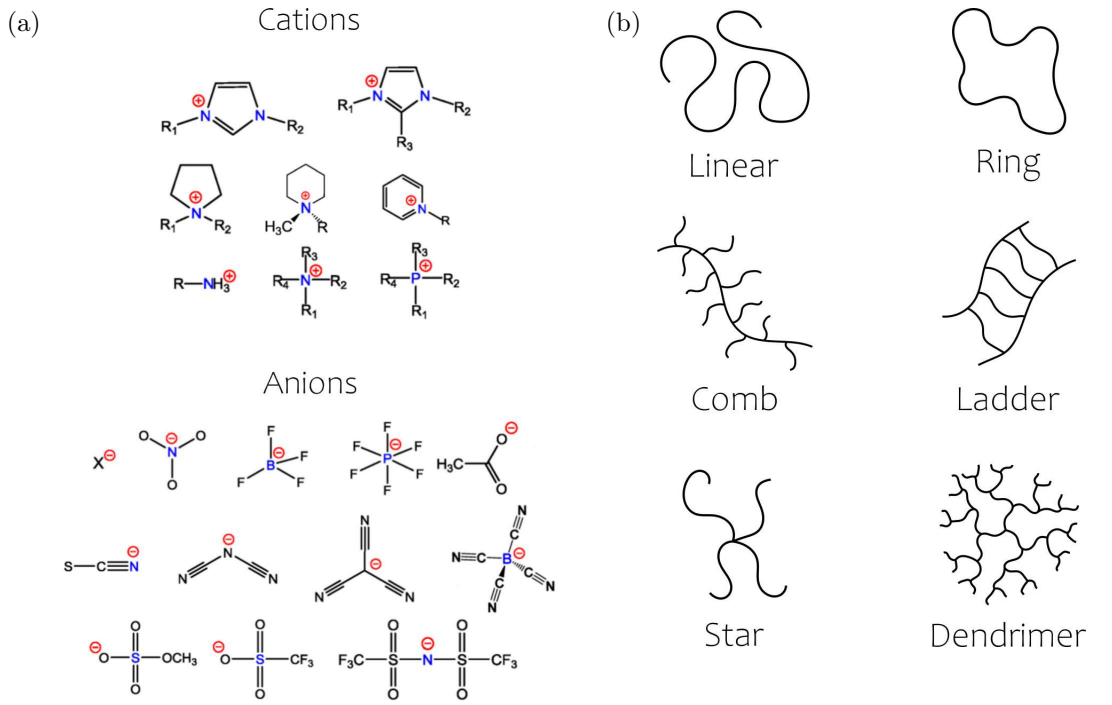

Figure 1.1: (a) Examples of Ionic Liquid (IL) chemical structure reproduced from ref. [1]. In reading order, cations : dialkylimidazolium, trialkylimidazolium, dialkylpyrrolidinium, 1-alkyl-methylpiperidinium, N-alkylpyridinium, alkylammonium, tetra alkylammonium, tetraalkylphosphonium. Anions : halides, nitrate, tetrafluoroborate, hexafluorophosphate, acetate, thiocyanate, cyanamide, tricyanomethanide, tetracyanoborate, methylsulfate, trifluoromethanesulfonates, bis(trifluoromethylsulfonyl)imide (TFSI) (b) Examples of polymer architectures inspired from ref. [2].

mainly as media for other chemical processes, such as electrochemistry of metal complexes [5] or synthesis and catalysis [6, 7]. Yet very little fundamental research was undertaken on neat ILs.

Some characterization of ILs and their structure started nonetheless to emerge in the 1980s [8, 9]. The introduction, by J. Wilkes *et al.*, of imidazolium based cations [10] which would become the most popular for IL ion pairs, triggered a debate around their structure. Some advocated the role of hydrogen bonding [11] which was rather popular at the time. However, reports on infrared spectroscopy of imidazolium ILs with varying substituting groups unveiled the limitation of such model and suggested instead a molecular picture of stacking of the anion on both sides of the imidazolium rings [12]. The controversies were only starting. Until then, ILs were regarded as homogenous solvents. The first breakthrough result suggesting otherwise was reported by R.G. Horn *et al.* who revealed the layering of ions at the solid-IL interface using aqueous solutions of ethylammonium nitrate $[EtNH_3][NO_3]$, the first IL reported by P. Walden, in a Surface Force Apparatus (SFA) [13]. This finding sparked increasing interest in ILs themselves instead of the chemical processes that could be performed using them.

The growing interest for these materials benefited from both chemistry developments and progress in characterization techniques [14]. While some ILs were already

sold as stationary phases for gas chromatography as early as the 1980s, their commercial availability really flourished towards the end of the 1990s [14]. The green chemistry movement was also gaining momentum and ILs appeared as a perfect alternative to conventional solvents, namely due to their very limited volatility. Their intrinsic ionic character called for use as electrolytes, which sparked research interest in the field [15] and really skyrocketed in the 1990s with the synthesis of less reactive ILs and an increasing demand for new battery technologies for smaller devices. Compared to conventional lithium batteries, ILs provide a safer nonflammable base material. They are also particularly well suited for fuel cells [16], dye sensitized solar cells [17] or supercapacitors [18].

The fundamental approach to ionic liquids

The turn of the century also marked the start of research into a deeper understanding of the structure of ILs, moving away from the direct application and into a fundamental approach. The use of X-ray scattering [19] and neutron diffraction [20] revealed the great influence of the counterion, either by its size or its ability to form hydrogen bonds, and of the length of alkyl tails on the cation granting the IL with liquid crystalline properties when long enough. Breakthrough numerical simulations unveiled a bicontinuous structure driven by the segregation of the apolar moiety from the ionic one at the nanoscale [21]. This was soon after confirmed experimentally by X-ray scattering [22, 23].

At that time, and motivated by R.G. Horn *et al.* SFA experiments mentioned above, ILs were also reported exhibiting promising lubrication properties [24] due to their layered interfacial structure. Considerable findings at interfaces were made using either SFA, Atomic Force Microscopy (AFM) or X-ray reflectivity. The molecular layering of ILs will be discussed further in section 1.3 and their lubrication properties in section 1.4.3. In part from these studies at interfaces emerged an important debate around ionic arrangements in ILs. Additionally, to the molecular layering, the presence of long range forces was also reported. Such observations imply that ILs behave as dilute electrolytes made of only a few free ions and larger neutral associated structures, ion pairs or aggregates. This debate, which will be the focus of section 1.4, is still unsettled today.

Polymerized ionic liquids

Although ILs present a promising panel of applications that go surprisingly beyond their high conductivity, they lack a precious requirement for most of them : robust mechanical properties. Their bulky and polyatomic structure offers nonetheless the possibility to functionalize them with a polymerizable group such as vinyl, acrylate or acrylamide to name the most usual ones. Hoping to benefit from polymeric properties such as viscoelasticity and processablity, polymerizing ILs appeared as a way to improve their mechanical properties. The interest in PILs picked up momentum in the fields already involved in IL research such as catalysis, separation, analytical chemistry, and electrochemistry but also became an emerging interdisciplinary topic among polymer chemistry and physics and materials science. Initially, they appeared to play a purely complementary role towards the amplification of the functions of ILs, delivering performances that could not readily be afforded by molecular

ILs [25–27]. However, they markedly differ from their parent IL and other polymer electrolyte mixture in the sense that polymerizing the cation, for example, hinders its mobility, thus forming a single ion conductor in which the unaltered counter ion provides the main contribution to conductivity.

Despite being first synthesized in the 1970s [28], the understanding of the macroscopic properties of these materials is still vague, and many challenges are yet to be overcome. Polymerization usually comes with a loss of conductivity of a few orders of magnitude compared to molecular ILs, which constitutes a major shortcoming for electrochemical applications. Improving such properties and precisely targeting the desired functionalities for these materials requires a complete understanding of their structure and dynamics. Yet, research on the morphology of homopolymer PILs is rather recent. As conductive materials, the main concern was their conductivity and how to enhance it. Therefore, a variety of PIL systems and their conductive or mechanical properties were reported, such as PIL copolymers forming lamellar phases [29]. These studies provide nonetheless some hints of universality across chemical structures. For example, larger anions lead to a decreased T_g and thus a higher conductivity [30], not unlike ILs. A clear picture of the morphology of PILs started to appear around a decade ago with similar techniques as the ones used for ILs including X-ray scattering [31–33] and numerical simulations [34, 35]. As will be discussed in section 1.2, their local bulk structure shares many features with that of ILs.

Rapid advances in the chemistry and physics of PILs have paved the way to the development of novel and versatile polymer electrolytes that are highly relevant for both applied and fundamental research [36–38]. Combining the variety of available ion pairs and polymeric architectures (Figure 1.1b) results in a wide range of possible chemical structures. The IL unit can also be arranged in different layouts, placed on the backbone or the side chain of either a homopolymer, block or random copolymer. PILs thus offer an ideal diversity and versatility to develop new materials for various applications including dye-sensitized solar cells, fuel cells, batteries, or sensors [29, 39–43].

Targeting these potential applications efficiently requires, however, a deeper understanding of the interplay between the morphology of PILs, now rather well known at local scales, and their properties. The complexity of these materials is better grasped by splitting it into two conceptual threads. The most straightforward one starts at the original IL building block, the molecular liquid form, to see how its structure and dynamics are affected by polymerization and to what extent they relate to the original material. However, by doing so, the polymeric nature of the resulting PIL is left out. As viscoelastic ion-containing polymers, their dynamics unfold from both polymeric systems and ionic interactions, let alone that PILs are a rare case of viscoelastic homopolymer polyelectrolyte offering a case study of polyelectrolyte bulk behaviour. Accordingly, along this chapter and the following, structure considerations will be mainly led as a comparison between PILs and ILs, from which the main focuses of this work such as chain conformation or interfacial structure of PILs will naturally arise. For the dynamics of these materials, their perception as associative polymers, as it will ensue from their structure, will appear as a much more relevant approach.

1.2 Local bulk structure

Due to their high density of charges, ILs inevitably present short-range organization due to charge ordering. Quite surprisingly, this short-range ordering does not lead to long-range order as in crystalline phases and this is sometimes considered as the defining trait of ILs [44]. The IL cation usually features an apolar part, most often an alkyl chains (Figure 1.1a) thus possessing an amphiphilic structure with polar and apolar moieties leading to a local solvophobic-induced phase separation. This nanoscale segregation drives the heterogeneity of their bulk structure, which was debated for quite some time.

1.2.1 The road to consensus on IL mesoscopic structure

The first suggestion of a mesoscopic, *i.e.* an intermediate-range, ordered structure of ILs was put forward by U. Schröder *et al.* [45]. The authors investigated the diffusion of compounds across ILs with controlled water content and revealed that traces of water enhance the diffusion of ionic species considerably more than that of neutral ones. The confirmation of a nanostructured media came from molecular dynamics (MD) simulations. Two groups independently revealed self-assembly of alkyl tails of imidazolium cations, governed by the chain length [46, 47]. However, both contributions allege cation head groups and anions are distributed homogenously. While supporting the first point, the breakthrough simulations performed by J. Canongia Lopes and A. Pádua unveiled the charged domains were not homogenously distributed, but instead formed a continuous ionic network [21]. In these large ionic domains, short aggregated apolar groups, depicted in green in simulation snapshots reproduced in Figure 1.2a, occupy small isolated globular regions. They become larger with increasing length of alkyl side-chains, until they interconnect across the bulk liquid, thus forming a bicontinuous sponge-like structure with intertwined apolar and ionic domains. The percolation threshold, as we will refer to it in the following, happens for 4 carbon-long side chains.

Experimentally, the bulk structure of various ILs was extensively investigated by X-ray [22, 49–52] or neutron scattering [20, 52–55]. The mesoscopic structure of ILs translates into a correlation peak, denoted I in Figure 1.2b, strongly dependent on the length of the alkyl tail, progressively sharpening and gaining in intensity towards longer alkyl chains. This so-called prepeak has been at the centre of long-lasting debates. The first attempt to explain it, and therefore describe the structure of ILs, relied on a natural analogy with surfactants and a micelle-like model of aggregates of apolar tails surrounded by a polar shell. While it was supported by scattering measurements suggesting for example enhancement of long-range order by longer alkyl tails, it failed to explain for instance the unusually wide range of surface tension values [56].

Despite being absent from X-ray scattering patterns for short side chains, evidence of the prepeak has been reported by neutron scattering [54], and substantiated by numerical simulations [23]. Notwithstanding the authors' conclusion that the correlation peak was not a signature of nanostructure, A. Triolo *et al.* settled the debate by comparing identical imidazolium based ILs, with either an alkyl tail or an ether one. The latter showed no prepeak due to higher ion solvating properties

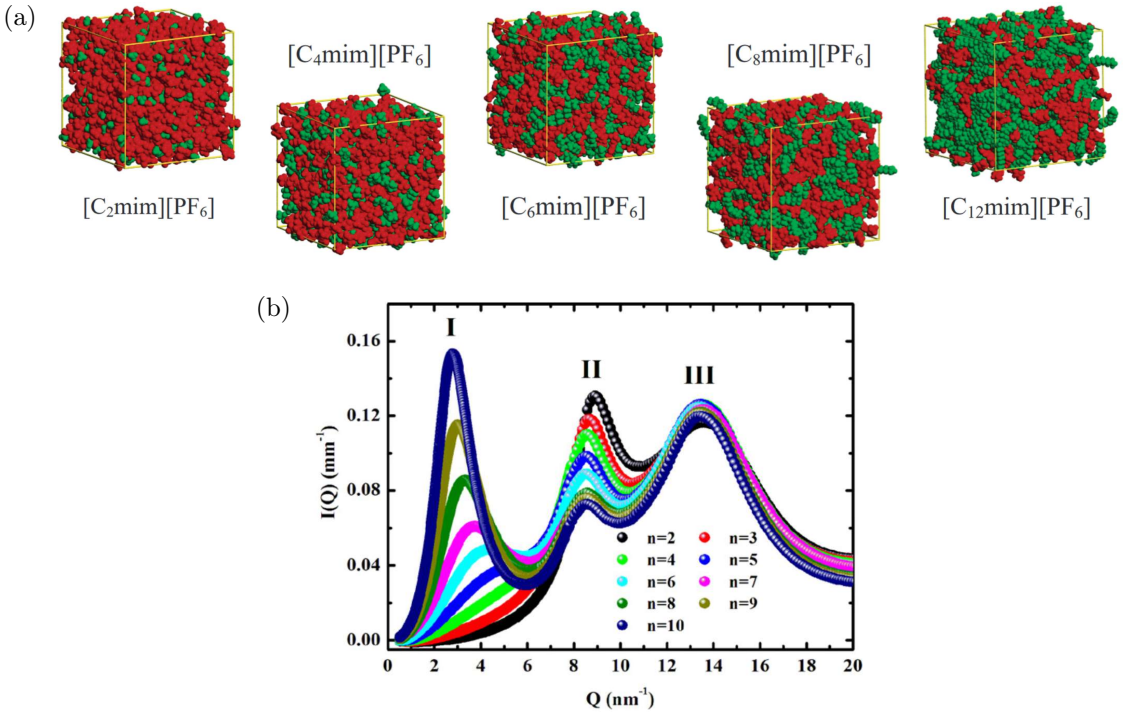

Figure 1.2: (a) Snapshot of simulation boxes for 700 ions of imidazolium based IL [$C_n$mim][PF_6]. Ionic and apolar domains appear respectively in red and green. Alkyl chain length n increases from left to right n = 2, 4, 6, 8 and 12. Figures reproduced from ref. [21] like in ref. [48]. (b) X-ray scattering patterns for a series of imidazolium based ILs with TFSI counter anion [$C_n$mim][TFSI] with n = 2-10 taken from ref. [49].

of ether tails [51]. The scattering patterns exhibit two other peaks at slightly larger values of scattering vector Q, essentially originating from first neighbour interactions and intramolecular correlations [49]. This will be discussed in more details in Chapter 3 dedicated to the bulk structure of PILs.

1.2.2 Consistency upon polymerization

Interestingly, the polymerized form of ILs exhibit rather similar local bulk structures. This stands out in the numerous X-ray scattering studies on PILs [32, 33, 57, 58]. The transition to PILs is well illustrated by F. Wieland *et al.* who investigated a series of ammonium based PILs with varying degrees of polymerization (N) ranging from molecular ILs to a hundred repeating units PIL. Their nanostructure was shown to be independent of N above 10 repeating units [59].

Given the importance of the polarity of interactions, controlled by the size of the apolar moiety, *i.e.* the side chain length, in shaping the bulk structure of ILs, it was natural for most of the works cited above to vary this parameter in PILs. Together with MD simulations, namely the work of H. Liu and S.J. Paddison [34, 35], a similar clustering of apolar domain was revealed as shown in Figure 1.3a. As the side chains become longer, clusters grow larger, finally percolating above 4 carbons and forming one large cluster spanning the whole simulation box. This growth of apolar domains is seen on X-ray scattering patterns such as the ones given

in Figure 1.3b, by the shifting motion of the low-Q peak with increasing n. This peak, signature of a mesoscopic structure as in ILs, can also be attributed to the distance between PIL backbones. This was confirmed by simulations and selective deuteration techniques [34, 35]. Earlier works on side-chain polymers such as a series of poly(n-alkyl methacrylates) or poly(n-alkyl acrylates) [60–62] supported the above observations with similar self-assembly of apolar domains and a similar scattering signature.

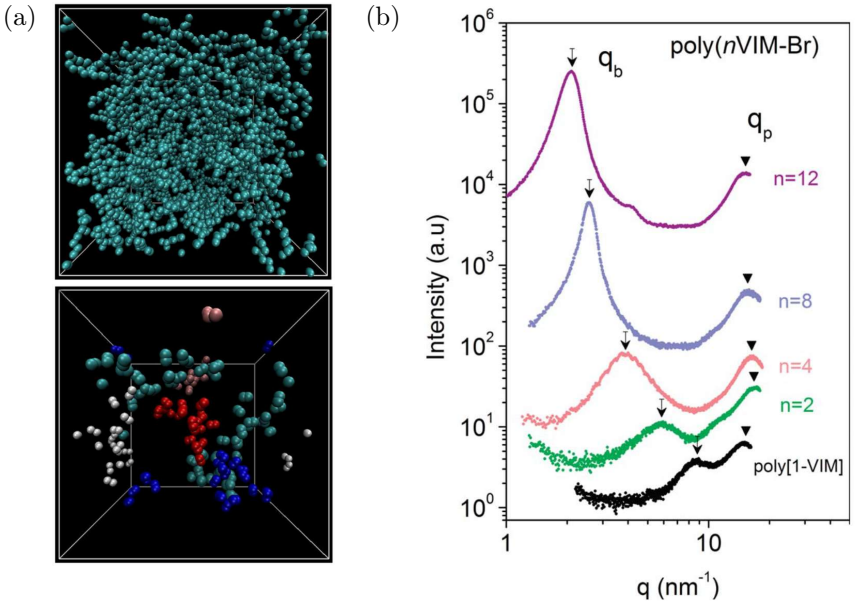

Figure 1.3: (a) Simulation snapshot of imidazolium based PILs with varying side chain lengths (from top to bottom) $n = 2$ and 8. Only the nonpolar domain is represented. Each individual cluster is given a specific colour, the larger one is coloured in cyan. Figures reproduced from ref. [35]. (b) X-ray scattering patterns for a series of imidazolium based PILs with bromide counter anion and varying side chain length n taken from ref. [32].

Notwithstanding the shared features between PILs and ILs' bulk structure, the implications on polymer chain conformation have been very little to not investigated at all. Our contribution to this matter will be discussed in Chapter 3 in which the conformation of PIL chains and their structure at the length scale of the whole polymer coil is investigated in bulk and solutions using neutron scattering, thus also overlapping with the more local structure. Regardless, from the local bulk structure of these materials alone naturally arises the question of how they behave at interfaces.

1.3 Interfacial structure

1.3.1 Interfaces in classical frameworks

It is well known that the presence of an interface disrupts the bulk structure in molecular liquids or polymer melts [63] and as such, physical characteristics usually

deviate from the bulk ones at interfaces. A good example is the surface melting of most crystalline materials, which leads to a thin liquid layer at their surface several degrees below the melting temperature. Conversely, surface freezing also occurs in some situations such as linear alkane melts. A monolayer of crystalline phase spontaneously forms at the surface of the melt above the freezing temperature due to the alignment of the rod-like molecules [64]. More generally, the glass temperature in thin polymer films is usually lower than the bulk value [65].

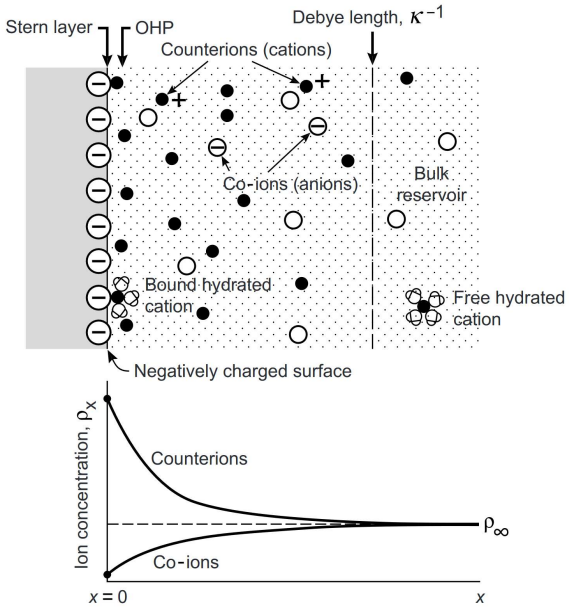

Figure 1.4: Schematic representation of the solid-electrolyte interface in the classical framework. Cations represented as filled black circles form an adsorbed layer, so-called Stern-layer, on the negatively charge surface. Beyond the so-called outer Helmoltz plane (OHP) is the diffuse layer in which the ion distribution verifies the Poisson Boltzmann equation. The decay of the diffuse layer happens over the Debye length, depicted as a dashed line. Figure taken from ref. [63].

The concentration of solutes in a solution also differs near the interface. The solid-electrolyte interface is generally well described by a so-called electrical double layer, as mentioned above and represented in Figure 1.4. As most substrates present at least a small surface charge, ions of opposite charge form a packed first layer of ions, the Stern layer, followed by a so-called Gouy Chapman diffuse layer in which the ion distribution verifies the Poisson Boltzmann equation. The charge excess in that layer, either cationic or anionic depending on the surface charge, decays over a characteristic length called the Debye length κ^{-1}, inversely proportional to the free ion concentration, *i.e.* the ionic strength. In such a medium, a second interface interacts with the first one by competing Van der Waals forces between the surfaces and electrostatic repulsion between the diffuse layers. This constitutes the DLVO description. [1] Describing ILs in such a way, as hazardous as it may seem, leads to

[1]Named after B. Derjaguin and L. Landau who introduced it in 1941, and independently later on in 1948 E. Verwey and T. Overbeek, to account for the dependence of colloidal dispersions' stability on the ionic strength of the medium which was not readily explained by Debye Hückel linearized theory of 1923.

a diffuse layer subatomically thin due to their high ionic density.

1.3.2 ILs novel interfacial behaviour

Many of the underlying assumptions in the DLVO description are not valid in the case of ILs due to their high density of charges and the absence of a solvent of constant permittivity. Charge correlations are consequently expected to be much harder to predict. There is, at first glance, no reason they should behave in a DLVO fashion, let alone that ILs are far from point-like spherical objects and instead have large and bulky structures. The first pioneering SFA report by R.G. Horn *et al.* [13] on ILs interfacial structure actually proceeds from a dilute DLVO-like solution of ILs to neat ILs. The authors observed a transition from a monotonous force profile, as predicted by a DLVO description, to an oscillating one as the concentration of ILs is increased. The extensive research this first report motivated in the SFA community delivers a rather straightforward idea of the molecular picture [66–69]. As plates of the SFA are brought together, the IL film is squeezed-out discontinuously, thus producing typical oscillatory force profiles such as the ones reproduced in Figure 1.5. This originates from molecular layers being squeezed out from in between the plates. Although surface layering is also found in apolar liquids, ILs present much larger force profile oscillation amplitudes over an extended range due to the strong electrostatic interactions to overcome to deform the layering.

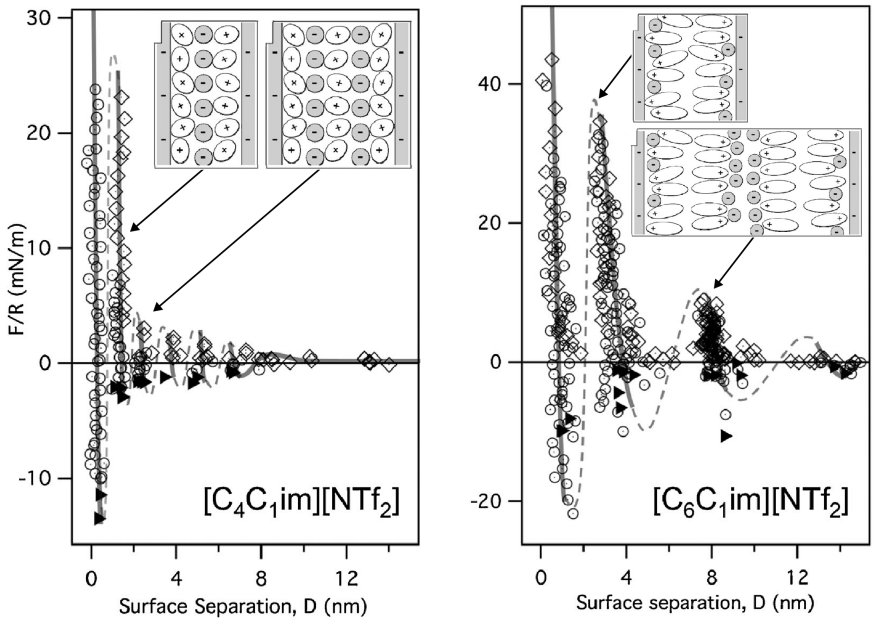

Figure 1.5: Force measured between two mica surfaces of a SFA normalized by surface curvature R as a function of film thickness D for imidazolium ILs with alkyl chain lengths $n = 4$ (left) and $n = 6$ (bottom) and TFSI anion taken from ref. [70]. Inset sketches represent the molecular interpretation of these oscillatory profiles.

Even though SFA gives a good intuition of molecular arrangements, it comes with two important drawbacks. It inevitably confines the material between two solid interfaces and, in the case of layering, can hardly inform about the layers' composition. X-ray reflectivity (XRR) measurements [71–73] nonetheless confirmed the

molecular layering over several ionic layers as observed in SFA but at an isolated interface, where confinement is not a factor, and provided additional details. XRR is an indirect technique, which will be detailed more thoroughly in Chapter 4, but fitting of the data delivers the density of electrons in the normal direction to the interface. The oscillatory profile at the IL-solid interface was shown to be best described as a succession of overlapping and broadening Gaussians representing cations and anions contributions [72] (Figure 1.6). The layering exponentially decays towards the bulk over several nanometres. For short alkyl chains, this layering was shown to correspond to charge alternating layers, but longer alkyl chains also cause amphiphilic self-assembly, leading to a tail-to-tail bilayer structures [67]. For imidazolium based ILs, the threshold between these two structures lies again at 4-carbon side-chain, similar to the percolation point of apolar domains in the bulk mesoscopic structure.

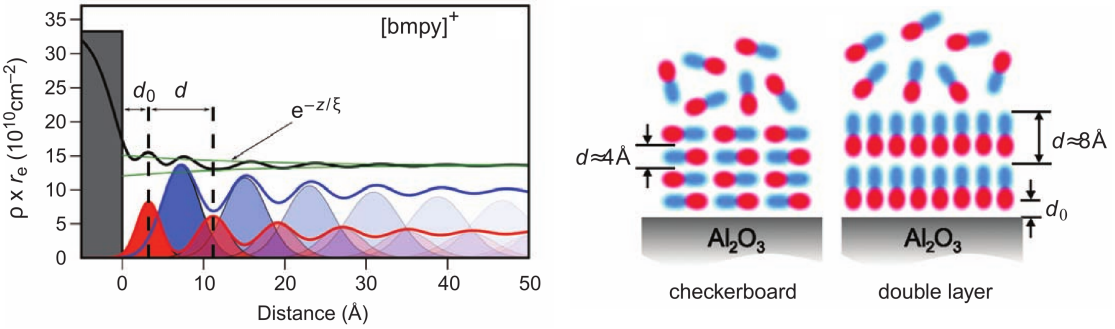

Figure 1.6: Electron density profiles at the solid-IL interface determined by X-ray reflectivity on a pyridinium based IL with $n = 4$ and tris(pentafluoroethyl)trifluorophosphate (FAP) anion at a charged sapphire surface. The right panel shows representations of two possible interpretations. Taken from ref. [72]

1.3.3 Solid-solid interfaces and confinement of poly(ionic liquid)s

An important drawback brought by polymerizing ILs is a loss of conductivity of a few orders of magnitude, which constitutes a major detrimental shortcoming for electrochemical applications. One way to enhance conductivity of the resulting PIL is to confine it. This proved efficient for ILs either confined in nanotubes, nanoporous matrices, [74, 75] or simply thin liquid films [76]. The benefits of confinement largely rely on the interfacial structure of the material near a substrate. Given the similarities of local bulk structure between ILs and PILs discussed in the previous section, it is only natural to expect a similar trend at interfaces. A significant difference between ILs and PILs, however, is the marked increase in glass transition temperature upon polymerization, switching the material from liquid-like to solid-like at room temperature for most PILs. On the one hand, this prevents the use of direct techniques such as SFA or AFM to probe the solid-PIL interface but, on the other hand, it allows easier ways to confine the material such as in thin solid films, for instance.

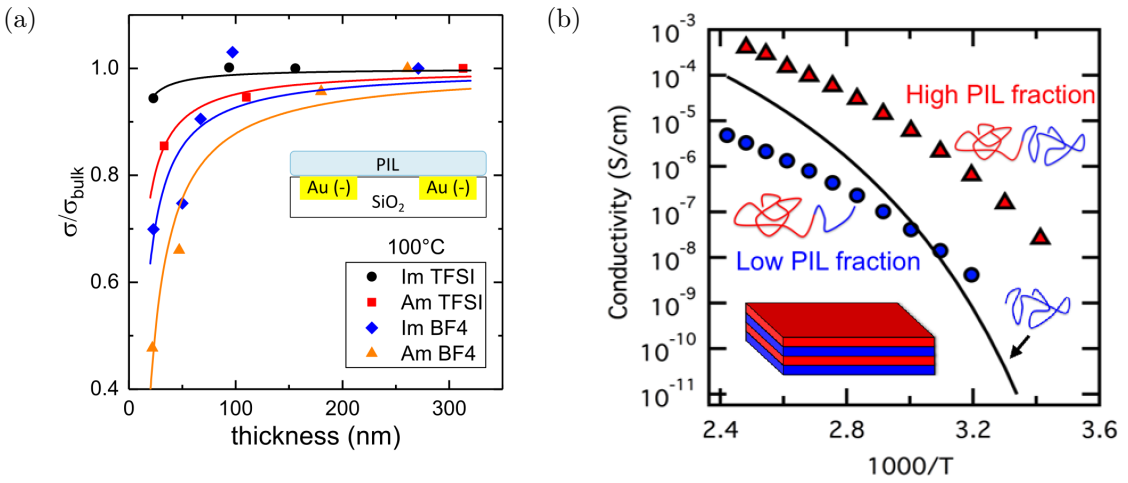

Figure 1.7: (a) In plane conductivity of PIL thin films normalized to the thickest film value against thickness for imidazolium and ammonium based PILs, inset is a schematic representation of a thin film deposited on gold interdigitated electrodes. Taken from ref. [77]. (b) Conductivity as a function of temperature for homopolymer PIL and two PIL fractions copolymers. Insets show a schematic of a PS-*block*-PIL copolymer lamellar morphology. Taken from ref. [78]

Some studies focused on *in situ* polymerization of imidazolium based ILs in nanoporous silica [79] or alumina [80] membranes. The resulting PILs exhibited an enhanced conductivity compared to their bulk polymerized counterparts [79]. The authors attribute this to the alignment of PIL chain in the pore's direction, benefiting the particular ion transport mechanism in PILs which will be addressed later on, to enhance conductivity [81, 82]. Heterogeneity in the nanopore is thought to contribute as well with a certain extent of cylindrical layering. It should be noted, however, that monomer conversion in these systems remained fairly low, around 75 % [79], resulting in a concentrated PIL solution in the corresponding IL.

Processability of PILs as opposed to other electrolytes and ILs themselves also allows for alternative confinement strategies. The simplest of these are thin films, in which the degree of confinement is simply controlled by the thickness of the film. Previous works focused on the ion transport in PIL thin films [83], using gold interdigitated [77], or nanostructured parallel-plate electrodes [57]. Above the glass transition temperature, ionic conductivity decreases sharply for increasing confinement, *i.e.* thinner films down to 7 nm. This is attributed to the strengthening of substrate interactions, which slows down segmental relaxation, thus hindering ionic mobility. This confinement effect is all the more pronounced when the ion pairs associate strongly.

A more elaborate confining strategy the polymeric nature of PILs offers is the use of copolymers. Block copolymers with a PIL as charged block exhibit improved conductivity compared to a random copolymer [84] and even compared to the homopolymer PIL in some situations. On this last point, C. Evans *et al.* showed that Polystyrene-*block*-poly(5-aminoethylimidazolium acrylamide) with TFSI counter anion confines the PIL block in lamellar phases which can be tuned *via* the copolymer relative composition. By doing so, the conductivity of the PS-

block-PIL copolymer exceeded that of the corresponding PIL homopolymer [78].

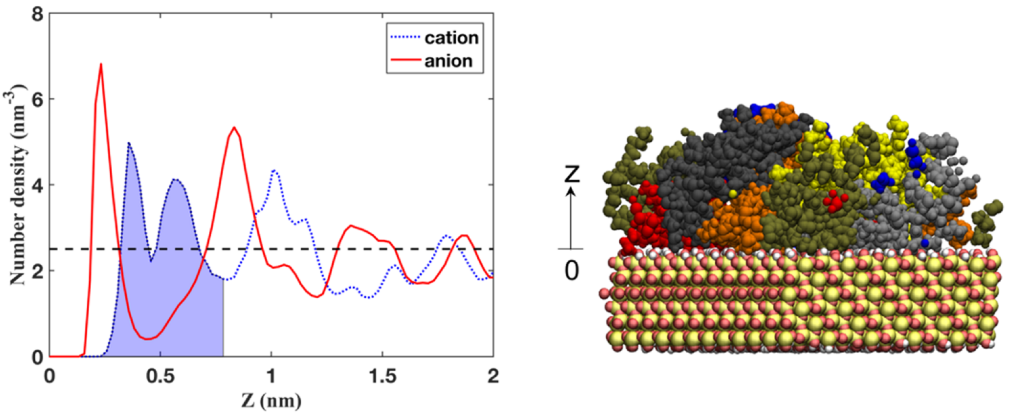

Figure 1.8: Numerical simulations of a poly(1-butyl-3-vinylimidazolium hexafluorophosphate) PIL near a neutral quartz substrate taken from ref. [85]. The left panel is the number density profile of both cations and anions. The right panel is a simulation snapshot of PIL chains with at least one of their pendant cations in the first cation layer, *i.e.* in the shaded region of the left panel.

Although ion conductivity of PILs is not the primary focus of this work, it is compelling how despite being used as an asset to enhance its properties, the interfacial structure of PILs is still poorly understood, and it is unclear how PILs organize locally in such confinement geometries. Numerically, Z. Yu *et al.* reported layering for poly(1-vinyl-3-butylimidazolium hexafluorophosphate) at both neutral and charged surfaces [85]. In the absence of surface charge, anions form the first layer due to steric interactions that prevent polymerized cations to move closer to the interface. For a negatively charged substrate, cations are adsorbed, with polymer chains more densely packed at the interface. The increase in anion coordination in the vicinity of the substrate slows down their diffusion, specially at the neutral surface, for which cations form smaller in-plane clusters. As far as we know, the only experimental results are those of R. Kumar *et al.* on poly(1-vinyl-3-ethylimidazolium) films several tens of nanometres thick using neutron reflectivity [83], revealing a single PIL-substrate interfacial layer depleted in counter anion.

Overall, the few reports dealing with PILs at interfaces suggest ion transport is strongly impacted by the presence of an interface or by confinement of the material. Whether it relates to a structural change compared to the bulk remains an open question. Nevertheless, considering what has been reported for ILs and discussed in previous section 1.3.2 as well as the similarities ILs and PILs share in terms of bulk structure, an interfacial layering is likely to develop at the PIL-substrate interface. Its implications on the material properties are crucial to energy storage and electrochemical applications.

1.4 Dynamics of ionic liquids

1.4.1 Ion associations in ILs

We come back in this section to the DLVO description, we so quickly discarded in section 1.3.2. As a matter of fact, such description of ILs is still under vigorous debate. Among the SFA community, M.A. Gebbie *et al.* reported several force-distance profiles across ILs featuring long range interactions, either attraction between gold and mica [86] or repulsion between two mica plates [87]. The authors concluded these forces were electrostatic in origin, and advanced ILs behaved as dilute electrolytes. As surprising as the conclusion seems, it supports the work of H. Tokuda *et al.* who compared molar conductivities Λ_{imp} measured by an electrochemical impedance method and Λ_{NMR} determined by the actual self-diffusion coefficient of cations and anions and the Nernst Einstein relation [88]. Therefore, if both are identical, the ionicity defined as their ratio of 1 and all ions contribute to the ionic conduction. In contrast, a diffusing ion-pair contributes to the diffusion coefficient but not to the charge transport. The authors reported ILs have ionicities below 1, suggesting they are poorly dissociated and the majority of ions are then paired as dipoles and only contribute as a dielectric network [87].

Subsequent reports either corroborate the dilute electrolyte behaviour of ILs or on the contrary disprove it. The general picture is nonetheless that ion pairing in ILs, if present, is transient and occurs in larger ionic aggregates with low interaction energies [89, 90]. One important aspect of ILs that has been left out of most of the above considerations is their nanoscale heterogenous structure. F. Ferdeghini *et al.* noted that most reports supporting a dissociated view of ILs focused on macroscopic scale measurements, whereas the ion pairing argument was generally used to interpret measurements at the nanometric scale. Suspecting an effect of the nanostructure of ILs, the same authors reported a multiscale analysis of diffusion processes based on a combined use of quasi-elastic neutron scattering (QENS), neutron spin echo (NSE) and Pulse-Field Gradient NMR [91, 92]. The authors observed a surprising discrepancy between a much shorter long range diffusion coefficient probed by PFG-NMR compared to short range ones using QENS/NSE. They attribute the latter to diffusion inside ion aggregates and between close neighbour aggregates, while the former corresponds to larger scale diffusion affected by the tortuous bicontinuous structure of the IL.

1.4.2 Non-Newtonian behaviour of ILs

Let us now take a step back from the molecular view and focus on macroscopic properties. The viscosity of a simple liquid is constant with respect to the applied shear rate $\dot{\gamma}$, which defines the Newtonian behaviour. Complex fluids on the other hand deviate from this and non-Newtonian behaviours closely relate to the microstructure of the fluid. A decrease of viscosity with increasing shear rate $\dot{\gamma}$, shear thinning, is usually attributed to an alignment of particles or aggregates with the flow. Shear thickening in contrast, for which viscosity increases with $\dot{\gamma}$, originates from friction between particles. This link between viscosity dependence and microstructure is particularly appealing for ILs on account of their mesoscopic

structure and ionic associations. Several ILs were reported to exhibit either shear thinning or shear thickening. G.L. Burrell *et al.* even reported both behaviours separated by a threshold in temperature [93] with a critical shear rate around 1000 s^{-1}. However, shear thinning behaviours revealed by numerical simulations [94, 95] happened above 10^6 s^{-1} thus raising considerable discrepancy with experiments. Furthermore, no theoretical explanation has been found so far for shear thickening of ILs. A. Piednoir *et al.* recently provided further experimental results comparing ILs and Newtonian fluids in the same conditions, suggesting such increases or decreases of viscosity reported in ILs could originate from instabilities [96]. Indeed, it is not uncommon, at the shear rates values mentioned, to observe viscous heating and consequently a decreased viscosity or geometry dependent instabilities inducing more dissipation and an apparent shear thickening. It is unclear thus far whether ILs exhibit intrinsic non-Newtonian behaviour. They do appear to exhibit, in any case, an extended Newtonian plateau.

1.4.3 Lubrication properties

Since lubrication is not the main focus of this work, we will give a very simple view on it as the force required to shear a thin liquid film between two solid substrates as a function of the applied load. As well summarized by R. Lhermerout *et al.* [97], a good lubricant should possess three main requirements : a controlled friction coefficient to ensure reproducible motion of the two plates, resistance to the applied load without the liquid film being squeezed out, robust properties, meaning a weak dependence on working variables. ILs exhibit low friction [66] and are promising lubricants regarding these three points.

Additionally, to measuring the normal force profiles across the layered structure of ILs, the shear force can also be probed in SFA. By doing so, A.M. Smith *et al.* revealed the kinematic friction force between the mica plates as a function of the applied load strongly depends on the number of ion layers between them. The friction coefficient is much larger when only a few layers separate the plates [98]. The authors also observed a stick-slip behaviour for slow lateral displacements of the upper plate due to either melting inside an isolated layer or relative slip between ion layers.

The friction across ILs can also be tuned by addition of solutes. The structural heterogeneity of ILs leads to an equally heterogenous distribution of solutes in these materials, as shown by their diffusion coefficient [45] as well as their effect on the bulk structure of ILs [99]. Depending on their polarity, solutes segregate into either the polar or apolar domain, which it has the most affinity with [100]. Due to the difference in layer composition at the IL-solid interface, A.M. Smith *et al.* reported a pronounced enhancement of lubrication for a double bilayer compared to a single bilayer when small quantities of water are added. The authors interpret this as a new sliding plane between the two bilayers due to a higher affinity of water with the charge head groups [101].

1.5 Poly(ionic liquids) as hybrid materials

1.5.1 Decoupling of ion transport from structural relaxation

Although conductivity is not the main focus of this work, it remains essential to understand the properties of PILs but also the purpose of these materials. For a dilute molecular electrolyte, the conductivity is given by $\sigma = \sum_i c_i q_i \mu_i$ in which c is the concentration of free ions, q their charge, and μ their mobility. The Einstein relation relates the mobility to the diffusion coefficient D as $\mu = {}^{qD}/_{kT}$ in which k is the Boltzmann constant and T the temperature. Furthermore, according to Stokes Einstein relation $D \sim T/\eta$ with η the viscosity, and for small glass forming molecules $\eta = G\tau$ with G and τ the elastic shear modulus of the glassy state and the structural relaxation time respectively. It comes that for a good electrolyte with dissociated ions, the diffusivity of ions and hence the conductivity itself is directly proportional to the fluidity $1/\eta$ or the structural relaxation rate $1/\tau$. In that sense, it is generally agreed that structural dynamics control ion transport. In spite of some exceptions, most polymer electrolytes answer to this rule even upon a change of molecular weight.

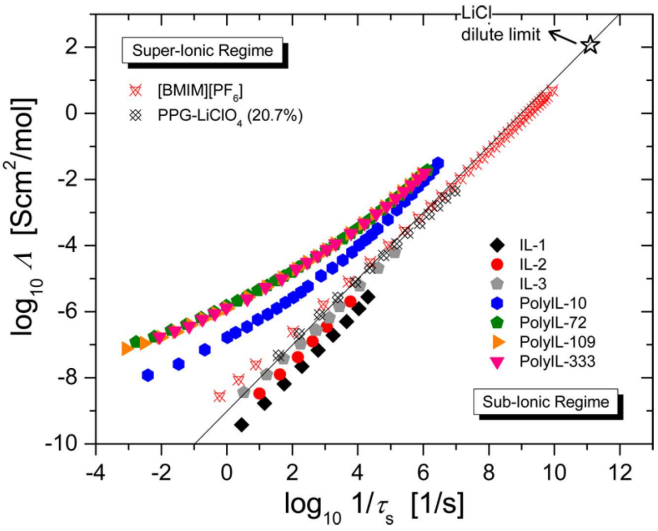

Figure 1.9: Walden plot of molar conductivity as a function of structural relaxation rate for acrylate based ammonium ionic liquids, corresponding dimers and trimers (IL-1, IL-2, IL-3) and poly(ionic liquid)s of different degrees of polymerization taken from ref. [102].

PILs, however, were shown to exhibit a strong decoupling between ion conduction and segmental relaxation [102–104]. This is well illustrated by the Walden plots of acrylate based ammonium ionic liquids and their polymerized counterparts by F. Fan *et al.* given in Figure 1.9. ILs and their dimers or trimers roughly follow the ideal line of Walden analysis, suggesting a strong coupling between ion conduction and structural relaxation rate. Some are slightly below the line, in the sub-ionic regime, meaning that ions are not well dissociated. This is actually put forward

to support the dilute electrolyte behaviour of ILs in the debate discussed in section 1.4.1. Still, above 10 repeating units, PILs evidently cross into the super-ionic regime and develop decoupling.

This observed decoupling is mainly attributed to packing frustration of the cation [58, 104], hence pointing out the importance of the structure/dynamic interplay. An increase in disorder induced by geometric frustration was shown to be strongly correlated to an enhancement of conductivity in model ion containing systems [105]. The underlying explanation is an increase of free volume, allowing the mobile ion more easily in loosely packed systems. The lower conductivity in PILs with long side chains and large anions was assigned to a better packing by B. Doughty *et al.* by a combined use of X-ray scattering and vibrational sum frequency generation (vSFG) [58]. Because packing frustration also leads to weaker ionic associations, the chemical structure and nature of side groups are fundamental in tuning properties of PILs [102, 106].

The decoupling between ion transport and segmental relaxations in PILs originates from a conduction mechanism that differs from that of ILs. S. Mogurampelly *et al.* revealed using MD simulations that the mobile anions hop from one branched cation to another [81, 82]. By following different types of hopping events, the authors further revealed the motion happens dominantly along a single chain, hence deeply contrasting with ILs.

1.5.2 Ionomers as associating ion containing polymers

Most of the above considerations were led in a local, molecular liquid point of view, focusing on how polymerization affects the structure inherited from ILs and their ion transport mechanisms. Nevertheless, PILs are polymeric systems and, as such, exhibit conventional relaxation of polymer chains. Ion associations have tremendous implications on polymeric viscoelastic properties by adding friction to the chain and naturally affecting the relaxation of the material.

Among associating polymers, a close relative of PILs are ionomers which can be simply defined as flexible polymers of which a fraction of repeating units bear a charge. The generally low dielectric constant of polymers promotes association of these ionic groups in clusters acting as association points. The purpose of this section is to take the second direction, mentioned at the beginning, of a polymeric system with increasing ionic content. We introduce the field of associating polymers, whether physical crosslinks are ionic in nature or not, narrowing it down to ionomers as a working case of associative polymers. As it will come out of this section and later on of Chapter 6, these materials offer a more accessible way into the understanding of more complex systems such as PILs.

Associating polymers

Polymeric materials can be hardened by binding chains together with covalent bonds called chemical crosslinks. They were actually first used since the early days of polymer science. Not more than a decade after the Swedish chemist J. J. Berzelius intro-

duced the term polymer [1][108], and surprisingly twenty years before M. Berthelot reported the first synthetic polymerization (of polystyrene), C. Goodyear patented the vulcanization of rubbers in the United States, concurrently with T. Hancock in England. The process discovered by chance consisted in heating rubber with sulphur thus creating covalent bonds between rubber chains and drastically improving its elasticity, resilience, tensile strength, hardness and weather resistance. The poorly elastic and often sticky natural rubber became through this crosslinking process the material of choice for tires, among other applications.

Chemical crosslinks are irreversible due to a high association energy of the order of 1000 kJ/mol, hundreds of times the thermal energy kT at room temperature. The lifetime of these associations, exponentially dependent on the interaction energy, is virtually infinite. These bonds can be turned reversible, over the working timescale, by lowering the interaction energy. They become thereby physical crosslinks. Such polymers are termed associating and their applications include, but are not limited to, reprocessable and self-healing materials [109].

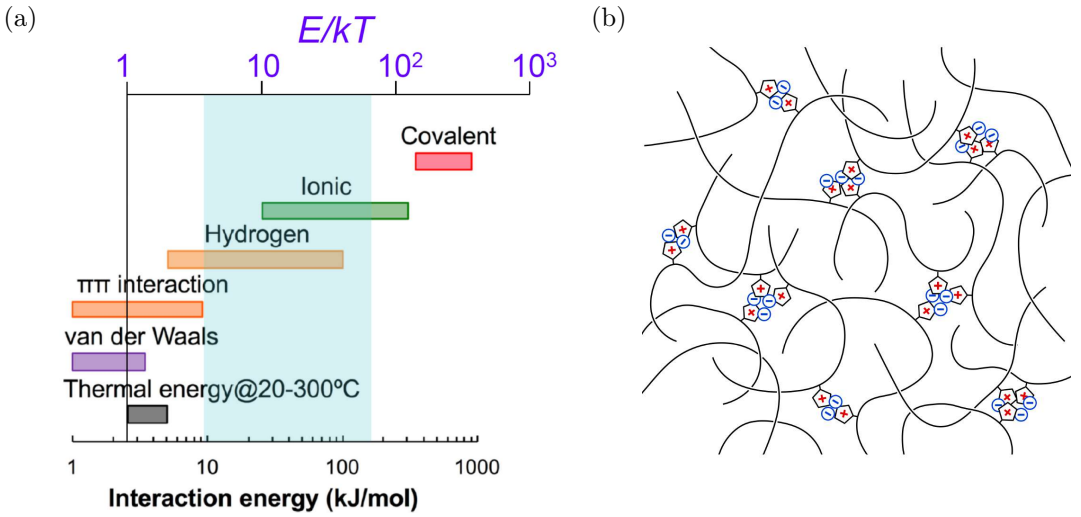

Figure 1.10: (a) Interaction energies of diverse bond types, ideal energies for reversible bond networks, are shown in light blue. Figure taken from Pr. R.H. Colby's lecture at the SOFTMAT summer school 2022, adapted from ref. [110]. (b) Schematic representation of an associating polymer network based on ionic bonds.

Linear viscoelasticity and relaxations of ionomers

Possible interactions weaker than covalent bonds but stronger than simple van der Waals interactions include hydrogen and ionic bonding, which energies are of the order of a few times and tens of times the thermal energy kT respectively. The diagram of Figure 1.10a summarizes these interaction energies for a variety of interactions. We focus in the following on ionic association and in particular ionomers,

[1]This first definition was far from today's usage and considered for example benzene as a polymer of ethylene. It was met with great criticism until H. Staudinger introduced the macromolecule picture in the 1920s [107].

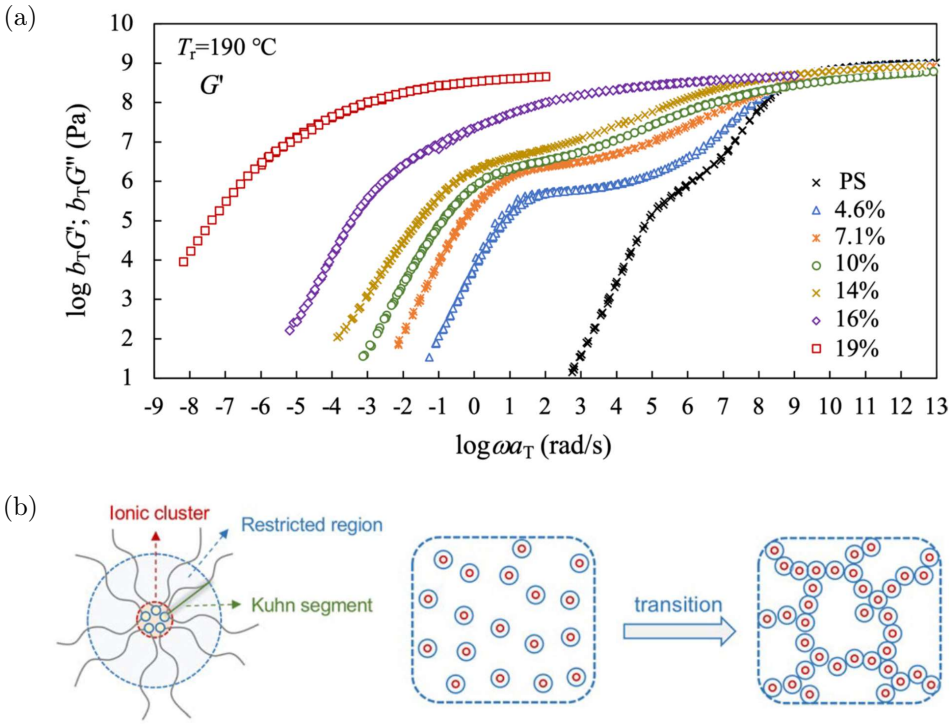

Figure 1.11: (a) Storage modulus G' from the LVE master curve of unentangled sulfonated PS with varying ion content. (b) Schematic representation of Eisenberg restricted region model [112, 113]. Figures taken from ref. [111]

defined above, and their linear viscoelasticity.

Q. Chen *et al.* [111] reported a systematic LVE study of unentangled sulfonated PS with increasing ion content, from which we show the evolution of storage modulus G' in Figure 1.11a. As ion content increases, *i.e.* more stickers are added to the system, a noticeable plateau emerges, although ionomers are unentangled, and increases in magnitude. The progressive delay of the terminal relaxation time of the ionomer chain is imparted to the ion dissociation time longer than the segmental relaxation.

For a high concentration of stickers, the transition becomes one single broad transition. A look at the microstructure of these systems is required to understand this behaviour. These ion-containing materials form ionic clusters, as mentioned above, which are covalently attached to the ionomer chains. There is therefore a region around the clusters in which segmental mobility is locally restricted, as put forth by A. Eisenberg [112, 113]. The addition of this longer relaxation time results in a bimodal distribution of relaxations as seen on LVE responses of the materials as in Figure 1.11a but also on DSC thermograms. At the point when restricted regions percolate, the two relaxations merge into one broad glass to terminal transition. Q. Chen *et al.* proposed that the threshold is actually reached when there is at least one sticker per Kuhn segment [111] in agreement with their experimental observations.

These systems were shown to be well predicted by adapting classical polymer relaxation theories such as the Rouse and reptation models respectively for unentangled and entangled polymers [114, 115]. Although we will develop more thoroughly these points in Chapter 6, the general idea is that only longer strands, at length

scales above the distance between associations, are affected. More elaborate theories of reversible gelation provide a more precise prediction of the diversity of behaviours displayed by ionomers [116–118]. The complex interplay between the number of stickers and their association strength leads to a large panel of LVE responses. We only show here the most conspicuous situation where a rubbery plateau is clearly visible, and leave other behaviours for Chapter 6.

1.5.3 Dynamics of PILs

In contrast with ionomers, only a few reports focused on the LVE of PILs. This is explained by some by the challenge of synthesizing high molecular weight PILs with low dispersity and characterizing them by conventional methods such as size exclusion chromatography (SEC) [120]. Similarly to the work of F. Wieland *et al.* on the nanostructure of a series ranging from ILs and their oligomers to short chain PILs [59], F. Fan *et al.* reported comparative LVE measurements between acrylate based ammonium ILs and their corresponding PILs. For a few tens of repeating units, PILs exhibit a chain relaxation at long times additionally to the segmental relaxation of the glassy state at shorter times, similar to ILs [102]. The same trends were reported for other PILs [120, 121]. An additional crossover in the transition region appears for higher molecular weights due to entanglements, similar to neutral polymers [122].

Considering our previous comments on ionomers, this simple behaviour alone is rather surprising for PILs which possess a high density of charges. K. Nakamura *et al.* conducted viscoelastic measurements along with X-ray scattering and dielectric spectroscopy on imidazolium based PILs with cationic alkyl tails of 2 [119] and 4 carbon units [123]. On ethylimidazolium PIL, LVE of which we show in Figure 1.12a, a broad glass-rubber transition and an enhanced rubbery plateau such as discussed in the case of ionomers, suggest an important effect of ion associations. A failure of the time temperature superposition (tTS) in the rubbery to terminal region, as illustrated by the pseudo-master curve of Figure 1.12b occurs above a certain threshold in degree of polymerization, corroborating the presence of ion associations. Just as entangled ionomers, if the temperature dependence of association lifetime differs from that of the reptation time, the two relaxation modes cause failure in tTS.

The same authors observe fast and slow dielectric relaxation (DR) modes, which they ascribe respectively to a rotational motion of the side chain and the lifetime of an ion pair. The authors also state, based on a good overlap of their time-temperature shift factors on a T_g-corrected scale $a_T(T - T_g)$ that counterions only affect segmental dynamics of PILs by changes of their T_g. Overall, large counter anions were reported to induce looser ionic aggregates, thus weaker associations [30]. Influence of the pendant group composition on viscoelasticity of unentangled PILs has also been reported either by the type of side chain [104], the size and composition of spacers [124], or the counter anion [123]. More generally, U.H. Choi *et al.* reviewed T_g values for a variety of PILs [125], revealing they are not only dependent on anion volume but in fact scale as the reciprocal molecular volume of the repeating unit regardless of their specific chemical structures as shown in Figure 1.13. The reciprocal of the monomer molecular volume also corresponds

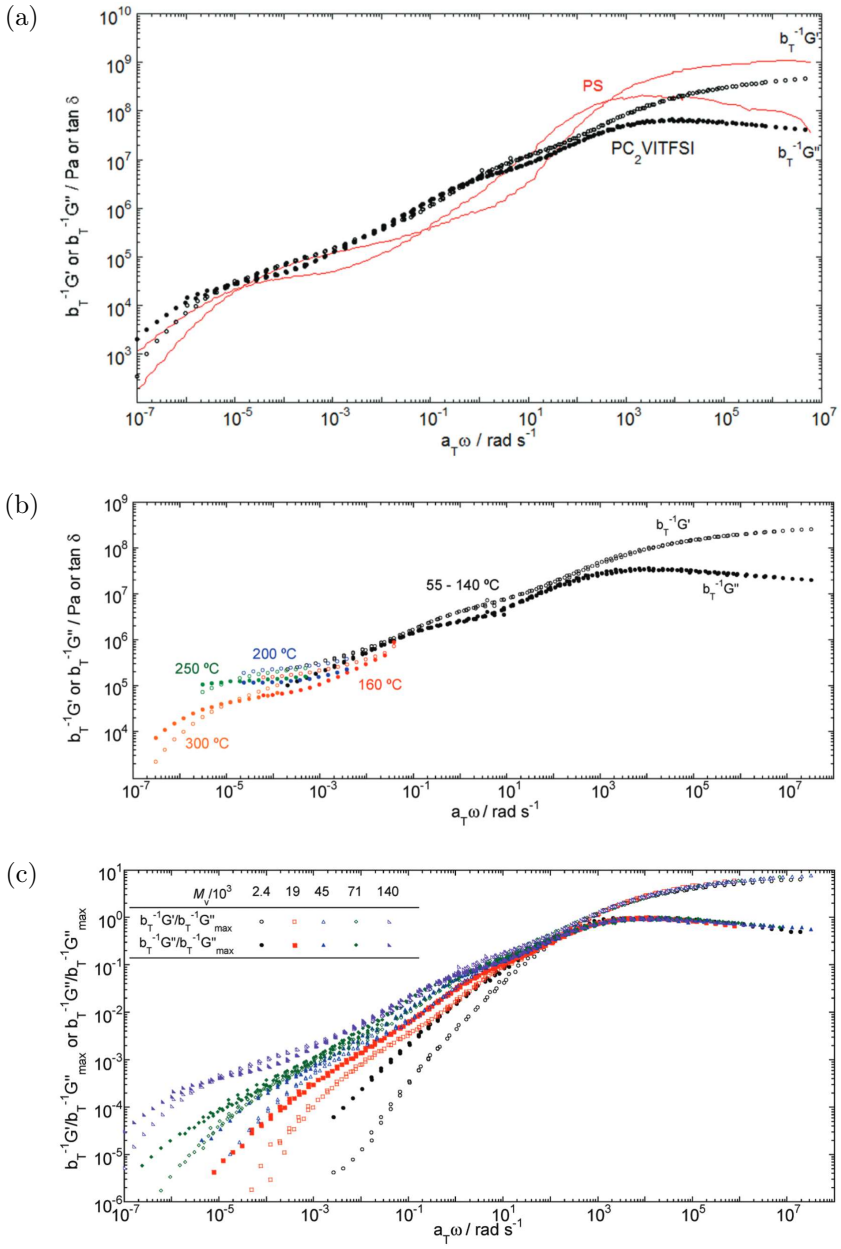

Figure 1.12: (a) Master curves for an entangled ethylimidazolium PIL at reference temperature $T_0 = 90°C$. Red solid lines indicate the master curves for polystyrene of same molecular weight at reference temperature 130 °C. (b) Pseudo master curves for second ethylimidazolium PIL with molecular weight 3 times larger at the same T_0. (c) Master curves of ethylimidazolium PIL at varying molecular weights. Curves are normalized by the maximum in loss modulus $b_T G''_{\max}$. Figures are taken from ref. [119].

to the density of ionic groups in PILs since every monomer bears a charge. The fact that it governs the glass transition substantiate the comparison with ionomers in which the increase of T_g with ionic fraction is imparted to growing restricted regions.

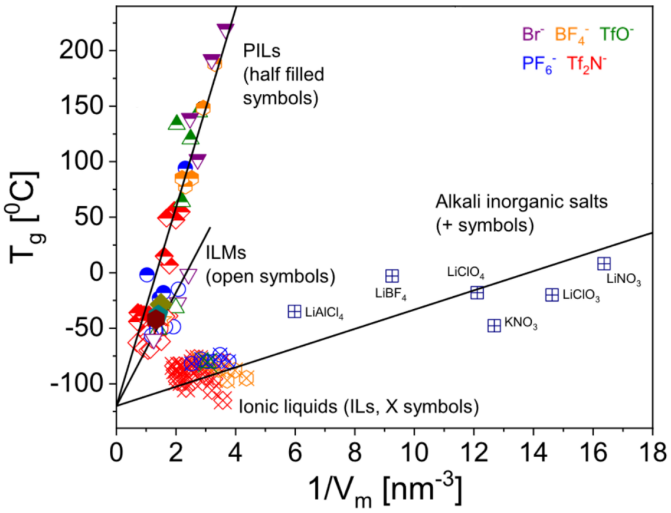

Figure 1.13: Correlation between the glass transition temperature T_g and number density of counterions $1/V_m$ including various counterions for imidazolium-based ILs (X symbols), vinyl IL monomers (open symbols), and their PILs (half-filled symbols). Taken from ref. [125]

From the efforts put into enhancing the conductivity of PILs ensues a common trend of chemical structures investigated. As well summarized by Iacob *i.e.*, side chain length affects the T_g-independent ionic conductivity of imidazolium-based PILs up to 1 order of magnitude due to changes in the size of apolar domains and the distance between neighbouring chains[33]. As for the anion, changes in conductivity of more than three orders of magnitude are imparted to its size. Overall, because conductivity is the intended material property to enhance, most reports focus on PILs with small counter anions and short side chains. Concerning the molecular weight, unentangled PILs only appear in a few reports, most of the time as part of series of varying molecular weights to retrieve viscosity scalings $\eta \sim M^{\alpha}$. While some reports suggest these scalings showed discrepancy compared to neutral polymers [123], others claim that conventional scalings apply [120, 121] and attribute different scalings to the significant dispersity of the reported PILs. This is briefly discussed in Chapter 2 to justify the unentangled state of our own PIL series.

Despite their numerous similarities, the comparison between ionomers and PILs is nonetheless far from trivial and should be done with caution. First and foremost, PILs, as opposed to ionomers, are composed of apolar clusters, percolated or not, in a predominantly ionic domain. This already contrasts with the segregated ionic clusters of Figure 1.10b. Moreover, the topic of ion associations in ILs is still largely under debate. The transient formation of ion pairs or aggregates is still poorly understood [87] and should play an extensive role in the dynamics of PILs.

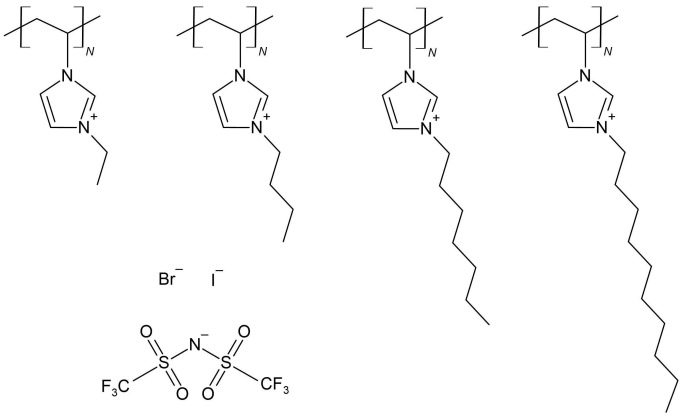

Figure 1.14: Chemical structure of the series of poly(1-vinyl-3-alkylimidazolium) PILs with varying side chain length n and counter anions bromide iodide and bis(trifluoromethylsulfonyl)imide (TFSI)

1.6 Focus

Although materials science is more fundamental today than it was during the rise of ILs, it is interesting to observe the understanding of PILs undergo a similar trend. A considerable number of reports on PILs are application-driven, with improvements of chemical structures or confinement methods to enhance conductivity. Yet, a lack of systematic approach to model systems hinders a deeper understanding of PILs behaviour. In that sense, this work focuses on model PILs, using the popular imidazolium IL as the building block of a series of poly(1-vinyl-3-alkylimidazolium) with varying side-chain length n as represented in Figure 1.14. The controlled synthesis as overseen by our collaborator E. Drockenmuller [1], ensures an identical degree of polymerization and dispersity for all n, which the strength of the results presented here relies on. Synthetic details and characterization of the PILs series are given in the following Chapter 2.

As discussed above, this side chain length shapes the polarity of interactions and accordingly the local bulk structure of ILs as well as PILs. Both share a surprising number of features, driven by the nanoscale segregation of these alkyl tails. If the PIL local bulk structure is rather well known today, how the conformation of the PIL chain is affected, as well as the role of temperature, is still unclear. Our results in that aspect using neutron and X-ray scattering are presented and discussed in Chapter 3. The disruption of bulk structure by a solid interface has surprisingly not been investigated so far, despite deep implications for their potential applications. Given the resemblance in bulk between PILs and ILs, it may be expected PILs also exhibit unconventional structures at interfaces. To this end, a combined use of specular X-ray reflectivity and grazing incidence X-ray scattering on thin film of our series of PILs is presented in Chapter 4. Confinement effects unfold from the variation of the film thickness, for which we propose a molecular picture.

The last point about the structure of these materials constitutes a side project of this work, resulting from our collaboration with E. Drockenmuller. Instead of so-

[1]Université Lyon 1, CNRS, Laboratoire d'Ingénierie des Matériaux Polymères, UMR 5223, Lyon, France

lution polymerization as performed for the above-mentioned PIL series, dispersion polymerization of PILs fashions structured nanometric particles [43, 126]. A combined use of X-ray scattering and Transmission Electron Microscopy (cryo-TEM) on triazolium based PIL nanoparticles, providing both particle shape and inner structure information, is presented in Chapter 5. A brief review of such dispersion polymerized PIL nanoparticles is given therein.

After closing the structural considerations, we will introduce our results on the dynamics of PILs with the linear viscoelasticity investigation of our PIL series in Chapter 6. To the best of our knowledge, no report has been made on such a PIL series with varying alkyl side chain length, including both globular and bicontinuous structures. Conventional oscillatory shear experiments on melt PILs were performed in collaboration with J. Peixinho and G. Miquelard-Garnier.[1]. The parallel between side chain length in PILs and ionic fraction in ionomers is discussed. An analogous approach is proposed in connection with their molecular structure and association dynamics in ILs.

Several directions for forthcoming works arose from these results and will be discussed in the concluding remarks. These perspectives, on both structure and dynamics, include the electric field responsiveness of the thin films' structures or the alternative probing of PIL dynamics to support an analogy with associating polymers. This last point might provide a way to better understand ionic associations in these systems and eventually cycle back to the debate over long-range interactions in ILs.

[1]Arts et Métiers Institute of Technology, CNRS, Cnam, HESAM Université, Laboratoire PIMM, UMR8006, Paris, France

Chapter 2

Materials and characterization

We present in this chapter the detailed chemical synthesis of the imidazolium based PC_nVImX series with varying side chain length n and counter anion X investigated in Chapters 3, 4 and 6 in section 2.1 and their characterization in section 2.2. Similarly, the synthesis and characterization of triazolium based PIL nanoparticles Chapter 5 focuses on are respectively given in sections 2.3 and 2.4. All of these are done by our collaborators at Laboratoire d'Ingénierie de Matériaux Polymères (IMP Lyon Univ., France) A. Jourdain, S. O'Brien and R. Akacha supervised by E. Drockenmuller. Only the thermal characterization of the imidazolium PIL series of section 2.2.2 was performed by us.

2.1 Synthesis of bulk imidazolium PILs

2.1.1 Materials and nomenclature

Imidazolium based PILs are designated in the following as **Y-PC$_n$VImX** with **X** the nature of the counter anion (**X** = **I**, **Br**, or **TFSI** for iodide, bromide, or bis(trifluoromethylsulfonyl)imide, respectively), n the number of carbon atoms of the N-3 alkyl side–chain (n = 1, 2, 4 or 10 carbon atoms), and **Y** the isotopic nature of the N-3 alkyl side–chain (**Y** = **h** or **d** for perhydrogenated or perdeuterated isotopologues, respectively). The isotopic nature is only relevant for neutron scattering experiments of Chapter 3. In chapters 4 and 6, all the samples are perhydrogenated and we drop the **Y** labelling for simplicity.

1-Vinylimidazole (**VI**, 99 %), 2,2'-azobis(2-methylpropionitrile) (AIBN, 98 %), iodomethane (99 %), iodoethane (99 %) 1-iodobutane (99 %), 1-bromodecane (98 %), iodomethane-d$_3$ (99.5 %), iodoethane-d$_5$ (99.5%), methyl 2-[methyl(4-pyridinyl)--carbamothioylthio]propionate (**CTA**, 97 %), lithium bis(trifluoromethylsulfonyl)--imide (LiTFSI, 99.95 %) were purchased from Merck and used as received. 1-Iodobutane-d$_9$ (98 %) and 1-bromodecane-d$_{21}$ (98 %) were purchased from CDN Isotopes and used as received. Deuterated tetrahydrofuran (THF-d$_8$ 99.5 %) was purchased from Eurisotop. 1-Decyl-3-methylimidazolium bis(trifluoromethyl sulfonyl)imide (99 %) was purchased from Iolitec. 1-butyl-3-methylimidazolium (98 %) and 1-ethyl-3-methylimidazolium (99 %) bis(trifluoromethylsulfonyl)imide were purchased from Sigma Aldrich. The ionic liquids were dried at 60 °C under vacuum for 24h before use.

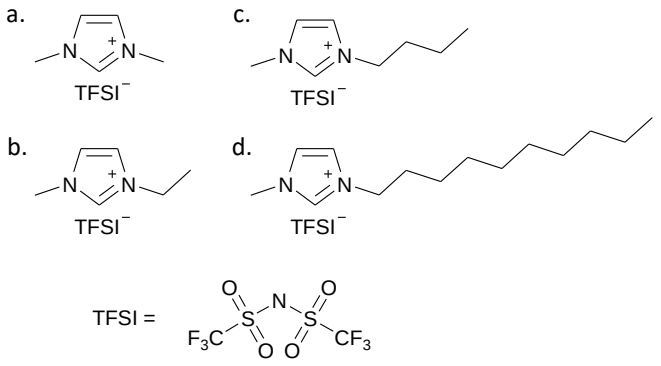

Figure 2.1: Chemical structure of 1-alkyl-3-methylimidazolium ILs (with alkyl chain lengths $n = 1$ (a), 2 (b), 4 (c) and 10 (d)).

2.1.2 Characterization methods

^{1}H (400 MHz) and ^{19}F (376.5 MHz) NMR data were recorded on a Bruker Avance 400 spectrometer in DMSO-d_6. Chemical displacements (δ) are listed with respect to the signal of residual internal CD_3SOCD_2H ($\delta = 2.50$) for ^{1}H spectra and to the signal of internal $CFCl_3$ ($\delta = 0.00$) for ^{19}F spectra. Size exclusion chromatography (SEC) was carried out at 50 °C on a chromatograph connected to a Viscotek pump (1 mL min^{-1}) and Rheodyne 7725i manual injector (100 μL loop) using a combination of detectors (Viscotek VE3580 refractometer RI at 50 °C and Viscotek T60A viscometer at room temperature), two Viscotek I-MBHMW-3078 columns and one Viscotek I-MBLMW-3078 column, 300 × 7.5 mm (polystyrene/divinylbenzene) and pre-column Viscotek I-GUARD-0478 and a 0.01 M solution of LiTFSI in DMF as the eluent. 3 mg/mL solutions of **h-PC$_1$VImTFSI**, **h-PC$_2$VImTFSI**, **h-PC$_4$VImTFSI** and **h-PC$_{10}$VImTFSI** in 0.01 M LiTFSI in DMF were filtered through 0.20 μm pore size PTFE filter prior to the measurements. Number average (M_n) and weight average (M_w) molar masses and dispersities ($Đ$) were derived from a calibration curve based on polystyrene standards. Omnisec software was used for the treatment of the results.

2.1.3 Synthetic path

The series of hydrogenated and deuterated poly(1-vinyl-3-alkylimidazolium) isotopologues having identical macromolecular parameters (*i.e.* N and $Đ$) but including either halide or TFSI counter-anions and different N-3 side-chains of varying length n were synthesized in three steps involving 1 - reversible addition-fragmentation chain transfer (RAFT) polymerization of vinyl imidazole (**VI**), 2 - N-alkylation of imidazole groups, and 3 - ion metathesis reaction (Scheme 2.2). Initially, **PVI** was obtained in 51 % yield by RAFT polymerization of **VI** in methanol using a dithiocarbamate chain transfer agent (**CTA**) and **AIBN** as initiator.

According to the initial [**VI**]/[**CTA**] ratio of 139 and the monomer conversion obtained by ^{1}H NMR of the crude polymerization mixture (*i.e.* 54 %), the resulting

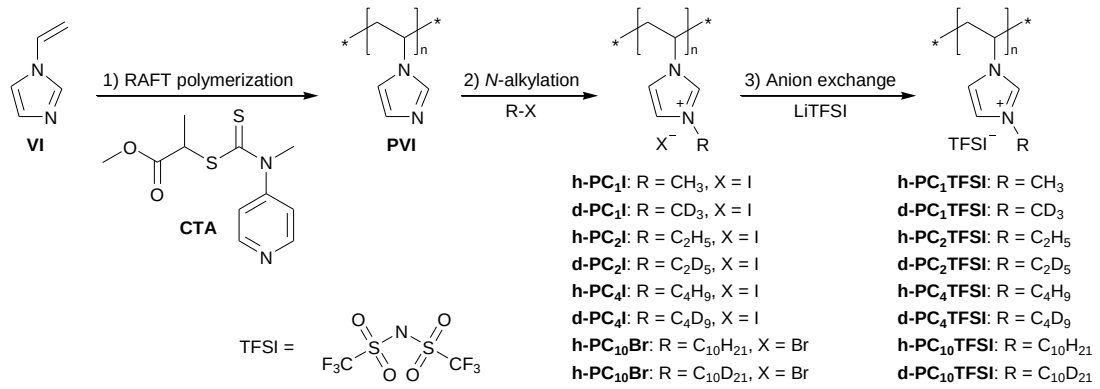

Figure 2.2: Synthesis of hydrogenated and deuterated poly(1-vinyl-3-alkylimidazolium) isotopologues.

polymerization degree (N) of **PVI** (and thus all their N-alkylated PIL derivatives) should be ca. 75. A series of poly(1-vinyl-3-alkylimidazolium) halides was then obtained in 73 % to 94 % yields by N-alkylation of the N-3 position of imidazole groups using hydrogenated and deuterated aliphatic halide isotopologues with $n =$ 1, 2, 4 or 10 carbon atoms. Finally, all hydrogenated and deuterated poly(1-vinyl-3-alkylimidazolium) halides were involved in an ion metathesis reaction with LiTFSI to afford the corresponding poly(1-vinyl-3-alkylimidazolium) TFSI isotopologues in 81 % to 98 % yields. We provide, in the following, additional details in the following for each synthetic step in case of **h-PC$_{10}$TFSI**.

RAFT Polymerization

Synthesis of PVI. Vinyl imidazole (7.70 g, 81.8 mmol) was added to a solution of **CTA** (0.16 g, 0.59 mmol) and AIBN (0.05 g, 0.30 mmol) in methanol (CH_3OH, 30 mL). The solution was sealed under reduced pressure after three freeze-pump-thaw cycles and further stirred for 16 h at 70 °C. The crude solution was reduced under vacuum, precipitated in cold diethyl ether and dialysed for 3 days in CH_3OH to remove monomer traces and freeze-dried to afford **PVI** as a white solid (3.93 g, 51.0 %).

N-alkylation Reaction

Synthesis of h-PC$_{10}$VImBr. A solution of **PVI** (602 mg, 6.40 mmol of imidazole groups) and 1-bromodecane (2.12 g, 9.58 mmol) in DMF (60 mL) was heated at 80 °C for 24h. The resulting mixture was evaporated under reduced pressure, dissolved in acetonitrile and precipitated twice in cold acetone to afford after drying under reduced pressure **h-PC$_{10}$Br** as a light yellow solid (1.89 g, 93.7 %).

Ion Metathesis

Synthesis of h-PC$_{10}$VImTFSI. A solution of **h-PC$_{10}$VImBr** (682 mg, 2.16 mmol of imidazolium bromide groups) and LiTFSI (1.55 g, 5.40 mmol) in 20 mL of a 1:1 (v/v) mixture of acetonitrile and methanol was heated at 40 °C for 24h. The resulting mixture was concentrated under reduced pressure and precipitated

in 40 mL of cold water. The crude product was redissolved in acetonitrile and precipitated in cold water to afford after filtration and thorough drying under vacuum **h-PC$_{10}$VImTFSI** as a light yellow solid (982 mg, 97.2 %).

2.1.4 Molecular weight consideration

There has been a slight controversy regarding the critical molecular weight for entanglements in PILs and the viscosity scalings below and above. For readers unfamiliar with these terms, they are discussed more in detail in Chapter 6. The only report on imidazolium based PILs was made by K. Nakamura *et al.* for an ethyl side chain [119]. The authors put forward viscosity scalings quite different from those of neutral polymers, which they attribute to electrostatic interactions between the backbone and the mobile anion. However, as pointed out by Q. Zhao *et al.*, there is no reason why this effect should depend on the molecular weight and thus affect the viscosity scaling [121]. They also performed viscosity measurements and found slopes of 1.0 and 2.3 for an acrylic based imidazolium PIL series, whereas F. Fan *et al.* observed a 1.1 slope in the unentangled regime of acrylate based ammonium PILs up until a few hundreds repeating units [102]. G. Liu *et al.* did find slopes of 1.1 and 3.6 for benzyl based imidazolium PILs and attribute the scalings found by K. Nakamura *et al.* to a limited number of samples and a higher dispersity in PILs obtained by free radical polymerization compared to RAFT [120]. Additionally, the considerably broader crossover region between entangled and unentangled regimes than what is typically obtained with neutral polymers is ascribed to the higher dispersity in PILs even with controlled radical polymerization [120]. Q. Zhao *et al.* rely on this broad transition to explain the 2.3 scaling obtained for entangled chains, explaining that they are not in fact fully entangled at these molecular weights yet [121].

Nevertheless, for all viscosity scalings reported, the critical molecular weight is above a hundred repeating units, suggesting our series of PILs are unentangled. This appears clearly in the measured viscoelastic properties of Chapter 6. Despite difficulties to obtain narrow molecular weights distributions, the real strength of the synthesis used in the present work is that regardless the values of molecular weight and dispersity, they remain identical across the PIL series with varying n since all PILs are synthesized from the same **PVI**.

2.2 Characterization

2.2.1 Chemical structures

We report in this section the ^{1}H NMR characterization of products synthesized at each step of the path leading to **h-PC$_{10}$VImTFSI** detailed above. ^{19}F NMR and size exclusion chromatography (SEC) on the whole series with varying n is given at the end respectively in Figure 2.6 and 2.7.

RAFT polymerization

^{1}H NMR (400 MHz, DMSO-d$_6$): δ 7.57–6.59 (3H, br, H$_c$, H$_d$), 3.23–2.74 (1H, br, H$_b$), 2.34–1.56 (2H, br, H$_a$). ^{1}H NMR of **PVI** (Figure 2.3) shows the quantitative removal of residual **VI** after purification (i.e. doublet of doublet at 7.17 ppm and doublets at 5.48 and 4.87 ppm) and the fair agreement between integrals of the imidazole protons (i.e. at 7.57–6.59 ppm) and the protons of the main–chain (i.e. at 3.23–2.74 and 2.34–1.56 ppm).

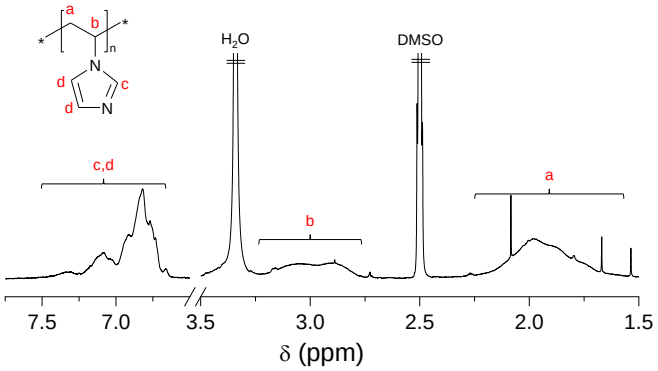

Figure 2.3: ^{1}H NMR spectrum (DMSO-d$_6$, 400 MHz) of **PVI**.

N-alkylation reaction

^{1}H NMR (DMSO-d$_6$, 400 MHz) (Figure 2.4): δ 10.17–9.16 (1H, br, H$_c$), 8.54–7.25 (2H, br, H$_d$), 5.06–3.70 (3H, br, H$_b$, H$_e$), 3.12–2.13 (2H, br, H$_a$), 2.13–1.58 (2H, br, H$_f$), 1.58–1.04 (14H, br, H$_g$), 1.04–0.68 (3H, br, H$_h$).

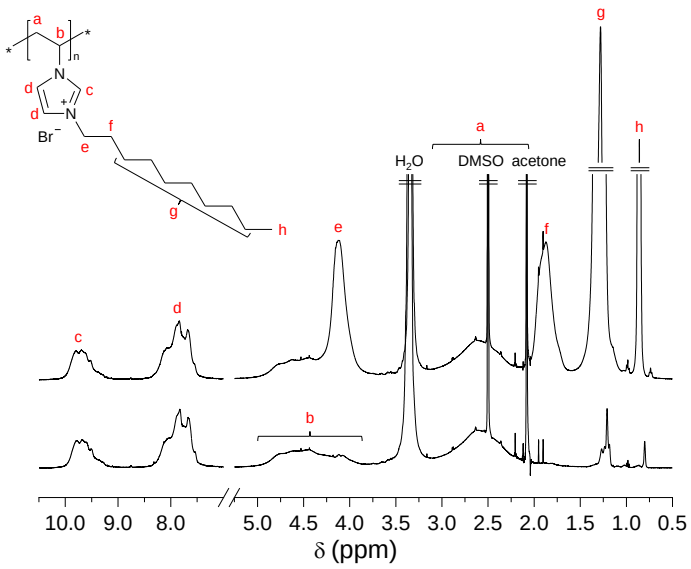

Figure 2.4: ^{1}H NMR spectrum (DMSO-d$_6$, 400 MHz) of **h-PC$_{10}$VImBr** (top) and **d-PC$_{10}$VImBr** (bottom).

Ion Metathesis

^{1}H NMR (DMSO-d$_6$, 400 MHz) (Figure 2.5): δ 9.45–8.33 (1H, br, H$_c$), 8.20–6.60 (2H, br, H$_d$), 4.82–3.56 (3H, br, H$_b$, H$_e$), 3.00–1.96 (2H, br, H$_a$), 2.96–1.52 (2H, br, H$_f$), 1.52–1.04 (14H, br, H$_g$), 1.04–0.66 (3H, br, H$_h$). ^{19}F NMR (DMSO-d$_6$ with 0.05 % v/v CFCl$_3$, 376.5 MHz): δ –78.38 (6F, s, $(CF_3SO_2)_2N$).

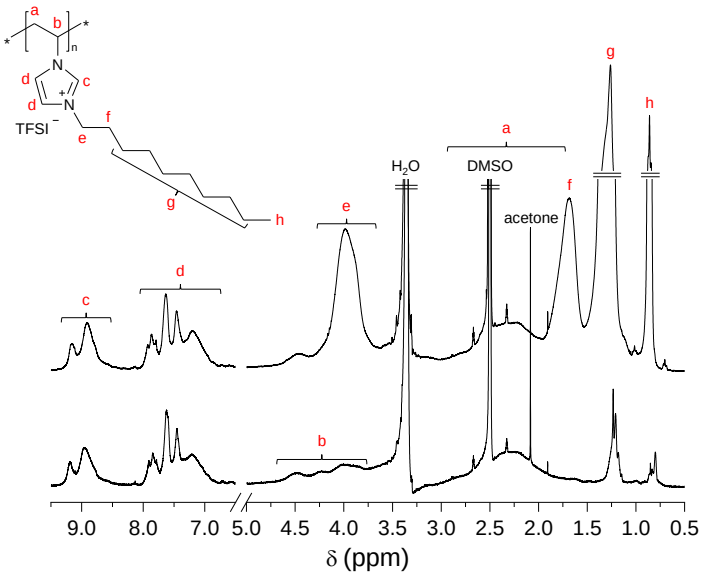

Figure 2.5: ^{1}H NMR spectrum (DMSO-d$_6$, 400 MHz) of **h-PC$_{10}$VImTFSI** (top) and **d-PC$_{10}$VImTFSI** (bottom).

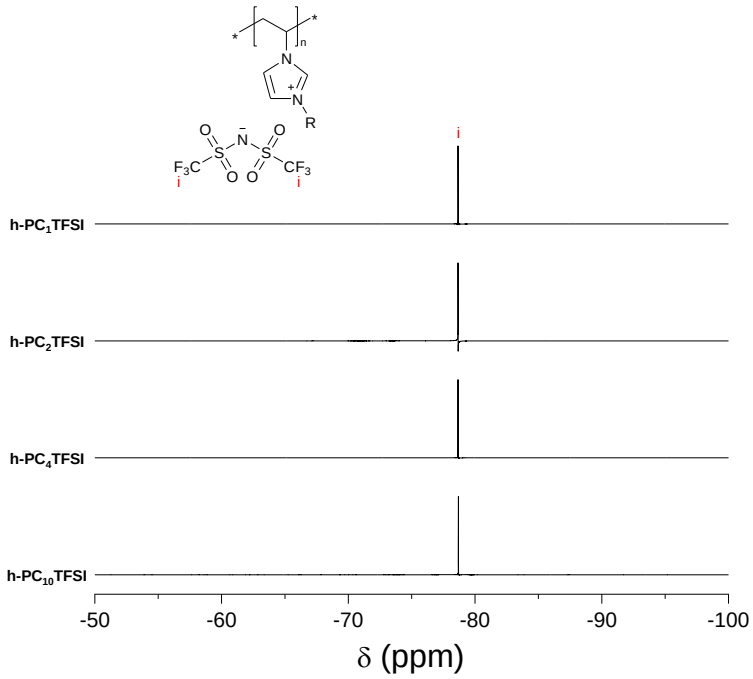

Figure 2.6: ^{19}F NMR spectrum (DMSO-d_6 with 0.05 % v:v $CFCl_3$, 400 MHz) of **h-PC$_1$VImTFSI**, **h-PC$_2$VImTFSI**, **h-PC$_4$VImTFSI**, **h-PC$_{10}$VImTFSI**.

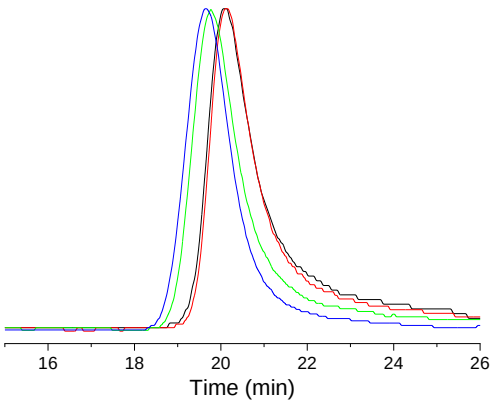

Figure 2.7: Size exclusion chromatography traces of **h-PC$_1$VImTFSI** (black solid line), **h-PC$_2$VImTFSI** (red solid line), **h-PC$_4$VImTFSI** (green solid line) and **h-PC$_{10}$VImTFSI** (blue solid line) in 0.01 M LiTFSI in DMF.

2.2.2 Thermal behaviour

PC$_n$VImTFSI samples were dried at 100 °C in a vacuum oven overnight prior to differential scanning calorimetry experiments (DSC). The measurements were performed on a DSC Q100 (TA Instruments) at heating and cooling rates of 10 °C/min over temperatures ranging from -20 °C to 150 °C. Thermograms at the second heating cycle for varying side chain length are given in Figure 2.8a and exhibit a single broad glass transition. Experiments at varying rates as well as modulated DSC were performed as well, but neither improved the measurement. The broad glass transitions are intrinsic to these systems, as discussed in Chapter 1. The assessment of the glass transition temperature is therefore challenging, and we use the derivative of the heat flow with respect to temperature, as represented in the inset of Figure 2.8a. The glass transition then translates into a peak fitted to a Gaussian function. Corresponding T_g values are reported in Table 2.1.

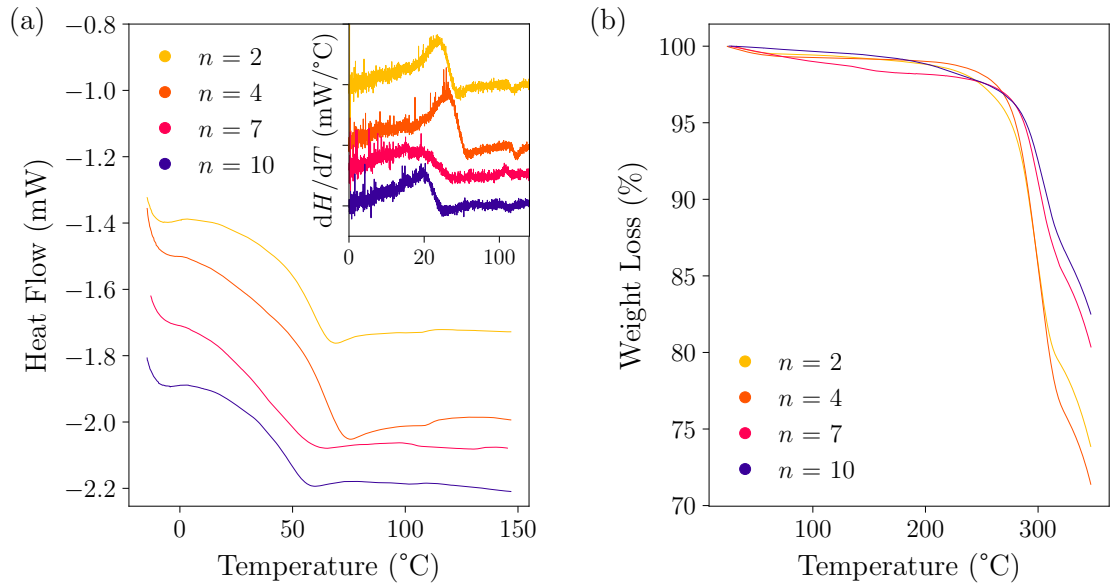

Figure 2.8: (a) DSC thermograms at the second heating cycle for the imidazolium PIL series **PC$_n$VImTFSI** with varying side-chain length n. Inset is the derivative of the heat flow with respect to temperature. Traces are vertically shifted for clarity. (b) Corresponding TGA weight loss.

Thermogravimetry analysis (TGA) was also performed on a TGA Q50 (TA Instruments) at heating rates of 7 °C/min and corresponding traces for varying side chain length are reported in Figure 2.8b. The degradation temperature $T_{d,5\%}$ is taken at a relative weight loss of 5% and given in Table 2.1.

Sample	T_g (°C)	$T_{d,5\%}$ (°C)
PC_2VImTFSI	58 ± 2	276
PC_4VImTFSI	65 ± 2	280
PC_7VImTFSI	46 ± 4	288
PC_{10}VImTFSI	47 ± 3	289

Table 2.1: Glass transition temperature T_g of the **PC_nVImTFSI** series as determined from the Gaussian fits to the heat flow derivative of Figure 2.8a and degradation temperatures taken at 5% weight loss on the TGA traces of Figure 2.8b.

2.3 Synthesis of triazolium based PIL nanoparticles

2.3.1 Materials

N-Succinimidyl methacrylate (TCI, 99%), N,N–diisopropylethylamine (DIPEA, Merck, 99%), propargyl amine (Merck, 99%), iodo(triethyl phosphite)copper(I) (CuP(OEt)3I, Merck, 97%), methyl iodide (Merck, 99%), hydroquinone (Merck, 99%), propargyl acrylate (TCI, 97%), propargyl methacrylate (TCI, 97%), Dowex 1X8-100 (chloride form, Merck) and solvents from the purest grades were used as received.

2.3.2 Characterization methods

NMR spectroscopy was carried out with a Bruker DRX 400 spectrometer operating at 400 MHz for ^{1}H, and 100 MHz for ^{13}C. Spectra were obtained with a 5-mm QNP probe at 363 K. Chemical shifts (δ) are given in ppm in reference to residual hydrogenated solvents for ^{1}H NMR, and to the signal of the deuterated solvent for ^{13}C NMR. The same abbreviations for peak multiplicity as for bulk synthesized imidazolium PILs are used, namely s for singlet, d for doublet, dd for doublet of doublet, t for triplet and m for multiplet.

2.3.3 Synthetic path

We detail in this section the full synthesis of a (1,2,3-triazolium chloride)-functionalized acrylate IL monomer. The same procedure is applied for the other methacrylate and acrylamide IL monomers, as represented in Figure 2.9a. Dispersion polymerization of the functionalized monomers in aqueous solution was subsequently carried out at 65 °C for 16 h, initiated by ACPA at a concentration of 0.05% by weight (Figure 2.9b).

CuAAC cycloaddition

Synthesis of 1,2,3-triazole-functionalized acrylate In a 100 mL RBF was added propargyl acrylate (0.92 g, 8.36 mmol), 1-azidotetradecane (1.30 g, 5.4 mmol), in tetrahydrofuran (15 mL) and allowed to stir over a period of 5 min at ambient temperature. To the above solution was added DIPEA (1.21 g, 9.3

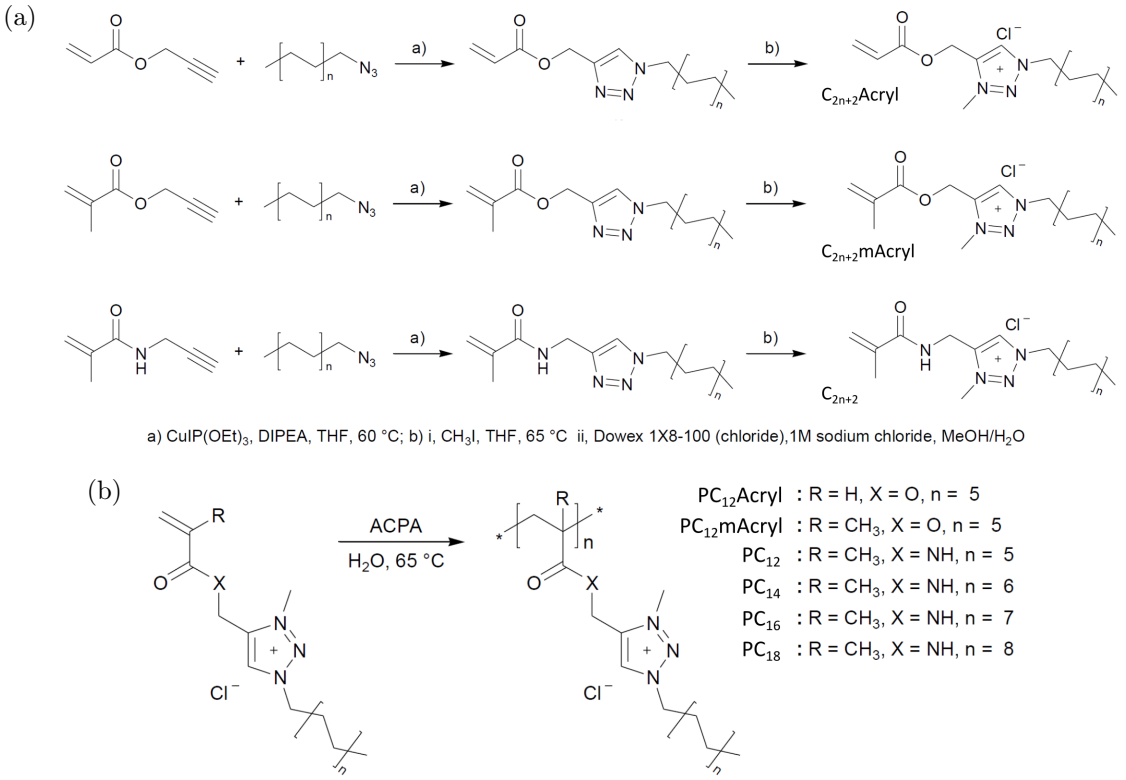

Figure 2.9: Synthetic path and chemical structure of aliphatic 1,2,3-triazolium chloride ionic liquid monomers (a) and corresponding PILs nanoparticles obtained by precipitation polymerization (b).

mmol), CuIP(OEt)3 (11 mg, 0.308 mmol) and the mixture was stirred for 16 h at ambient temperature. The mixture was evaporated to dryness under reduced pressure and the crude product was purified by column chromatography using a 1:1 mixture of petroleum ether and ethyl acetate as eluent to yield, after evaporation of the solvents under reduced pressure, the 1,2,3-triazole-functionalized acrylate as a half white solid (1.59 g, 75.0%).

N-alkylation and anion exchange reactions

Synthesis of (1,2,3-triazolium chloride)-functionalized acrylate 1,2,3-Triazole-functionalized acrylate (500 mg, 1.43 mmol), methyl iodide (4.05 g, 28.3 mmol) in tetrahydrofuran (5 mL) were introduced in a glass tube that was sealed under vacuum. The solution was stirred for 16h at 60 °C and was further evaporated to dryness under vacuum. The resulting (1,2,3-triazolium iodide)-functionalized acrylate intermediate was then dissolved in a 1:1 mixture of methanol and water (20 mL) and allowed to stir for 15 minutes. The homogenous solution was charged to an anion exchange column (Dowex 1X8-100, chloride form, 5 g) saturated with a 1M sodium chloride aqueous solution, and eluted with methanol (50 mL). The eluent was evaporated under reduced pressure at room temperature to quantitatively obtain 614 as a pale yellow solid (420 mg, 73.6%).

2.4 Characterization of nanoparticles

2.4.1 Chemical structure of precursor ILs

1,2,3-triazole-functionalized acrylate
^{1}H NMR (400 MHz, $CDCl_3$) (Figure 2.10a) δ (ppm) :
7.54 (s, C**H**=CN, 1H), 6.42 (dd, J_1 = 1.2 Hz, J_2 = 17.4 Hz, trans C**H**$_2$=CH, 1H),
6.12 (dd, J_1 = 10.4, Hz, J_2 = 17.4 Hz, CH_2=C**H**, 1H),
5.84 (dd, J_1 = 1.2 Hz, J_2 = 10.4 Hz, cis C**H**$_2$=CH, 1H), 5.24 (s, COOC**H**$_2$, 2H),
4.29 (t, J = 7.2 Hz, NC**H**$_2$$CH_2CH_2CH_2(CH_2)_7CH_2CH_2CH_3$, 2H),
1.94-1.83 (m, NCH_2C**H**$_2$$CH_2CH_2(CH_2)_7CH_2CH_2CH_3$, 2H),
1.34-1.29 (m, NCH_2CH_2C**H**$_2$C**H**$_2$$(CH_2)_7CH_2CH_2CH_3$, 4H),
1.29-1.16 (m, $NCH_2CH_2CH_2CH_2$(C**H**$_2$$)_7$C**H**$_2$C**H**$_2$$CH_3$, 18H),
0.79 (t, J = 6.8 Hz, $NCH_2CH_2CH_2CH_2(CH_2)_7CH_2CH_2$C**H**$_3$, 3H).

^{13}C NMR (100 MHz, $CDCl_3$) (Figure 2.10b) δ (ppm) :
166.0 (**C**$OOCH_2$), 142.10 (CH=**C**N), 131.4 (**C**H_2=CH),
128.0 (CH_2=**C**H), 123.6 (**C**H=CN), 57.7 (COO**C**H_2),
50.4 (N**C**$H_2CH_2CH_2CH_2(CH_2)_7CH_2CH_2CH_3$),
31.9 ($NCH_2CH_2CH_2CH_2(CH_2)_7$**C**$H_2CH_2CH_3$),
30.2 (NCH_2**C**$H_2CH_2CH_2(CH_2)_7CH_2CH_2CH_3$),
29.6, 29.5, 29.4, 29.3 (NCH_2**C**$H_2CH_2CH_2$(**C**$H_2$$)_7CH_2CH_2CH_3$),
28.9 ($NCH_2CH_2CH_2$**C**$H_2(CH_2)_7CH_2CH_2CH_3$),
26.4 (NCH_2CH_2**C**$H_2CH_2(CH_2)_7CH_2CH_2CH_3$),
22.6 (NCH_2CH_2**C**$H_2CH_2(CH_2)_7CH_2$**C**H_2CH_3),
14.1 ($NCH_2CH_2CH_2CH_2(CH_2)_7CH_2CH_2$**C**$H_3$).

HRMS (ESI) m/z: $[M+Na]^+$ calculated for $C_{20}H_{35}N_3NaO_2$, 349.2621; found, 372.2620.

1,2,3-(triazolium chloride)-functionalized acrylate IL monomer
^{1}H NMR (400 MHz, DMSO-d_6) (Figure 2.11a) δ (ppm) :
9.14 (s, NC**H**=C, 1H), 6.45 (dd, J_1 = 1.2 Hz, J_2 = 17.2 Hz, trans C**H**$_2$=CH, 1H),
6.25 (dd, J_1 = 10.4 Hz, J_2 = 17.2 Hz, CH_2=C**H**, 1H),
6.08 (dd, J = 1.2 Hz, J_2 = 10 Hz, cis C**H**$_2$=CH, 1H), 5.51 (s, COOC**H**$_2$, 2H),
4.62 (t, J = 7.0 Hz, NC**H**$_2$$CH_2CH_2CH_2(CH_2)_7CH_2CH_2CH_3$, 2H),
4.32 (s, NC**H**$_3$, 3H), 1.92-1.84 (m, NCH_2C**H**$_2$$CH_2CH_2(CH_2)_7CH_2CH_2CH_3$, 2H),
1.32-1.25 (m, NCH_2CH_2C**H**$_2$C**H**$_2$$(CH_2)_7CH_2CH_2CH_3$, 4H),
1.25-1.19 (m, $NCH_2CH_2CH_2CH_2$(C**H**$_2$$)_7$C**H**$_2$C**H**$_2$$CH_3$, 18H),
0.84 (t, J = 6.8 Hz, $NCH_2CH_2CH_2CH_2(CH_2)_7CH_2CH_2$C**H**$_3$, 3H).

^{13}C NMR (100 MHz, DMSO-d_6) (Figure 2.11b) δ (ppm) :
164.6 (**C**$OOCH_2$), 138.4 (CH=**C**N), 133.3 (**C**H_2=CH), 130.3 (CH_2=**C**H),
127.1 (**C**H=CN), 53.7 (COO**C**H_2), 53.1 (N**C**$H_2CH_2CH_2CH_2(CH_2)_7CH_2CH_2CH_3$),
38.2 (N**C**H_3), 31.2 ($NCH_2CH_2CH_2CH_2(CH_2)_7$**C**$H_2CH_2CH_3$),
29.0, 28.9, 28.8, 28.7, 28.7, 28.5, 28.2 (NCH_2C**H**$_2$$CH_2$C**H**$_2$C**H**$_2$$CH_2)_7CH_2CH_2CH_3$),
25.3 (NCH_2CH_2**C**$H_2CH_2(CH_2)_7CH_2CH_2CH_3$),
22.0 ($NCH_2CH_2CH_2CH_2(CH_2)_7CH_2$**C**$H_2CH_3$),

13.9 ($NCH_2CH_2CH_2CH_2(CH_2)_7CH_2CH_2\mathbf{C}H_3$).

HRMS (ESI) m/z: $[M]^+$ calculated for $C_{21}H_{38}N_3O_2$, 364.2959; found, 364.2961.

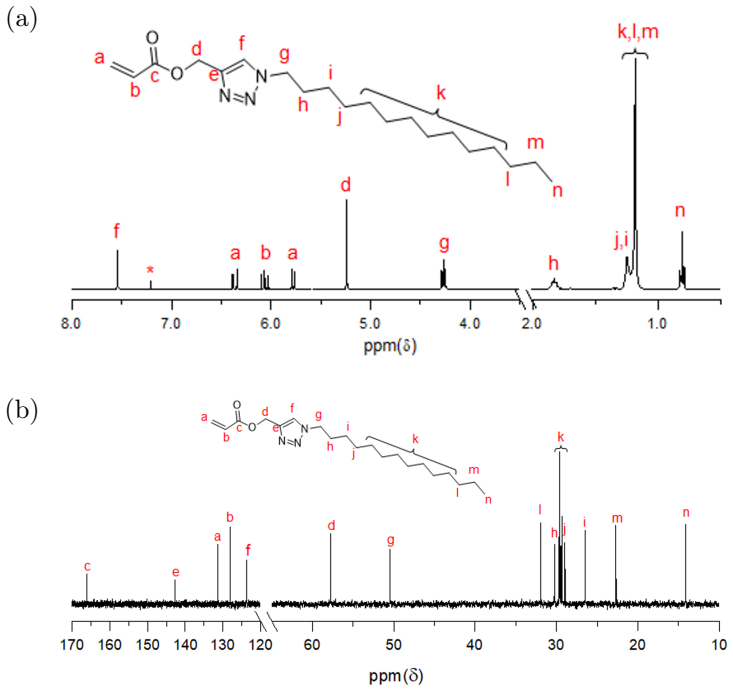

Figure 2.10: ^{1}H NMR (400 MHz, $CDCl_3$) (a) and ^{13}C NMR (100 MHz, $CDCl_3$) (b) of 1,2,3-triazole-functionalized acrylate (Peaks assigned to $CDCl_3$ are denoted *).

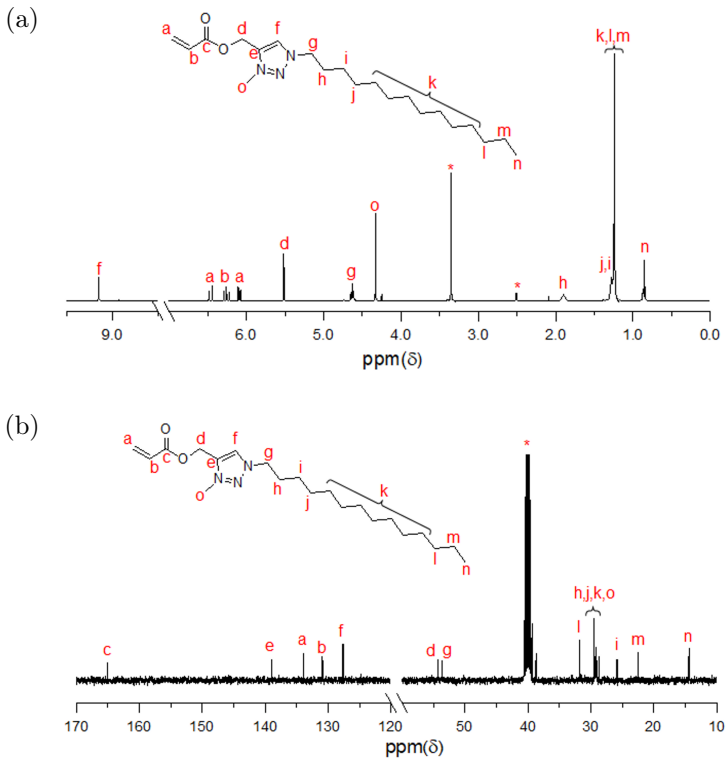

Figure 2.11: ^{1}H NMR (400 MHz, DMSO-d_6) (a) and ^{13}C NMR (100 MHz, DMSO-d_6) (b) of (1,2,3-triazolium chloride)-functionalized acrylate (Peaks assigned to DMSO are denoted *).

2.4.2 Particle size

Particle sizes are determined by Dynamic Light Scattering (DLS) measurements, performed on a Zetasizer Nano ZS. The sample concentration was 1 mg/mL and experiments were performed in triplicate. We give in Figure 2.12 the distribution of hydrodynamic diameter for the samples considered in our investigation *i.e.* PIL NPs obtained from dispersion polymerization of 25 mM aqueous solutions of acrylate, methacrylate based triazolium PIL with dodecane side chains and the acrylamide based triazolium PIL series with side chains from dodecane to octadecane.

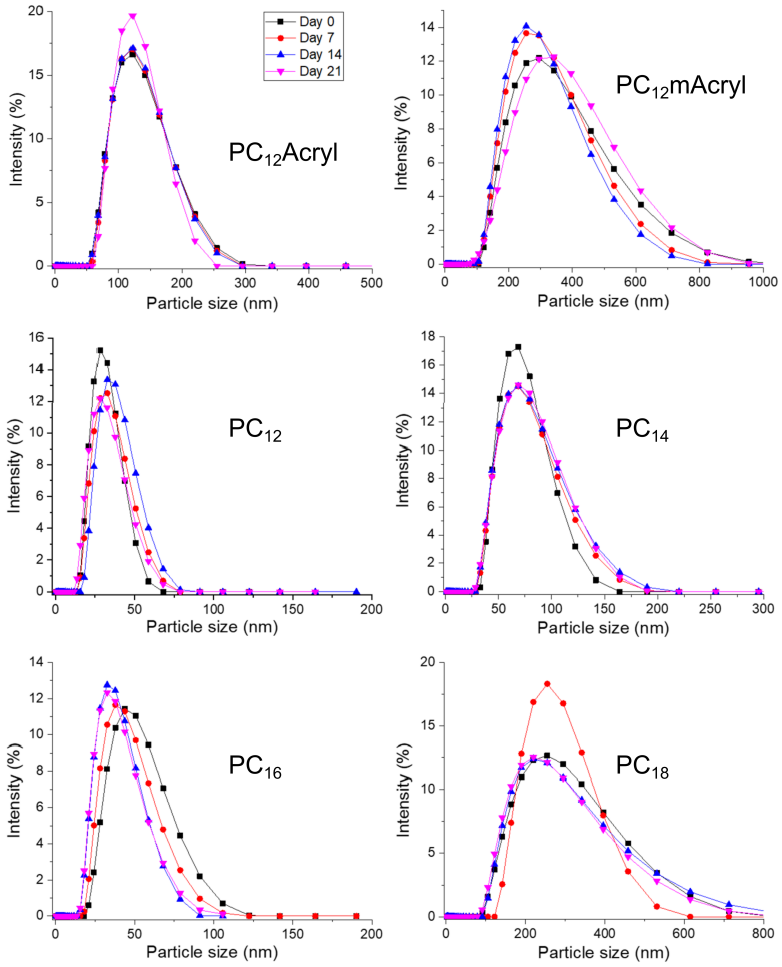

Figure 2.12: Hydrodynamic diameter distribution as measured by DLS at different storage times at room temperature for poly((1,2,3-triazolium chloride) nanoparticles.

Chapter 3

Bulk structure

As discussed in Chapter 1, molecular dynamics (MD) simulations and wide-angle X-ray scattering (WAXS) have shown that the same kind of nanoscale segregation between apolar and ionic domains in ILs also occurs in PILs. Such nanostructure was shown to be independent of the PILs polymerization degree (N) above a certain threshold [59] and was found to play a significant role in both their ionic conductivity [32, 33, 58] and rheological behaviour [119, 121, 123, 127]. Yet, the influence of the local structure on the macromolecular conformation of PIL chains in melts and solutions have not been investigated.

We present in this chapter our investigation of the influence of the side-chain length and the chemical nature of the counter-anion on the conformation of poly(1-vinyl-3-alkylimidazolium) (**PC$_n$VImX**) using small angle neutron scattering (SANS), the lone technique able to measure such features. The local structure of these materials was investigated using WAXS. The principle of scattering is detailed in section 3.1 in the case of neutrons and its specific application to polymeric systems in section 3.2. Three cases were investigated in this study: dilute solutions of PILs in deuterated tetrahydrofuran (THF-d$_8$), dilute solutions in imidazolium ILs with identical alkyl substituents and finally, PIL melts. Further experiments were performed to identify the role of temperature on these structural features.

3.1 Scattering premises

Several experimental techniques rely on scattering and thereby share a common formalism. Scattering experiments involve sending a beam onto a sample and recording the so-called scattering pattern. What distinguishes each technique is essentially the nature of the beam, which determines the type of interactions with the sample but also the range of characteristic sizes that can be probed. Visible light, such as a laser beam, make up for the simplest kind of scattering experiment to put in place. Two other radiations are often used in soft matter and will be considered hereafter: X-rays and neutrons. We will mainly focus on the latter, in this section, for both theoretical and experimental aspects. A word will be given on the specificities of X-rays later on, but the main formalism is identical. Readers familiar with these scattering techniques can skip to section 3.2 for specificities of scattering applied to polymeric samples, or section 3.3 for results on our PIL series.

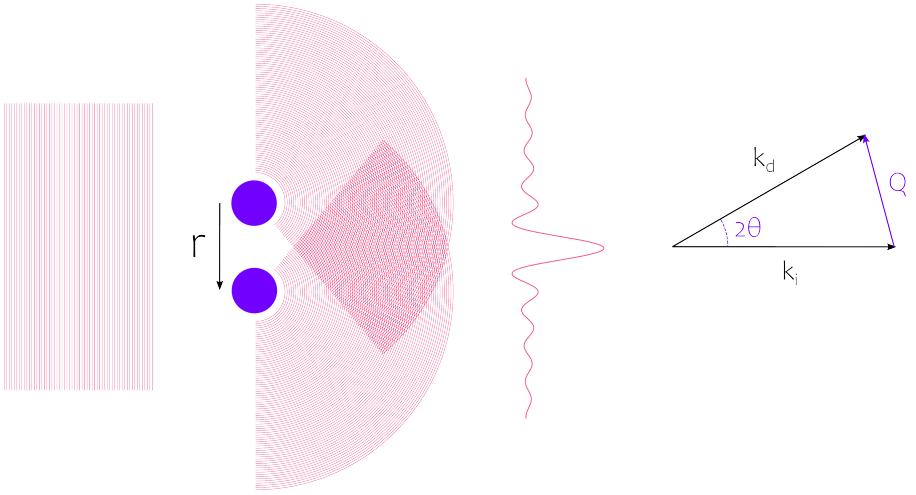

Figure 3.1: Schematic representation of scattering. Figure adapted from reference [128].

3.1.1 Scattering theory

Neutrons are particularly handy when it comes to probe the structure of condensed matter. The energies of thermal neutrons used for the investigation of soft matter systems, between a few meV and hundreds of meV, fall into the order of magnitude of intramolecular energies. Moreover, their wavelength of a few Ångströms corresponds to characteristic intramolecular lengths. The general phenomenon of scattering is schematically represented in Figure 3.1 in which the planar incident wave on the left-hand side is characterized by a wavelength λ or alternatively a wave vector of norm $k_\mathrm{i} = 2\pi/\lambda$ and a pulsation ω such as the incident wave function is given by:

$$\psi_\mathrm{i}(x,t) = \psi_0 e^{\mathrm{i}(\omega t - k_\mathrm{i} x)} \tag{3.1}$$

As the incident wave goes through the sample and interacts with an atom, it scatters in all directions, hence generating a spherical wave. A neutron has a given probability of interacting with an atom, which is proportional to a quantity called the scattering cross section σ. We also define its one dimensional counterpart, the scattering length b as a characteristic range of interaction between the neutron and the atom :

$$\sigma = 4\pi b^2 \tag{3.2}$$

All in all, the scattered wave from one scatterer recorded on a detector at a distance D is given by :

$$\psi(x,t) = \psi_0 \frac{b}{D} e^{\mathrm{i}(\omega t - k_\mathrm{d} D)} \tag{3.3}$$

A sample is evidently composed of a large number n of atoms and thus scatters n spherical waves that interfere as represented in Figure 3.1 in the simple case of two scatterers. The resulting wave is the superposition of all of them, corrected by a phase shift $\Delta\Phi$ given by:

$$\Delta\Phi = \vec{r}\cdot(\vec{k}_\mathrm{d} - \vec{k}_\mathrm{i}) = \vec{r}\cdot\vec{Q} \tag{3.4}$$

Equation 3.4 introduces the scattering vector $\vec{Q}$ as the difference between incident and scattered wave vectors. Simple geometrical considerations on the right-hand panel of Figure 3.1 gives a norm $Q = \frac{4\pi}{\lambda}\sin\theta$. Not only is $\vec{Q}$ a convenient variable in the following calculations, it is also our main variable in reciprocal space, meaning it directly relates to the inverse of characteristic distances of the system, as we will see later on.

The scattering angle θ is considered the same for all scatterers, since the sample is virtually always much smaller than the distance to the detector. Furthermore, we consider that neutrons are weakly scattered by the sample, hence neglecting multiple scattering events (Born Approximation) [128]. The coherent[1] sum over all scatterers leads to a resulting wave:

$$\psi = \frac{\psi_0}{D}\sum_{i=1}^{n} b_i e^{\mathrm{i}\vec{Q}\cdot\vec{r}_i} \tag{3.5}$$

A neutron detector is sensitive to the intensity, defined as the square of the wave amplitude, in which the ensemble average is denoted $< \cdot >$:

$$I_\mathrm{det} = \psi\cdot\psi^* = \left(\frac{\psi_0}{D}\right)^2 \sum_{i,j}^{n} \left\langle b_i b_j e^{\mathrm{i}\vec{Q}\cdot(\vec{r}_i - \vec{r}_j)} \right\rangle \tag{3.6}$$

In order to drop the prefactor $(\psi_0/D)^2$, we introduce the differential of the scattering cross section σ of equation 3.2, denoted $\Sigma(\vec{Q})$ in the following, such as :

$$\Sigma(\vec{Q}) = \frac{\mathrm{d}\sigma}{\mathrm{d}\Omega}(\vec{Q}) = \sum_{i}^{n}\sum_{j}^{n} \left\langle b_i b_j e^{\mathrm{i}\vec{Q}\cdot(\vec{r}_i - \vec{r}_j)} \right\rangle \tag{3.7}$$

Physically, this quantity represents the scattering probability at a given scattering vector $\vec{Q}$, in other words the probability to find two scatterers of scattering length b_i and b_j separated by a vector $\vec{r}_i - \vec{r}_j$. In practice, however, the measured intensity also depends on the volume V of sample seen by the beam:

$$I(Q) = \frac{1}{V}\frac{\mathrm{d}\sigma}{\mathrm{d}\Omega}(Q) \tag{3.8}$$

This form of the measured intensity is homogenous to the reciprocal of a distance, generally expressed in cm^{-1}, as commonly used to represent experimental data after the treatment detailed in 3.1.5. Nonetheless, in order to lighten the following calculations and explanations, we consider the scattering intensity to be simply the differential scattering cross section $\Sigma(Q)$.

The key interest of scattering unfolds from the exponential term $\exp(\mathrm{i}\vec{Q}\cdot(\vec{r}_i - \vec{r}_j))$. It comes that the measured intensity is a Fourier transform of the scattering length fluctuations within the sample. It implies that the modulus of the scattering vector acts as a magnifying glass, and the characteristic lengths probed are of the order of Q^{-1}. This means that travelling along the Q-axis amounts to zooming

[1] We assume for now the term coherent and will come back to it in section 3.1.2

into the structure and scanning increasingly smaller features. We represent this schematically in Figure 3.4.

The objects considered are usually larger than isolated atoms and are often taken to be particles, entire molecules or monomers. It is then convenient to introduce the notion of elementary scatterer as building blocks of the system considered. Similarly to the scattering length, an elementary scatterer of molar volume v composed of n atoms of scattering lengths b_i, *i.e.* a molecule, is characterized by a scattering length density (ρ) given by :

$$\rho = \frac{\sum_i^n b_i}{v} \tag{3.9}$$

Let us now consider N_{ES} elementary scatterers, the differential scattering cross section then reads:

$$\Sigma(Q) = \sum_{\alpha,\beta}^{N_{\mathrm{ES}}} b_\alpha b_\beta \sum_{i,j}^{n_\alpha, n_\beta} \left\langle e^{\mathrm{i}\vec{Q}\cdot(\vec{r}_i^{\,\alpha} - \vec{r}_j^{\,\beta})} \right\rangle = \sum_{\alpha,\beta} b_\alpha b_\beta S_{\alpha\beta}(Q) \tag{3.10}$$

where $S_{\alpha\beta}(q)$ are the partial structure factors of the different elementary scatterers of the system. These terms are only dependent on how the scatterers are arranged across the sample, in other words the structure of the sample.

Let us now take a step down in complexity and focus on a binary system composed of two types of elementary scatterers. This is the fairly usual situation of objects in a continuous media, such as a polymer solution, for example. It can be derived that :

$$\Sigma(Q) = \left(b_2 - b_1\frac{v_2}{v_1}\right)^2 S_{22}(Q) = (\rho_2 - \rho_1)^2 v_2^2 S_{22}(Q) \tag{3.11}$$

In which the last step was introducing the scattering length densities of equation 3.9. The term $(\rho_2 - \rho_1)^2$ hereafter denoted as $\Delta\rho^2$ is called the contrast factor and will be discussed in the following section 3.1.3.

Suppose now the system is slightly more elaborate and each of the n objects contains N elementary scatterers. The system remains binary with n objects in a continuous media. The intra-object and inter-object interferences can be isolated, such as the scattered intensity can be rewritten :

$$\begin{aligned}
\frac{\Sigma(Q)}{(\Delta\rho)^2 v_{\mathrm{obj}}^2} &= \sum_{\alpha,\beta}^{n}\sum_{i,j}^{N} e^{\mathrm{i}\vec{Q}\cdot(\vec{r}_i^{\,\alpha} - \vec{r}_j^{\,\beta})} = nN^2\left(P(Q) + nQ(Q)\right) \\
P(Q) &= \frac{1}{N^2}\sum_{i^\alpha}^{N}\sum_{j^\alpha}^{N} e^{\mathrm{i}\vec{Q}\cdot(\vec{r}_i^{\,\alpha} - \vec{r}_j^{\,\alpha})} \\
Q(Q) &= \frac{1}{N^2}\sum_{i^\alpha}^{N}\sum_{j^\beta}^{N} e^{\mathrm{i}\vec{Q}\cdot(\vec{r}_i^{\,\alpha} - \vec{r}_j^{\,\beta})}
\end{aligned} \tag{3.12}$$

The intra-object contribution, otherwise called the form factor $P(Q)$, holds information on the correlation between elementary scatterers of a single object, while

the structure factor $Q(Q)$ accounts for the correlations between elementary scatterers of different objects. Modelling of the system will take place in these terms, allowing the calculation of the expected scattering pattern and the fitting of the experimental data. It should be stressed at this point that equation 3.12 is the general form of the scattered intensity. In the case of rigid and centro-symmetrical objects such as colloids, the intra and inter object contributions to the scattering can be decoupled by choosing the centre of mass of the objects as their origin [128]. Such transformation in the coordinate systems enables a factorization in equation 3.10 leading to $\Sigma(Q) \sim P(Q) \times S(Q)$. The structure factor $S(Q)$ then describes the correlations between the centre of mass of the objects.

3.1.2 Incoherent scattering

Some assumptions or shortcuts were made in the previous section, such as considering an atom has a fixed scattering length b_i. In reality, it depends on the spin state of the atom and an averaging of fluctuations over position and spin states is required. For a system composed of n identical atoms, the scattered intensity can be expressed as :

$$\Sigma(Q) = n b_{\text{inc}}^2 + b_{\text{coh}}^2 \sum_i^n \sum_j^n e^{\mathrm{i}\vec{Q}\cdot(\vec{r}_i - \vec{r}_j)} \tag{3.13}$$

Only the second term, the coherent scattering, holds information on the structure probed. The first term, the incoherent scattering, which was omitted before, contributes as a Q-independent signal, a flat background which is removed during data treatment. This incoherent scattering is highly dependent on the composition of the sample and particularly its hydrogen content, much like the contrast term, which will be discussed next.

3.1.3 Contrast

A contrast term $\Delta\rho$ arises in the previous calculations and was introduced in equation 3.11 as a prefactor to the scattered intensity. In a binary system, this contrast term is the squared difference of scattering length densities ρ between the object and the continuous matrix. Scattering lengths vary considerably across the periodic table and one specificity of neutrons is the high contrast between hydrogen H and its isotope deuterium D. Since the former can be replaced by the latter without altering the structure of the material, neutrons offer the possibility to tune the contrast in order to target the observations[1]. In the particular situations of dilute solutions and polymer melts we will focus on, a precise mixture of hydrogenated and deuterated species maximizes the contrast, hence the signal-to-noise ratio. They will be detailed in sections 3.2.3 and 3.2.2. It must be pointed out here that contrast is a crucial difference between neutrons and X-rays. The latter interact with the electronic cloud surrounding atoms instead of their nuclei. Thus, X-ray scattering lengths increase proportionally to the number of electrons across

[1]Contrast matching experiments consists in tuning the SLD of the solvent through the ratio of deuterated and hydrogenated solvent in order to match the SLD of a particular component. The latter is then invisible to neutrons since there is no contrast with the solvent.

the periodic table, denying the possibility to tune the contrast with isotope substitutions. Furthermore, because it favours large atoms, contrast can be a severe drawback in soft matter studies with X-rays.

3.1.4 Absorption

The scattering lengths b were considered as real values in the previous calculations. However, they are complex values with an imaginary part quantifying the absorption by the scatterer. Absorption depends on both atoms present and the energy of the incident beam. X-ray absorption increases regularly with atomic number Z along the periodic table, and depends again on the number of electrons. Neutron absorption is conversely random. As a matter of example, H atoms considerably absorb neutrons but hardly not X-rays. In contrast, higher Z atoms such as silicon Si or aluminium Al absorb X-rays but not neutrons. This is particularly interesting for neutron imaging or experimental setups, since all kinds of surrounding metallic holders or containers have little impact on the beam.

Due to absorption, a sample has a certain transmission T regarding the considered beam, defined as the ratio of direct beam intensities with and without sample. It relates to the thickness d as $T = e^{-\mu d}$ in which the linear attenuation coefficient μ is a function of the wavelength and the imaginary part of the scattering length. In practice, a sample composed of strongly neutron absorbing atoms scatters weakly, which can be a severe drawback and has to be accounted for in the data treatment explained in the next section. Such transmission considerations will be a particular matter of discussion in section 3.4.3.

3.1.5 Experimental aspects

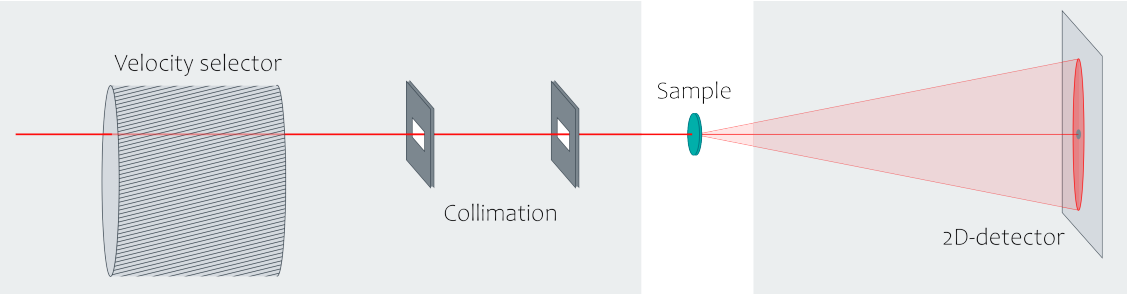

Figure 3.2: Schematic representation of the experimental setup of a SANS spectrometer. Grey areas represent vacuum tanks.

The experimental data presented in the following sections were collected on two different spectrometers, PAXY at Laboratoire Léon Brillouin (CEA Saclay, France) and SANS-I at Paul Scherrer Institute (Villigen, Switzerland) both of them sharing a common layout depicted in Figure 3.2. The moderated neutron beam, *i.e.* of thermal neutrons, goes through a velocity selector which acts as a monochromator [1] to select a working wavelength λ. This mechanical selection is made by a rotating

[1] Other monochromator include crystals or mirrors which deliver a precise selection but a poor neutron flux.

helix which only let through the neutrons with the right velocity, thus the desired wavelength, with a selectivity of approximately $^{\Delta\lambda}/_{\lambda} \approx 10$ %. The monochromatic beam is nevertheless highly divergent as it exits the neutron guide and requires collimation before use. This is achieved by two diaphragms which size, of the order of the centimetre and separation distance, of a few meters, impacts the resolution achieved. The thinnest the collimation, the highest the resolution but the greatest the loss in flux as well. These parameters must be carefully chosen. The monochromatic collimated beam scatters in the sample, and the resulting scattering pattern is recorded on a 2D detector. Such detector is made of neutron absorbing gases such as ^{3}He, which produce high energy ions as they absorb neutron. These fast ions produce a trail of secondary ionization, hence producing detectable electrical pulses. All these components must be under vacuum in order to avoid residual scattering and absorption by ambient air. We provide pictures of both neutron spectrometers used in this work in Figure 3.3.

(a)

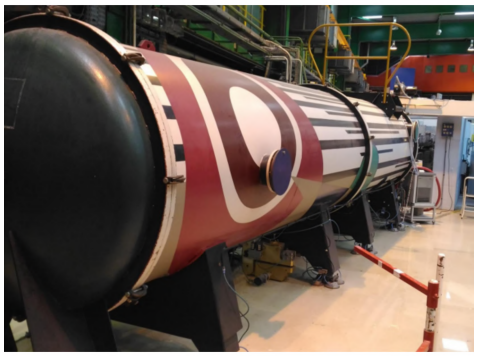

(b)

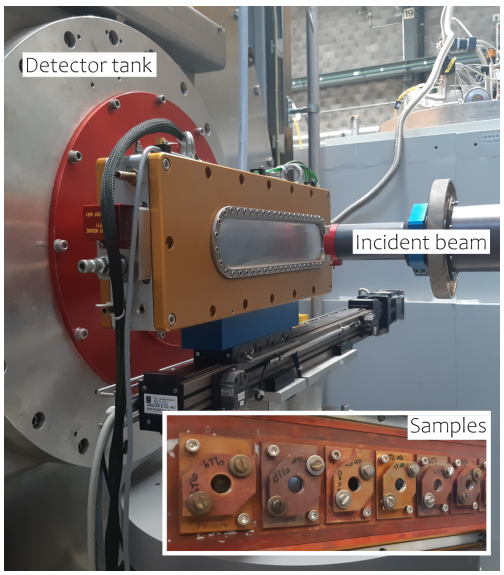

Figure 3.3: Pictures of Small Angle Neutron scattering spectrometers. (a) Detector tank of PAXY spectrometer at Laboratoire Léon Brillouin (CEA Saclay, France) and sample environment of SANS-I spectrometer at Paul Scherrer Institute (Villigen, Switzerland).

The detector records a 2D picture of the scattering pattern which requires some treatment to retrieve the differential scattering cross section per unit volume given by equation 3.8, hereafter referred to as absolute intensity or simply scattering pattern [129]. The contributions of background signal, the direct beam and the container must be subtracted to the 2D data. For isotropic situations such as ours, the 2D data is averaged over 2π for each scattered angle θ so as to retrieve an intensity as a function of scattering vector Q. The 1D intensity must also be corrected by some experimental parameters namely the neutron beam flux Φ, the detector's efficiency ε and solid angle $\Delta\Omega$, the sample's transmission T and thickness d and the area illuminated by the beam A :

$$I(\theta) = \Phi(\lambda)A\varepsilon(\lambda)\Delta\Omega dTI(\theta) \tag{3.14}$$

3.2 Conformation of a polymer chain

The purpose of this section is to apply neutron scattering to textbook model situations for a better understanding of our own situation later on. Main results of the theory of polymer physics are evidently discussed, but not in detail. Useful references can be found along the discussion. For the sake of simplicity and application to our studies, only linear polymer chains will be considered here. Other architectures including star-branched or H-branched, dendrimers or rings will not be addressed.

3.2.1 Neutron scattering of polymeric systems

In order to describe a polymeric system, one must first focus on an isolated chain. To describe such a chain statistically, each little chain segment, a bond between monomers, is associated to a vector $\vec{r}_i$. One measurement of the size of a coil made of N segments is the sum over all the segments, $\vec{R} = \sum^N \vec{r}_i$. In the often encountered situation of an isotropic system, the average of this so-called end-to-end vector over all configurations is null. Therefore, the mean-square end-to-end distance $< R^2 >$ is a better measurement of the polymer coil's size. Its square-root will simply be called radius hereafter. In practice, though, the radius of gyration R_g is preferred to the end-to-end vector, which can hardly be defined for branched polymers such as stars. The radius of gyration is defined as the average square distance between monomers, at positions $\vec{R}_i$, and the centre of mass ($\vec{R}_{cm}$) of the polymer coil :

$$R_g^2 = \frac{1}{N}\sum_{i=1}^{N}\left(\vec{R}_i - \vec{R}_{cm}\right)^2 \quad \text{with} \quad \vec{R}_{cm} = \frac{1}{N}\sum_{j=1}^{N}\vec{R}_j \tag{3.15}$$

After some calculation, it can be shown that the radius of gyration relates to the mean-square end-to-end distance as $< R_g^2 >=< R^2 > /6$.

Before moving on to characteristics of neutron scattering in polymeric systems, let us focus a little longer on the chain itself. Most of them are self-similar over a wide range of length scales, in the sense that the whole chain behaves the same way as a portion of it [2, 130]. This self similarity is characteristic of fractal objects, to which most polymer chains belong. Put simply, this means the number of monomers g of a portion of the chain is proportional to the mean-square size of the same portion to an exponent α called the fractal dimension :

$$g \sim \left(\sqrt{< r^2 >}\right)^{\alpha} \tag{3.16}$$

Self similarity of the polymer chain ends at small length scales below the so-called persistence length. The chain strand is then better described as a rigid cylinder. This will be of importance on our PIL systems.

As mentioned in section 3.1.1, scattering experiments probe different length scales $1/Q$ reciprocal of the scattering vector. In the case of polymeric systems, three regimes are commonly identified [128] and represented in Figure 3.4. At very low Q values, $^1/_Q \ll {}^1/_{R_g}$ the whole size of the polymer coil is probed. This so-called Guinier regime allows the radius of gyration of the chain to be measured. As the Q

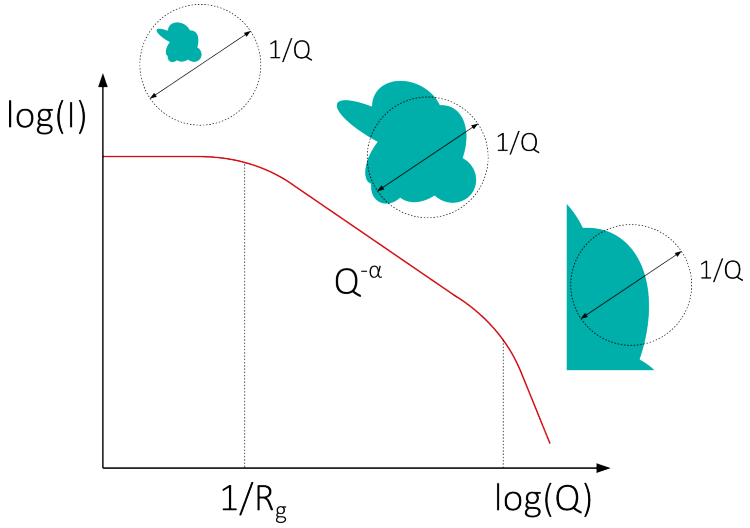

Figure 3.4: Simple view on the scattered intensity for a random object. From left to right : the Guinier regime probing the radius of gyration of the object, the intermediate regime in which the exponent α of the power-law decay provides information on the shape of the object, the Porod regime dependent on its specific surface. Inspired from ref. [128].

value increases, we enter the intermediate regime in which the scattering intensity decreases as $Q^{-\alpha}$. The exponent α is the fractal dimension of the object on equation 3.16, thus characteristic of the shape of the object. Representative examples will be addressed in the following to detail how the fractal dimension can vary in polymeric systems. Finally, for even higher values of Q, the magnifying is such that only the interface between the object and its surrounding medium is seen. The scattered intensity follows a Q^{-4} power-law decay called the Porod regime. This is similar to what can be derived in neutron reflectivity, which formalism will be detailed in Chapter 4.

3.2.2 Neutron scattering from a polymer solution

The easiest way to have an isolated polymer chain is in a dilute solution. In such a scenario, two interactions have to be taken into account : monomer-monomer and monomer-solvent interactions. Depending on the balance between the two, the chain will rather be surrounded by solvent molecules (case of a good solvent) or expel them from the polymer coil, which then collapses (case of a bad solvent). This is quantified by the Flory interaction parameter χ. Interactions felt by the monomers are quantified by an excluded volume parameter v such as $v = a^3(1-2\chi)$ in which a is the size of the Kuhn segment [130]. If χ is smaller than $1/2$ the interaction between monomers is repulsive, and they rather be surrounded by solvent molecules. The polymer coil is then naturally swollen by solvent. Such a state comes at an entropic cost, some configurations are no longer accessible to the chain. This simple picture reveals the competition between an entropic contribution, the loss of accessible conformations, and an enthalpic one, the interactions between monomers. The most often used model was developed by P. J. Flory in 1953 who calculated the free energy F of such a chain as the sum of both contributions [131] :

$$\frac{F}{kT} = \frac{R^2}{Na^2} + v\frac{N^2}{R^3} \tag{3.17}$$

Minimizing this free energy with respect to the radius R of the polymer chain leads to a power law for the Flory radius of a swollen linear chain :

$$R_F \sim N^{3/5} \tag{3.18}$$

It must be stressed that this theory, despite some approximations, is in good agreement with more sophisticated ones and gives in fact a universal scaling $R \sim N^{\nu}$. The exponent ν is the inverse of the fractal dimension $\alpha = 1/\nu$, accessible using neutron scattering as mentioned above. More quantitatively, a chain with excluded volume effects can be modelled by the form factor given by [132–134] :

$$P_{\text{excl}}(Q) = 2\int_0^1 \mathrm{d}x(1-x)\exp\left(-\frac{Q^2a^2}{6}N^{2\nu}x^{2\nu}\right) \tag{3.19}$$

Up until this point, only dilute solutions were considered, where chains can be regarded as isolated and do not interact with other chains. This is valid as long as the volume fraction ϕ is below the overlap volume fraction ϕ^* corresponding to contact between spheres representing the volume occupied by chains. Above ϕ^* is the semi-dilute regime in which chains overlap and excluded volume interactions can no longer apply to a single chain only. Regarding neutron scattering, once in the semi-dilute regime, the structure factor $Q(Q)$ must be accounted for whereas in the dilute regime only the form factor $P(Q)$ is considered.

The prefactor to the form factor in the expression of the scattered intensity includes a contrast term $\Delta\rho$ mentioned in section 3.1.3 and arising in equation 3.12. In a dilute polymer solution, the scattered intensity becomes :

$$I(Q) = \phi N v(\Delta\rho)^2 P(Q) \tag{3.20}$$

in which ϕ is the volume fraction of polymer. Thus, in practice, the solvent is often deuterated and the chains hydrogenated to maximize the scattered intensity while keeping the hydrogen content low so as to limit incoherent scattering.

3.2.3 Neutron scattering from a polymer melt

A polymer melt is characterized by the absence of solvent, the system being only composed of polymer chains. Regardless of other chains, we focus on a single one and consider it to be an ideal and more specifically a freely jointed chain in the theoretical sense [2]. Monomers of such a chain are free to move around with no interactions between them, and are linked together through infinitely flexible bonds. Mathematically, this is described by a three-dimensional random walk of N steps of length a being the size of a monomer, such as the mean-square end-to-end distance introduced in section 3.2.1 becomes, for an ideal chain :

$$R_0 = a\sqrt{N} \tag{3.21}$$

The corresponding radius of gyration is simply $R_{\text{g}} = R_0/\sqrt{6}$.

Particular attention should be given to this simple equation, as it gives the fractal dimension of 2 for an ideal chain. In practice, this means the SANS pattern of an ideal chain system exhibits an intermediate regime scaling as Q^{-2}. J.P. Cotton *et al.* first reported experimentally that it did apply to polymer melts [135]. Meaning, quite counter intuitively, that a single chain in a polymer melt behaves as an ideal one. The explanation lies in a compensation of interactions between monomers belonging to one common chain and those from two distinct chains [1]. Quantitatively, the form factor for an ideal chain was first calculated by P. Debye in 1947 [136] by averaging the form factor of individual isotropic scatterers pondered by the probability distribution for distances between monomers R_{ij}, leading to :

$$P_{\text{Debye}}(Q) = 2\,\frac{\exp\left(-Q^2R_{\text{g}}^2\right) - 1 + Q^2R_{\text{g}}^2}{Q^4R_{\text{g}}^4} \tag{3.22}$$

Just as for dilute solutions, it can be derived from equation 3.12 that the scattered intensity exhibits a contrast-dependent form factor. In the case of a melt, there is no solvent to deuterate thus we use a mixture of hydrogenated (h-) and deuterated (d-) chains with respective volume fraction x and $1-x$ such that :

$$I(Q) = x(1-x)Nv(\Delta\rho)^2P(Q) \tag{3.23}$$

The scattered intensity is thus optimized for a 1:1 mixture of hydrogenated and deuterated polymer chains.

Form factors of equations 3.22 and 3.19 will be used in the modelling of the experimental SANS data in the following sections.

3.3 Multiscale bulk structure of poly(ionic liquid)s

3.3.1 Experimental aspects

Sample preparation

For SANS experiments in bulk, thick PIL films were prepared by solution casting of **PC$_n$VImTFSI** solutions in tetrahydrofuran. The drying of the solutions deposited on a 1 mm quartz plate was first performed at room temperature during 24 h in a 20 cm diameter desiccator with a small aperture to allow a slow evaporation rate so as to prevent the formation of crust or cracks. The films were then heated in an oven (VacuTherm, Thermo Fisher Scientific) at 40 °C for 24 h in order to remove a maximum of remaining solvent without bubble formation. The third 24 h annealing step is performed at 70 °C. Finally, the sample is heated at 100 °C under vacuum for 24 h. The thickness of the films was measured using a Palmer and averaging 10 measurements over the film area. The resulting films are 10 mm in diameter and around 0.8 mm thick. The same procedure was used to prepare **PC$_n$VImI** and **PC$_{10}$VImBr** films using N,N-dimethylformamide as the casting solvent.

[1] In other words, two monomers cannot possibly know whether they belong to the same chain or not.

As the PIL series of interest is glassy at room temperature, the protocol described above is sufficient for measurements in ambient conditions. However, for measurements at varying temperature, presented later on in section 3.4.3, PILs are heated above their glass transition temperature T_g. Consequently, the sample has to be contained in a cell composed of a stack of a circular spacer in between two windows. For WAXS experiments at varying temperature, samples are solvent cast as before but in a small washer, with inner and outer diameter respectively 10 and 4 mm. After the drying steps, the films are covered by Kapton tape on both sides. Neutron experiments require larger samples, and hence a more robust containing stack. We use a circular Teflon spacer, stamped from a Teflon sheet using a cylindrical die, and two circular quartz windows as depicted in Figure 3.14. A perfectly regular disk with controlled thickness is required so as to avoid any air in between the quartz windows, which would allow the sample to flow to the bottom of the container during the experiment.

To shape such disks, we use a homemade compression moulding cell[1]. The cell, shown in Figure 3.14, is composed of a vacuum chamber in which the powder is weighed. The open cell is then placed in a heated vacuum desiccator (Vacuo-Temp, Selecta) set at 110 °C under vacuum for a day as to degas the PIL and avoid capturing air when moulding the sample. It is afterwards enclosed by a piston, connected to a vacuum pump, placed back on the heating plate at 110 °C and left overnight. Since the chamber is under vacuum, the sample is moulded at a pressure of approximately 1 bar and cell temperature was measured at 100 °C for this setting. Once back at room temperature, the cell is taken apart and the polymer disk removed. Samples showed very little defects by transparency, nonetheless we check their quality using X-ray scattering in section 3.4.2. The stack composed of the quartz windows and the Teflon spacer is afterwards assembled and clamp-pressed in a vacuum oven at 100 °C.

To study the chain conformation in THF, in which **PC$_n$VImTFSI** exhibited very good solubility, hydrogenated **h-PC$_n$VImTFSI** were diluted at 0.5 w% in deuterated THF (THF-d8), thus below the overlap concentration estimated according to the polymerization degree ($\phi^* = N^{-4/5} \approx 3$ %). Semi-dilute solutions of hydrogenated **PC$_4$VImTFSI** (1.5, 4.2 and 11 w%) and **PC$_{10}$VImTFSI** (1.9, 3.8 and 9.8 w%) were also prepared. The solutions were stored in 2 mm thick quartz cells. For solutions of PILs in ILs, we used a concentration of 1 w% of deuterated PILs in hydrogenated ILs. Prior to mixing, ILs were dried under vacuum for 15 h. The quartz cell thickness was 1 mm in this case to keep incoherent background at a minimum and optimize the transmission.

Experimental setup

SANS in ambient conditions was performed on the small angle diffractometer PAXY at Laboratoire Léon Brillouin, CEA Saclay (Figure 3.3a). Three different sample-to-detector distances of 1, 3 and 5 m were used together with neutron wavelengths of 4, 5 and 8.5 Å respectively. The Q-range available was thus 0.006 Å^{-1} < Q < 0.6 Å^{-1}. Standard corrections were applied for sample volume, neutron beam

[1]We thank A. Hélary (Laboratoire Léon Brillouin, CNRS CEA Saclay, France) for the design.

transmission, empty cell signal, and detector efficiency to the raw signal to obtain scattering spectra in absolute units as mentioned in section 3.1.1 [129].

SANS at varying temperature was performed on the small angle diffractometer SANS-I at Paul Scherrer Institute[1] in Villingen, Switzerland (Figure 3.3b). A single wavelength of 5 Å is used together with the whole length of the detector tank with three sample to detector distances 1.6, 4.5 and 18 m, thus providing a similar Q-range. The samples composed of stacks with quartz windows and a Teflon spacer are smaller for this experiment and a diaphragm of 7 mm diameter is placed at the exit of the neutron guide shown in Figure 3.3b. The temperature is set *via* a MFU resistance furnace controlled by a Eurotherm 2416 device. To ensure proper thermalization, the samples are loaded between two copper plates screwed to the copper block of the MFU. For lower temperatures, a Haake Phoenix II P1-C25P refrigerated circulator (Thermo Fisher Scientific) is connected to the MFU. The typical temperature cycle starts at room temperature, goes up to 130 °C, cools down to room temperature, proceeds to -10 °C, and comes back one last time to room temperature.

Wide Angle X-ray Scattering (WAXS) was performed on the same films of hydrogenated PILs **h-PC$_n$VImX** measured by SANS in ambient conditions. The films were cut in 2 × 2 mm squares and placed on the sample holder. We used a Xeuss 2.0 diffractometer (Xenocs) equipped with a Pilatus 1M detector placed at 200 mm from the sample and a Genix 2D Cu HF source (λ = 1.542 Å). The same data correction procedure used for SANS was applied to WAXS spectra. For temperature-resolved WAXS, a Linkam THMS600 hot stage system was added to the sample environment of the diffractometer.

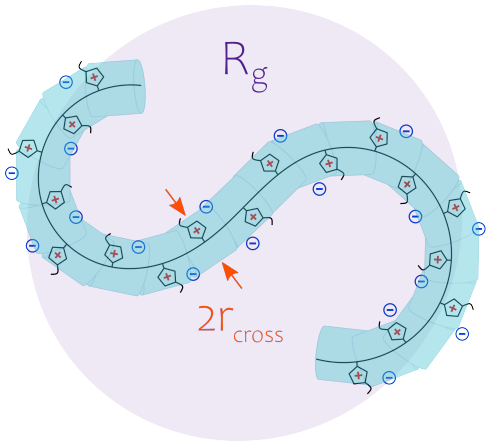

Figure 3.5: Schematic representation of the flexible cylinder model used to fit the data. Relevant chain parameters such as the radius of gyration R_g and the chain cross section r_{cross} are shown.

[1]We thank our local contact V. Lütz-Bueno (ETH Zurich / Paul Scherrer Institute, Villigen, Switzerland) an M. Grzelka (Université Paris Saclay, Laboratoire Léon Brillouin, CNRS-CEA, Gif-sur-Yvette, France) for her precious help.

3.3.2 Conformation of a poly(ionic liquid) chain

Solutions in THF

The SANS spectra of diluted **h-PC$_n$VImTFSI** solutions in deuterated THF presented in Figure 3.6a exhibit distinct regimes, as illustrated in Figure 3.4. For all side-chain lengths, a clear transition is observed from the Guinier regime at low Q to an intermediate regime with a regular slope of $-5/3$. For higher values of the scattering vector Q, a change in slope occurs and its onset depends on n. The larger n, the lower the Q value at which this change in slope occurs.

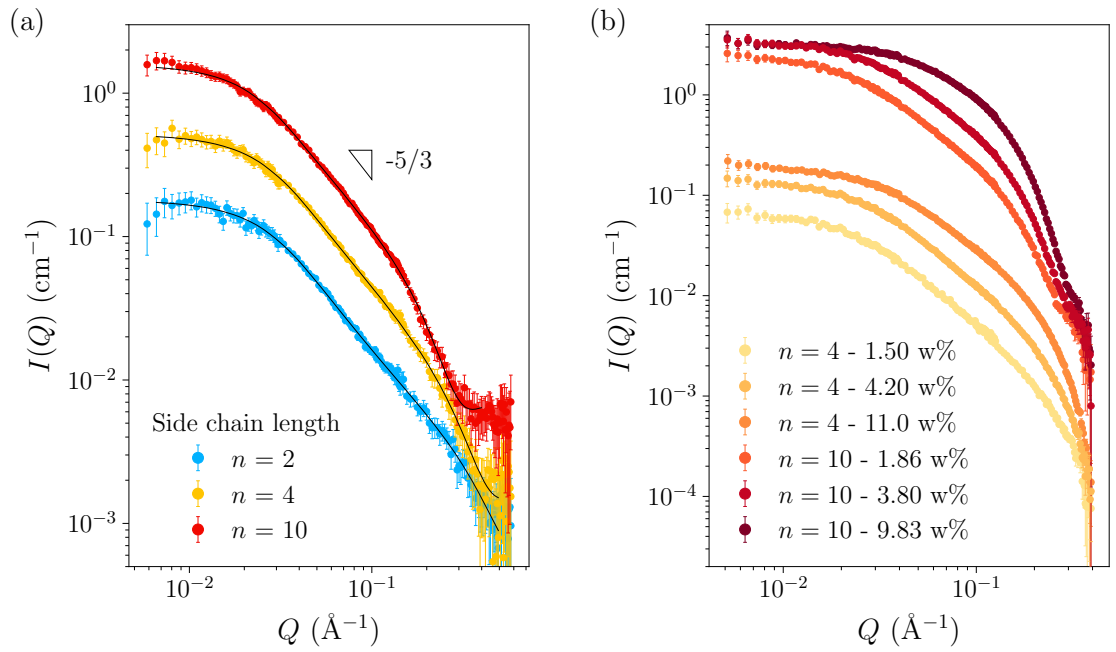

Figure 3.6: SANS spectra of **PC$_n$VImTFSI** solutions in THF-d$_8$ for different alkyl side-chain length n. (a) Dilute regime 0.5 w%, 0.55 w%, 0.5 w% respectively for $n = 2, 4, 10$. Solid lines correspond to the best fits according to equation 3.24. (b) Semi-dilute regime with varying concentrations for alkyl chain lengths $n = 4$ and 10. Data are shifted vertically for clarity.

The intermediate regime scaling as $Q^{-5/3}$ is in good agreement with the fractal dimension of a chain in good solvent [130, 131] independently of the alkyl side-chain length n. As for the further change in slope, it is most likely the point in Q at which the diameter of the chain, its cross section as represented in Figure 3.5, is probed, and which understandably depends on n. In order to account for both R_g in the Guinier regime and the cross section of PILs (r_{cross}) at higher Q-values, the data were fitted using an excluded volume polymer chain form factor $P_{excl}(Q)$ given by equation 3.19 and a cross section term $P_{cross}(Q)$ from a rigid rod, in other word a disk [137]. The contour length of the chains being significantly larger than the cross section, their respective scatterings can be separated by means of a decoupling approximation [138], giving:

$$P(Q) = P_{\text{excl}}(Q) \times P_{\text{cross}}(Q)$$
$$P_{\text{cross}}(Q) = \left(2\frac{J_1(Qr_{\text{cross}})}{Qr_{\text{cross}}}\right)^2 \tag{3.24}$$

where $\nu = 5/3$ is the excluded volume parameter. Regarding the cross section term, J_1 denotes the first order Bessel function of the first kind. As can be seen in Figure 3.7, such product tends to unity in the low-Q limit as is expected for a form factor. Such model provided very satisfying fits to the scattering patterns for all side chain lengths studied here (Figure 3.6a).

SANS spectra of semi-dilute **h-PC$_n$VImTFSI** solutions in THF are also reported in Figure 3.6b. The absence of polyelectrolyte peak, assigned to intermolecular electrostatic interactions between charged chains [139, 140] is noteworthy. A scaling of the intermediate regime as Q^{-1} is also expected in this type of system when counterions dissociate and the charged polyelectrolyte chain stretches into a rod-like structure under intrachain repulsive electrostatic interactions [141]. Together with the absence of polyelectrolyte peak, this represents clear evidence of at least partial condensation of the anions on the PIL chains in solution in THF which may result from the low dielectric constant of THF and the strong hydrophobicity of TFSI anions [142].

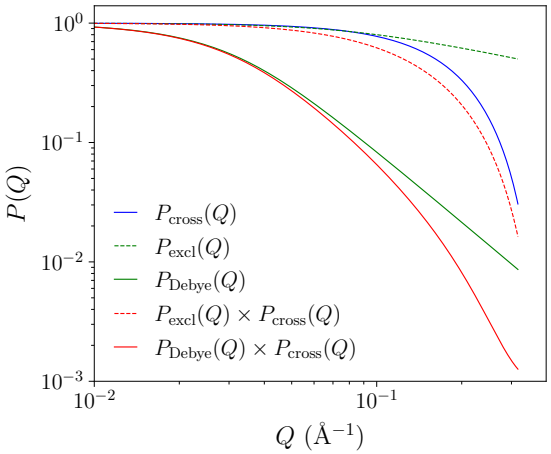

Figure 3.7: Plots of the form factor of a chain with excluded volume effects $P_{\text{excl}}(Q)$ (equation 3.19), the Debye form factor of an ideal chain $P_{\text{Debye}}(Q)$ (equation 3.22), the cross section term $P_{\text{cross}}(Q)$ (equation 3.24) and their respective product, showing all of the low-Q limits are unity, as expected.

Solutions in ionic liquids

SANS patterns of dilute **d-PC$_n$VImTFSI** solutions in their corresponding hydrogenated 1-alkyl-3-methylimidazolium IL with the same alkyl substituent and the same counter-anion reported in Figure 3.8 have a significantly weaker signal-to-noise ratio. Nevertheless, the Guinier regime appears clearly at low-Q values as well as the intermediate regime, this time with a slope of -2. An interesting new

feature is a correlation peak, clearly visible for $n = 10$ but outside the working Q-range for shorter side chains. Only a slight upturn of intensity can then be observed at high Q-values. This correlation peak is also visible on the SANS patterns of neat ILs.

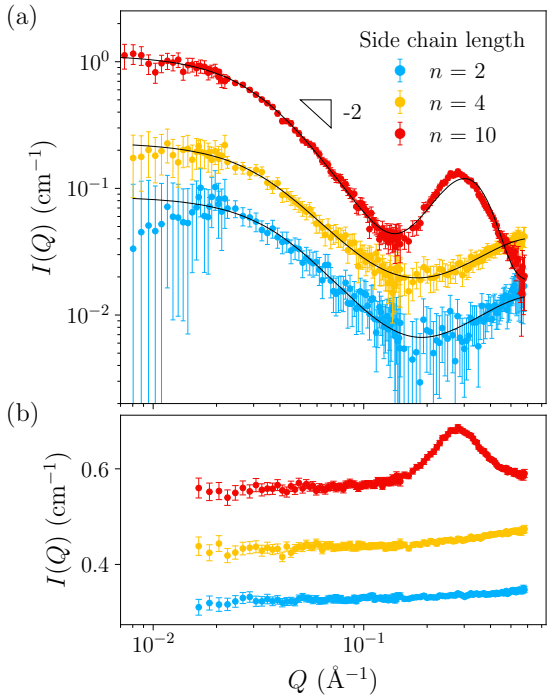

Figure 3.8: SANS spectra of (a) **PC$_n$VImTFSI** with different alkyl side-chain length n in solution in the corresponding hydrogenated IL (*i.e.* with the same n and counter-anion) at a concentration of PIL of 1 w% and (b) hydrogenated 1-alkyl-3-methylimidazolium ILs (with $n = 2, 4, 10$ and TFSI$^-$ counter-anion).

The Q^{-2} decay in the intermediate regime suggests ILs behave as near Θ solvents, in which the PIL chain behaves as ideal. This can be understood by the similarity between monomer-monomer and monomer-solvent interactions, since monomers and solvent molecules are structural analogues in this case. The pronounced noise, particularly in the case of $n = 2$ is due to the low contrast inherent from the low proportion of deuterium at small n, we recall that only the side chain is deuterated. As for the correlation peak, it arises from the scattering signal of the IL itself [23, 54]. The well-defined peak observed for $n = 10$ is a consequence of the amphiphilic nature of this IL leading to the existence of structural heterogeneities extensively discussed in Chapter 1 [49]. We chose not to subtract the volume weighted scattering from the solvent due to its dependence on water content, which can cause the incoherent background scattering to vary between pure IL and the IL solvent in solution. Furthermore, even though solutions are dilute, addition of PILs can alter the structure of ILs [143], this point would deserve further investigation. By restraining the analysis to the lower Q values of the spectra in which ILs alone do not coherently scatter (Figure 3.8b), the conformation of PIL chains can still be retrieved. All things considered, a good candidate to model the scattering spectra of dilute solutions of PILs in ILs can be inferred from equation 3.24 by replacing

the excluded volume polymer chain form factor by the Debye model $P_{\text{Debye}}(Q)$ of equation 3.22 for ideal chains [136, 144]. The fitting model can then be written as follows:

$$I(Q) = I_0 P_{\text{Debye}}(Q) \times P_{\text{cross}}(Q) + I_1 \exp\left(-\frac{(Q-Q_0)^2}{2\sigma^2}\right) \tag{3.25}$$

where the Gaussian function describes the contribution from the IL. As shown in Figure 3.8, such model provides a good description of the experimental data but with a rather low precision on the determination of r_{cross}. This can be explained by the lower signal-to-noise ratio at high scattering vectors, compared to the previous case of deuterated THF, and by the dominant contribution of the IL solvent at high Q. The determination of R_{g} remains nevertheless accurate.

Melt

The WAXS patterns of bulk **PC$_n$VImTFSI** films, reported in Figure 3.9 for several alkyl side-chain lengths n, feature three peaks in the Q range 0.1 Å^{-1} $< Q <$ 2.5 Å^{-1}. Previous works attributed these peaks to three specific correlation lengths of the system based on either simulated or experimental data and using selective deuteration to unravel the contributions of the different characteristic lengths of the system [32, 34, 53, 60]. Although these attributions were addressed in Chapter 1, we recall them briefly here. The low-Q peak (below 0.5 Å^{-1}) is highly dependent on n and shifts to low-Q values while sharpening and gaining in intensity as n increases. It is assigned to the backbone-to-backbone correlation length d_{bb}, in other words the distance between two neighbouring macromolecular chains [33, 35]. This distance increases as n grows larger due to progressively larger alkyl domains. The enhanced peak intensity stems from both larger nanodomains and an increasing contrast. The high-Q peak is a common feature of X-ray scattering from molecular liquids and amorphous polymers and is attributed to close contact between alkyl side-chains inside the alkyl domain [32, 60]. As for the intermediate peak (slightly below 1 Å^{-1}), it is ascribed to close contact between same charges, *i.e.* the correlation length of the counter-anion network. This last peak shows very little dependence on n. The ionic and pendant peaks will not be addressed in the following discussion. As for the WAXS signals of **PC$_n$VImI**, the high electron density of the iodide counter-anion hinders any kind of interpretation. As such, we do not show the data here.

Our WAXS patterns are consistent with the many reports on the local structure of PILs in melt we mentioned in Chapter 1, whether using simulated neutron scattering [34, 35, 145] or experimental X-ray scattering at wide angles [32, 33, 58]. Yet, to the best of our knowledge, the macromolecular conformation of PIL chains in melt had not been investigated so far. Although polymer coil sizes in solution can be determined by other techniques such as light scattering, SANS is the only technique allowing to do so in melt. This results from the contrast-tuning possibilities it offers, as discussed in sections 3.1.3 and 3.2.3.

When the sample is only composed of hydrogenated (h-PILs) or deuterated (d-PILs) PIL chains, SANS patterns only exhibit a n-dependent correlation peak and a slight increase in intensity at low Q-values, as shown in Figure3.10b. The peak shares the same origin as the low-Q peak of the WAXS patterns (Figure

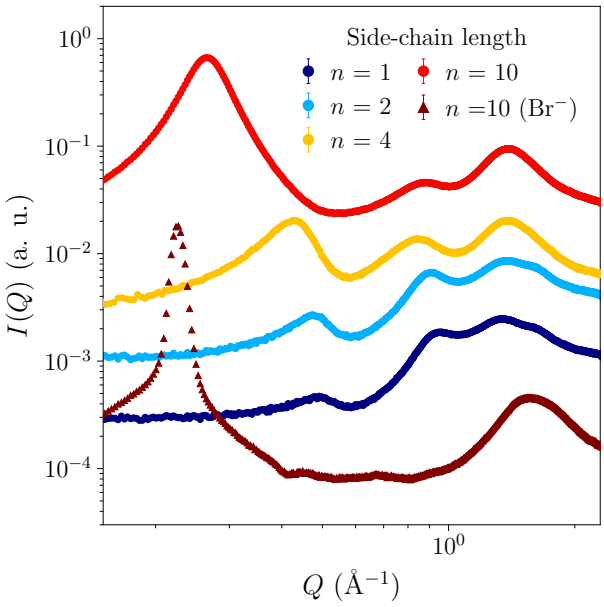

Figure 3.9: WAXS spectra of **PC$_n$VImTFSI** melts (○) with different alkyl side-chain length n and **PC$_{10}$VImBr** (△). Data are shifted vertically for clarity.

3.9) corresponding to the backbone-to-backbone correlation length. The intensity upturn is attributed to the presence of micro cracks in the samples inherent to the drying step in the sample preparation and which scatter at very low angle.

Figures 3.10a and 3.10c present the SANS spectra of H/D mixtures of **PC$_n$VImTFSI** and **PC$_n$VImI/Br** respectively for n = 1, 2, 4 and 10. The expected regimes appear once more, with a slight increase at very low-Q which also stems from micro cracks in the sample. The Guinier regime is here followed by a Q^{-2} intermediate regime. At higher angles is a change of slope similar to the SANS patterns of Figure 3.6a followed by a correlation peak, also n-dependent.

The marked difference in patterns between **d-PC$_n$VImX** samples and their respective H/D mixtures stems from equation 3.23. Since h-PILs and d-PILs have identical N values, it can be derived that the scattering intensity of a mixture of both is directly proportional to the form factor of PIL chains $P(Q)$ [146]. An ideal chain behaviour is suggested by the slope of -2, as expected for a polymer melt [135] and the further change of slope is imparted to the chain cross section, as before. All in all, the same model as equation 3.25 gives a very satisfying description of the scattering spectra of PILs in melt with a peak function describing the backbone-to-backbone distance $d_{bb} = \frac{2\pi}{Q_0}$ (Figure 3.10b and 3.10c). The lower contrast of **PC$_1$VImTFSI**, leading to a weaker scattering as well as shorter cross section and interbackbone distance in this case, prevented the latter to be estimated correctly with this fitting model. The nature of the anions do not appear to change the SANS patterns, hence suggesting the intrinsic conformation of the PIL chains remains the same. It must be noted at this point that the correlation peak for **PC$_{10}$VImBr** is of peculiar shape compared to other PILs. This is due to partial crystallization of the material, supported by the very sharp low-Q peak on the WAXS signal (Figure 3.9). Resulting fitting parameters give a more quantitative description of the system.

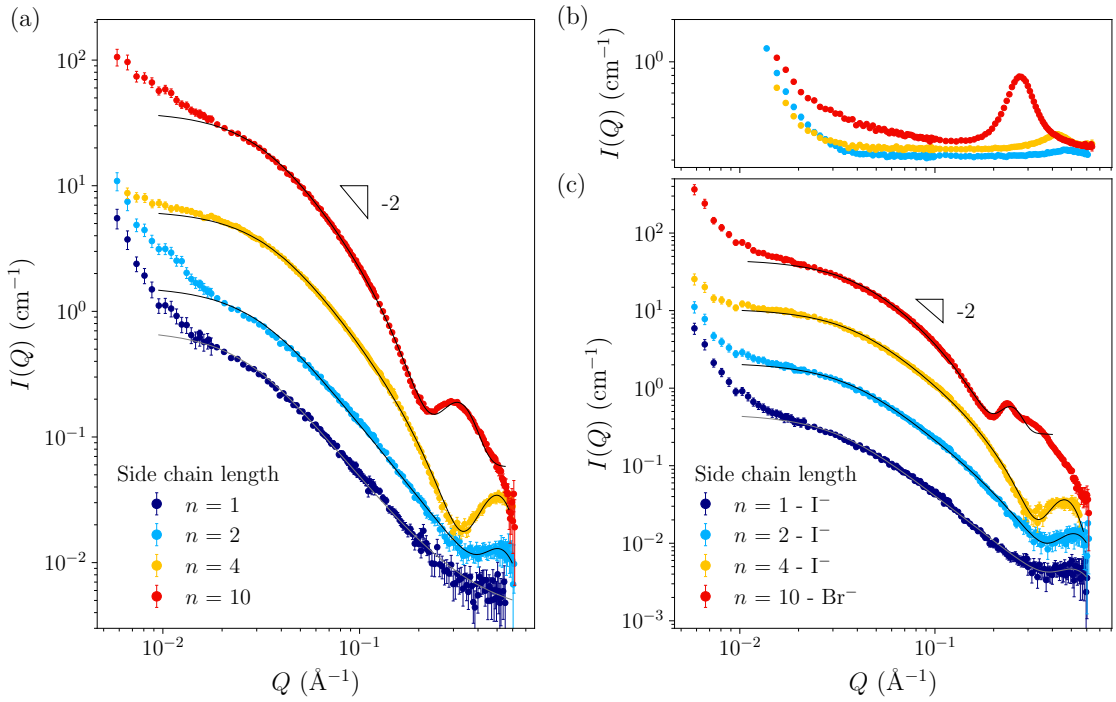

Figure 3.10: SANS spectra of (a) **PC$_n$VImTFSI** H/D (1:1 w/w) melts, (b) purely deuterated **PC$_n$VImTFSI** melts and (c) **PC$_n$VImI** and **PC$_{10}$VImBr** H/D (1:1 w/w) melts and, with varying alkyl side-chain length n. Solid lines correspond to the best fits according to equation 3.25. Data are shifted vertically for clarity.

Inferred structure sizes

From the modelling of the SANS spectra, we follow the influence of the side chain length n on the radius of gyration, R_g, the cross section r_{cross} and the backbone-to-backbone distance d_{bb} in the three cases of interest. The evolution of R_g is reported in Figure 3.11b and shows a general increase with n for PIL chains diluted in both THF and ILs with larger values in the former. PIL chains are larger in THF because of its good solvent properties. Mathematically, this is accounted for by a swelling ratio unfolding from Flory calculations we omitted in equation 3.18. As the size of the monomer increases, the Kuhn length increases because of local steric effect originating from the side-chains, which leads to an overall increase of the chain's coil size. The most astonishing effect is on the evolution of R_g in melt, for which the coil size first decreases until $n = 4$ observed for both TFSI and iodide anions, with slightly smaller values for the latter. Above $n = 4$, R_g seems to increase slightly for TFSI counter anion, but is lower for **PC$_{10}$VImBr** than for **PC$_4$VImI**.

The non-monotonic evolution along the **PC$_n$VImTFSI** series is at odds with a simple steric effect of the side-chains since, here, an increasing crowding of the monomer induces a progressive collapse of the coil for short side-chains. The vertical shift observed for the values of the **PC$_n$VImI** series is imparted to the smaller size of the iodide counter anion compared to TFSI. The following increase above $n = 4$ cannot be readily confirmed by our experiments, but considering the radius of the bromide counter-anion is again smaller than the iodide, it seems to remain consistent with the non-monotonic behaviour described above. As macromolecular

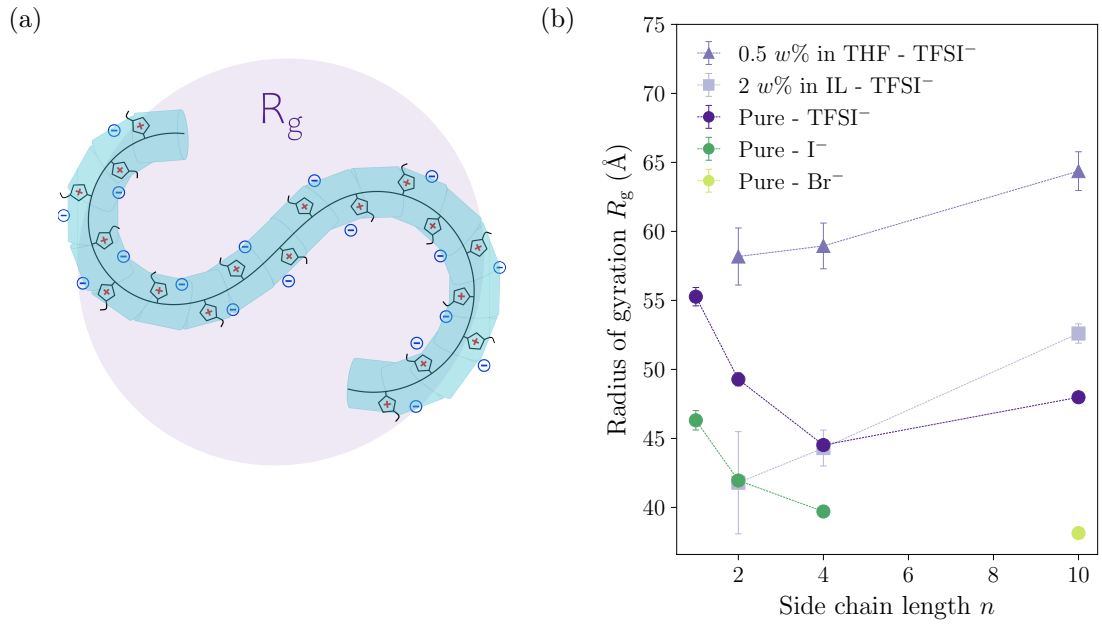

Figure 3.11: (b) Radii of gyration, schematically represented in (a), of $\mathbf{PC}_n\mathbf{X}$ as a function of n, diluted in THF-d_8 (▲), in 1-alkyl-3-methylimidazolium ionic liquids with identical alkyl groups (■) and of melt $\mathbf{PC}_n\mathbf{VImX}$ with anions TFSI (●), I^- (●) and Br^- (●). The dashed lines are eyes guideline.

parameters (*i.e.* N and $Đ$) of all the samples are strictly identical, this behaviour can only be attributed to the length of the side-chain and may reflect a change in the flexibility of PILs' backbone. Atomistic Molecular Dynamics Simulations performed by H. Liu *et al.* [34, 35] on poly(1-vinyl-3-alkylimidazolium) with TFSI anions have shown that longer side chains are more flexible and can form a bicontinuous sponge like nanostructure similar to ILs. Still, the lone flexibility of the side-chain does not necessarily explain the overall decrease of the backbone flexibility. Analysis of WAXS signals from the same samples (Figure 3.9) shows that the backbone-to-backbone distance increases by ≈ 1.26 Å per carbon, which is very consistent with the work of C. Iacob *et al.*[33] on poly(1-vinyl-3-alkylimidazolium)s with varying anions (including TFSI) and alkyl chain lengths n comprised between 2 and 6, obtained by free radical polymerization (*i.e.* comparable N but higher $Đ$). Such increase is slower than expected by assuming that pendant groups do not interdigitate [32, 34, 35, 147] thus providing indirect evidence of the interpenetration of long alkyl chains.

The above SANS experiments can probe both the backbone-to-backbone distance and the chain's cross section, only estimated in previous works either by MD simulations or density functional theory (DFT) calculations in the scope of the same kind of comparison [58, 145, 147]. Figure 3.12 represents the influence of the side chain length on both the diameter ($2r_{\text{cross}}$) of PIL chains in melt and the backbone-to-backbone distance for both TFSI and iodide counter-anion. The increase in $2r_{\text{cross}}$ appears to be more sensitive to n than d_{bb}. Moreover, for $n \geq 4$ the backbone-to-backbone distance becomes smaller than the chain diameter.

This is clear evidence that pendant chains tend to interpenetrate as their length

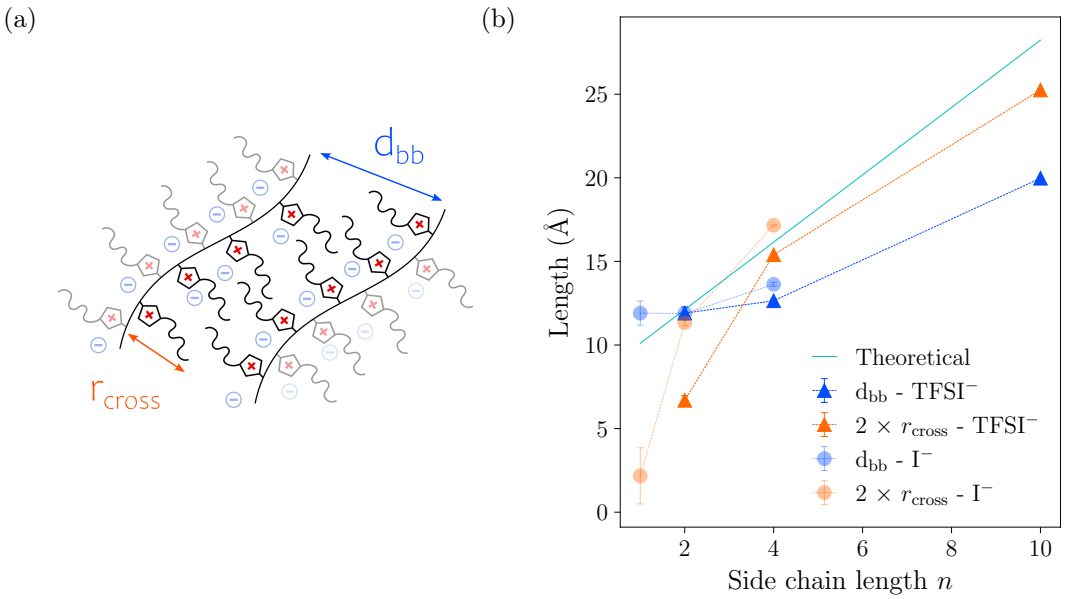

Figure 3.12: (a) Schematic representation of the local structure parameters (b) Evolution of $2 \times r_{cross}$ (▲) and d_{bb} (▲) of **PC$_n$VImTFSI** (△) and **PC$_n$VImI** (○) melts as a function of the alkyl chain length n. The solid line represents the theoretical chain diameter. The dashed lines are eyes guideline.

increases and allows us to suggest a description of the molecular mechanisms responsible for the non-monotonic evolution of R_g in Figure 3.11b. For small n, the side-chains are relatively stiff and do not interdigitate, which results in an overall low chain flexibility. As n increases, a competition between the steric crowding of neighbouring side chains along the backbone tends to increase the Kuhn length as observed in dilute solutions (Figure 3.6a and 3.8). Also, an increase in side-chain flexibility and interdigitation makes the chain more flexible, this being dominant for large values of n according to our experimental data. In such a scenario, the contribution of the electrostatic interactions between monomers is not taken into account. They may also play an important role at small scales and are highly dependent on the degree of ion pairing, as proposed by M.A. Gebbie *et al.* [87] for ILs using Surface Force Apparatus experiments. Increasing the length of the side-chains can play a significant role in the screening of electrostatic interactions between cations also resulting in an increase of chain flexibility. However, a direct comparison between SFA experiment on ILs and our results may be hazardous because of the introduction of intra- and inter-chain Coulombic interactions, which may differ due to the hindered cation mobility compared to ILs. Here, the probed radii of gyration only depend on the intra-chain interaction, as the scattering signal from a mixture of hydrogenated and deuterated chains cancels the interchain terms of the partial structure factors [135]. Elucidating such difference may be of great interest but remains challenging since it requires to uncouple steric and electrostatic interactions. Additionally, B. Doughty *et al.* have shown that PVI quaternized with ethylene oxide side chains present a smaller backbone-to-backbone distance, which may be attributed to a higher flexibility of this kind of side group [58]. Hence, the chemical nature of the side chain also plays an important role on the local structure.

The influence of this side chain flexibility on the radius of gyration has not been investigated so far and could be an interesting perspective of this study.

3.4 Influence of temperature on the bulk structure of poly(ionic liquid)s

All results presented above, as most reports about PIL structure, are gathered in ambient conditions. However, when it comes to ion transport or other dynamical processes, their temperature dependence is crucial. The effects observed are often interpreted independently of the structure, and its potential temperature-dependence, is often overlooked. Some results have nonetheless been reported on the temperature dependence of ILs bulk structure. Using X-ray scattering, A. Triolo *et al.* reported two regimes in the evolution of the intermediate-range ordering with temperature for an imidazolium IL with rather long side chain of $n = 8$ [22]. The temperature-dependence of the characteristic length is well described at low temperature by the thermal expansion of the IL. However, this trend is suddenly reversed above T_g and the intermediate-range ordering progressively contracts with increasing temperature, at odds with density measurements. The authors put forward a possible phase transition in the segregated apolar domains. D. Salas-de la Cruz *et al.* reported WAXS patterns at varying temperature for **PC_2VImTFSI** and only observed a slight increase of the backbone correlation length from $T_g - 30°C$ to $T_g + 90°C$, which they ascribe to thermal expansion [32]. However, as we revealed above, these short side chains do not interdigitate, hence whether interdigitation of PILs' side chains is sensitive to temperature remains unclear.

We present in this section some results regarding this matter. We use WAXS and SANS experiments at varying temperature. The former is performed on our X-ray lab source and the latter at the SINQ neutron source of the Paul Scherrer Institute in Switzerland. Both experiments and their respective sample preparation were described in section 3.3.1 above.

3.4.1 Local structure and temperature-dependent interdigitation

Following the same experimental procedure as for the WAXS experiments presented in section 3.3.2 and Figure 3.9, a Linkam hot stage was added to vary the temperature of the sample. As specified in section 3.3.1, the sample preparation hardly differs from those of previous experiments, the only difference being that the solution casting is done inside a small washer, followed by identical drying step. WAXS signals for both side-chain lengths $n = 7$ and 10 for varying temperatures up to 150 °C are reported in Figure 3.13a. Although TGA measurements showed no signs of degradation at these temperatures as discussed in Chapter 2, above 150 °C the samples blacken slightly. We chose to set this as the maximum temperature to be cautious. The WAXS signal only slightly change with increasing temperature. A variation of baseline can occur due to small bubbles appearing in the sample, but do not interfere with the rest of the analysis. Indeed, we mainly focus on the position of the interbackbone (low-Q) peak, of which a magnified representation in linear

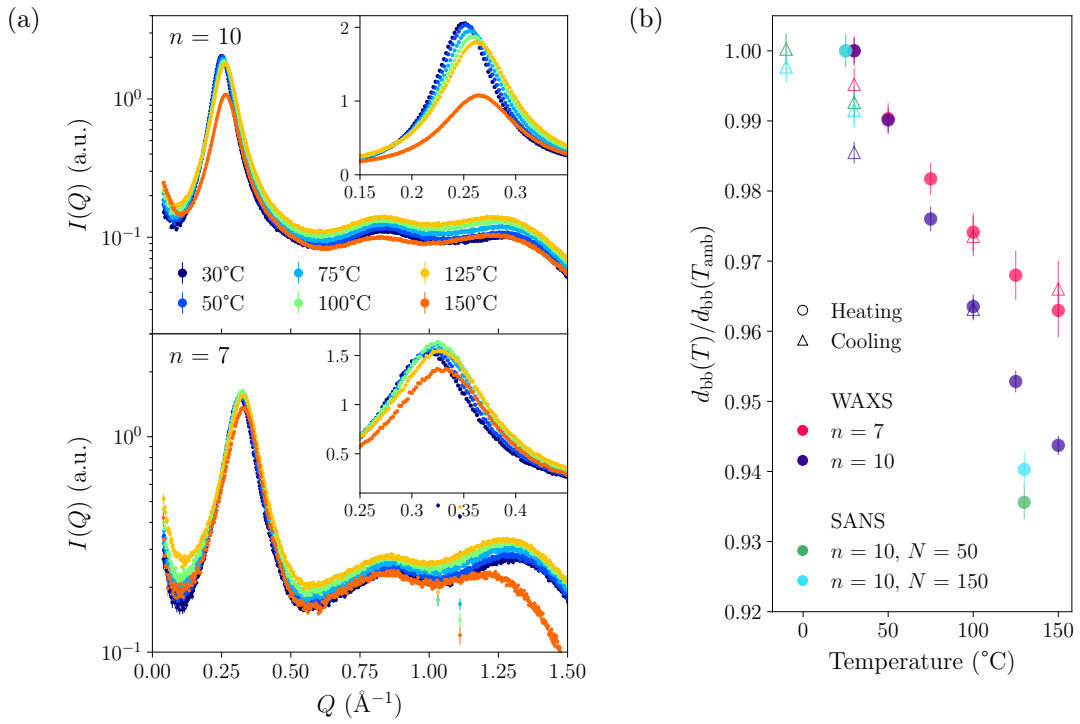

Figure 3.13: (a) WAXS patterns of $PC_{10}VImTFSI$ (top) and $PC_{10}VImTFSI$ (bottom) melts at varying temperatures The low-Q interbackbone correlation peak is shown in linear scale as insets. Corresponding correlation lengths $d_{bb}(T)$ normalized by the value at ambient temperature $d_{bb}(T_{amb})$ upon heating ($\circ$) and cooling ($\triangle$). Data from temperature resolved SANS experiments of section 3.4.3 are also represented.

scale is given as insets. As temperature increases, the peak slightly shifts to higher Q values, meaning shorter correlation lengths. To quantify this observation, peaks are fitted using a Lorentzian model, like in previous sections, the corresponding correlation lengths $d_{bb}(T)$ are calculated from peak positions and reported in Figure 3.13b normalized by the correlation length at ambient temperature $d_{bb}(T_{amb})$. The distance between main chains shortens as temperature increases, this effect being more pronounced for the longer side-chain $n = 10$. Temperature seems to promote interdigitation of side chains, which can be explained by a higher mixing entropy in the apolar domains.

3.4.2 Control of sample's quality

We discussed the presence of microcracks above, as they translate into an intensity upturn at low Q-values in the SANS patterns. As the sample preparation changed from solution cast to compression moulded for the results presented below, the purpose of this section is to provide a method to check for microcracks in glassy polymeric samples using X-ray scattering prior to a neutron scattering experiment when an X-ray lab source is available.

The same experimental procedure and data treatment as for WAXS experiments (section 3.3.1) is used on the Xeuss 2.0 diffractometer (Xenocs) apart from the

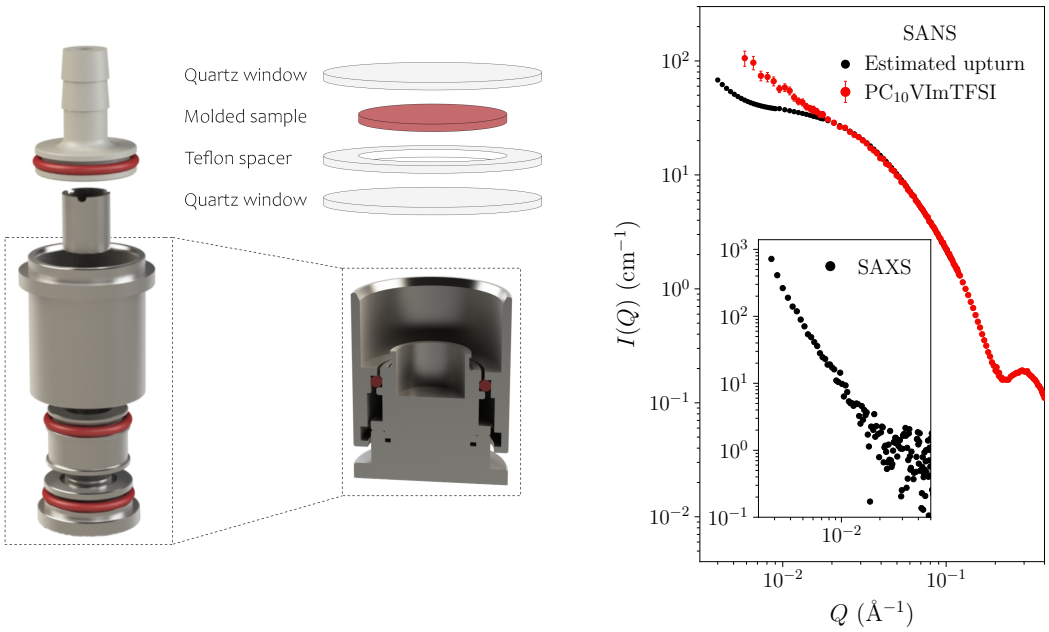

Figure 3.14: (Left) Representation of the compression cell used for the sample preparation. A cross section view of the vacuum chamber is on the right side. The piston and connector to the vacuum pump are present on the left-hand representation. Schematics represent the stack formed with the compression moulded sample. (Right) Sample quality control using SAXS. SANS spectra of melt **PC_{10}VImTFSI** H/D (1:1 w/w) compared to the fit previously reported with an added upturn estimated from the SAXS pattern reported as inset.

sample to detector distance and the collimation. The SAXS configuration sets a distance $D = 2502$ mm and a collimation of 0.3 x 0.3 mm and 0.25 x 0.25 mm respectively for the first and second collimation slits. The poor signal-to-noise ratio is imparted to both the large distance and thin collimation. Still, the SAXS signal reported in the inset of Figure 3.14 does exhibit the low-Q upturn we needed. In order to predict how this would translate into using neutrons, a contrast correction has to be introduced to account for different scattering length densities of the sample regarding neutrons and X-rays. The expected scattered intensity using neutrons is then related to the measure SAXS signal by :

$$I_{\text{SANS}} = \left(\frac{\Delta\rho_{H/D}}{\Delta\rho_X}\right)^2 I_{\text{X}} \simeq 0.078 I_{\text{X}} \tag{3.26}$$

The contrast terms $\Delta\rho_{H/D}$ between a 1:1 mixture of **h-PC_{10}VImTFSI** and **d-PC_{10}VImTFSI** and air, and $\Delta\rho_X$ between a **h-PC_{10}VImTFSI** and air, are calculated based on density values, chemical structures and tabulated atomic scattering length densities. The contrast-corrected upturn is then added to the fit of the SANS pattern of Figure 3.10, hence removing the upturn reminiscent of microcracks of that particular sample, and compared to the former experimental data in Figure 3.14. These predictions are therefore most encouraging, with an onset of the intensity upturn at much lower Q-values for the compression moulded samples. Far from claiming this estimation is exact, we do find it to be a convenient way to

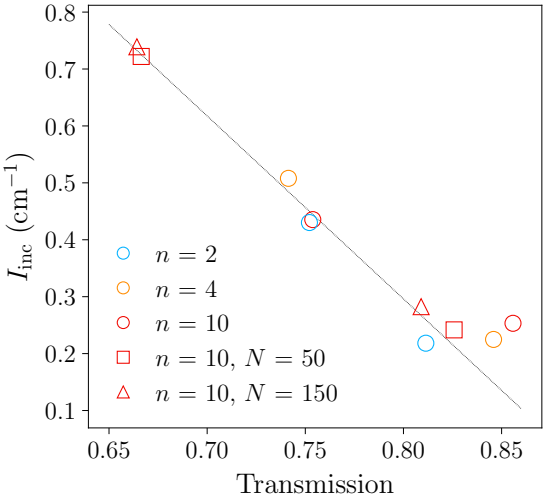

Figure 3.15: Incoherent plateau level against sample transmission at room temperature for **PC$_n$VImTFSI** samples. The dashed line is a linear fit to guide the eye.

prepare for a neutron scattering experiment when an X-ray lab source is available.

3.4.3 Chain conformation under varying temperature

Data treatment

Despite all the caution taken during the sample preparation, some bubbles did appear for increasing temperature. As a consequence, the conventional SANS data treatment explained above failed. This occurred in the subtraction of the incoherent plateau discussed in section 3.1.2 stemming mainly from the hydrogen content. It is generally well subtracted by estimating the incoherent scattering from both fully hydrogenated and deuterated samples as the ones shown in Figure 3.10b and subtracting each one pondered by their volume fraction in the 1:1 mixture. In the present case, bubbles caused macroscopic heterogeneities which had to be accounted for. To do so, we plot in Figure 3.15 the incoherent scattering level against the transmission of samples. Hydrogenated samples have lower transmissions due to the enhanced neutron absorption of hydrogen compared to deuterium. The conventional treatment indirectly relies on this plot. A mixture of H and D chains has a transmission in between the H and D samples, and pondering their incoherent level by their volume fraction is taking the point on the dashed line corresponding to that transmission. Since bubbles spikes the transmission, subtracting the corresponding incoherent level might account for their presence. Unfortunately it also failed.

Data were finally subtracted by hand until a reasonable background level was reached and patterns resembled the ones of section 3.3.2. We report them in Figure 3.16a. Considering the focus of this experiment is the polymer coil size only, *i.e.* the radius of gyration R_g, the most important data are located at small Q values where the intensity is the largest and the signal shows the weakest dependence on the subtraction.

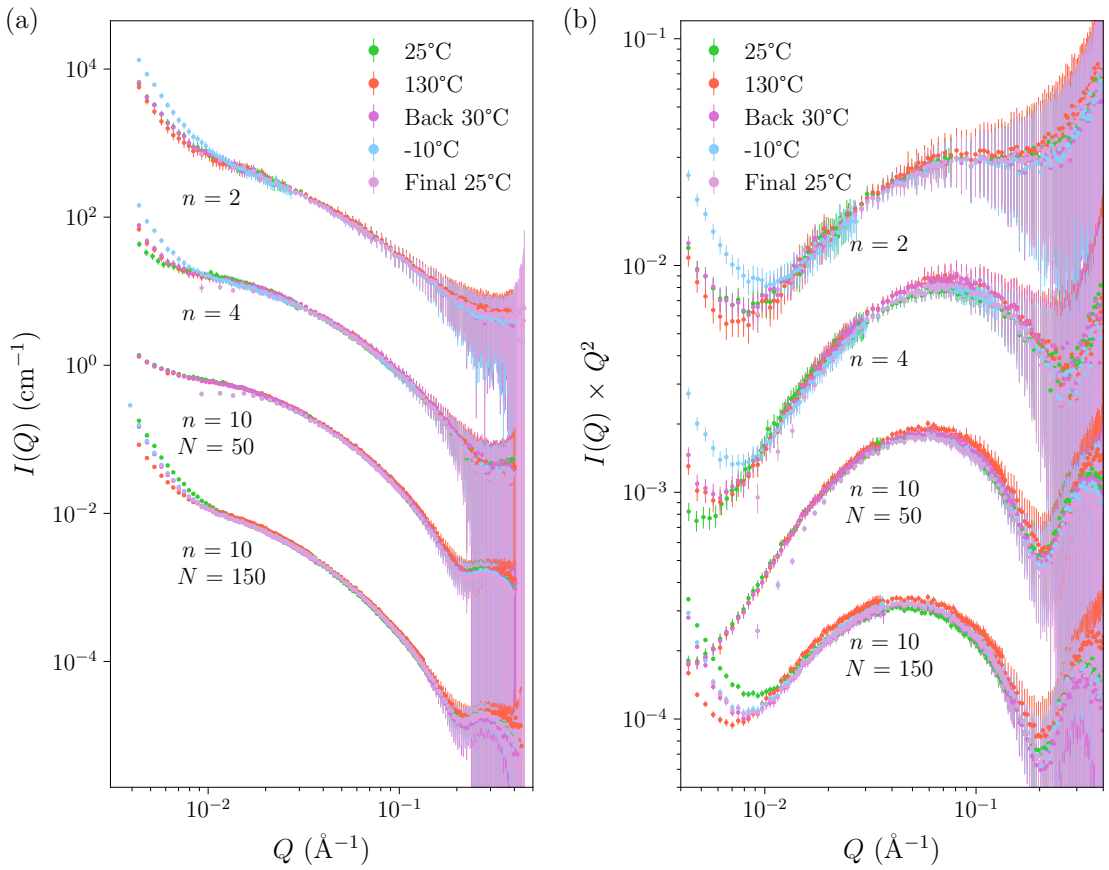

Figure 3.16: SANS patterns over the full temperature cycle (room temperature (RT), 130 °C, RT, -10 °C, RT) for **PC_2VImTFSI**,**PC_4VImTFSI** and two **PC_{10}VImTFSI** samples of polymerization degree $N = 50$ and 150 in (a) conventional representation $I(Q)$ against Q and (b) Kratky representation $I(Q) \times Q^2$ against Q.

Discussion

SANS patterns reported in Figure 3.16a show little to no effect of temperature. The upturn at low Q is the most temperature dependent feature. It should be noted that it is generally higher at -10 °C, and we suspect cracks form when cooling down to that temperature. Around the Guinier regime no changes seem to occur, neither at high nor low temperatures. The Kratky representation $I(Q) \times Q^2$ against Q is usually adapted to observe fine changes and is given in Figure 3.16b. Still, very little effect of temperature is observed and can hardly exceed the error bars. Consequently, we can safely assume the polymer coil size does not exhibit any temperature dependence worth mentioning.

This is nonetheless a result in itself. In section 3.3.2 we put forward that as the side chain length increases, they start to interdigitate above $n = 4$. Simultaneously, the radius of gyration decreases up until said side-chain length, suggesting an increasing main-chain flexibility. The interdigitation observed above $n = 4$ does exhibit a temperature dependence, as shown above in Figure 3.13b and yet, it appears to have no effect whatsoever on the radius of gyration. The temperature-dependence

of side chain interdigitation is further confirmed by these SANS results. We follow the correlation peak on the SANS pattern of deuterated **d-PC$_{10}$VImTFSI** with $N = 50$ and 150 such as the one observed in Figure 3.10b at varying temperatures. The corresponding interbackbone correlation lengths normalized by the values at room temperature are plotted alongside values measured using WAXS in Figure 3.13b and show good agreement. Interestingly, the temperature-dependence appears to level off at low temperatures. Additional experiments are in progress to better resolve this temperature range.

Overall, these results on the temperature dependence of PILs' structure both at the local and coil size are fundamental for their applications. Hopefully they will provide some insight on the conductivity of these materials, in which temperature dependence plays a pivotal role, to unravel what unfolds from structural changes alone and what indeed originates from ion transport.

3.5 Conclusion

In summary, an extensive use of small angle neutron scattering provides a multi-scale description of the conformation of poly(1-vinyl-3-alkylimidazolium)s in dilute solutions in good solvent, Θ solvent, and in melt as a function of the side-chain length and counter-anion. The modelling of the scattering patterns supported by physical arguments provided a quantitative measurement of both the radii of gyration R_g, the chain cross-sections r_{cross} and the backbone-to-backbone distances d_{bb}. The overall results have shown a monotonic increase in R_g as a function of n for PILs in dilute solution, in agreement with increasing steric interactions between monomer units. In melt, a non-monotonic increase of R_g of PIL chains appears and is interpreted as a competition between steric interactions, side-chain flexibility and potential electrostatic screening. Overall, the main chain gains in flexibility, resulting in a smaller polymer coil as n increases, before crowding effects take over for longer side-chains. Interpenetration of the latter was first suggested by the slow increase of backbone-to-backbone correlation length with n. It was then confirmed by a simultaneous measurement of both the chain diameter and the inter-chain distance leading to their crossover. Such interdigitation was shown to be sensitive to temperature and side chains are pulled together as temperature increases, hence at odds with an expected thermal expansion effect. Yet, no consequence was observed on the fairly temperature-independent radius of gyration. Subsequently, the local interaction inherited from the IL monomer translates into a change of PILs conformation at the macromolecular scale, which may be used to probe them.

Chapter 4

Interfacial structure

PILs and ILs share some structural features, in bulk, as a consequence of the nanoscale segregation of apolar domains driven by solvophobic interactions. The previous chapter focused on the implications of such nanostructure on the conformation of PILs chains as well as their local structure, which proved to be very similar to ILs. In this chapter, we move from the bulk to the interface. A lower dimensionality usually disrupts the bulk structure. In ILs, this leads to molecular layering over several ionic layers revealed by specular X-ray Reflectivity [71–73] or surface force apparatus experiments [70]. Once again, a threshold exists, for imidazolium ILs, around 4 carbons side-chains between a simple charge alternating layering to a bilayer structure resulting from amphiphilic self-assembly.

We addressed in Chapter 1 how confinement was of particular use in enhancing the conductivity of PILs. Diverse strategies relying on their polymeric nature have been explored, such as PIL-based block copolymers or thin films. Such confinement markedly impacts the conductivity increasing it in the former and lowering it in the latter. Yet, conversely to ILs, there is a lack of reports on the structure of the PIL-solid interface. The numerical results of Yu *et al.*, also mentioned in Chapter 1, are the only report revealing a similar layering for poly(1-vinyl-3-butylimidazolium hexafluorophosphate) at both neutral and charged quartz surfaces [85].

In the aim of providing an experimental description of PIL's interfacial structure, this chapter presents a study of spin-coated thin films of the **PC$_n$VImTFSI** series. As before, the main parameter of interest is the side-chain length n. The thickness of the films, measured by ellipsometry, is a simple way to control the confinement of the material. We use a combination of two X-ray techniques to probe the interfacial structure. The out of plane structure is probed by specular X-ray reflectivity, performed on a lab source. Additionally, grazing incidence X-ray scattering (GIWAXS), performed at a synchrotron light source, provides information on the in-plane structure near the interface to complement and confirm the proposed molecular picture. The first sections detail the sample preparation and the principle of these techniques before moving on to the experimental results.

4.1 Thin films fabrication and characterization

4.1.1 Protocol for thin films fabrication

PIL thin films are prepared by spin-coating, a preparation technique relying on the spreading and drying of a polymer solution induced by the rotation of the

substrate. It can be shown that the thickness of the resulting film scales as the reciprocal square-root of the rotation speed $t \sim \omega_{\text{spin}}^{-1/2}$ and linearly with the solution concentration $t \sim c$, making the latter the main control parameter [148]. It requires precise protocols and cleaning steps. First, the wafers used are 1 x 2 cm^2 pieces cleaved out of larger single side polished silicon wafers (4" in diameter, 1 mm thick, Siltronix). They are washed in consecutive ultrasonic baths (FB15055, Fisher Scientific) in acetone, toluene, and ethanol for 20 min each, dried under argon flow and finally cleaned by UV/O_3 treatment[1] (UV/Ozone ProCleaner, Bioforce Nanosciences) for 60 min prior to spin-coating. Clean substrates are transferred from the UV/O_3 treatment to the POLOS SPIN150i spin-coater straight away. The solvent is a 1:1 mixture of tetrahydrofuran (THF) and propylene glycol methyl ether acetate (PGMEA). The former ensures good solubility of **PC_nVImTFSI** and the latter lowers the evaporation rate so as to improve the spreading of the solution and the quality of the resulting film. The solutions, at concentrations of the order of 0.1 w%, are filtered twice using PTFE syringe filters (pore size 0.2 μm, FisherScientific). Deposition volume is 150 μL, angular velocity is 2000 rpm for 50 s followed by 3000 rpm for 20 s. Samples are then annealed at 100 °C in a vacuum oven (VacuTherm, Thermo Fisher Scientific) overnight to ensure complete drying and removal of any residual stress originating from the fabrication process.

4.1.2 Thickness measurements by ellipsometry

In order to get a quick and yet precise measurement of the thickness of the fabricated films, we use ellipsometry. This section will first provide a brief explanation of the principles of such measurements. Then, additional details will be given on how it was applied to the samples considered here.

Principle

Ellipsometry is a non-destructive optical method to determine either thickness of thin films or optical properties, such as their refractive index. It relies on changes of polarization state light experiences upon reflection by a flat surface. Because it depends on the surface properties, it can be used to probe thin films.

Let us consider a light beam shining onto an interface between two media with a certain non-zero incident angle θ_1 with the normal to the interface, as depicted in Figure 4.1a. Each medium m can be described by a complex refractive index $N_m = n_m + \mathrm{i}k_m$ in which n_m and k_m are respectively the real refractive index and the extinction coefficient. After reflection by the surface, the incident wave is split into reflected and transmitted waves. The reflected wave is symmetrical to the incident one with respect to the normal to the surface, yielding $\theta_1^R = \theta_1$. The transmitted wave is slightly deflected, *i.e.* refracted, in medium 2 with an angle θ_2 defined by Snell-Descartes law $n_1 \sin(\theta_1) = n_2 \sin(\theta_2)$.

Each wave is described by its electric field with a component parallel to the plane of incidence and another parallel to the surface considered, respectively denoted p and s and represented in Figure 4.1. Each of these components will be affected

[1] By generating two UV wavelengths, the device simultaneously generates ozone and enhances the reactivity of organic surface contaminants leading to their break down.

differently by the reflection and a reflection matrix R can be defined such as [149]:

$$\begin{bmatrix} E_{1\mathrm{p,r}} \\ E_{1\mathrm{s,r}} \end{bmatrix} = \begin{bmatrix} r_{\mathrm{pp}} & r_{\mathrm{sp}} \\ r_{\mathrm{ps}} & r_{\mathrm{ss}} \end{bmatrix} \begin{bmatrix} E_{1\mathrm{p}} \\ E_{1\mathrm{s}} \end{bmatrix} \tag{4.1}$$

For an isotropic material such as we will consider ours for now, evidence of this being given in the following sections, the cross terms r_{sp} and r_{ps} are null. The other two terms are given by :

$$\begin{aligned} r_{\mathrm{pp}} &= \frac{E_{1\mathrm{p,r}}}{E_{1\mathrm{p}}} = |r_{\mathrm{pp}}| \exp(i\delta_{\mathrm{pp}}) \\ r_{\mathrm{ss}} &= \frac{E_{1\mathrm{s,r}}}{E_{1\mathrm{s}}} = |r_{\mathrm{ss}}| \exp(i\delta_{\mathrm{sp}}) \end{aligned} \tag{4.2}$$

in which $|r_{\mathrm{pp}}|$ and $|r_{\mathrm{ss}}|$ account for a change in amplitude and δ_{pp} and δ_{ss} denote a phase shift induced by the reflection.

In practice, we introduce the so-called ellipsometric angles Δ, Ψ as the ratio of amplitudes and the relative phase shift between the two components:

$$\begin{aligned} \frac{r_{\mathrm{pp}}}{r_{\mathrm{ss}}} &= \frac{|r_{\mathrm{pp}}|}{|r_{\mathrm{ss}}|} \exp\left[i(\delta_{\mathrm{pp}} - \delta_{\mathrm{ss}})\right] \\ \tan\Psi &= \frac{|r_{\mathrm{pp}}|}{|r_{\mathrm{ss}}|} \\ \Delta &= \delta_{\mathrm{pp}} - \delta_{\mathrm{ss}} \end{aligned} \tag{4.3}$$

When a single layer or several ones are deposited on the substrate, multiple reflections occur. That formalism will not be addressed here, a similar one will be derived in the case of specular X-ray reflectivity further on. Ellipsometric angles Δ and Ψ are in this case functions of both refractive indices and thicknesses of each layer.

Technical set-up

A schematic representation of an ellipsometer is given in Figure 4.1b. In practice, we use an Accurion EP3 (Park Systems) with an incident laser beam of wavelength $\lambda = 632.8$ nm. Technically speaking, the instrument is composed of a series of optical devices to tune the polarization of the incident beam and analyse the reflected one. The incident laser beam goes through a linear polarizer and an optical retarder commonly called compensator, which we will denote P and C, to produce an elliptical polarized beam. After reflection by the sample at an incident angle θ the beam goes through an analyser and is recorded on a CCD camera. Among several ellipsometry techniques, nulling ellipsometry essentially consists in exploring PC and A configurations to find the conditions in which the reflected light is cut off. At that point, the PC devices shaped an elliptical polarization such as the reflected beam is linearly polarized, meaning the analyser can indeed cut it off. Through the relative orientations of P and A, ellipsometric angles Δ and Ψ are retrieved. Fitting of these values, either at a given incident angle or as a function of it, with an appropriate model, provides the thickness and roughnesses of the different layers composing the sample.

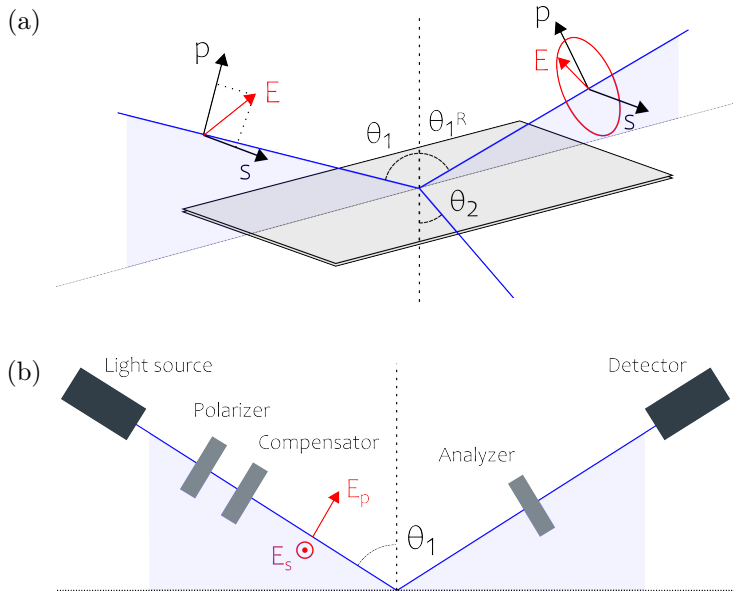

Figure 4.1: Schematic representations of (a) the reflection of a polarized beam on a flat surface and (b) the experimental setup of an ellipsometer.

4.2 Specular X-ray reflectivity

4.2.1 Principle

Much like ellipsometry, specular X-ray Reflectivity (XRR) allows thickness and roughness measurements of thin layers. The use of X-rays has several benefits that are not afforded by visible light, such as their penetration in the material and a contrast that relies on electronic density, as mentioned in Chapter 3. Thus, it is perfectly adapted to probe layers with fine variation in composition and therefore with very close refractive indices.

Index of refraction

The index of refraction for X-rays can be written as a function of two parameters δ and β accounting respectively for scattering and absorption in the material [150]. The dependence of δ and β will not be formally derived here, and detailed information can be found in the work of M. J. Tolan [151]. The expression for the index of refraction for a wavelength λ is then:

$$\begin{aligned} n_X &= 1 - \delta - i\beta \\ n_X &= 1 - \frac{\lambda^2}{2\pi} r_e d_{e^-} - i\frac{\lambda}{4\pi}\mu \end{aligned} \tag{4.4}$$

where μ is the linear absorption coefficient. The interaction of X-rays with electrons appears in this expression as a dependence in electronic density d_{e^-}, $r_e = 2.814 \times 10^{-5}$ Å being the classical radius of the electron. The density of electrons considered here is proportional to the scattering length density (SLD) of X-rays by $d_{e^-} = \mathrm{SLD}/r_e$. Hence, the formalism is identical to that of neutron reflectivity. The definition of a refractive index for X-rays means their reflection on a substrate can

be handled by classical optics, and namely Snell-Descartes law once again. Unlike ellipsometry with visible light, the refractive index n_X is by definition smaller than unity. Therefore, there exists a critical incident angle ω_c below which total external reflection is verified :

$$\sin \omega_c = \lambda \sqrt{\frac{r_e d_{e^-}}{\pi}} \tag{4.5}$$

Case of an ideal interface

Similarly to what was discussed for neutron and X-ray scattering in Chapter 3, we define a scattering vector $\vec{Q}$ as the difference between incident $\vec{k_i}$ and reflected $\vec{k_r}$ wave vectors. Since specular observations are, by definition, made at an outgoing angle equal to the incident angle ω, simple geometrical considerations lead to :

$$\begin{aligned} \vec{Q} &= \vec{k_r} - \vec{k_i} \\ Q &= \|\vec{k_r} - \vec{k_i}\| = \frac{4\pi}{\lambda} \sin \omega \end{aligned} \tag{4.6}$$

The amplitude of the scattering vector Q is equal to twice the projection of the incident wave vector k_i on the normal to the interface. This projection will be denoted as $q = Q/2$ as it is a more convenient variable for the following calculations.

Considering the system represented in Figure 4.2 with a perfectly smooth and flat interface, the Fresnel coefficient for reflection is defined as the ratio of amplitudes of the reflected and incident waves. The expression of these amplitudes can be derived based on the continuity condition of the wave and its derivative at the interface, giving :

$$r_F = \frac{q - q_n}{q + q_n} \tag{4.7}$$

Experimentally, the detector records intensities rather than field amplitudes, hence what is actually assessed is the Fresnel coefficient in intensity :

$$R_F = |r_F|^2 \tag{4.8}$$

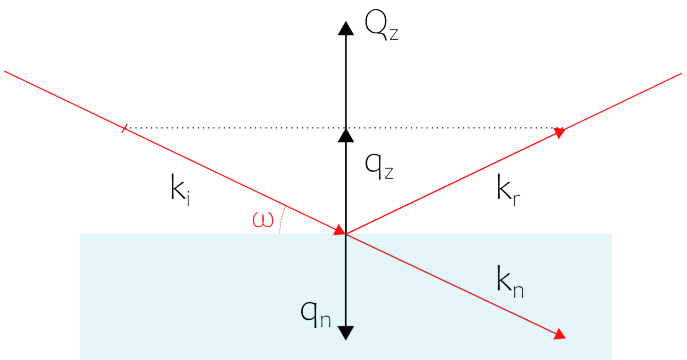

Figure 4.2: Schematic representation of the reflection of an X-ray beam by a flat surface.

Case of a stack of layers - Parratt formalism

Most systems of interest are more sophisticated than a bare interface. A thin film is composed of several chemical species distributed homogeneously or not along its thickness. Such chemical distribution leads to a varying SLD, or electron density d_{e^-}, with z across the material. Such variation in SLD is accounted for by dividing the film into a stack of layers, each having its own SLD. Let us consider such a stack of N layers numbered in increasing order (m =0,1,...,$N-1$,N), as shown in Figure 4.3a, from ambient air to the supporting substrate. Each layer is characterized by its thickness t_m and its constant SLD SLD_m. At each interface between a layer $m-1$ and m, the Fresnel coefficient is given as in equation 4.7:

$$r_{m-1/m} = \frac{q_{m-1} - q_m}{q_{m-1} + q_m} \tag{4.9}$$

At interface number m, represented in Figure 4.3b, part of the transmitted wave is reflected on interface $m+1$ thus producing interferences with the wave reflected on interface m which depends on their phase difference, directly related to the difference in optical path, in other words to the thickness of the layer. This is accounted for by the complex reflection coefficient for the interface m :

$$\tilde{r}_{m-1/m} = \frac{r_{m-1/m} + \tilde{r}_{m/m+1} \exp(-2iq_m t_m)}{1 + r_{m-1/m}\tilde{r}_{m/m+1} \exp(-2iq_m t_m)} \tag{4.10}$$

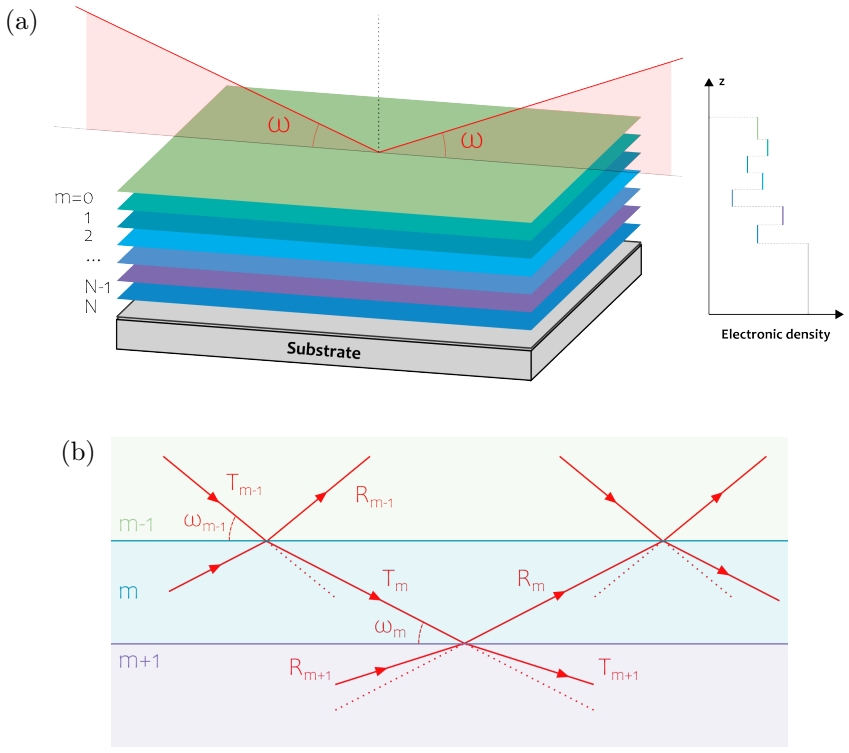

Figure 4.3: Reflectivity off stratified systems. (a) Schematic representation of a structured film composed of a stack of layers of different electronic densities. The electronic density profile across the film is shown on the right-hand side. (b) Focus on the optical path in layers $m-1$, m and $m+1$ inspired from ref. [152].

The problem turns out to be recursive, hence in need of an initial value. This is given by the reflection at the last interface, between the stack of layers and the substrate. Since no intensity reminiscent from the reflection of a transmitted wave comes from below, *i.e.* $z = -\infty$, the reflection coefficient is simply the Fresnel coefficient $r_{N/N+1}$ given by equation 4.9 with $m = N + 1$. This formalism was introduced by L.G. Parratt in 1954 [152]. We will discuss in section 4.2.2 how it is widely used to analyse XRR data.

We focused in the previous calculations on the reflected beam, as defined by an outgoing angle equal to the incident one. This is the so-called specular condition. It is achieved in practice by either changing both the angles of the source and the detector for a fixed sample position, or progressively tilting the sample at an angle ω and placing the detector at an angle 2ω.

Roughness and interdiffusion

Up until this point, every interface has been considered sharp, perfectly smooth and flat. While the flatness condition is usually verified or at least to a satisfying extent, interfaces are never perfectly smooth. Deviations from the ideal sharp interface originate from two physical phenomena, roughness and interdiffusion. In the case of roughness, the interface is not located at a constant value of z across the xy plane due to an irregular topography. In the case of a solid-solid or liquid-liquid interface, the two materials can also mutually diffuse in one another in the close vicinity of the interface, thus again blunting the ideal interface. This causes a damping of the reflectivity, meaning a faster decrease with increasing incident angle. [1] Mathematically, the most common approach is to assume a Gaussian profile of interdiffusion or a Gaussian probability density for the surface defects. Then both phenomena are accounted for by replacing the step function of a sharp interface's density profile between layer m and $m + 1$ by an error function defined as [153]:

$$erf\left(\frac{z - z_{m/m+1}}{\sigma_{m/m+1}}\right) = \frac{2}{\sqrt{\pi}} \int_0^{(z-z_{m/m+1})/\sigma_{m/m+1}} \exp(-t^2)dt \tag{4.11}$$

In which $\sigma_{m/m+1}$ controls the thickness over which the electronic density smoothly varies from one layer to the other. It is hereafter referred to as the roughness of the layer, $m + 1$ regardless of whether it originates from actual roughness (at the air-solid and solid-substrate interface) or interdiffusion (inside a layered thin film).

4.2.2 Reflectivity Analysis

The underlying point of the principle described above is that through the shape of a reflectivity curve, the structure normal to the substrate, *i.e.* the density profile across the thin film, can be inferred. Direct fitting of the data with a proper model, as usually done with any kind of experiment, is a powerful method, yet it presents some inherent limitations here. Before addressing this, however, we first

[1] A way to discriminate between roughness and interdiffusion is to look at the off-specular scattering. The lateral inhomogeneities of a rough interface act as numerous reflecting surfaces with different orientations, absent in the case of interdiffusion

give some qualitative features of XRR patterns of model systems based on which some indications on the structure can be deduced visually.

Qualitative approach to reflectivity

Let us consider the simplest case of an homogenous layer deposited on substrate, each of them are characterized by a constant electronic density and the layer has a given thickness. The resulting reflectivity curve features oscillations due to interferences between waves reflected on the air-layer and the layer-substrate interfaces. The oscillations commonly called Kiessig fringes [153] are a common interference phenomena, similar to what happens in a Fabry Pérot interferometer [154]. The interfringe spacing thus relates to the thickness of the layer. In other words, a given characteristic thickness in real space induces a signal oscillating at a corresponding spacial frequency in reciprocal space. This type of situation is represented in Figure 4.4a.

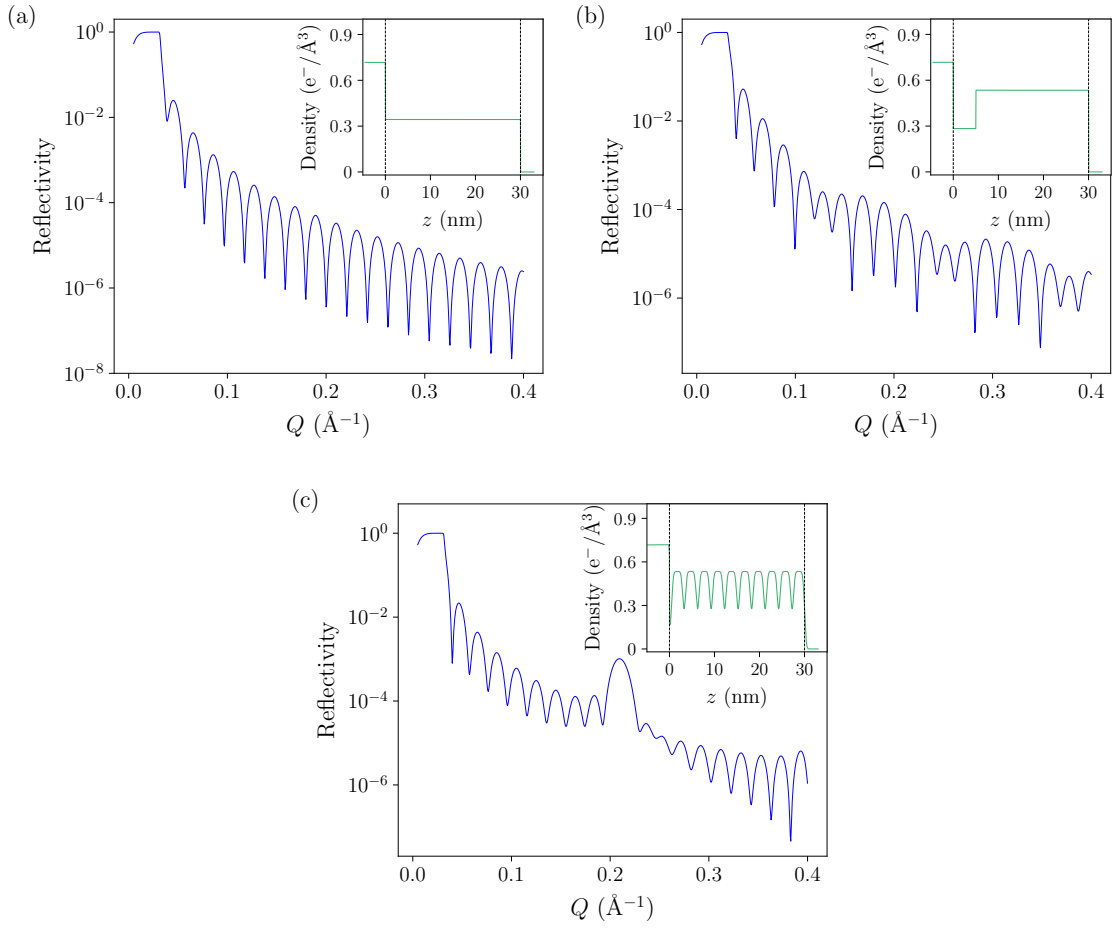

Figure 4.4: Simulated examples of XRR curves for (a) an homogenous layer, (b) a bilayer and (c) a multilayer; corresponding electronic density profiles are given as insets in which vertical dashed lines represent the substrate-film and film-air interfaces.

If instead of a single homogenous layer we consider a bilayer and proceed with the same reasoning as above, two characteristic thicknesses are now present and will act

as two spacial frequencies in reciprocal space. The resulting reflectivity curve then exhibits a beating pattern with modulated Kiessig fringes (Figure 4.4b). Last but not least, a more sophisticated system worth mentioning is a multilayer in which the electronic density profile oscillates periodically, as shown in the inset of Figure 4.4c. In this rather interesting situation, the system features a characteristic thickness, that of the whole film, and a characteristic frequency of oscillation of the electronic density. Therefore, the reflectivity curve exhibits Kiessig fringes modulated by a Bragg peak at a position corresponding to the profile's oscillation frequency. All these considerations are the starting point to the analysis of any XRR data. They give fairly good indications as to what kind of model should be used in order to reach a quantitative description of the structure.

Fitting of reflectivity data

As it will come out of this section, fitting XRR data can often be quite demanding and time-consuming. The fitting strategy thus requires some thoughts. It ultimately comes down to finding the right parameters so that the chosen model's prediction is as close as possible to the experimental data points. How well the model fits the observed data, the so-called goodness of fit, can be estimated by the χ^2 parameter defined as the sum of the squared differences between the observed data X_i and their expected value E_i according to the selected model divided by the variance σ_i^2 :

$$\chi^2 = \sum_{i=1}^{n} \frac{(X_i - E_i)^2}{\sigma_i^2} \tag{4.12}$$

Taking this as the measurement of the goodness of fit, the best solution is the one which minimizes χ^2. Its value as a function of all adjustable parameters forms the parameter space. In the simple situation of two parameters, it is a surface and the best solution is found in a valley of its topography. One way to find said minimum is to use a gradient-based algorithm known as the least-square method. In other words, starting from initial conditions, one should travel down to the nearest valley in parameter space. Such an algorithm has the benefit of being rather straightforward, thus delivering short calculation times. It is undeniably the most commonly used type of regression method, and was actually used to fit SANS patterns or correlation peak positions in Chapter 3. It does, however, present the significant drawback of not exploring the parameter space enough.

In situations where the number of adjustable parameters is low, the parameter space is fairly regular and we can reasonably say that the minimum found is indeed a global one, provided the initial guess is rationally chosen. If it happens that the minimum is not a global one, the solution usually lacks physical meaning and can easily be invalidated. In complex situations with numerous input parameters, the multidimensional parameter space is much more intricate and the minimum closest to the initial conditions is most likely not the global one. Hereditary methods, instead of gradient-based ones, address this issue by providing another way to explore the parameter space. The differential evolution algorithm, introduced in the 1990s, selects an initial population of candidate solutions across the parameter space which are then combined to form other candidate solutions. In other words, instead of

following a continuous path from initial guess to the best solution, it jumps around the parameter space. New candidates are kept if they are a closer match to the experimental data, and discarded otherwise. It is less accurate than a least-square method and does not necessarily converge, but it allows to broadly explore the parameter space and is therefore particularly useful in multidimensional problems, in the case of numerous input parameters.

Coming back to XRR data, the qualitative descriptions of previous section 4.2.2 provide good insight into what kind of SLD profile better describes the system of interest. The reflectivity of that arbitrary profile can be calculated from the slicing method illustrated in Figure 4.3a and Parratt formalism of equation 4.10. Each of the individual layers is given a thickness t, a SLD and roughness σ, either originating from interdiffusion between two adjacent layers or from the film's roughness for the top layer. By starting the calculation at the interface between the stack of layers and the substrate and progress layer by layer up until the interface with the first one, we retrieve the reflectivity of the multilayer $R(q) = |\tilde{r}_{0/1}|^2$. This procedure is used by most XRR fitting software programs such as `REFLEX` [155], `GenX` [156] or `refnx` [157]. Although all of them have been used at some point along this work, `refnx` allows a certain liberty in the choice of regression method, hence being particularly adapted to our situation. Because each additional layer possesses three adjustable parameters, their total number rapidly builds up. Therefore, a choice of fitting strategy based on the previous considerations is done in section 4.4.2 to address this numerical complexity.

The kinematical approximation

An important aspect comes out of previous section 4.2.2 concerning the measurements and Parratt's equations themselves. Because an XRR experiment measures intensities rather than amplitudes, all phase information is lost. Therefore, a direct inversion of the data to reconstruct a single SLD profile is impossible. Strictly speaking, this means one electron density profile is never equivalent to a given XRR data set. This major drawback of X-ray reflectivity, and scattering in general, is known as the "phase problem" [151]. Nevertheless, in some conditions, an analytical expression relates the electron density profile to the reflectivity.

In the so-called "weak scattering regime", a single scattering event is sufficient to describe the problem, hence neglecting multiple-scattering. This so-called kinematical or Born approximation is valid at high angles but fails around the total reflection condition. In practice, it is considered to hold for $Q > 3Q_c$, Q_c being the critical scattering vector of total reflection [151]. It can then be shown the scattering cross section is then proportional to the Fourier transform of the electron density. This is in fact general to all scattering events, and it translates, for surfaces, into a direct relation between the reflectivity and the gradient of the electron density profile $n(z)$ [151, 158]:

$$\frac{R(Q)}{R_F(Q)} \sim \left| \int_{-\infty}^{+\infty} \frac{dn}{dz} \exp(iQz) dz \right|^2 \tag{4.13}$$

wherein $R_F(Q)$ is the Fresnel reflectivity of the substrate given by equation 4.8 and $n(z)$ is the laterally averaged electron density profile. The qualitative considerations

led above actually stem from this approximation. Indeed, the fact that a single homogenous layer translates into Kiessig fringes on the reflectivity originates from a Fourier transform. The modulation of said fringes in the case of a bilayer or multilayer leading to a beating pattern or a Bragg peak also comes down to a Fourier transform effect. This approach is particularly useful in complex systems and captures subtle details in stacks with very low contrast [159, 160]. It will be used on our experimental data and discussed further in section 4.4.3.

4.2.3 Original protocol on a Xeuss 2.0

XRR experiments presented below are performed on a Xeuss 2.0 diffractometer (Xenocs). The instrument is originally dedicated to SAXS or WAXS measurements and was introduced in Chapter 3 in that regard. For that reason, we present more thoroughly, in this section, the original experimental procedure by which reliable reflectivity data can be obtained. The experimental set-up and how measurements are carried out are discussed in the first part, whereas the second one focuses on the data treatment routine, moving from a series of 2D pictures featuring the specular spot for varying incident angles to a reflectivity pattern.

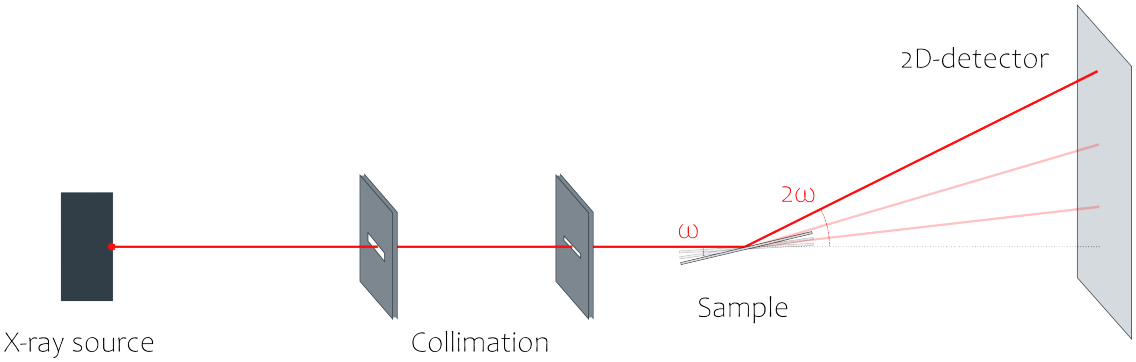

Figure 4.5: Schematic representation of the XRR configuration on the Xeuss 2.0

Experimental setup

The setup is essentially the same as in Chapter 3, including a Genix 2D Cu HF source, of wavelength 1.542 Å and a Pilatus 1M 2D detector (Dectris) placed, this time, at 1214 mm from the sample's centre as represented in Figure 4.5. The whole X-ray path from source to detector is put under vacuum in order to avoid absorption or residual scattering from ambient air. The silicon wafers supporting the PIL thin films are attached to a 3D printed sample holder placed in the sample environment equipped with a goniometer additionally to the translation motors. Samples are aligned using the direct beam by scanning the motor's position in the vertical direction (z) and the tilting angle in the direction of the beam (ω). The region of interest (ROI) is set to a horizontal slit of a single pixel in width for accurate alignments. There is usually an offset in ω which is determined precisely using the specular position as function of ω during data treatment. The standard XRR acquisition uses two collimation slits set to 0.5 x 1 mm and 0.3 x 1 mm (height x width) thus shaping a horizontally elongated beam, to maximize the flux,

but narrow in the vertical direction to limit the uncertainty in incident angle and consequently in scattering vector Q. Acquisition times are 1 s per incident angle θ up to 1° (resp. $Q_z = 0.14$ Å^{-1}), followed by 30 s up to 3° (resp. $Q_z = 0.43$ Å^{-1}). Thus, for each value of incident angle ω a 2D picture is acquired on the detector. Measurements are done at two different vertical positions of the detector in order to fill gaps of the detector.

Data treatment

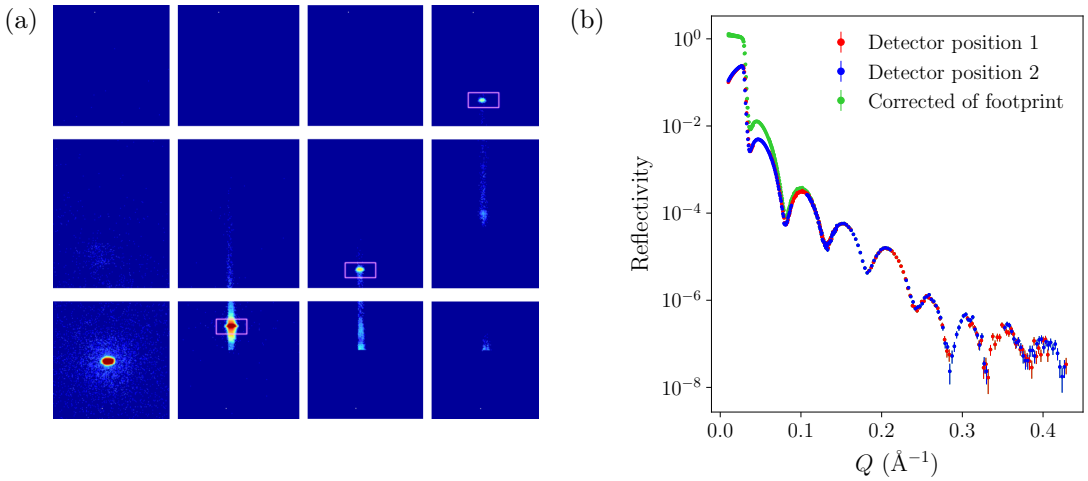

Figure 4.6: (a) Detector picture during a XRR experiment. From left to right the direct beam, incident angles of 0.18°, 0.48°, 0.86°, 1.37°. The ROI is shown as a pink rectangle. (b) Resulting XRR curve for the two detector position and the final curve corrected of the footprint.

The experimental procedure detailed in the previous subsection delivers a series of 2D pictures from the detector, one for each incident angle ω, and at two different detector positions. Examples of such pictures are given in Figure 4.6a. The data are treated using the Python package `pygdatax`. The treatment of these data relies on a moving ROI across the different pictures to follow the specular spot. It requires several parameters such as the beam centre on the detector, the sample-detector distance, the offset in ω and the size of the ROI. The beam centre is determined by fitting the direct beam by a 2D Gaussian. The size of the ROI is adapted to the direct beam by taking 15 times the width of a Gaussian fit in both directions. The intensity in the ROI is then integrated for each values of ω thus delivering a reflectivity curve as shown in Figure 4.6b. Once data for both detector positions have been treated, they are superimposed to obtain an uncut reflectivity curve.

The last step in the treatment is to correct for footprint. As XRR experiments start at low ω below the critical angle, the beam of size w_b in the vertical direction covers an area much greater than the sample length L in the beam direction, as illustrated in Figure 4.7. This leads to a deformation of the reflectivity at low Q as can be observed in Figure 4.6b. Assuming an uniform beam intensity, the corrected reflectivity is then given by [161] :

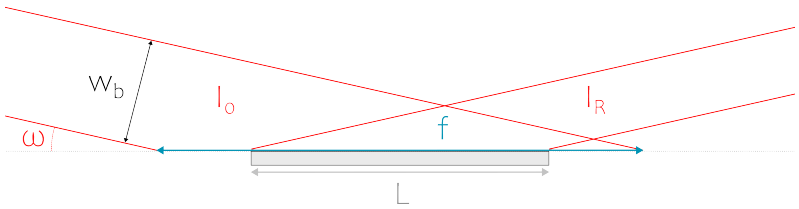

Figure 4.7: Illustration of the beam footprint being larger than the sample.

$$R_{\text{corr}}(\omega) = R(\omega) \times \frac{L}{w_{\text{b}} \sin \omega} \tag{4.14}$$

The length L of the sample is measured using a calliper. The beam width w_{b} is precisely determined by fitting the intensity measured on the whole detector upon scanning a sample in the vertical direction. Due to its divergence, the beam size on the sample is slightly larger than the collimation slit. An example of XRR curve at every step of the treatment is shown in Figure 4.6b.

Improvement of the acquisition

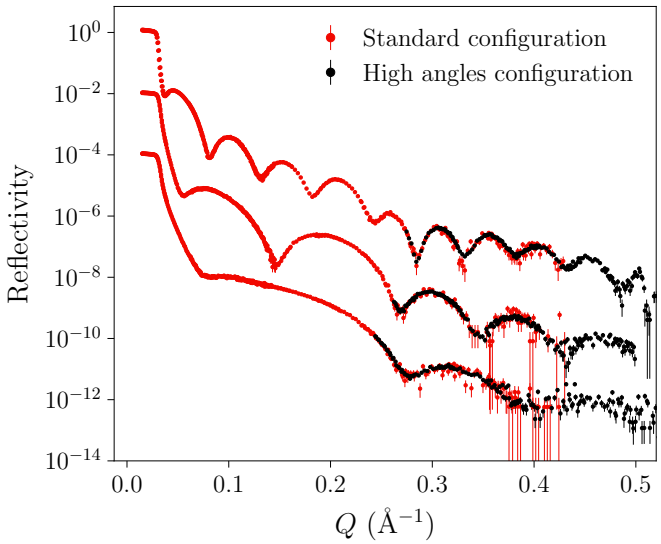

Figure 4.8: XRR curves after treatment for three samples in both standard and high angles configurations. The data considered hereafter are the concatenation of both. Data are shifted vertically for clarity.

To improve the signal at higher angles, as well as pushing the maximum Q-value further, an additional acquisition is performed, setting a larger collimation (1 x 1.2 mm and 0.6 x 1.2 mm) and an acquisition time of 150 s from $\theta = 1.75°$ (resp. $Q_{\text{z}} = 0.25$ Å^{-1}) to $\theta = 3.8°$ (resp. $Q_{\text{z}} = 0.54$ Å^{-1}). A larger collimation provides a higher flux which, together with longer acquisition times, ensures a better signal-to-noise ratio. The reflectivities measured in both collimation settings are shown in Figure 4.8. Inevitably, a larger collimation comes with a drawback on the

uncertainty in incident angle $\delta\omega$ since it depends on the size of the slits, S_1 and S_2, and the collimation distance D_c, fixed at 1200 mm on the instrument :

$$\tan(\delta\omega) = \frac{S_1 + S_2}{2D_c} \tag{4.15}$$

However, the relative uncertainty $\delta\omega/\omega$ at these angles remains satisfying.

4.3 Off specular scattering - GIWAXS

As the name suggests, grazing incidence wide angle X-ray scattering (GIWAXS) is very similar to WAXS. Its specificity however is to probe the vicinity of an interface, whether it is an air-liquid or air-solid one, instead of the bulk. Experimentally, the setup is comparable to specular XRR experiments. A schematic of the sample and detector region is given in Figure 4.9 namely to introduce notations such as the incident angle α_i and wave vector $\vec{k}_i$ and outgoing wave vector $\vec{k}_{out}$.

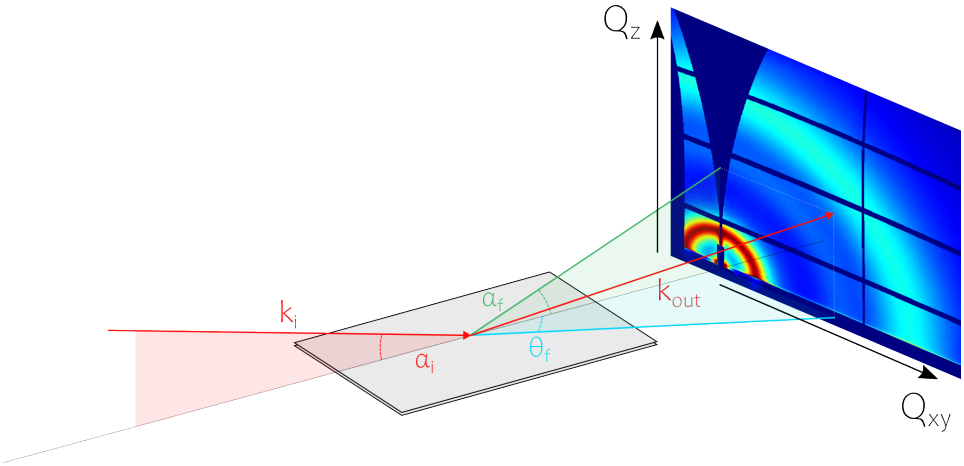

Figure 4.9: Schematic representation of grazing incidence X-ray scattering experiments.

As mentioned above, X-rays have a refractive index slightly smaller than unity, allowing total external reflection for incident angles below ω_c given by equation 4.5. In these conditions, it can be shown that the modulus of the electric field below the interface describes an evanescent wave, *i.e.* an exponentially decaying wave, which travels parallel to the interface. The penetration depth Γ can be expressed as [151]:

$$\Gamma = \frac{\lambda}{\sqrt{2}\pi}\left[\sqrt{(\alpha_i^2 - \alpha_c^2)^2 + 4\beta^2} - (\alpha_i^2 - \alpha_c^2)\right]^{-\frac{1}{2}} \tag{4.16}$$

For incident angles approaching 0, $\omega \to 0$, the penetration depth becomes $\Delta_0 = 1/\sqrt{4\pi r_e d_{e^-}}$ with r_e the classical electron radius and d_{e^-} the density of electrons inside the material. This limit is independent of the wavelength and gives a few nanometers for usual polymeric materials. Consequently, a 2D detector placed after the sample records the scattering pattern from this interfacial nanometric layer.

Except for more elaborate experiments in which it is varied so as to change the penetration depth given by equation 4.16, the incident angle is kept at a fixed

value α_i. Considering a single point on the resulting 2D pattern, the corresponding scattered beam is described by a wave vector $\vec{k}_{out}$. It makes an angle α_f with respect to the sample surface and θ_f with the incidence plane. The resulting scattering vector is still defined as in equation 4.6 as $\vec{Q} = \vec{k}_{out} - \vec{k}_i$. In contrast to XRR, however, it not only has a component Q_z along the normal to the interface but also another, Q_{xy} parallel to the interface. Considering only elastic scattering, each component of the scattering vector is geometrically given by [162]:

$$\begin{aligned} Q_x &= k_i[\cos(\theta_f)\cos(\alpha_f) - \cos(\alpha_i)] \\ Q_y &= k_i[\sin(\theta_f)\cos(\alpha_f)] \\ Q_z &= k_i[\sin(\alpha_f) + \sin(\alpha_i)] \end{aligned} \tag{4.17}$$

Just like the normal scattering vector $\vec{Q}_z$ allows observations on the out of plane structure, *i.e.* normal to the interface, the Q_{xy} component probes the in-plane structure near the interface.

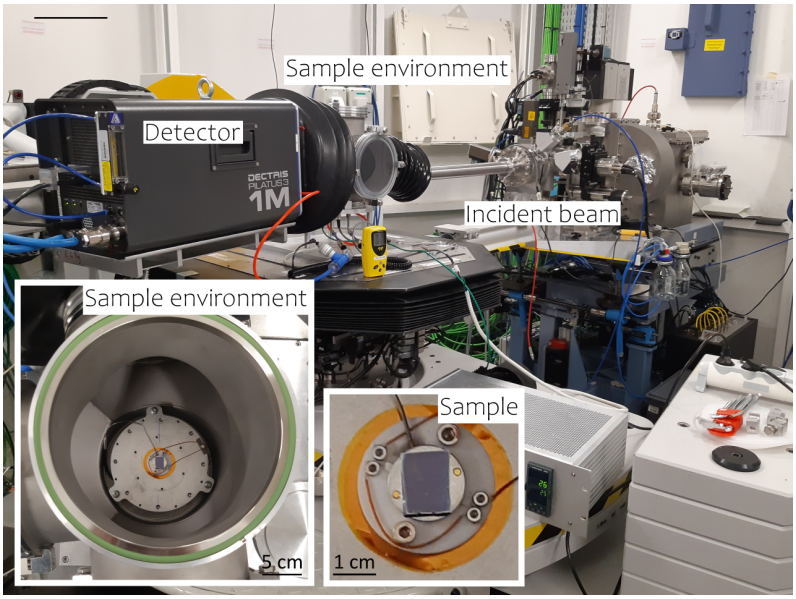

Figure 4.10: Picture of the GIWAXS configuration of the SIRIUS beamline at the SOLEIL synchrotron. X-rays travel from right to left. Insets are a top view of the unsealed sample environment and a magnified view of the wafer placed at the centre.

In terms of intensity, off-specular scattering is several orders of magnitude less intense than the specular spot. Hence, it requires a considerably higher incident flux, not afforded by the X-ray lab source of the Xeuss 2.0 used for XRR experiments. Such a flux is only provided by synchrotron light sources. Consequently, GIWAXS experiments reported in the present work were performed on the SIRIUS beamline at the SOLEIL synchrotron light source [163], a picture of which is given in Figure 4.10. The Soft Interfaces and Resonant Investigation on Undulator Source beamline is dedicated to both specular reflectivity and grazing incidence scattering with an energy range between 1.4 and 13 keV. As a matter of comparison, the Cu K_α source

used on the Xeuss 2.0 provides an X-ray beam at 8.05 keV. The beamline is suitable for both soft interfaces, semiconductors, or magnetic nanostructures communities. For soft interfaces, both the air-solid, solid-solid and air-liquid interfaces can be investigated.

4.4 Out of plane interfacial structure

We present in this section the experimental specular X-ray reflectivity results obtained using the protocol detailed in section 4.2.3. Data are first addressed qualitatively using the arguments of section 4.2.2. A quantitative description is then achieved by both data fitting and an additional Fourier transform analysis based on the kinematical approximation of section 4.13.

4.4.1 Qualitative approach

Experimental XRR data gathered with the protocol detailed in section 4.2.3 are plotted in Figures 4.11 and 4.12. For both **PC_2VImTFSI** and **PC_4VImTFSI** thin films the specular XRR curves display conventional features of an homogenous film, with regular Kiessig fringes whose spacing decreases with increasing thickness, similar to the simulated example of Figure 4.4a. For longer side-chains ($n = 7$ and 10), XRR results are significantly different in aspect (Figure 4.12a and 4.12b). Kiessig fringes appear to be modulated by a shorter spacial frequency signal, resembling, to a certain extent, the example of a multilayer given in Figure 4.4c. Without any fitting of the data at this point, this is already a clear sign of a layered structure of the thin film, as an interlayer spacing acts as an additional spacial frequency on the reflectivity [153].

4.4.2 Usual fitting and limitation

Data are fitted using the `refnx` Python package [157]. Qualitative considerations around data for 2 and 4 carbons side-chain, respectively plotted in Figure 4.11a and 4.11b, motivates the choice of an homogenous model with a native oxide layer around 20 Å thick. The corresponding scattering length density (SLD) profiles are given in the bottom panels of Figure 4.11. Exact values of parameters obtained from the fitting are given in Appendix 1. The electron-rich Si substrate on the left-hand side has the largest SLD, followed by the native SiO_2 oxide layer. The PIL layer has a constant SLD across its thickness as imposed by the model. Above the PIL film, the SLD drops to zero as experiments are performed in vacuum. The slight drop of SLD for the thinnest films can be attributed to a certain degree of film inhomogeneity. Indeed, these thicknesses approach the limits of the spin-coating technique. An actual decrease of the material's density would go against what is commonly observed in polymeric thin films in which density usually increases with decreasing film thickness. The amplitude of the density variation observed is furthermore considerably larger.

To reproduce the data of Figure 4.12 for **PC_7VImTFSI** and **PC_{10}VImTFSI** thin films, a simple homogenous layer is no longer sufficient and a multilayer model is used to account for the fringes' modulation as it came out of the previous section.

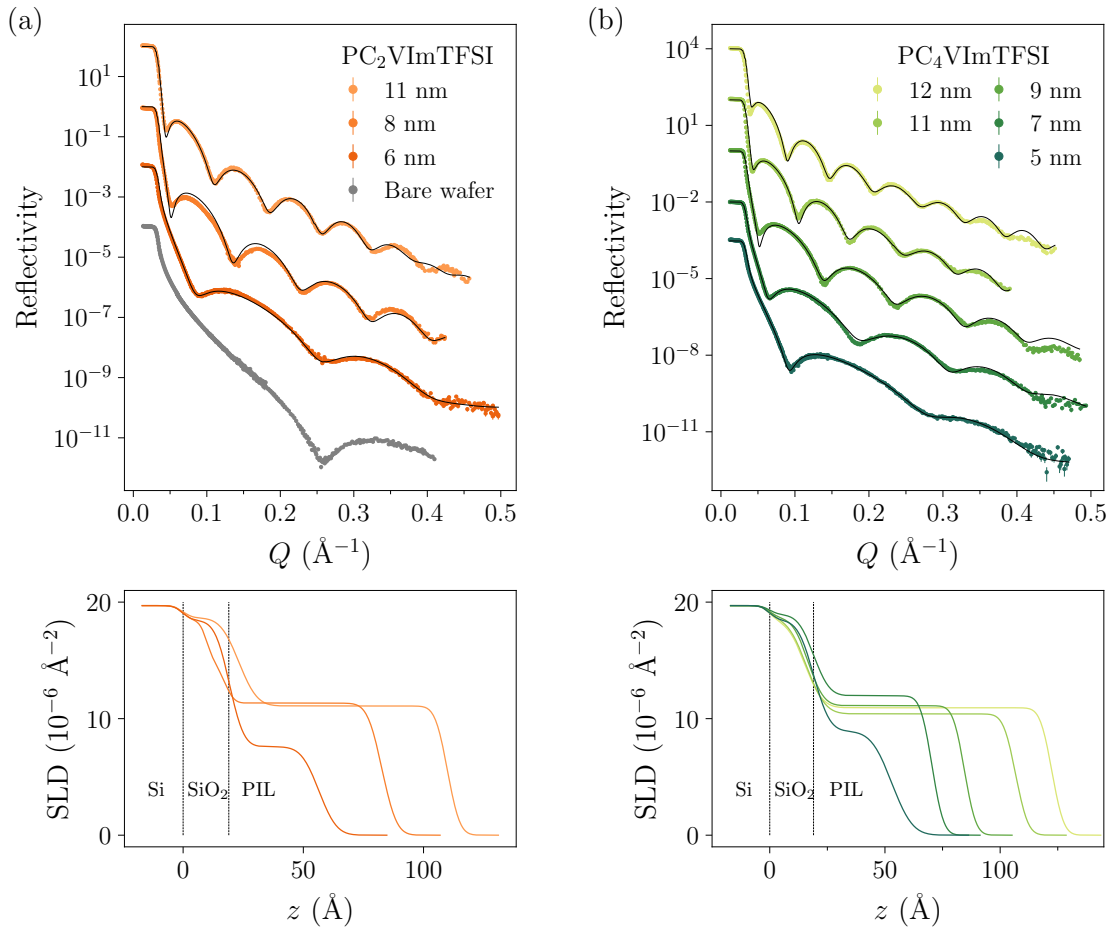

Figure 4.11: X-ray reflectivity results for **PC_2VImTFSI** (a) and **PC_4VImTFSI** (b) thin films with varying thickness. Data are shifted vertically for clarity. Grey solid lines are the best fits. The corresponding SLD profiles are given below.

The slicing of the PIL layer sharply increases the number of fitting parameters, and the method has to be carefully chosen based on section 4.2.2. To ensure the convergence of the algorithm and limit the calculation times, the fitting proceeds in two steps. A differential evolution algorithm is used with thicknesses as the only adjustable parameters to broadly explore the phase space. The SLD and roughnesses are afterwards adjusted by a least-square method known as Levenberg Marquardt algorithm. For this reason, some parameters appear as fixed in the fitting parameters list of Appendix 1.

SLD profiles thus obtained for both 7 and 10 carbons in side-chain length are shown in the bottom panels of Figure 4.12. The layering suggested by the modulation of the Kiessig fringes clearly stands out. The SLD is no longer constant across the PIL layer, as before, but instead exhibits oscillations. Some parts of the film have SLDs either above or below the average material's SLD, suggesting some layers are either enriched or depleted in electrons. Looking at the chemical structure of the material, it seems reasonable to attribute the maxima of SLD to layers rich in $TFSI^-$ anion, composed of electron-rich atoms such as fluorine or sulphur whereas the minima in SLD are where the imidazolium groups with attached alkyl chains

essentially settle. Only the thinnest films up to 7 nm for **PC$_7$VImTFSI** and 8 nm for **PC$_{10}$VImTFSI** were fitted using this method. At these thicknesses, it already takes three layers in addition to the oxide layer to describe the system, leading to a total number of 12 fitting parameters. For even thicker films, additional layers are needed and the fitting procedure hardly converges to anything physical due to the numerical complexity.

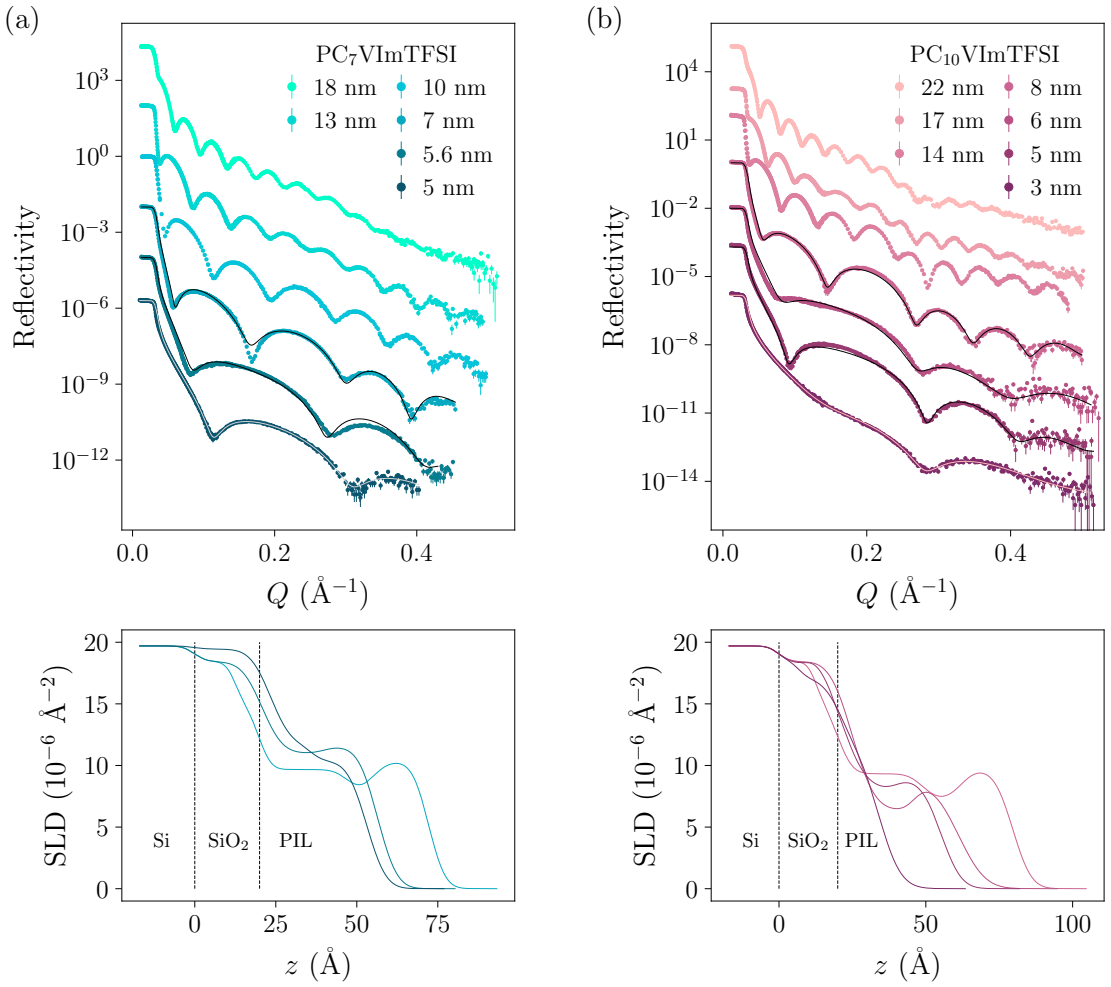

Figure 4.12: X-ray reflectivity results for **PC$_7$VImTFSI** (a) and **PC$_{10}$VImTFSI** (b) thin films with varying thickness. Data are shifted vertically for clarity. Grey solid lines are the best fits. The corresponding SLD profiles are given below.

At this point, there is still a possibility that short side-chain PILs ($n = 2$ and 4) develop an inner structure. Looking at the data for the longer side-chains in Figure 4.12, the modulation of the Kiessig fringes has a smaller spacial frequency for $n = 10$ than $n = 7$, most likely originating from a larger interlamellar distance for $n = 10$, consistent with WAXS results on their corresponding bulk structure. Such interlamellar distance would be expected to be even shorter for $n = 4$ and 2 if lamellar structures were still present, hence the spacial frequency would be higher and the visible dip in the XRR curves might fall outside our working Q-range. This is specially plausible since numerical simulation of imidazolium ILs at a charged mica surface showed side-chains arrange parallel to the interface for n

below 4 carbons and perpendicular above, due to amphiphilic self-assembly [164], leading to a potential decrease of the interlayer spacing all the more pronounced. Additionally, the modulation would be less visible as side-chains become shorter because the contrast itself decreases. Nevertheless, it appears reasonable to assume the layering only develops above $n = 4$ since it is also the threshold of percolation of apolar domains in both ILs [21] and PILs [34].

4.4.3 Fourier transform analysis

Principle and numerical validation

To pursue the analysis further, in spite of the numerical challenges of fitting with a multilayered model and many parameters, we present the use of the Fourier transform of the reflectivity. Such method relies on the kinematical approximation introduced in section 4.2.2, in which the reflectivity is related to the gradient of electron density in equation 4.13. Let us define the autocorrelation function $g(z)$ of the gradient of the electron density. Its purpose will be discussed below, and we give for now its expression as:

$$g(z) = \int_{-\infty}^{+\infty} \frac{\mathrm{d}n}{\mathrm{d}z}(t)\frac{\mathrm{d}n}{\mathrm{d}z}(t-z)dt \tag{4.18}$$

From equation 4.13, it can be further expressed in terms of reflectivity as follows:

$$g(z) = \int_{-\infty}^{+\infty} \frac{R(Q)}{R_F(Q)}\exp(-\mathrm{i}Qz)\mathrm{d}Q \simeq \int_{Q_{z,\mathrm{low}}}^{Q_{z,\mathrm{high}}} \frac{R(Q)}{R_F(Q)}\exp(-\mathrm{i}Qz)\mathrm{d}Q \tag{4.19}$$

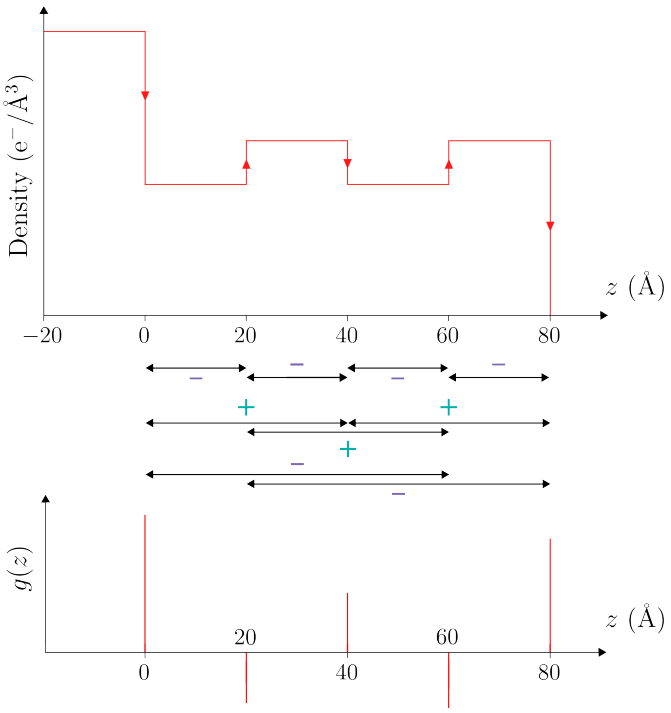

Figure 4.13: Schematic representation of the relevance of the autocorrelation function of the gradient of electron density. The top graph represents the density profile of an ideal layered film without any roughness or interdiffusion. Black horizontal arrows correspond to each correlation between interfaces, standing on the bottom graph of the $g(z)$ as sharp peaks.

In practice, data only span a fixed Q-range and the integration cannot be done on infinite bounds. This leads to the introduction of higher and lower bounds of

integration $Q_{z,\text{high}}$ and $Q_{z,\text{low}}$. A lower bound $Q_{z,\text{low}} = 0.06$ is chosen in the following as to verify the Born approximation while optimizing the working window.

The purpose of the autocorrelation function $g(z)$ is to highlight correlations between interfaces, where the gradient is the largest, as illustrated in Figure 4.13. Hence, an homogenous film should display at least one peak at the z value corresponding to the total thickness. In other words, there is only one correlation between the substrate-film and film-air interfaces. Any additional peak would suggest a structured film with additional interfaces. Before any use on our experimental data, however, we check the validity of this approach on simulated reflectivity curves using two model SLD profiles close to our case study. The first one is a homogenous layer of constant SLD on a silicon wafer with a native oxide layer of 20 Å. The second model is a multilayer of same average SLD but a contrast between layers of 2×10^{-6} Å^{-2}. Both SLD profiles and the corresponding calculated reflectivities are represented in Figure 4.14a. The autocorrelation functions of equation 4.19 are calculated using these reflectivities and are plotted in Figure 4.14b.

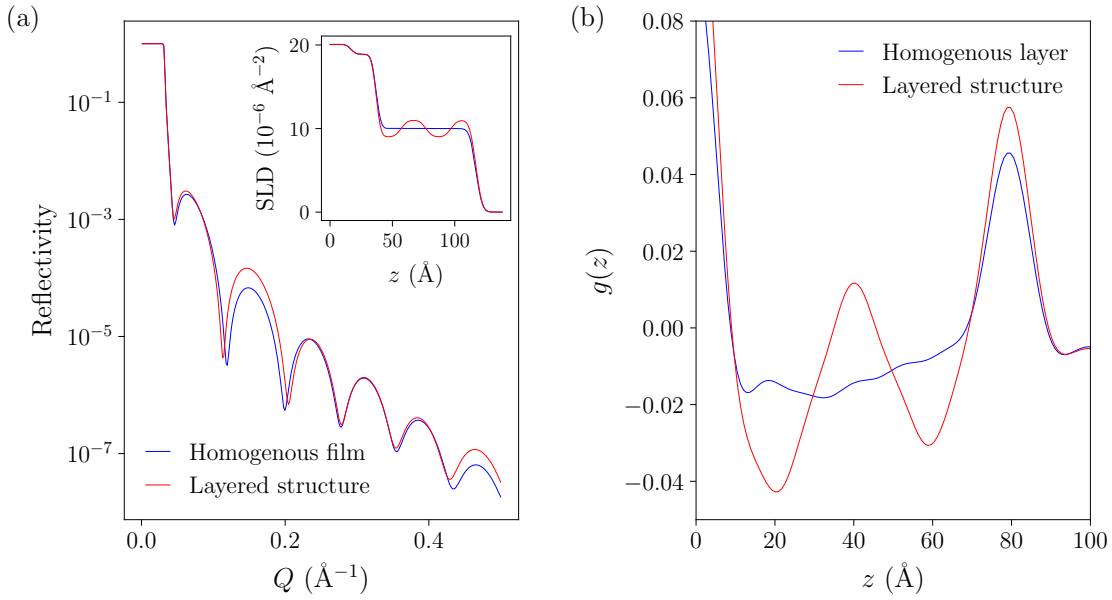

Figure 4.14: Numerical validation of the autocorrelation function use. (a) Simulated XRR data. SLD profiles from which they are calculated are given as insets. (b) Corresponding Fourier transforms $g(z)$ calculated as in equation 4.19

In spite of the molecular layering of the second model, the difference in reflectivities is very subtle due to the low contrast. This stresses the struggle of directly fitting the data. In spite of that, the calculated Fourier transforms are drastically different. An homogenous film model leads to a single peak in $g(z)$ for the total thickness of the film (80 Å) as expected. For the layered model, however, other peaks at 20, 40 and 60 Å are present and actually resemble the ideal situation represented in Figure 4.13. Each of these peak positions correspond to a distance between interfaces, hence seemingly validating the adequacy of the method.

It should be mentioned nonetheless that the autocorrelation signal of the homogenous model exhibits slight variations and a weak dip at low-z values. In order to find where this feature originates from, we varied several parameters including

the average SLD of the film, its external roughness, its thickness, interdiffusion between layers or SLD contrast between them, but no physical parameters appeared to affect the position of this dip. It did prove to be highly dependent on the upper limit of integration $Q_{z,\text{high}}$. Such dependence is well illustrated by Figure 4.15 in which the square of the autocorrelation function $g(z)$ is represented as a function of both z and $Q_{z,\text{high}}$. Solid lines represent $k \times 2\pi/Q_{z,\text{high}}$ functions and follow the $Q_{z,\text{high}}$-dependent peaks for both models. Hence, the low-z dip can be safely attributed to a numerical artefact with no physical meaning. It fixes the lowest length scale at around $2\pi/Q_{z,\text{high}}$ that can be probed with reflectivity data ranging up to a fixed value $Q_{z,\text{high}}$. This artefact has very little effect on the physical correlation peaks of both models. This numerical approach thus confirms a Fourier transform of the reflectivity is safe to use to evidence potential layering in our systems.

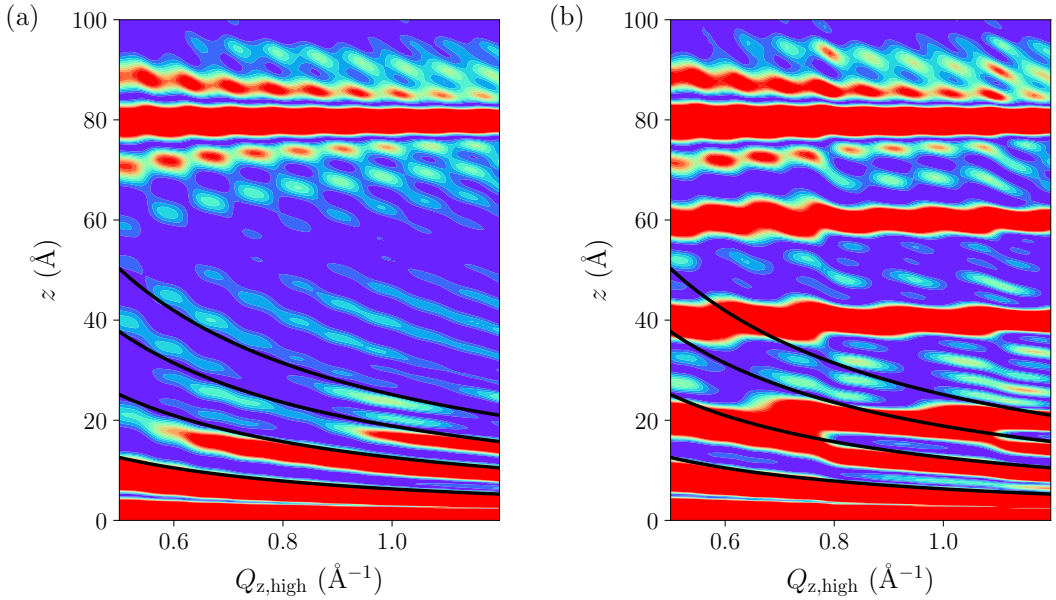

Figure 4.15: Dependence of $g(z)$ on the higher bound of integration $Q_{z,\text{high}}$. Calculated $g^2(z)$ as in equation 4.19 for varying $Q_{z,\text{high}}$ for an homogenous model (b) and a layered one (c). Both models are identical to the ones of Figure 4.14 with only ideal interfaces, *i.e.* no roughnesses. Black solid lines are functions $k^{2\pi}/_{Q_{z,\text{high}}}$ with k and integer.

Application to experimental data

Autocorrelation functions $g(z)$ calculated using equation 4.19 on the experimental data of Figures 4.11 and 4.12 are plotted in Figure 4.16 for the thickest films of the whole **PC$_n$VImTFSI** series. The largest intensity peaks, hereafter referred to as high-z peaks, are indicated by arrows and are ascribed to the whole thickness of the PIL film. Due to the very low contrast between Si and SiO_2 this thickness is of the PIL film only and does not include the native oxide layer. **PC$_2$VImTFSI** and **PC$_4$VImTFSI** thin films show no additional feature apart from the high-z peak, in good agreement with an homogenous film. In contrast, g functions for **PC$_7$VImTFSI** and **PC$_{10}$VImTFSI** display additional peaks, hence highlighting

an interfacial layering for all thicknesses. The low-z peak stemming from first neighbour correlations appears between 15 and 20 Å which is consistent with the SLD profiles obtained for the thinnest films in Figures 4.12a and 4.12b. This strongly supports the appearance of lamellar structures for these materials, concurrently validating the multilayer model used to fit the reflectivity of the thinnest films.

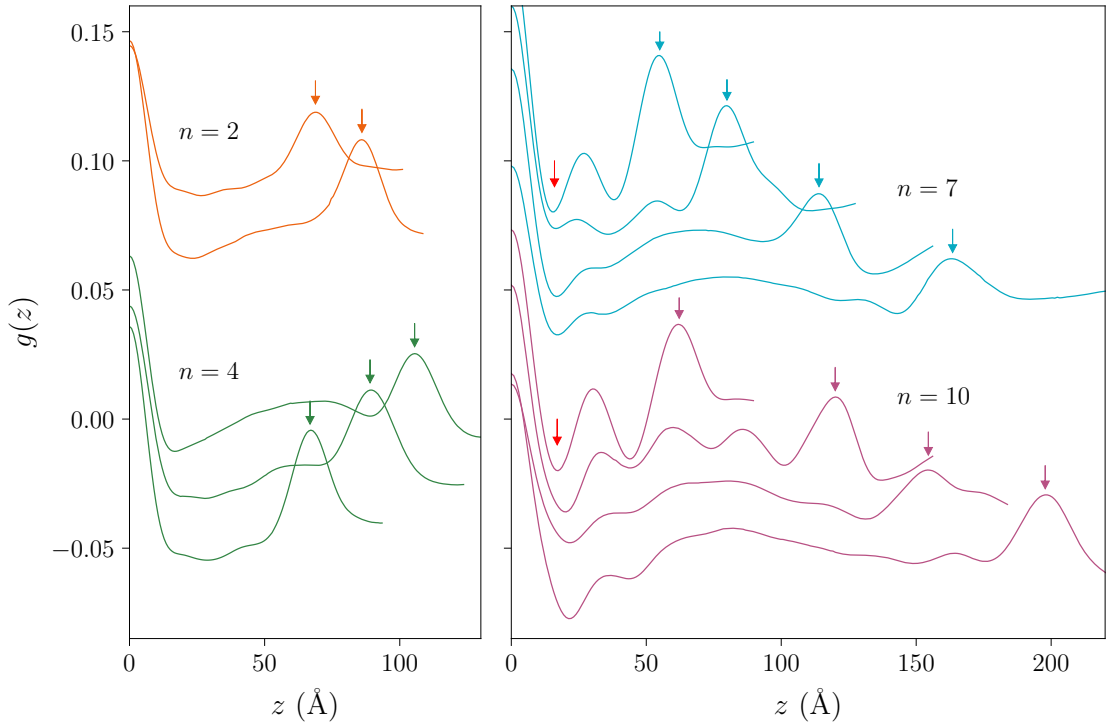

Figure 4.16: Fourier transforms of XRR data for **PC$_n$VImTFSI** thin films as calculated from equation 4.19, $n = 2$ and 4 in (left), $n = 7$, and 10 (right). Arrows with line colours indicate the thickness peak. Data are shifted vertically for clarity. The position of the low-z peak is indicated by a red arrows.

It must also be pointed out that intermediate peaks between the interlamellar distance and the total thickness tend to flatten out and no additional peak appears. This suggests the structure only develops in the vicinity of the interface, the rest of the film being a bulk-like region, otherwise additional peaks would appear due to longer range correlations such as second consecutive interfaces and so forth, which are not observed here. This is also partly visible in the SLD profiles of Figures 4.12a and 4.12b and resembles the interfacial structure of ILs in which the layering progressively fades away from the interface [72].

It is unclear at this point whether the structure develops preferentially at the Si/SiO_2-PIL or the PIL-vacuum interface. SLD profiles for the thickest films suggest the latter case, with an averaged SLD value in between a structured region and the oxide layer. Yet, the thickness of the bulk-like region is still comparable to the interlayer spacing at these film thicknesses. The Fourier transforms do not allow discriminating between the two options either. The correlations they uncover can either be with the substrate or the vacuum interface. Both option are furthermore consistent with ILs. Even though their interfacial structure has been extensively

studied at the solid-liquid interface, some works also focused on the air-liquid one, unveiling a similar layering [165, 166].

Figure 4.17 represents the position of the low-z peak as a function of the high-z one, *i.e.* the interlamellar distance z_{inter} as a function of film thickness. Values of z_{inter} for **PC_7VImTFSI** and **PC_{10}VImTFSI** thin films fall in the ballpark of the distance between neighbouring chains in bulk, as determined using SANS and WAXS in our previous work [167]. Interestingly enough, as the thickness of the films decreases, so does the interlamellar distance and the effect is slightly more pronounced for the longest side chain. Furthermore, it is not clear whether the interlamellar distance levels off to a plateau value over the range of thicknesses investigated here. Yet, it must be pointed out that the maximum thickness is already around 4 times the radius of gyration R_g of the chains measured by SANS [167]. A further study is required to elucidate the physical origin of such potential levelling.

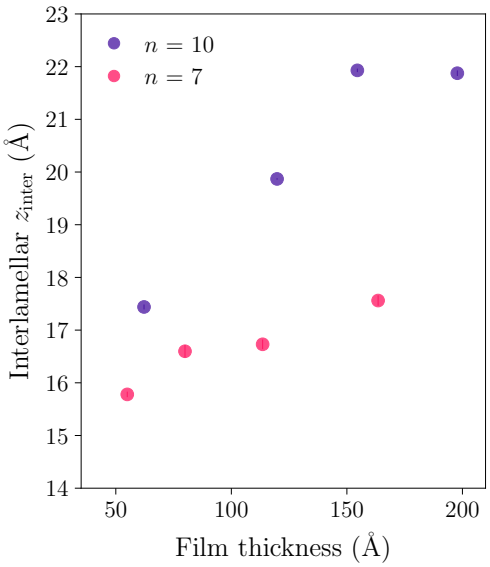

Figure 4.17: Position of the low-z peak of the autocorrelation signals, indicated by red arrows on Figure 4.16 and corresponding to the interlamellar distance z_{inter}, as a function of film thickness for **PC_{10}VImTFSI** and **PC_7VImTFSI**.

4.5 In-plane interfacial structure

XRR analysis provides excellent description of the interfacial layering and its alterations upon increasing confinement. It unveiled the onset of layering above $n = 4$ and a decrease of the interlamellar distance with film thickness. Assuming no changes occur on the in-plane structure, such observations would lead to a rather counterintuitive increase of density for thinner films. In order to achieve a complete structural characterization of PILs film, we complement the above observations with GIWAXS experiments to probe the in-plane structure. Grazing incidence wide angle X-ray scattering (GIWAXS) experiments, which principle was addressed in section 4.3, are performed on the SIRIUS beamline at the SOLEIL synchrotron light

source[1], also briefly presented therein. Spin-coated thin films are prepared according to the same procedure as for XRR experiments (section 4.1.1), and their thicknesses measured by ellipsometry. The following sections present technical aspects of the experiments and outline the specificities of the data treatment before laying out the experimental results gathered.

4.5.1 Methods

Experiment

The SIRIUS beamline was set in GIWAXS configuration with a Pilatus 1M 2D detector at a distance of 329 mm from the horizontally placed sample. The wavelength is 1.234 Å and the beam is collimated to a size of 0.07 mm x 0.5 mm (height × width). Incident angle was set at $\alpha_i = 0.12°$. After sealing of the sample environment chamber, air is flushed and replaced by a Helium atmosphere to prevent absorption and scattering of X-rays. For each sample, a 2D picture, as the one reported in Figure 4.18a, is acquired on the detector and requires some treatment.

Data treatment

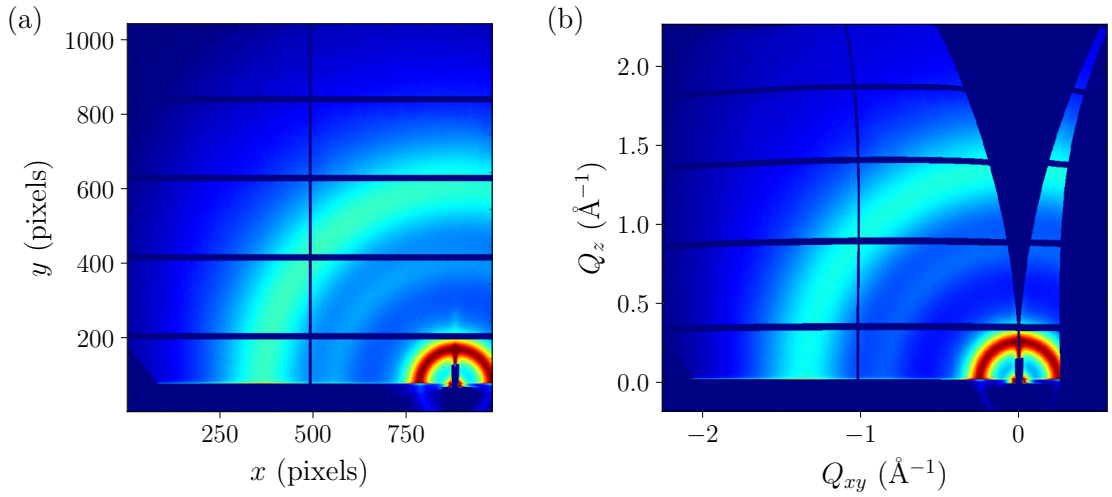

Figure 4.18: 2D data for a **PC_{10}VImTFSI** 143 nm thin film. (a) Detector picture in pixels. (b) 2D data after corrections and remapped to the Q_z/Q_{xy} plane.

Data treatment is performed with the Matlab based software GIDVis [168]. After selecting the experimental parameters such as the incident and detector angles and eventually correcting a slight tilt of the detector if needed, a solid-angle correction is applied, accounting for pixels far from the point of normal incidence not facing the incoming beam. The 2D picture in pixels is then remapped to a Q_{xy}, Q_z

[1]We thank our local contact A. Hemmerle (Université Paris-Saclay, Synchrotron SOLEIL, Saint-Aubin, France) and S. Lafon (Université Paris-Saclay, CNRS, Laboratoire de Physique des Solides, Orsay / Université Paris Saclay, Laboratoire Léon Brillouin, CNRS-CEA, Gif-sur-Yvette, France) for her precious help.

plane, corresponding to a projection of the Ewald sphere on a plane. A comparison between initial and treated 2D data is shown in Figure 4.18. The missing wedge around the Q_z axis on the remapped picture of Figure 4.18b is a geometrical consequence of flattening the Ewald sphere on a plane.

2D pictures thus obtained exhibit regular rings over the whole 180° around the beam centre, suggesting an isotropic system. Another feature of these pictures is the presence of a horizontal streak of intensity at small values of Q_z so-called Yoneda peak from Y. Yoneda who first focused on its origin in 1963 [169]. When the exit angle matches the critical angle, the scattered intensity is enhanced due to a waveguide effect in the sample. Since the system is isotropic, the Yoneda peak is a convenient way to retrieve information for a fixed value of Q_z with a high intensity. This way, the in-plane structure of the interface alone is probed with a scattering vector of varying Q_{xy} component. The Yoneda peak is integrated over a Q_z range of 0.01 Å^{-1}, thus leading to 1D data of scattered intensity $I(Q_{xy})$.

4.5.2 Experimental observations

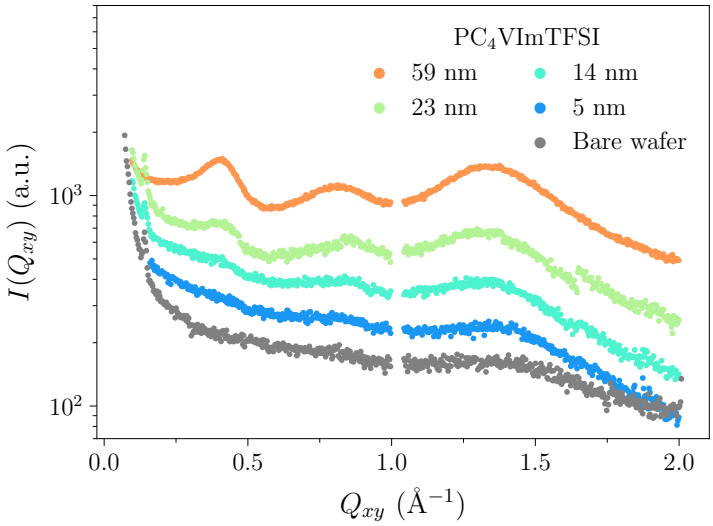

Figure 4.19: Integrated intensity along the Yoneda peak for **PC$_4$VImTFSI** thin films for varying film thickness, along with the signal of the bare wafer. Data are shifted vertically for clarity.

We report the intensity signals $I(Q_{xy})$ obtained in this manner for **PC$_4$VImTFSI** thin films in Figure 4.19. These samples weakly scatter and the signal is very close to that of the bare wafer also shown in Figure 4.19. **PC$_2$VImTFSI** and **PC$_4$VImTFSI** already showed rather weak scattering in bulk as discussed in Chapter 3. For this reason, they will not be discussed further in this section. The upturn at low-Q is most likely due to the direct beam not being fully blocked by the beam stop. Consequently, we subtract it from the reported signals in the following. Implications of such subtraction will be discussed later on.

The subtracted intensity signals $I(Q_{xy})$ for **PC$_7$VImTFSI** and **PC$_{10}$VImTFSI** thin films are reported in Figure 4.20. They are fairly similar to WAXS patterns of the bulk structure [167] discussed in a Chapter 3 and feature the same three peaks.

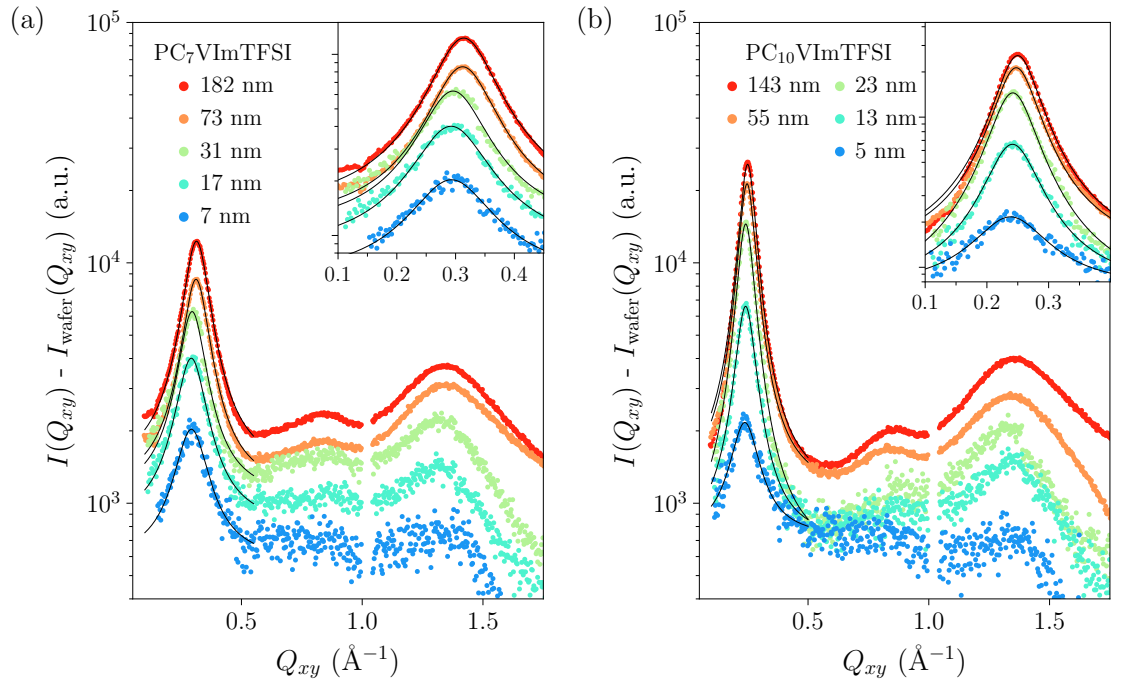

Figure 4.20: Integrated intensity along the Yoneda peak for (a) **PC_7VImTFSI** and (b) **PC_{10}VImTFSI** thin films for varying film thickness. Signal from the bare silicon wafer is subtracted. Black lines are Lorentzian fits to the interbackbone correlation peak. Data are shifted vertically for clarity. Insets represent the region of the interbackbone peak alone.

As a reminder, the low-Q peak (below 0.5 Å^{-1}) which is our main focus in this section, is assigned to the backbone-to-backbone correlation length d_{bb}, in other words the distance between two neighbouring macromolecular chains [33, 35].

Before anything else, it should be pointed out that the signal-to-noise ratio declines for thinner films due to less material quantity in the film, resulting in reduced scattering. Apart from this experimental limitation, the interbackbone peak slightly shifts to lower Q-values as the thickness decreases, suggesting a subtle but nonetheless remarkable dependence in film thickness. Fitting of this scattering peak using a Lorentzian form delivers a quantitative determination of the interbackbone distance at the interface $d_{\mathrm{bb}}^{\mathrm{int}}$. Reported in Figure 4.21 is the ratio of $d_{\mathrm{bb}}^{\mathrm{int}}$ and the interbackbone distance in bulk $d_{\mathrm{bb}}^{\mathrm{bulk}}$ as determined by WAXS. It is noteworthy that the interbackbone correlation length increases considerably below a film thickness of the order of 80 nm.

A word should be given at this point on the substrate contribution to the signal, mentioned at the beginning of this section. The intensity upturn at low-Q (Figure 4.19 slightly influences the position of the peak, specially for the thinnest films which scatter much weakly. Subtracting the whole signal, as it has been done, is the only way to remove this contribution. More thoroughly, a prefactor smaller than one should be applied to the wafer signal to account for the presence of the PIL layer. The correlation lengths corresponding to both subtracted and unsubtracted signals are represented in Figure 4.21 respectively as filled and empty symbols. For the thickest films, the low-Q correlation peak is intense enough so that the

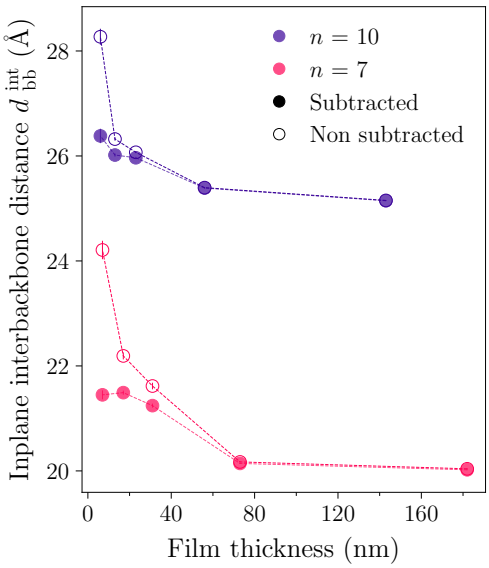

Figure 4.21: In-plane correlation lengths between backbones in the vicinity of the interface for **PC$_7$VImTFSI** and **PC$_{10}$VImTFSI** thin films for varying film thickness, calculated as $2\pi/q_{bb}$ with q_{bb} the correlation peak position on subtracted signals of Figure 4.20a and 4.20b (•) and unsubtracted ones (∘).

influence of this signal and therefore its subtraction can be neglected. Nevertheless, the observation of an increasing interbackbone correlation length with decreasing film thickness holds, as both the subtracted and unaltered data exhibit the same trend and represent respectively the lower and upper bounds for the true substrate-independent value. Therefore, a confinement effect also occurs in-plane.

4.6 Conclusion on the molecular picture and perspectives

A combined use of XRR and GIWAXS provides a characterization of spin-coated **PC$_n$VImTFSI** thin films' structure in both in-plane and out of plane directions. Through conventional fitting of XRR data and additional analysis of their Fourier transform, it was shown that **PC$_n$VImTFSI** for $n = 2$ and 4 form homogenous thin films. Increasing n to 7 and 10 leads to a spontaneous layered structure which exhibits a decreasing interlayer spacing with decreasing film thickness. Concurrently, the in-plane distance between neighbouring chains, or interbackbone correlation length d_{bb}^{in}, increases. We summarize the measurements of these characteristic distances in Figure 4.22a and 4.22b. Interlamellar distances of the thinnest and thickest films, respectively determined by direct fitting and Fourier transform analysis of XRR data, are consistent. Some deviation from the general trend is observed for the Fourier transform estimation on the thinnest films. This may be explained by the small number of layers in the lamellar structure, in other words less spacial periods for the Fourier transform to sample, hence impairing the accuracy of the method. A overall trend of decreasing z_{inter} with film thickness is nonetheless observed.

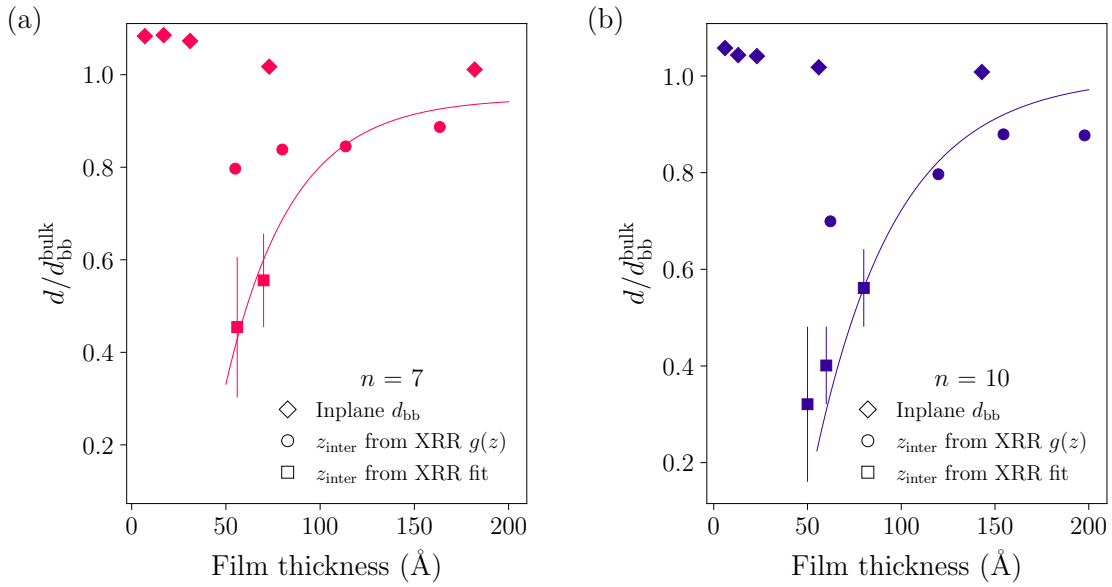

Figure 4.22: Summary and comparison of the in-plane interbackbone distance measured in GIWAXS (◊) and the interlamellar distance extracted from the SLD profiles obtained by XRR data fitting (□) and their Fourier transform analysis (○) as function of film thickness for **PC_7VImTFSI** (a) and **PC_{10}VImTFSI** (b) thin films. All lengths are normalized by the interbackbone correlation lengths d_{bb} measured in bulk. Solid lines are guides for the eye.

In light of these results, a possible interpretation is the preferential alignment of imidazolium groups parallel to the interface as the thickness decreases. A scheme of such behaviour is represented in Figure 4.23a. The decrease of the in-plane d_{bb}^{in} distance substantiates our interpretation. If imidazolium groups tend indeed to align with the substrate, the long side chains would overcrowd the in-plane region, thus forcing the backbones apart. An illustration of such behaviour is also given in Figure 4.23b.

Imidazolium ILs were themselves reported exhibiting this type of preferential alignments with an electrified substrate, depending on its surface charge [170]. What is explained by electrostatic interactions with the substrate, in the case of ILs, stems, in the present case, from steric effects since only the thickness of the film changes and not the surface charge. Nevertheless, electrostatic interactions with the substrate may also slightly vary, as anion mobility was shown to decrease with the thickness of the film due to a stronger charge-substrate interactions [57] and not only to the slowing down of segmental dynamics as for neutral polymers [171].

The chemistry of the surface should play an important role in these observations. Seeking to observe such effect, we coated the silicon wafers with a gold layer by sputtering. Unfortunately two issues hindered the use of these results. The spurious signal of gold was too intense and the coated layer was of rather poor quality because of the weak interaction between silicon and gold. A coating of better quality should be obtained by evaporation deposition of gold on an intermediate layer of chromium.

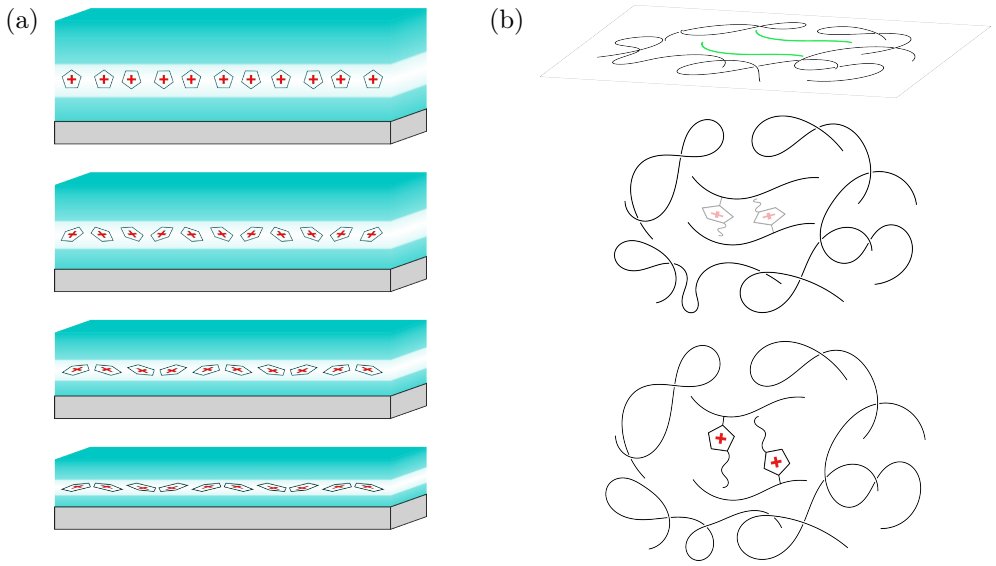

Figure 4.23: Schematic representation of the molecular picture of the confinement effect. Side view of a $\mathbf{PC}_n\mathbf{VImTFSI}$ thin film (a) represented in blue. Monomers of a single layer depleted in anions are represented without their side chains. Thickness of the film decreases from top to bottom. A top view of the near interface region is represented in (b). Top sketch highlights the two backbones considered. Thickness of the film vary from top to bottom.

Chapter 5

Self-assembled Poly(ionic liquid) nanoparticles

The purpose of this chapter is to present a side project of the present work on nanoparticles (NP) obtained by dispersion polymerization of IL monomers. As opposed to the solution polymerized PILs considered so far, the following systems rely on water as a selective solvent, in which the precursor IL monomers are soluble but not the resulting PIL. Consequently, self-assembly of the resulting PIL drives the formation of structured NPs in suspension. This constitutes a project led by E. Drockenmuller[1] in collaboration with the group of A. Leforestier[2] for electron microscopy imaging performed together with J. Degrouard. Our contribution to this project was investigating the inner structure of these nanoparticles by means of X-ray scattering. We briefly detail, in the following, what has been reported on PIL nanoparticles, which was left out of the introductory considerations of Chapter 1, concurrently emphasizing yet another potential application of PILs.

5.1 Dispersion polymerization and self assembled nanoparticles

Diverse synthetic methods such as emulsion and dispersion polymerization [172], or intramolecular cross-linking [173] lead to self-assembled polymer nanoparticles [174]. Most of these strategies have been directed towards controlling their dimension, exterior morphology and surface functionality. However, there has been an increasing demand for NPs with well-defined inner structures for applications such as encapsulation, transport, and drug delivery [175, 176]. Simultaneous control of size, shape and internal morphology in a single nanoscopic material remains a major challenge in polymer materials.

5.1.1 PILs as promising candidates for inner structured particles

Given their interesting local structure in bulk alone and the large panel of available chemical structures, PILs appear once again as a solution. The nanoscale

[1]Université Lyon 1, CNRS, Laboratoire d'Ingénierie des Matériaux Polymères, UMR 5223, Lyon, France

[2]Université Paris-Saclay, CNRS, Laboratoire de Physique des Solides, UMR 8502, Orsay, France

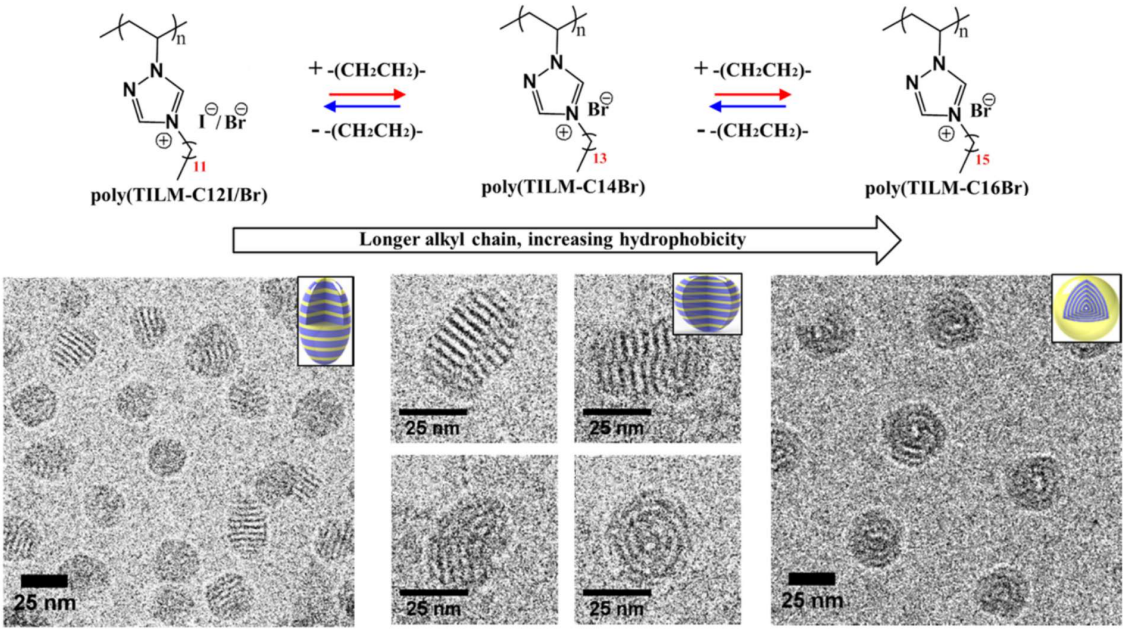

Figure 5.1: Top: chemical structures of triazolium-based PILs with varying side chain length, from left to right n = 12, 14, 16, investigated by W. Zhang *et al.*. Bottom: corresponding representative cryo-EM images of the obtained nanoparticles in aqueous solutions. Insets show schematics of the inferred morphologies. Adapted from ref. [126]

segregation of apolar moieties, in such a restricted environment, could open avenues for such structured particles since it can be easily tuned by the chemical structure. Using imidazolium homopolymer PILs, J. Yuan *et al.* observed onion shaped multilamellar vesicles for side chains of 12 carbon units but unilamellar ones for 18 [43]. Other structures have been achieved since then like wasp-like lamellar ellipsoids [126, 177], shown in Figure 5.1, obtained by W. Zhang *et al.* using triazolium based PILs. The authors also observed onion shaped morphologies and attributed the structure selectivity to the PIL hydrophobicity. Short side chains, slightly more hydrophilic, allow for wasp-like structures with some contact between apolar moieties and the surrounding water. As side chains are lengthened, their hydrophobicity increases and the multilamellar vesicle morphology is preferred as it prevents any contact of the hydrophobic part with water. K. Manojkumar *et al.* reported a switch from unilamellar to bilamellar vesicles by adding a phenyl group to the side chains of methacrylamide based PILs containing different alkylimidazolium bromide groups [178]. The authors also demonstrated their dye encapsulation and transfer properties from aqueous to organic phases. Increasing the concentration of precursor IL monomers can also lead to one dimensional superstructures with an extended multilamellar inner structure, designated as nanoworms [43].

5.1.2 Synthesis of triazolium based PIL nanoparticles

We only give in this section the main outlines of NP synthesis, additional details are given in Chapter 2. We consider a series of six 1,2,3-triazolium chloride ILs monomers having polymerizable groups, acrylate, methacrylate and methacry-

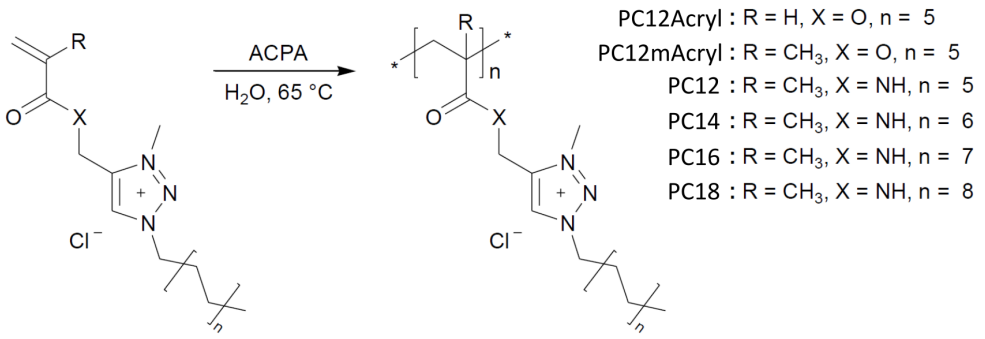

Figure 5.2: Chemical structures of PIL obtained by precipitation polymerization of aliphatic 1,2,3-triazolium chloride ionic liquid monomers in water.

lamide respectively denoted in the following $\mathbf{C_{12}Acryl}$ $\mathbf{C_{12}mAcryl}$ and $\mathbf{C}_n$. The latter methacrylamide IL monomer was synthesized with varying alkyl side chain length on the N-1 position including dodecane $n = 12$, tetradecane $n = 14$, hexadecane $n = 16$ and octadecane $n = 18$. The chemical structures of the IL monomers are given in Figure 5.2 and were synthesized in three steps, including :

- Copper (I)- catalyzed azide-alkyne cycloaddition (CuAAC) ligation between aliphatic azides and either propargyl acrylate, propargyl methacrylate or propargyl methacrylamide, all of them commercially available.
- N-alkylation of the resulting 1,2,3-triazole group with iodomethane.
- ion-exchange to substitute iodide for chloride counter anions.

The aim of the last ion exchange step is only to improve the solubility of the monomer in water, which quite surprisingly was rather poor with iodide counter anions.

The free radical dispersion polymerization of the chloride functionalized monomers was then carried out in aqueous solutions at 65 °C for 16 h, initiated by ACPA at a concentration of 0.05 w% delivering the corresponding suspension of triazolium based PILs nanoparticles. Chemical structures are given in Figure 5.2

5.1.3 Particle size

Several monomer concentrations of 10 mM, 18 mM, 25 mM and 50 mM were tested in order to find out the appropriate one. Turbidity of suspensions resulting from concentrations above 25 mM suggests precipitation occurred during the polymerization. However, when conducted at 25mM or less, it provided translucent and stable suspensions for acrylate $\mathbf{PC_{12}Acryl}$ and methacrylate $\mathbf{PC_{12}mAcryl}$ based NPs. Particle sizes in these suspensions were measured by dynamic light scattering (DLS) and the number average hydrodynamic diameters D_h are given in Table 5.1 and plotted in Figure 5.3a against the monomer concentration. Their evolution over time is additionally given in Figure 5.3b and the full particle size distributions in Chapter 2. The particles' diameter were larger than intended for $\mathbf{PC_{12}Acryl}$ and $\mathbf{PC_{12}mAcryl}$ NPs, possibly due to the partially or fully hydrophobic nature of

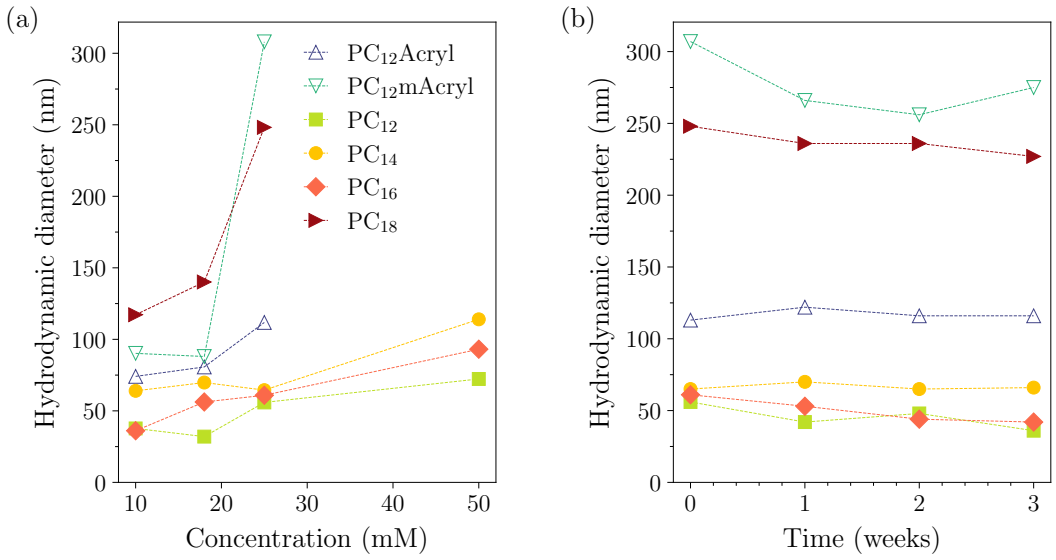

Figure 5.3: Hydrodynamic diameter of poly((1,2,3-triazolium chloride) nanoparticles against monomer concentration (a) and time after polymerization of 25 mM solutions (b).

acrylate and methacrylate backbones, hence a less soluble compound and stronger self-assembly. The interest in the methacrylamide series $\mathbf{PC}_n$ aimed at introducing a hydrophilic backbone, which proved efficient in reducing the size of resulting NPs. Over time, the suspensions were stable for side chain lengths of 12 to 16. $\mathbf{PC}_{18}$ polymerization exhibited precipitation or resulted in highly turbid dispersions even at 10 mM, thereby preventing subsequent characterizations.

We focus, in the following, on the structural investigation of NPs obtained by dispersion polymerization of IL monomers at a concentration of 25 mM, for which particle sizes are similar across the series and suspensions were stable and did not precipitate. We report Transmission Electron Microscopy (TEM) performed by H. Thankappan[1] with A. Leforestier and J. Degrouard[2] to unveil the shapes of such particles. Our contribution is presented afterwards, providing additional details on the inner structure of said particles using X-ray scattering (WAXS).

5.2 Structural characterization of PIL nanoparticles

5.2.1 Transmission Electron Microscopy

Since our contribution to the present project did not involve these electron microscopy experiments, we will not detail the full principle of the technique. We simply recall that it relies on the interactions of a focused beam of electrons with

[1]Université Lyon 1, CNRS, Laboratoire d'Ingénierie des Matériaux Polymères, UMR 5223, Lyon, France

[2]Université Paris-Saclay, CNRS, Laboratoire de Physique des Solides, UMR 8502, Orsay, France

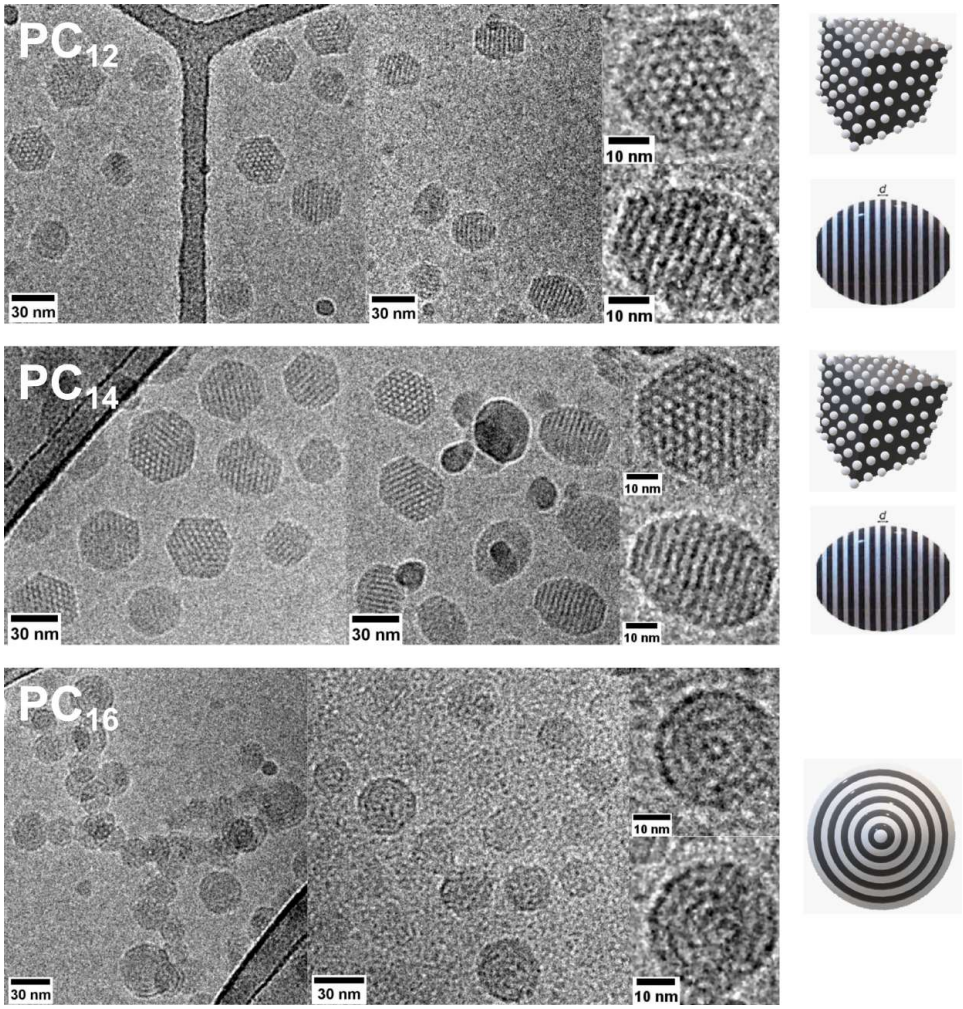

Figure 5.4: Representative cryo-TEM images of PIL nanoparticles obtained by dispersion polymerization of triazolium functionalized acrylamide IL monomers with varying side chain length in aqueous solutions at a concentration 25 mM (from top to bottom : $\mathbf{C}_{12}$, $\mathbf{C}_{14}$, $\mathbf{C}_{16}$). Last panel on the right are representations of the observed structures, wasp-like multilamellar ellipsoids and cubosomes for $\mathbf{PC}_{12}$, $\mathbf{PC}_{14}$ NPs and onion-like multilamellar vesicle for $\mathbf{PC}_{16}$.

a sample. Electrons considerably enhance resolution, as it is limited by the wavelength of the beam used. At an accelerating voltage of 80 kV, an essential experimental parameter in TEM, an electron has a wavelength of 4 pm, hence 5 orders of magnitudes shorter than visible light.

Electron microscopy images were obtained on a Philips CM120 electron microscope at an accelerating voltage of 80 kV. Samples for TEM were prepared by placing a drop of dispersion (1 mg/mL) onto a Formvar-coated copper grid. The excess solution was carefully removed using a filter paper and samples were dried for a few minutes before analysis. For cryo-TEM, 4 μL of sample solution was deposited onto a holey carbon grid (Quantifoil R2/2) and subsequently vitrified in liquid ethane cooled by liquid nitrogen using a Vitrobot Mark IV (Thermo Fisher Scientific).

Representative cryo-TEM images for the acrylamide based series $\mathbf{PC}_n$ are given

Sample	D_h (nm)	d_{WAXS} (Å)	d_{TEM} (Å)
PC_{12}Acryl	112	34.9	/
PC_{12}mAcryl	308	35.0	/
PC_{12}	56	35.2	32.0
PC_{14}	64	39.5	39.4
PC_{16}	61	43.9	43.9
PC_{18}	248	/	/

Table 5.1: Hydrodynamic diameter D_h and inner correlation length d_{WAXS} and d_{TEM} respectively determined using WAXS patterns and cryo-TEM images for poly((1,2,3-triazolium chloride) nanoparticles.

in Figure 5.4. $\mathbf{PC_{12}}$ and $\mathbf{PC_{14}}$ systems exhibit rather similar structures. Both PILs form multilamellar wasp-like ellipsoids, as mentioned above for vinyl triazolium based PILs with alkyl chains of similar length in previous reports [126]. In contrast with these systems, however, these structures coexist, in the present suspensions, with cubic arrangements of segregated apolar globules referred to as cubosomes. When side chains are lengthened to 16 carbon units, only onion like lamellar vesicles are observed. Interestingly, W. Zhang *et al.* almost observed such cube shaped particles on their vinyl triazolium PILs. Some of their onion-like vesicles presented vague facets, but not as well-defined as the acrylamide based particles shown here. The authors attribute such straightening of the vesicles curvatures to the crystallization of the alkyl side chains [126] which they confirm by DSC on dried samples.

All these inner structures have in common that they possess a characteristic length hereafter referred to as d. It is estimated in the present systems through image analysis of grey levels across the particles and denoted d_{TEM}. We report the corresponding values in Table 5.1. However, these represent a measurement on carefully chosen particles. To access an averaged value and characterize more accurately the inner structure at these length scales, we combine these results with X-ray scattering.

5.2.2 WAXS

Wide Angle X-ray Scattering measurements were performed on aqueous dispersions of PIL nanoparticles. Solutions were stored in flame-sealed borosilicate capillary tubes of 1.5 mm in diameter and placed on the sample holder. The same setup as for WAXS experiments on bulk synthesized PIL in Chapter 3 was used, involving a Xeuss 2.0 diffractometer (Xenocs) equipped with a Genix 2D Cu HF source (λ = 1.542 Å) and a Pilatus 1M detector placed at 543 mm from the samples. A second sample-to-detector distances of 1181 mm was used to increase the Q-range available in an attempt to capture the shape of the particles. The standard corrections were applied for sample volume, X-ray transmission, empty cell signal, and detector efficiency to the raw signal, as detailed in Chapter 3, to obtain the scattering spectra in absolute units.

A correlation peak stands out on the WAXS patterns of the NP series of Figure 5.5 at a Q-value around 0.17 $\mathrm{Å}^{-1}$. The correlation peak was fitted using a Lorentzian peak function and the corresponding correlation lengths were calculated as d_{WAXS} =

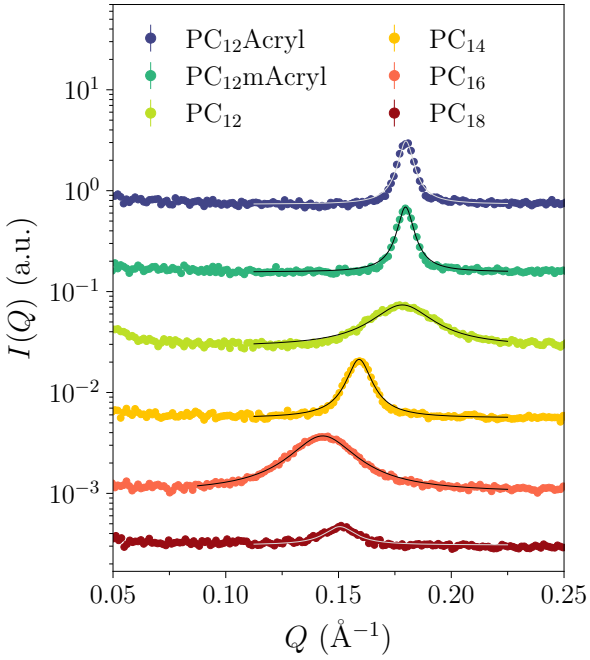

Figure 5.5: Wide-angle X-ray scattering patterns of aqueous dispersions of 1,2,3-triazolium based PIL nanoparticles. Data are shifted vertically for clarity. Fits of the correlation peaks using a Lorentzian peak function are shown as solid black lines.

$2\pi/Q_{\text{peak}}$ for every sample. Values are given in Table 5.1 alongside the estimation from cryo-TEM images and show very good agreement. This length corresponds to the inner characteristic length d mentioned above. It is either an interplanar spacing in wasp-like and onion-like structures or the square lattice parameter of the cubosomes. We report the d_{WAXS} length for all samples on a side chain length axis in Figure 5.6. The values are remarkably similar for $n = 12$ regardless of the backbone chemistry and consequently the particle size. The inner structure of the particles is thus controlled by the side chain length. The linear trend of $d_{\text{WAXS}}(n)$, with a slope around 2.2 Å per added carbon unit, suggests side chains are stretched and only slightly interdigitating. Although variation is observed in the increasing rates reported for bulk synthesized PILs due to different organization inside the apolar domains, values around 1.3 Å/CH_2 are usually reported [32, 33, 35]. It appears here that the constraints of the nanoparticle's structure prevents such interdigitation of side chains in the inner structure. Regarding the amplitude and the width of the correlation peaks, there are observable differences. However, they are rather difficult to discuss because they might stem from several physical parameters. An increase in the amplitude, for instance, can be due to either an increase in the particles' size, which then present more lamellae, a higher concentration or a more ordered inner structure. Therefore, the WAXS data alone do not allow us to conclude on the differences observed on the peak's shape.

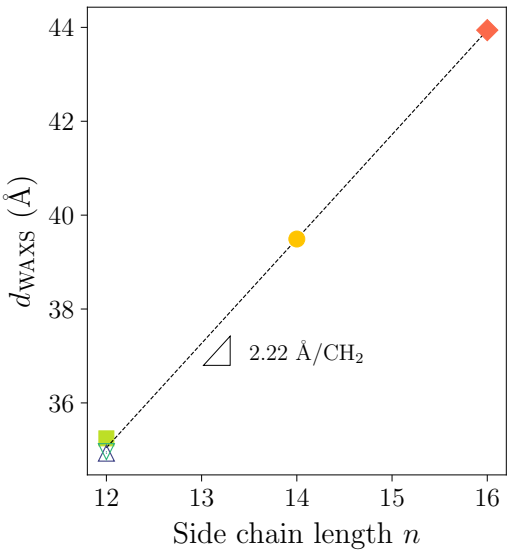

Figure 5.6: Correlation lengths as estimated from the fits of the WAXS signals from aqueous solutions of acrylate **PC$_{12}$Acryl**, methacrylate **PC$_{12}$mAcryl**, and methacrylamide **PC$_n$** 1,2,3-triazolium PIL nanoparticles as a function of alkyl chain length.

5.3 Polymerization kinetics

In an attempt to follow the polymerization kinetics, glass tubes containing identical 25 mM aqueous solutions of 1,2,3-triazolium chloride monomers **C$_{12}$** and **C$_{16}$** and ACPA initiator at a concentration of 0.05 w% were prepared and sealed under vacuum. Each tube was then heated at 70 °C in an oil bath for a given amount of time (2, 4, 6, 15.5, 26 hours). Once the selected polymerization time elapsed, the tube was cooled down to room temperature under cold running water, thereby quenching the sample and interrupting the polymerization. Glass capillary tubes of 1.5 mm in diameter were then filled with the partially polymerized suspensions, flame-sealed and measured using WAXS. The resulting patterns are reported in Figure 5.7a and 5.7b for 12 and 16 side chain lengths, respectively. We also made sure that no further polymerization occurred on the quenched sample at room temperature by performing subsequent measurements 24 h after the quenching. These second acquisitions are represented in Figures as magenta points. Their good overlap suggests no evolution of the structure, at least at these length scales, hence confirming polymerization does indeed stop after cooling down to room temperature.

For both **PC$_{12}$** and **PC$_{16}$**, the initial WAXS patterns exhibit a rather smooth bump which may originate from the aggregation of IL monomers in small droplets which sizes are not measurable here. Upon polymerization, the correlation peak emerges clearly, resulting from the formation of the inner structure of the particles. According to our data, complete polymerization of PIL NP occurs after 2 h for **PC$_{16}$** and 15 h for **PC$_{12}$**. It remains unclear why these two characteristic times are so different. It may relate to a very different reactivity of the initial monomers or to different oxygen contents remaining in the sealed tubes and hindering polymer-

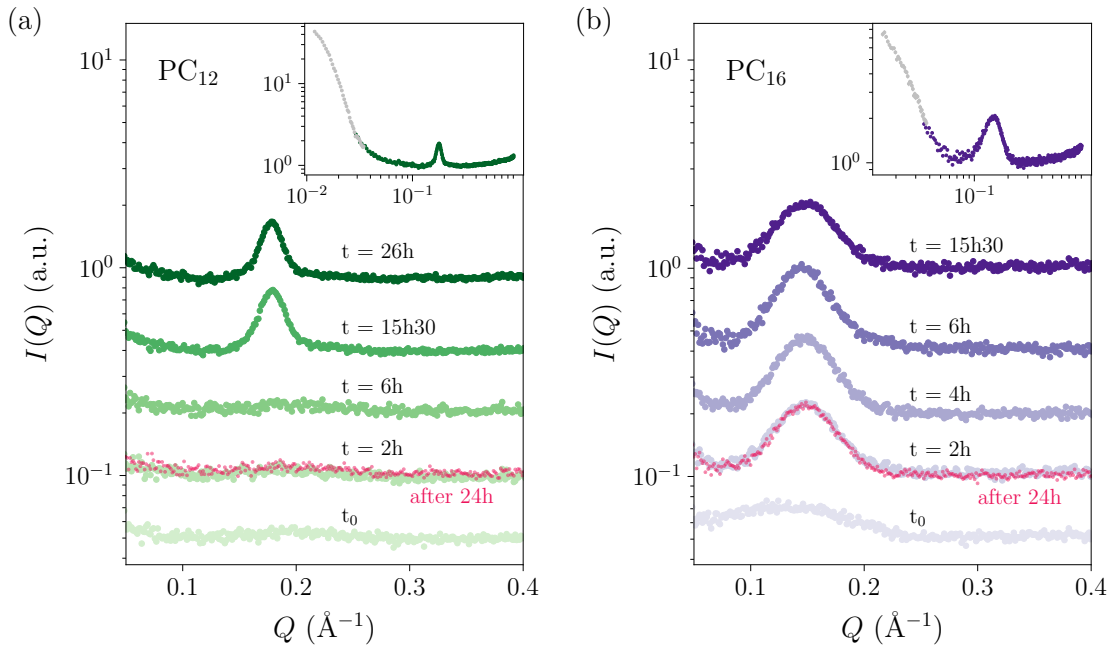

Figure 5.7: Evolution of WAXS patterns during the dispersion polymerization at 70 °C of 25 mM aqueous solutions of acrylamide based 1,2,3-triazolium chloride monomers $\mathbf{C}_{12}$ and $\mathbf{C}_{16}$. Data are shifted vertically for clarity. Magenta points represent the WAXS pattern of the sample polymerized 2 hours after 24 hours at room temperature. Insets show the superposition with the scattering pattern acquired at a larger sample-to-detector distance.

ization.

Still on Figures 5.7a and 5.7b, we extend the Q range in the inset by showing the pattern acquired at a larger sample-to-detector distance for the longest polymerization times. As a reminder, lower Q-values probe larger length scales, such as the shape and size of the particle in the present situation. A slight variation of the upturn observed at low-Q suggests changes in the particle size could be captured by X-ray scattering during the polymerization, as should be expected. Unfortunately, the solutions were too dilute and did not scatter enough to have a decent signal-to-noise ratio in that Q-range or access even lower Q values, estimate the form factor of NPs and follow their shape during polymerization. This would nonetheless be possible using a synchrotron light source. The high flux it provides would considerably shorten the acquisition times, and the polymerization could be followed both *in situ* and at earlier polymerization times with good accuracy.

5.4 Conclusion on PIL nanoparticles

A series of acrylate, methacrylate and methacrylamide dispersion polymerized triazolium based PILs was investigated by a combined use of DLS, cryo-TEM and WAXS. Due to a higher hydrophilicity of methacrylamide backbones, corresponding NPs are smaller and their sizes show little variation with monomer concentration, time and side chain length n. The latter controls the inner structure of NPs, tran-

sitioning from a mixture of wasp-like ellipsoids and cubosomes for $n = 12$ and 14 to multilamellar onion-like vesicles for $n = 16$. The characteristic length of such structures is independent of the backbone's chemistry and, therefore, of the particle's size. However, the slope of $d(n)$ suggests a strongly diminished interdigitation of side chains compared to bulk synthesized PILs.

These results are interesting for nanoparticles chemistry alone but also in the scope of the present work. The nanoscale segregation inherited from ILs has deep implications on the local structure of their polymerized counterparts, as we showed both in bulk and at interfaces in the previous Chapters 3 and 4. Self-assembly upon dispersion polymerization appears to be yet again controlled by a complex balance between hydrophilic and hydrophobic parts. Not only does the side chain length influence the local structure, *i.e.* particles' inner structure, as it did before, but also the overall shape of the particle. This type of tunable inner structured NPs can pave the way to engineer nanomaterials and precisely tune their structure. On a fundamental note, such particles can be viewed as another confinement geometry. As such, the shape and size of the particle also affect the local structure of PILs as illustrated by the pronounced change in side chain interdigitation compared to the bulk.

Chapter 6

Viscoelastic properties

This chapter redirects the focus on solution polymerized bulk PILs to present some results on the dynamics of an identical **PC$_n$VImTFSI** series with varying side-chain length investigated in Chapters 3 and 4. As explained in Chapter 1, a lot can be understood on the structure of PILs in light of their comparison with their IL counterparts. It is mostly governed by the ionic and solvophobic interactions which also confers ILs with their specific properties and structure, both in bulk and at interfaces. The same high density of charges is also expected to affect the viscoelastic behaviour of PILs. By means of the controlled synthesis of our **PC$_n$VImTFSI** series, the effect of the side chain length, hence of the polarity of interactions itself, on such properties can be precisely probed with a fixed degree of polymerization and dispersity along the series. The polymeric nature of PILs, which ILs alone cannot help predict, calls for a comparison with ion-containing polymers such as ionomers. Although they were introduced in Chapter 1, we detail more thoroughly their behaviour after giving a brief reminder of the concept of viscoelasticity and rheological measurements. Just like in Chapter 3 and 4, readers familiar with linear viscoelastic measurement techniques can skip to section 6.2 for specificities on viscoelastic models of polymeric systems, section 6.3 for those of associating polymers, or section 6.4 for the results of the present work on the imidazolium based PIL series.

6.1 Principles of rheology

The notion of viscoelasticity progressively appeared in the second half of the 19$^{\text{th}}$ century when materials such as gum rubber or silk showed an instantaneous relaxation to an applied load, either in shear or torsion, followed by a slower one at longer times [179]. This time-dependent response characterizing viscoelasticity is typical of polymeric materials.

6.1.1 Step strain and stress relaxation

A rheology experiment consists in applying a deformation, the strain γ and measuring a stress σ, or the other way around, as schematically represented in Figure 6.1a. Two aspects are noteworthy, the first one is the difference in behaviour between a viscous liquid, an elastic solid and viscoelastic fluids and solids. All comes down to their relaxation to the applied strain. A viscous liquid relaxes as soon as the strain is constant, while an elastic solid does not, and the stress remains proportional

to the strain by Hooke's law. Viscoelastic materials relax exponentially, either as a fluid to zero stress or to an equilibrium stress reminiscent of an elastic solid nature. Quite intuitively, the stress σ depends on the strain γ. To address this, the stress relaxation shear modulus is defined as:

$$G(t) = \frac{\sigma(t)}{\gamma} \tag{6.1}$$

In doing so, all data collapse as long as the strain remains below a threshold value γ_c delimiting the linear response of the material. We focus on this small strain regime in the following and will verify this condition in the experimental part as well.

It can be noted that equation 6.1 is somewhat a time dependent generalization of Hooke's law for elastic solids $\sigma = E\varepsilon$ in which E is the Young modulus and ε the extension, equivalent to γ in an uniaxial stretch experiment. Newton's law provides an equivalent of the shear modulus G for simple liquids with their viscosity being $\eta = \sigma/\dot{\gamma}$, the strain rate $\dot{\gamma}$ replacing the strain.

Both elastic solid and viscous liquid behaviours are captured in the simplest viscoelastic model, the Maxwell element, depicted in 6.1a. As viscous and elastic elements are in series, the total strain is simply the sum of the strains γ_v and γ_e. Each of the elements also bears the same stress $\sigma = G_M\gamma_e = \eta_M\dot{\gamma}_v$. The ratio of the viscosity of the viscous element η_M and the modulus of the elastic one G_M is homogenous to a time and defines the relaxation time of the Maxwell element as:

$$\tau_M = \frac{\eta_M}{G_M} \tag{6.2}$$

If a Maxwell element is subject to a step strain, the total strain γ is kept constant. From the above considerations, it comes that the strain in the viscous element verifies:

$$\tau_M\dot{\gamma}_v(t) = \gamma - \gamma_v(t) \tag{6.3}$$

Considering all the strain is initially in the elastic element, meaning $\gamma_v(t = 0) = 0$, and the above equation is verified by:

$$\gamma - \gamma_v(t) = \gamma \exp\left(-\frac{t}{\tau_M}\right) = \gamma_e(t) \tag{6.4}$$

Then the stress relaxes exponentially with a characteristic time τ_M:

$$\sigma(t) = G_M\gamma \exp\left(-\frac{t}{\tau_M}\right) \quad \text{and} \quad G(t) = \frac{\sigma(t)}{\gamma} = G_M \exp\left(-\frac{t}{\tau_M}\right) \tag{6.5}$$

The above solution is true for a viscoelastic liquid, for which the stress relaxes to zero. For viscoelastic solids, the asymptotic non-zero value is called the equilibrium shear modulus G_{eq}. The relaxation times τ are fundamental properties of viscoelastic materials. Polymers exhibit multiple ones which can be attributed to molecular events, which we will discuss later on, and are a precious way to understand their specificities.

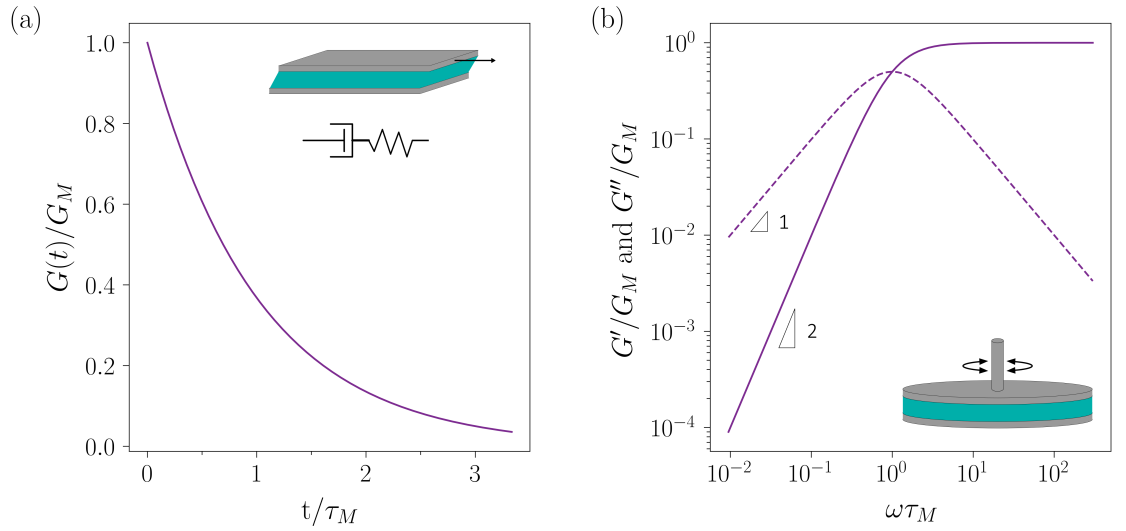

Figure 6.1: Linear viscoelastic response of a Maxwell element, as represented as inset in (a). Stress relaxation modulus $G(t)$ in the time domain (a) and dynamic moduli $G'(\omega)$ and $G''(\omega)$ in the frequency domain (b). Schematic representations of simple shear and oscillatory shear experiments are respectively given as insets in (a) and (b)

In order to model the first observations of viscoelastic behaviour, Boltzmann suggested in 1876 that the stress originating from any strain profile is a linear combination of the response to small step strains $\delta\gamma_i$ applied at time t_i, implying that, in the linear regime, every step strain response is independent. The past deformations are remembered by the modulus $G(t)$. By definition, the elementary step strain can be expressed in terms of strain rate $\delta\gamma_i = \dot{\gamma}_i \delta t_i$. By summing every increment in a smooth strain history, the stress becomes :

$$\sigma(t) = \int_{-\infty}^{t} G(t-t')\dot{\gamma}(t')dt' = \int_{0}^{\infty} G(s)\dot{\gamma}(t-s)ds \tag{6.6}$$

From the first step in the above relation unfolds that the stress in the material is a result of all past deformations [2]. The second step was made with the transformation $s = t - t'$. This constitutive equation provides the basis for the modelling of any experiment in the linear regime. One of them is steady shear in which the strain rate $\dot{\gamma}$ is kept constant, incidentally simplifying equation 6.6 in which $\dot{\gamma}$ can be pulled out of the integral.

6.1.2 Oscillatory shear in the linear regime

We focused, in the above, on step strain experiments, in which the strain is kept constant, and mentioned the simple shear. Let us nonetheless move on to a more common experiment in the study of polymeric materials : oscillatory shear. Instead of imposing a constant or linearly increasing strain, the sample is deformed sinusoidally, as represented as inset of Figure 6.1b and the strain is then:

$$\gamma(t) = \gamma_0 \sin(\omega t) \tag{6.7}$$

After some short transient state over a few cycles, the stress also oscillates at the same frequency ω. For a linear elastic solid, the stress is directly proportional to the strain, hence both oscillate in phase. For a pure viscous liquid, the stress is proportional to $\dot{\gamma}$ and, as such, oscillates out of phase. Intuitively, it can be generalized that for a viscoelastic material, stress and strain oscillate with a phase shift δ such that :

$$\sigma(t) = \sigma_0 \sin(\omega t + \delta) \tag{6.8}$$

Since the stress oscillates at the same frequency ω it can be separated into two orthogonal functions oscillating at ω, one in phase with the strain, the other out of phase:

$$\sigma(t) = \gamma_0 G'(\omega) \sin(\omega t) + \gamma_0 G''(\omega) \cos(\omega t) \tag{6.9}$$

We introduce this way the storage $G'(\omega)$ and loss $G''(\omega)$ moduli, related to the stress relaxation modulus in the time domain by sine and cosine transforms respectively. As such, we can calculate the dynamic moduli G' and G'' for a Maxwell element from the stress relaxation modulus given in equation 6.5 :

$$G'(\omega) = \frac{G_M \omega^2 \tau_M^2}{1 + \omega^2 \tau_M^2} \quad G''(\omega) = \frac{G_M \omega \tau_M}{1 + \omega \tau_M^2} \tag{6.10}$$

Representation of such functions are given in Figure 6.1b. The relaxation time τ_M appears as the threshold between a solid-like behaviour at high frequency, *i.e.* short times, and a liquid-like one at low frequency, *i.e.* long times. Oscillatory shear is a very convenient way of probing viscoelastic properties of materials, since a simple change of the frequency ω shifts the observable time scales to roughly $1/\omega$. It is particularly useful to accurately measure the material behaviour at short times, which simple shear can hardly capture. Another way of changing the timescale is to vary temperature, which will be discussed below in section 6.2.3 after introducing the main models of polymer viscoelasticity.

6.2 Rheology of neutral polymers

From the increasing demand for polymer materials in the second half of the 20$^{\text{th}}$ century came the need to understand and control the processing of polymer melts. Based on early works including that of W. Kuhn [180] and later on P.J. Flory [131], discussed in Chapter 3, and W.H. Stockmayer [181] concerning the shape and size of polymer chains arose the question of their dynamics. To tackle such a fundamental question, single-chain models were first derived by P.E. Rouse [182] and B.H. Zimm [183] in the 1950s to describe the dynamics of short, *i.e.* unentangled, polymer chains, which will be our primary focus. After detailing such models, a brief word will be given on entangled polymers before adding association point between chains, hence introducing the field of associating polymers and their respective models.

6.2.1 Rouse model of unentangled chains

Monomers as diffusing beads

A polymer coil can be mapped by a chain of beads connected by springs. In the case of a melt, we consider the fluid made of other chains flows freely around a diffusing bead of radius a and omit for the moment it is connected to other beads. Its motion is then governed by diffusion laws, and we only recall here that its mean-square displacement is linear in time t with the prefactor being the diffusion coefficient D of the particle. The diffusion coefficient is given by Einstein's relation as a balance between kT, the driving force of Brownian motion, and the drag force opposing it, accounted for by a friction coefficient ζ :

$$D = \frac{kT}{\zeta} \tag{6.11}$$

The friction coefficient can be calculated in simple cases such as a hard particle in a fluid of viscosity η by Stokes' law $\zeta = 6\pi\eta a$. A way to estimate the timescale of its motion is to calculate the time it takes the particle to diffuse over its own radius :

$$\tau_0 \sim \frac{a^2}{D} \sim \frac{a^2\zeta}{kT} \tag{6.12}$$

Let us consider now the succession of N beads connected by springs, as first proposed by P.E. Rouse in 1953 [182]. The total friction coefficient of the chain in such model is then $\zeta_\mathrm{R} = N\zeta$. Using ζ_R in equation 6.11 gives the diffusion coefficient of the whole chain D_R. The Rouse time τ_R required for the polymer coil to diffuse over its own radius R is then:

$$\tau_\mathrm{R} \sim \frac{R^2}{D_\mathrm{R}} \sim \frac{R^2}{kT/(N\zeta)} \sim \frac{\zeta}{kT} N R^2 \tag{6.13}$$

As discussed in Chapter 3, polymer chains are fractal objects, hence their radius scales as their length by a power law $R \sim aN^\nu$ with the inverse of the fractal dimension $\nu = 1/2$ for a linear polymer melt. Simple mathematical considerations relate the Rouse time to the monomer relaxation time by $\tau_\mathrm{R} \sim \tau_0 N^2$.

A few years later, B.H. Zimm proposed an extension to this model, accounting for hydrodynamic interactions between the beads and the fluid [183]. For polymer melts these considerations are not necessary, but they are more accurate to describe dilute solutions. The Zimm model will not be discussed further in the present work.

Rouse modes

The shortest τ_0 and longest τ_R relaxation times are given above in equations 6.12 and 6.13 and correspond to the monomer and chain relaxation times respectively. Since a polymer chain is self similar, a portion of the chain relaxes the same way as the whole chain. Therefore, the dynamics of a polymer chain can be subdivided into N relaxation modes, with mode p being the relaxation of a portion of the chain composed of N/p monomers. This implies that at a time $t = \tau_p$ after a step strain solicitation, modes of index higher than p, meaning portions of the chains shorter

than N/p monomers, have relaxed, but longer portions of the chain have not. Each portion of N/p monomers, of number density $\phi/(Na^3/p)$, then contributes to the stress relaxation modulus by an energy kT. Given that the index p is related to τ_p by $\tau_p \sim \tau_0(N/p)^2$, it comes :

$$G(t) \approx \frac{kT}{a^3}\phi \left(\frac{t}{\tau_0}\right)^{-\frac{1}{2}} \exp\left(\frac{t}{\tau_R}\right) \tag{6.14}$$

wherein the last term is an added exponential cut-off, accounting for the liquid-like terminal relaxation. It comes from this approximation that the Rouse model exhibits a $-1/2$ exponent in the transition region and consequently $1/2$ in the frequency domain. The exact calculation leads to a stress relaxation modulus written as a succession of Maxwell element relaxations, such that:

$$G(t) = kT\frac{\phi}{Na^3}\sum_{p=1}^{N} \exp\left(-\frac{t}{\tau_p}\right) \quad \text{with} \quad \tau_p = \frac{\zeta a^2 N^2}{6\pi^2 kT p^2} \tag{6.15}$$

6.2.2 Reptation of entangled chains

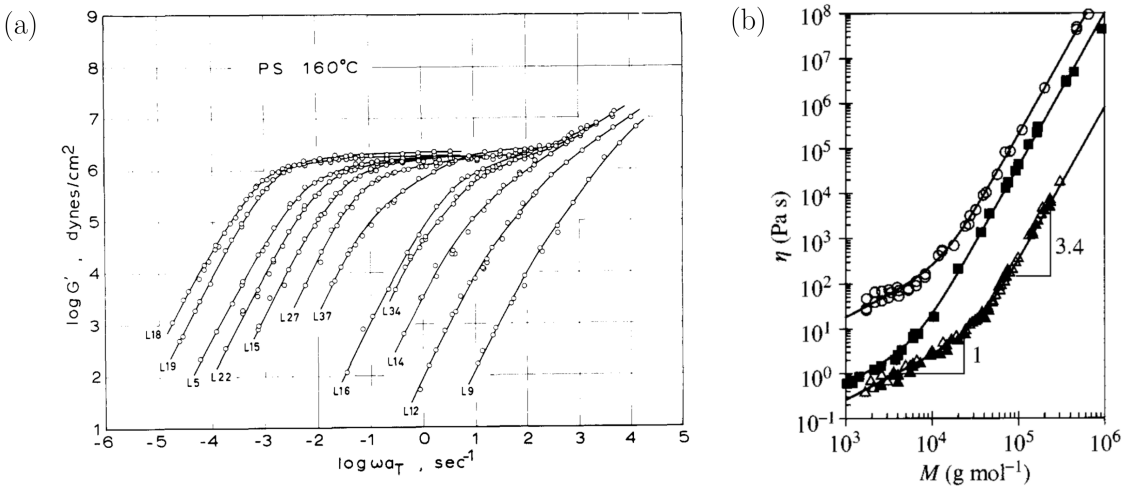

Figure 6.2: (a) Storage modulus G' for polystyrene of varying molecular weight (increasing from right to left) taken from ref. [184]. (b) Viscosity against molecular weight for linear polyisobutylene (open circles), polybutadiene (filled circles) and polystyrene (open and filled triangles) taken from ref. [2].

Single chain models, such as the Rouse model, are strikingly simple considering the complexity of a polymer melt. They rely on strong assumptions, such as neglecting longer range interactions and assuming an infinitely flexible chain. These limitations are discussed for example by P.-G. de Gennes [130]. It is nonetheless successful in describing short polymer chains. As chains become longer, the topological constraints of surrounding chains can no longer be overlooked. These so-called entanglements have deep consequences on viscoelastic properties of polymers. This complex theoretical problem can be solved by replacing the many-body constraints by an effective field acting onto a single chain, as put by T.C.B. McLeish [185].

This was originally made possible in the 1960s when S.F. Edwards built a statistical mechanics description of polymeric materials [186] and soon after introduced the tube model to account for topological constraints of entangled chains [187]. P.-G. de Gennes first investigated the implications of such model on polymer dynamics [188] leading to a whole theory of entangled dynamics namely developed by M. Doi and S.F. Edwards in a series of papers [189]. An entangled chain then exhibits a sliding or slithering motion along a tube [187] formed by all the entanglement points around it. This serpent-like motion has provided the designation of reptation model. Polymer strands shorter than the distance between entanglements do not see the topological constraints and relax as unentangled chains. Hence, at high frequencies, the LVE response is still Rouse-like with a ½ slope for both $G'(\omega)$ and $G''(\omega)$ down to a critical onset of entanglement effects which translates into a G' G'' crossing point followed by a plateau of G' (Figure 6.2a). At times scales longer than the motion of a chain over its length along the reptation tube, the system reaches a liquid-like terminal region as before. The onset of entanglement effects also translates into a different molecular weight dependence of viscosity as shown in Figure 6.2b. Up until a critical molecular weight, short unentangled chains exhibit a linear dependence in molecular weight. Since the following PILs are unentangled, we will not discuss the reptation model further.

6.2.3 Time Temperature superposition

Temperature dependence

The viscosity of a polymer melt, as for viscous liquids, decreases with temperature with an overall complex dependence. At elevated temperature, though, it is well described by an Arrhenius-like dependence :

$$\eta \sim \exp\left(\frac{E_\eta}{RT}\right) \tag{6.16}$$

in which E_η is an activation energy corresponding, to put it simply, to the slip of relative molecular planes [179].

This description nonetheless fails at low temperatures, close to T_g, because of an additional temperature-dependence of the activation energy E_η. The reason for such dependence is that the density becomes high enough so that monomers hinder one another's motion in the flow. A.K. Doolittle proposed an equation relating viscosity to the free volume surrounding the molecules rather than temperature [190] and accurately described experimental observations. The underlying assumption is that E_η is inversely proportional to the available free volume. Because of the thermal expansion of most materials, of coefficient α_f, we can assume in first approximation that the free volume is $f = \alpha_f(T - T_\infty)$ with T_∞ the Vogel temperature, typically 50 °C below T_g and at which the free volume is zero. All in all, equation 6.16 becomes the Williams, Landel and Ferry (WLF) equation [2, 191] :

$$\frac{\eta}{\eta_0} = \exp\left(B\left[\frac{1}{f} - \frac{1}{f_0}\right]\right) = \exp\left(\frac{B}{f_0}\frac{(T_0 - T)}{(T - T_\infty)}\right) \tag{6.17}$$

Where f_0 is the free volume at the reference temperature T_0.

The superposition

One assumption the Rouse modes relies on, as seen in equation 6.12 and 6.15, is that all relaxation times share the same temperature-dependence as the monomer relaxation time $\tau_0 \sim \zeta/T$. All other factors are temperature-independent. Consequently, it is possible to superimpose linear viscoelastic responses taken at different temperatures and the stress relaxation modulus can be built up by horizontally shifting the data by shift factors a_T with respect to a reference temperature T_0 such that it becomes :

$$G(t,T) = b_T G\left(\frac{t}{a_T}, T_0\right) \tag{6.18}$$

Since the temperature dependence of all relaxation modes is governed by the ratio of the friction coefficient and temperature, the timescale shift factors a_T are :

$$a_T = \frac{\zeta T_0}{\zeta_0 T} \tag{6.19}$$

The vertical shift factors b_T are determined by the temperature dependence of the modulus at any given relaxation time $G(\tau) \sim \rho T$. The mass density appears here as a consequence of the kT contribution per unrelaxed strands leading up to equation 6.15. The density of a polymer melt is weakly dependent on temperature, much less than the friction coefficient ζ, hence b_T factors are small compared to a_T and often ignored.

Beyond a simple master curve build up, these shift factors reflect the temperature dependence of several polymeric properties. The Newtonian viscosity, for instance, is proportional to the product of relaxation time and corresponding modulus $\eta \sim \tau G(\tau)$. This stems from equation 6.6 combined with Newton's law of viscosity $\eta = \sigma/\dot{\gamma}$ and considering an exponential decaying stress. Then the viscosity renormalized to the viscosity η_0 at reference temperature T_0 is simply the product of shift factors :

$$\frac{\eta}{\eta_0} = \frac{\rho\zeta}{\rho_0\zeta_0} = a_T b_T \tag{6.20}$$

Thus, in practice not only the making of a superimposed master curve is useful to get the full LVE response of the material at frequencies virtually impossible to measure at a fixed temperature, it also captures temperature dependencies of the material's properties.

6.3 Case of associating polymers - Ionomers

We introduce in this section the case of associating polymers with a particular emphasis on ionomers, mentioned in Chapter 1. They bear associations points along the chain which we will refer to as stickers and which can form reversible bonds with each other. Understandably, breaking and reforming of such bonds has deep implications in the dynamics of the system. Nevertheless, these polymers are well described by modified Rouse or reptation models depending on whether they are entangled or not

6.3.1 The association lifetime

Let us consider a little amount of ionic stickers in a polymeric system, such as partially sulfonated polystyrene. Using Dynamic Secondary Ion Mass Spectrometry, R.H. Colby *et al.* measured concentration profiles across bilayers of hydrogenated and deuterated ionomers at different annealing times, hence tracing back the diffusion of ionomer chains and their counter ions [192]. The LVE of a lightly sulfonated PS showed two dissipation processes as two maxima on the loss modulus G''. They attribute the longest relaxation time to a polymeric terminal time of the full ionomer chain. The fast one, at high frequency, was attributed to the ion association lifetime, denoted as τ in Figure 6.3. This is a great example of an association lifetime being clearly visible in LVE, but unfortunately it is also rare.

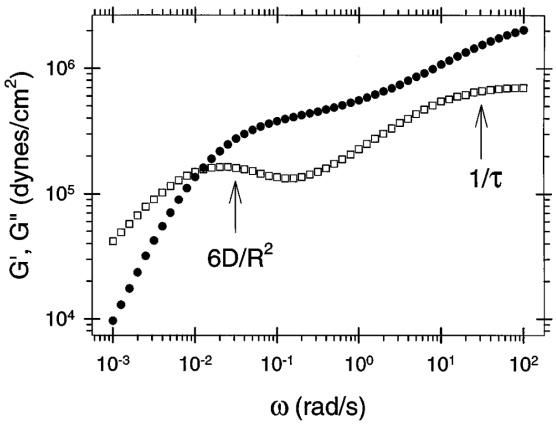

Figure 6.3: LVE response for a lightly sulfonated PS of ion content 0.85 mol% taken from ref. [192] G' and G'' are respectively filled circles and open squares. Arrows denote reciprocals of timescales determined independently. D is the chain diffusion coefficient, R its radius, τ is the ion pair association lifetime.

The association lifetime τ_s, as we will refer to in the following, is governed by a competition between the association strength E_a and the thermal energy, which promotes dissociation, and can thus be described by an Arrhenius law [118]:

$$\tau_s = \tau_0 \exp\left(\frac{E_a}{kT}\right) \tag{6.21}$$

For a reasonable number fraction of associating groups p along the chain, a rubbery plateau of G' emerges between the segmental relaxation time τ_0 and the lifetime of associations. In that timescale, associations have not yet relaxed and act as effective crosslinks. The width of the rubbery plateau is controlled by the ratio τ_s/τ_0, hence by the strength of associations. Such additional relaxation time can be accounted for using previous considerations on the classic viscoelastic models for polymers.

6.3.2 Sticky Rouse model

Despite being a hot topic today, due to reprocessability and self-healing applications, the relaxation of systems by association and dissociation of reversible

crosslinks traces back to the work of Green and Tobolsky in 1946 [114]. It was shown later on that the Rouse model holds on timescales longer than the association lifetime [193]. Since the relaxation of unentangled polymers is the sum of the relaxation of varying portions of the chain, strands shorter than the distance between stickers, *i.e.* the high order Rouse modes, do not feel their effect. As such, their relaxation remains unchanged and governed by the segmental time τ_0. Longer strands, *i.e.* the low order Rouse modes, have their relaxation delayed and governed by the association lifetime τ_s of the stickers. This occurs for strands larger than the distance N_s between stickers in number of monomers. Since they are also Rouse-like, the relaxation of the chain becomes, using equation 6.15 [193, 194]:

$$G(t) = kT\frac{\phi}{Na^3}\left(\sum_{p=N_s+1}^{N}\exp\left(-\frac{tp^2}{\tau_0 N^2}\right)+\sum_{p=1}^{N_s}\exp\left(-\frac{tp^2}{\tau_s N_s^2}\right)\right) \tag{6.22}$$

In which the first term includes the unaffected high order Rouse modes and the second one the delayed low-order ones.

L. Leibler *et al.* have developed a scaling model for entangled associating polymers [115]. They show a strong coupling between the topological constraints of entanglements and the dissociation of stickers. Since the focus of this chapter and this work as a whole are unentangled PILs, these considerations will not be required.

6.4 Rheology of PILs

Following the overview of viscoelastic models of polymeric materials, including associating polymers, we discuss in the present section the results of oscillatory shear experiments on our **PC$_n$VImTFSI** series with varying side chain length. These experiments were performed in collaboration with G. Miquelard-Garnier and J. Peixinho[1]. The sample preparation and experimental procedure are detailed before moving on to the experimental observations on the LVE response of these PILs which are further discussed in section 6.5 in connection with their structure and the comparison with ionomers.

6.4.1 Experimental methods

Sample preparation

Disks were prepared by compression moulding under vacuum at 100 °C using a homemade compression cell described in Chapter 3 in which it was used for SANS experiments at varying temperature. The disks thus obtained are 10 mm in diameter and around 1.2 mm in thickness. To cut them to the desired diameter, they are heated at 100 °C together with a cylindrical die of 7 mm in diameter, afterwards pressed onto the sample by hand.

[1]Arts et Métiers Institute of Technology, CNRS, Cnam, HESAM Université, Laboratoire PIMM, UMR 8006, Paris 75013, France

Experimental setup

Oscillatory shear measurements were performed on a strain controlled Anton Paar MCR502 rheometer. The geometry was an 8 mm parallel plate and temperature was controlled by a CTD180 convection controlled device (AntonPaar) under nitrogen flow. The slightly smaller diameter of the samples compared to the geometry allowed to gently press them at around $T_g + 30$ °C and ensure complete adhesion over both plates. Temperature is then lowered to 30 °C and oscillating frequency sweeps from 100 to 0.1 rad/s are performed for increasing temperatures up to 140 °C for the PIL presenting the highest T_g (short side chains). The strain was 0.01 % at low temperatures and increased to 0.05 % and 0.1 % when the torque reached values of a few tens of μN.m to improve the signal-to-noise ratio. The full sequence was automated on the AntonPaar RheoCompass software. The temperature is left to increase with an equilibrium condition over around 7 min, with a tolerance of 0.5 %. The whole temperature step lasts 20 min in practice. Once temperature is stabilized, a control of normal force at 0.2 N over 2 min allows the gap to be adjusted to ensure contact with the sample and avoid delamination or dewetting from the upper plate, which would translate in a negative normal force. The following frequency sweep is performed before moving to the next temperature.

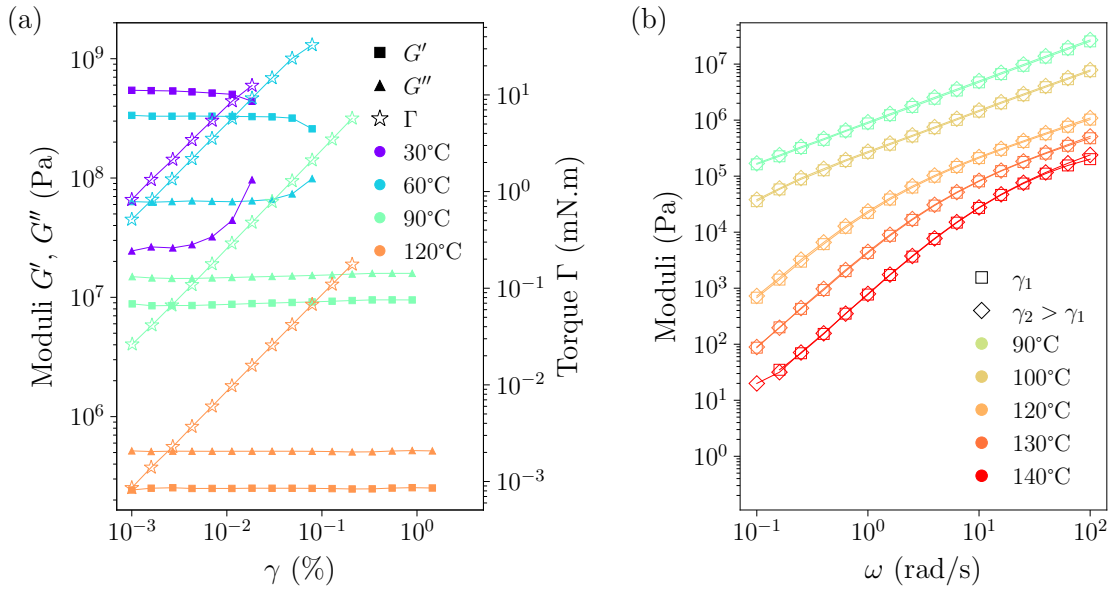

Figure 6.4: Strain check on a **PC_2VImTFSI** sample. (a) Amplitude sweeps at different temperatures and $\omega = 10$ rad/s. The measured torque is represented on a secondary axis. (b) Comparison of frequency sweeps at two strain values for different temperatures show a good overlap. For visibility only the storage modulus G' is plotted. Strain values γ_1 and γ_2 are 0.01 % and 0.05 % up to 100 °C, 0.05 % and 0.1 % for 120 °C, 0.1 % and 0.5 % above.

In order to check the measurements are made in the linear regime, we perform amplitude sweeps at an angular frequency $\omega = 10$ rad/s. An example of this on a **PC_2VImTFSI** sample is given in Figure 6.4a. The measured torque Γ is also represented and was used to ensure a satisfying signal-to-noise ratio across the

acquisitions. Frequency sweeps at two strain values were also performed and showed a perfect overlap (Figure 6.4b). Time temperature superposition is made using the `RepTate` (Rheology of Entangled Polymers: Toolkit for Analysis of Theory and Experiment) open source Python software [195]. Only a horizontal shift of the data in frequency was necessary and the corresponding a_T shift factors were retrieved with a reference temperature $T_{\text{ref}} = T_{\text{g}}$.

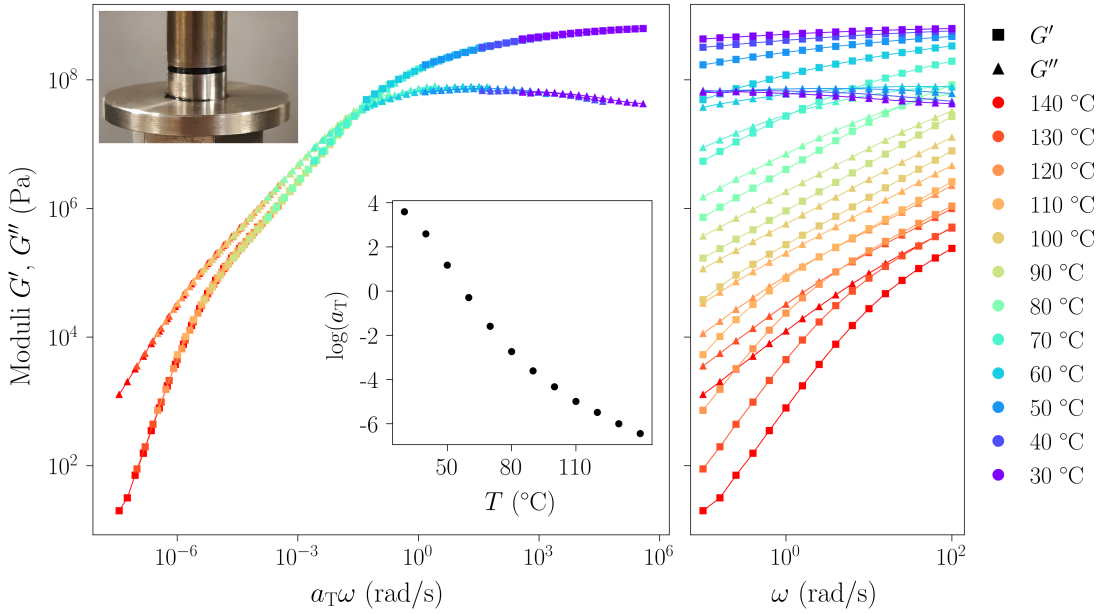

Figure 6.5: Time temperature superposition detailed for a **PC_2VImTFSI** sample. Frequency sweeps as measured are represented on the right-hand side. Superposition as obtained using the `RepTate` software using only horizontal shifts is given on the left-hand side for $T_{\text{ref}} = T_{\text{g}}$ (values of T_{g} are given in Table 2.1). Shift factors $a_T\omega$ as a function of temperature are given as inset. A picture of the sample is given as top left inset.

6.4.2 Experimental results

Time temperature superposition

The horizontal shift factors a_T used to build the superpositions are fitted to a WLF equation 6.17 and reported in Figure 6.6 on a temperature axis corrected by the glass transition temperature $T - T_{\text{g}}$. Above $n = 2$, they appear to overlap reasonably well. The shortest side-chain of $n = 2$ does not, however, and it is also the one for which the fit to a WLF is slightly less satisfying. This might originate from ionic interactions being the strongest at short side chains, although it is not completely clear. It should be stressed nonetheless at this point that the WLF turns out to fail at lower temperature, which contrasts with an often observed failure at high temperature where strongly associating polymers exhibit an Arrhenius-like temperature dependence [194]. At low temperatures, however, the material is in its glassy state, hence displaying weak dependence of both G' and G'' on frequency ω. Consequently, there is a considerably higher error margin

in translation when building the superimposed master curve. Whether the failure of the WLF description really stems from a physical origin has to be confirmed by looking at the resulting LVE response.

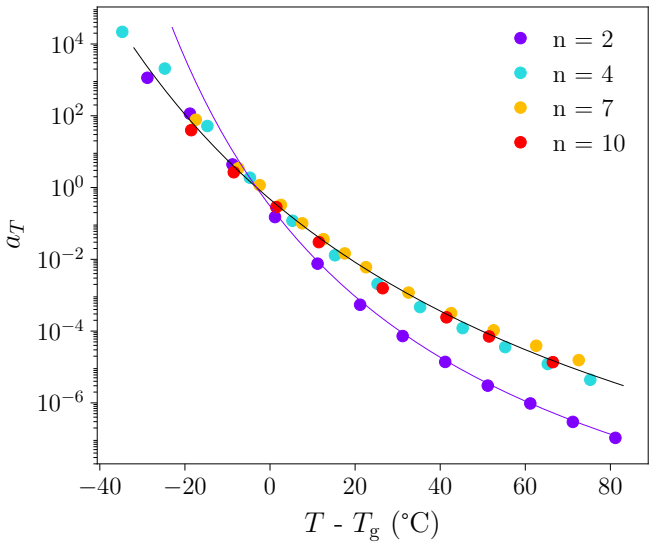

Figure 6.6: Temperature dependence of viscoelastic shift factors a_T used for the superimposed LVE responses of Figure 6.7 at $T_{ref} = T_g$ (values of T_g are given in Table 2.1). Solid lines represent fits to a WLF.

General shape

The linear viscoelastic response of **PC$_n$VImTFSI** with varying n are shown in Figure 6.7. For all side chain lengths considered, the LVE response is rather similar. A glassy region is identified at high frequency, with a plateau in storage modulus G' around 100 MPa. At low $a_T\omega$ the terminal region is achieved with storage moduli G' below 10 kPa. Slopes of 1.0 and 1.7, respectively for G'' and G', do not exactly match the expected 1.0 and 2.0 but are consistent with other reports [120, 121]. The transition region, for $a_T\omega$ between 10^{-5} and 10^{-1} rad/s for $n = 2$ or 10^{-3} and 1 rad/s for $n = 4$, 7 and 10, displays a regular power-law of both G' and G'' with slopes of 0.8 and 0.7 respectively. The absence of rubbery plateau in this frequency range together with a single crossover point confirms our considerations on their molecular weight in Chapter 2 stating our PILs are unentangled.

One feature that should be mentioned is the absence of conventional Rouse-type exponents of ½ for both G' and G''. It is not uncommon for rather stiff, *i.e.* semi-flexible, non-ionic chains, such as polycarbonate or polysulfone melts, to exhibit different exponents [2]. The Rouse model effectively assumes long, *i.e.* large N, and infinitely flexible chains, hence many relaxation modes. The stiffness of the chain translates into a larger Kuhn length and as such, a stiffer chain has less Rouse modes, leading to a slightly different scaling of the moduli in that regime. Still, effects of the ionic groups should not be ruled out and steeper slopes have been attributed, in the case of highly sulfonated polystyrene, to the high ionic content [111]. This regime is observed for relaxations at length scales between a Kuhn

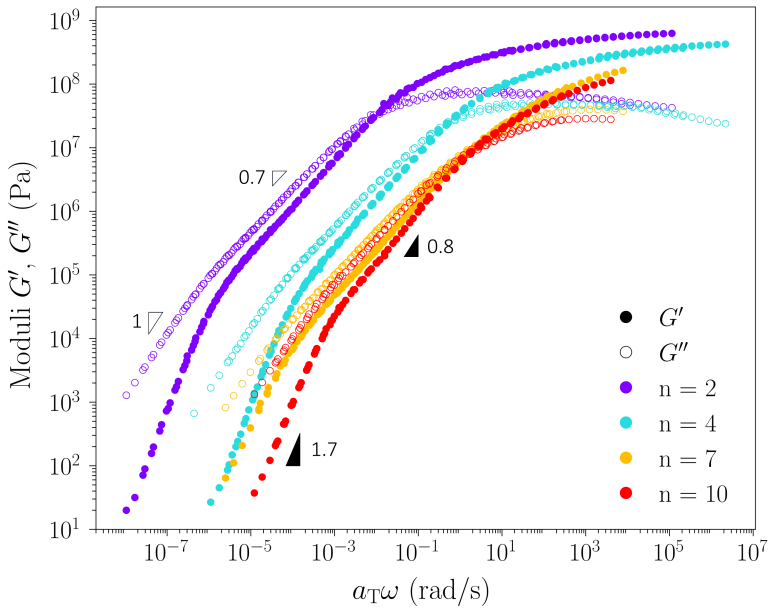

Figure 6.7: LVE response for **PC$_n$VImTFSI** samples of varying side chain length n. Reference temperature is $T_{\text{ref}} = T_{\text{g}}$ (values of T_{g} are given in Table 2.1).

segment and a sticky strand, *i.e.* longer than the distance between stickers. For a high ionic content, there are very few Kuhn segments between stickers, restricting the Rouse region to a narrow frequency range. More will be said on this matter later on. Overall, the LVE responses of the PIL series are quite similar to the few reports on unentangled PILs [102, 104, 120, 121]. Nevertheless, as it was pointed out in Chapter 1, these reports rarely focus on a single type of side chain with varying length. It should be recalled here that our synthesis strategy ensures the same degree of polymerization and dispersity are kept along the series, hence any observed difference in viscoelastic properties stems from the side chain length alone.

Effect of side chain length

Although the above description applies to all LVE responses across the PIL series, a trend stands out with varying side chain length. As n increases, LVE responses shift both vertically, to lower moduli, and horizontally, to higher frequencies (Figure 6.7). This is well illustrated by following the single crossing point $G' = G''$. Both the frequency ω_{cross} and the modulus G'_{cross} at the crossover are represented in Figure 6.8 against side-chain length n. The transition happens at increasingly smaller frequency, or longer times, for decreasing n, suggesting a delay when shortening the side chains. Figure 6.8 additionally emphasizes the singularity of **PC$_2$VImTFSI** which manifested a different temperature dependence of its shift factors in Figure 6.6 compared to the rest of the PIL series.

The vertical shift corresponds to a decrease of G' for increasing n and can be attributed, in a first attempt, to a plasticizing effect of the increasingly longer side-chains [122, 196]. Data of Figure 6.8 additionally suggests dynamics level off and only slightly vary between $n = 7$ and 10. This is further consistent with the similar temperature dependence above $n = 4$ illustrated by the shift factors reported

in Figure 6.6. To understand the origin of such levelling, a closer look at the microstructure, which happens to have been extensively investigated in Chapter 3, is needed.

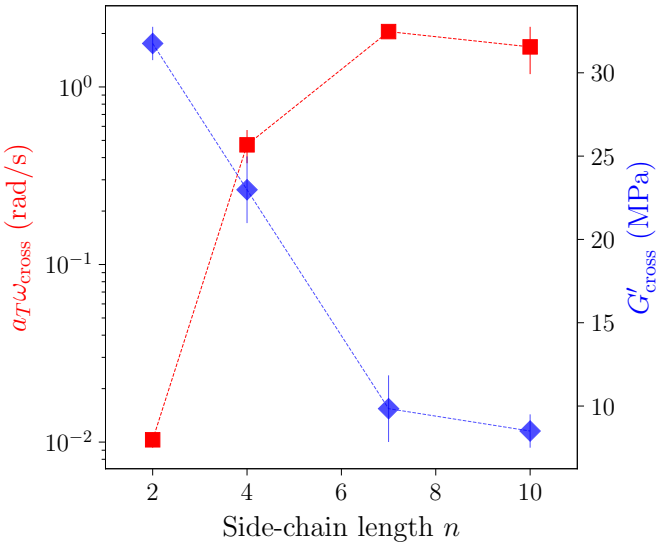

Figure 6.8: Position of the crossover point $G' = G''$ on LVE responses of Figure 6.7 as a function of side chain length n. Frequency $a_T\omega_{\text{cross}}$ and modulus G_{cross} are respectively represented in red and blue.

6.5 Discussion on viscoelasticity and nanostructure

The purpose of the remainder of this chapter is to provide some interpretation attempts based on the microstructure of these materials. We first make a brief comment about the use of the time temperature superposition on such systems, and why it may not be intuitive that it holds. Some of the viscoelastic behaviours observed above are then discussed in connection with the structural features investigated by SANS and WAXS in Chapter 3. Finally, the comparison with ionomers provides an appealing interpretation of some of these results. Nonetheless, we point out how these materials differ by returning to their parent ILs which were left out of this chapter.

6.5.1 Non-trivial superposition

The time temperature superposition (tTS) was applied without questioning in the investigation of this PIL series. Nevertheless, there were reasons to believe it would fail. As explained in section 6.2.3, the underlying assumption to the tTS is that all relaxation times of non-ionic linear chains are proportional to the monomer relaxation time τ_0 with temperature-independent factors. Hence, all relaxation times share the same temperature-dependence, that of τ_0. Yet, both ionomers and

PILs differ from non-ionic polymers by the presence of ion associating groups. Naturally, stickers do not share the same temperature-dependence and instead follow an Arrhenius-like behaviour of equation 6.21 of activation energy E_a related to the association strength. Such a difference with polymeric relaxation times should cause the tTS to fail, and yet it holds for an extensive number of reports on ionomers and the few reports on viscoelasticity of PILs. When it does nonetheless fail, it often occurs around the plateau region [111] or at the terminal time [118] for rather strongly associating ionomers. K. Nakamura *et al.* showed the same kind of failure at low frequency for **PC_2VImTFSI** above a critical molecular weight [119] but this falls outside the scope of the present discussion because of the complex interplay between topological constraints and stickers associations mentioned in section 6.3.2.

For unentangled PILs, the superposition seems to hold in all reports so far. Even though ion associations are not necessarily an issue, as demonstrated in the case of ionomers, PILs possess a temperature-dependent structure. As shown in Chapter 3, side chains longer than $n = 4$ increasingly interdigitate upon heating, particularly for the longest side chain $n = 10$. Hence, surprisingly, tTS holds despite such temperature-dependent local structure. Additional experiments on the dynamics of PILs at these length scales, which will be discussed in the concluding remarks, would be required to get a full picture.

6.5.2 Role of microstructure

As illustrated by the crossover between storage and loss moduli plotted in Figure 6.8, our series of **PC_nVImTFSI** experience a weaker cohesion as n increases. As mentioned above, side-chains play a role of plasticizer, and it makes sense that moduli decrease as they become longer. Nonetheless, the levelling off observed for the G' G'' evolution with n also reminds of the conformation of PIL chains discussed in Chapter 3. We recall here that using SANS, the chain's radius of gyration R_g was shown to exhibit a non-monotonous behaviour for increasing side-chain length. Since the first decrease of R_g as n increased from 1 to 4 carbons was ascribed to an increase in chain flexibility, it is consistent that it should stand out on the viscoelastic properties of the material as well. The threshold at $n = 4$ also corresponds to the percolation of apolar domains in both ILs [21] and PILs [34] and the onset of interdigitation of side chains. Above the threshold, the microstructure showed less variation with chain diameter, with both distance between main chains and radius of gyration increasing more regularly with n due to steric effects. Consequently, both structural features at the nanometre scale and macroscopic viscoelastic response appear to level off for increasing side chain length. Whether this unfolds from the bicontinuous structure inherited from ILs or a screening of ionic interactions remains an open question.

6.5.3 Insights from the ionomer comparison

Absence of rubbery plateau

Ionomers, and associating polymers in general, were introduced in Chapter 1 and mentioned again in section 6.3 based on partially sulfonated polystyrene (PSS) [111] with increasing ion fraction. The most conspicuous effect of associations in these

strongly associating systems is a rubbery plateau corresponding to the timescale over which stickers associate and dissociate. The association strength is fundamental in understanding or predicting the behaviour of associating polymers. Q. Chen *et al.* reported comparative study of unentangled poly(ethylene oxide) (PEO) and poly(tetramethylene oxide) (PTMO) based ionomers [194]. PTMO based ionomers, which LVE response is shown in Figure 6.9 share strong similarities with PSS, namely the presence of a rubbery plateau. The PEO-based ionomers, however, do not exhibit any plateau, despite a rather close chemical structure, and their terminal dynamics are only weakly delayed with increasing ionic fraction. The authors attribute this to the strong solvation properties of PEO compared to PTMO, hence increasing the dielectric constant thereby promoting ion dissociation, and weakening the sticker's association.

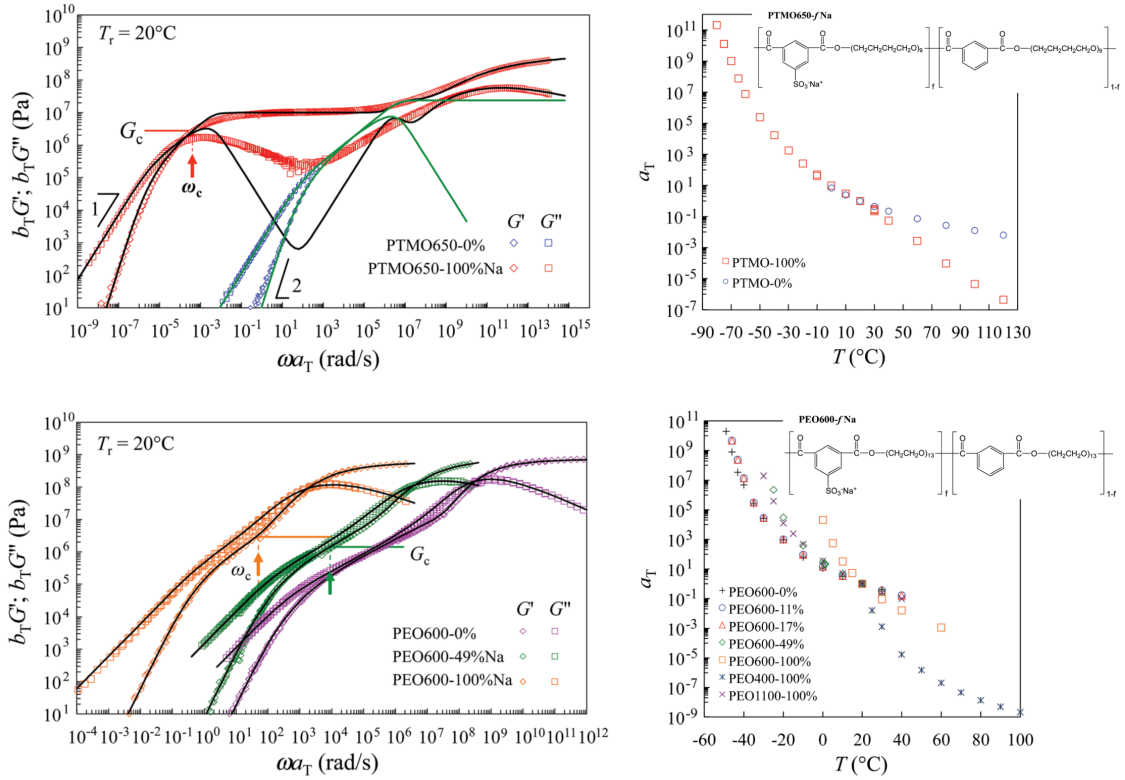

Figure 6.9: (Left panel) LVE response of unentangled PTMO based (top) and PEO (bottom) based ionomers for varying ionic fraction in %. Corresponding shift factors a_T used to build the complete LVE responses are given in the right panel, with chemical structures as insets. Figures taken from ref. [194]

The temperature dependencies are also impacted. While shift factors a_T for PEO-based ionomers shown in Figure 6.9 follow a WLF law, when associations are strong enough, as in the PTMO based ionomers, they abruptly shift from a WLF-type dependence at low temperature to an Arrhenius-like one at high temperature when ion dissociation dominates. These two closely related examples illustrate the range of behaviours associating polymers can exhibit. Other systems, with finely tuned association strength, were shown to smoothly shift from one situation to another by increasing the sticker content and reveal a rich panel of exponents in

the LVE response [197, 198]. On no account does the absence of rubbery plateau mean ion associations do not contribute to the dynamics of the system. They are fundamental to understand the delayed transitions and enhanced moduli. These systems, even the PEO based ionomers, were shown to be well predicted by modified relaxation theories such as the sticky Rouse model presented in section 6.3.2, and the sticky reptation model [115] respectively for unentangled and entangled polymers. A more sophisticated theoretical framework of reversible gelation exists [116–118] and succeeded in predicting much more accurately the behaviour of associating polymers. We choose not to develop this model any further in the present work since it is not necessary in the following discussion and its direct use would require additional data.

The LVE responses of the PIL series considered here, despite the absence of rubbery plateau, do present both delayed transitions and enhanced moduli with decreasing side chain length, similar to an increase of ion fraction in ionomers. As far as we know, not a single contribution on unentangled PILs has reported a clear plateau reminiscent of a strongly associating system. This is supplemented by the surprising fact that our series of **PC$_n$VImTFSI**, as well as other reported PILs, do not exhibit a broad glassy to terminal transition alone as would be expected from their high ionic fraction (all monomers bear charges). This may originate, just as the low melting temperature of their parent ILs, from the rather bulky and asymmetric chemical structures of the ion pair, particularly enhanced in our situation by the TFSI counter anion, hence lowering the strength of ion associations.

Ion dilution effect

Following up on the association strength, we come back to the crossing point $G_c = G' = G''$ reported above which we reproduce in Figure 6.10a. While its decrease with increasing n was simply attributed to a plasticizing effect of long side chains, we should not forget that increasing the size of the apolar moiety inevitably reduces the fraction of the ionic one like a charge dilution effect, schematically represented in Figure 6.10b. In other words, lengthening the side chains is a way to prevent ion aggregation, hence weakening the cohesive energy of the system.

In the absence of clear plateau for PEO based ionomers, Q. Chen. *et al.* defined the ion dissociation frequency as the frequency at which the modulus reaches an estimated critical value of kT per ionic group [194]. This approach was further supported by the good agreement with a relaxation mode observed in DRS. The number density of ionic groups is here the reciprocal of the molecular volume V_m of the repeating unit, since all monomers bear a charge. We estimate the volume of the repeating unit using either Van der Waals volumes of the corresponding IL series found in literature [199], density measurements of the same PIL series also reported in literature [147] and our own density values. The estimations $G_c \approx kT/V_\mathrm{m}$ are plotted alongside the experimental G_cross in Figure 6.10a. It remarkably captures the trend for $n = 7$ and 10, but a large discrepancy is observed for short side chains.

There is still a debate regarding this kind of estimation, and the good agreement between the corresponding dissociation frequency in LVE and the DRS measured relaxation mode observed for PEO based ionomers failed in other systems [200]. The authors put forward that such failure might be due to the stickers rearranging

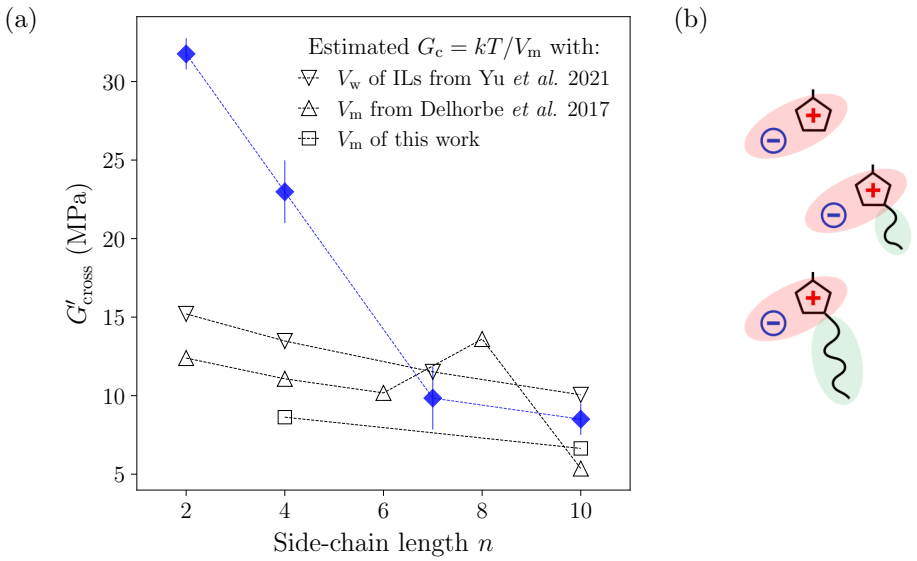

Figure 6.10: Modulus value at the crossover point $G' = G''$ on LVE responses of Figure 6.7 as a function of side chain length n. Black symbols are prediction of the modulus value as kT per ionic group as explained in the text with Van der Waals volumes of the IL series from ref. [199] (filled triangles) or calculated molecular volumes from density measurements from ref. [147] (empty triangles) and our own (solid squares). The effect of side chain length on the ionic contribution to the molecular volume of a repeating unit is schematically represented in (b).

and returning to the same association point multiple times before the effective break-up. Based on this interpretation, associations in PILs with long side chain above $n = 7$ have a single lifetime, effectively contributing to the modulus as kT per ionic group, whereas for short side chains they exhibit more complex relaxation processes involving multiple dissociations. This may be further supported by the change of connectivity of apolar domains in the bulk structure. Isolated, globular apolar domains formed by short side chains restrict the ionic sticker. In contrast, a bicontinuous structure formed by long side chains should facilitate the dissociation. This is also in line with dielectric relaxation spectroscopy measurements reported by K. Nakamura *et al.* showing that the ion dissociation time of **PC_2VImTFSI** and **PC_4VImTFSI** lies in the glassy region and is several orders of magnitude shorter than the segmental time τ_0 [119, 123]. Unfortunately, to our knowledge, such data on **PC_7VImTFSI** and **PC_{10}VImTFSI** were not reported but would be precious so as to verify the difference in scenario between short and long side chain in our series.

In the absence of such data, another possible interpretation for the resemblance of the LVE responses across the PIL series is that the ion dissociation lives at high frequency for all n. Hence, most stickers are already dissociated in the observed timescale and only act in increasing the friction in the transition and terminal region.

6.5.4 Potential limits to the comparison with ionomers

The comparison with ionomers has proven insightful at multiple occasions and has consequently been suggested in other reports [119, 123]. It is quite straightforward at first glance, since both materials are ion-containing polymers with a characteristic microphase separation. However, the underlying differences between these systems are often overlooked and could either be misleading or on the contrary enrich our understanding of PILs. The scattering peak, apparently shared by ionomers and PILs, is actually quite different in origin. In ionomers, it corresponds to the distance between ion aggregates in an apolar matrix. In PILs the incompatibility is internal to the repeating unit itself. The material is dominantly ionic and the aggregated phase is the apolar one. These apolar globules percolate around $n = 4$, hence forming a bicontinuous structure inherited from ILs, widely mentioned along this work. Remarkably, such drastic change of structure and connectivity between domains do not change the LVE response of the material across the PIL series. Conversely, the percolation of the restricted regions around ion aggregates in ionomers suppresses the transition zone. The segregated apolar domains might also fulfil the role of stickers, such as in block copolymers with immiscible polymer components [201]. Even though they rely on undeniably weaker associations and their effect might be negligible in the case of discrete apolar islands for short side chains, the onset of a bicontinuous structure should enhance their effect.

6.6 Conclusion and perspectives

Viscoelastic properties of the PIL series, which structure was extensively studied throughout this work, were investigated in the present chapter. The time temperature superposition holds across the whole series from ethyl to decyl side chains. The LVE responses look strikingly alike, despite changing the connectivity of the microstructure with increasing n by moving from globular apolar domains to a bicontinuous structure. Nevertheless, the shortening of side chains leads to an increasing delay of transitions and enhancement of moduli. This highlights somewhat similar molecular processes with ionomers and motivates their comparison. An ionomer-like estimation of a critical modulus based on the density of stickers suggests a drastic change in ion dissociation for short and long side chains, reminiscent of their respective structure.

Unfortunately there is a lack of data both in the present work and in literature regarding the viscoelasticity of intermediately long side chain PILs, above the percolation threshold, but below the onset of liquid crystalline or semicrystalline behaviours [202]. Evidently, since short side chains PILs exhibit a higher conductivity, which most targeted applications rely on, they are the focus of most reports. Nonetheless, to a fundamental point of view as well as for other types of applications such as self-healing or reprocessable materials, additional data on PILs with long side chains would be valuable. Among them, a systematic study of the dielectric relaxation of the PIL series and their respective dielectric constant appears, from the discussion above, as a necessary requirement to better grasp their dynamics. It is also still unclear what are the dynamics of a single PIL chain, which should be

considerably different below and above the $n = 4$ threshold. To do so, quasi elastic neutron scattering, neutron spin echo and NMR are among the techniques which should bear precious results, through the dynamic structure factor $S(Q, \omega)$, as they did for the scale-dependent dynamics of ILs discussed in Chapter 1 [91, 92]. All in all, although, or perhaps because, LVE responses of our imidazolium PILs with varying n at fixed degree of polymerization and dispersity differ rather weakly, they raise fundamental questions regarding the dynamics at the molecular scale and call for further investigation.

General Conclusion

Poly(ionic liquid)s are versatile and tremendously promising materials for many applications, ranging from solid-state electrolytes for energy storage devices to self-healing materials. Such versatility relies on the combination of ILs and polymeric properties, which is also why they are intriguing. In imidazolium PILs, this work focused on, the side chain length n deeply affects both the structure and the properties of the material as it does for the corresponding ILs. It all comes down to the nanoscale segregation of the apolar moiety in globules for short side chains, percolating as n increases to form a bicontinuous sponge-like structure. Most reports to date aimed at improving the conductivity of PILs and therefore focused on certain chemical features such as short side chains and large anions. Consequently, a considerable number of fundamental questions remains unanswered, and it is often unclear whether the observed behaviours stem from ionic interactions, polymeric properties or structural heterogeneities. Evidently, such gap of knowledge is often a shortcoming in the targeting of desired applications.

To address these questions, the aim of the present work was to provide a systematic study of a PIL series with finely tuned interactions. To that end, we focused across chapters on an identical imidazolium PIL series with varying side chain length n. The strength of the synthetic strategy, and as such of the results of the present work, is the prior polymerization of poly(vinylimidazole) from which each PIL is then synthesized. Consequently, the degree of polymerization and dispersity is strictly identical across the series and any difference in behaviour stems from the side chain length n.

Using small angle neutron scattering, we revealed for the first time, in the present work, that the size of the polymer coil in bulk, quantified by its radius of gyration R_g, does not follow an expected monotonous increase due to the increase of molecular volume and steric effects. It instead first decreases with increasing n up until $n = 4$ suggesting an increase in chain flexibility. This threshold seems to match that of the percolation of apolar domains revealed by MD simulations. The same SANS experiments provided a direct and simultaneous measurement of both the chain diameter and the distance between main chains, so as to reveal interdigitation of long side chains. Until now, only indirect experimental evidence relying on the increasing rate of the interchain distance with n had been reported. The temperature dependence of the local structure is rather surprising as well, and contrasts with an expected thermal expansion effect. Neighbouring chains are instead pulled together for increasing temperatures, suggesting interdigitation is promoted at high temperature. Nevertheless, the temperature-dependence of the local structure has no significant, or at least measurable, implications on the macromolecular conformation, measured in a subsequent neutron scattering experiment.

A detailed description of the bulk structure of any material is a precious insight to predict or at least understand its viscoelastic properties. It happens that those

of PILs receive considerably less attention than their conductivity. Given the pronounced structural changes along the series with increasing n, the non-monotonous behaviour of the coil size, the onset of interdigitation of side chains and the temperature dependence the latter confers the local structure with, we would expect some effect on the LVE responses of the series. Yet, they share strong similarities. Still, as side chains are shortened, the material hardens, translating into increased moduli, and the relaxations are delayed to longer times. Beyond the plasticizing effect of long side chains, decreasing n is a way to concentrate charges in the system, like ionomers with increasing ion fraction. The estimation of a modulus of kT per ionic group is in line with the crossing point $G' = G''$ for long side chains, but not for short ones. The rearrangement of ion associations in larger clusters before the effective relaxation is a possible interpretation. The change of connectivity of apolar domains for long side chains together with weaker interactions would then lead to simpler dissociation processes.

Dielectric measurements with varying n naturally comes as the crucial next step towards a comprehensive picture of dynamics across the PIL series by providing independent measurements of the relaxation times. Because the PIL chain relaxes in a globally ionic domain, as opposed to ionomers, it should be interesting to perform quasi elastic neutron scattering (QENS) and neutron spin-echo (NSE) experiments on these systems to investigate their scale-dependent dynamics, similar to what Ferdeghini *et al.* have reported on imidazolium ILs [91, 92]. K. Sinha and J.K. Maranas did so on PEO based ionomers and revealed an heterogenous segmental motion closely related to the picture of restricted regions around association points [203]. It has yet to be shown how the differences in PILs' bulk structure would affect such observations.

Moving from the bulk to the interface, we put forward the first experimental evidence, by X-ray reflectivity, of spontaneous layering in spin-coated PILs thin films. The onset of such layering is again in line with a threshold around $n = 4$. The film thickness dependence of such layering was evidenced by a Fourier transform analysis of XRR data, successful in unveiling very fine details despite the low contrast. Combining the out of plane with in-plane observations through grazing incidence wide angle scattering, we propose a molecular picture of a confinement effect. Imidazolium pendant groups align preferentially parallel to the interface as the thickness decreases, consequently bringing long side chains in-plane and pushing neighbouring main chains apart in the vicinity of the interface. Such observations are of substantial significance for applications in energy storage devices or electrochemistry in general. Indeed, the material performance in such systems is highly dependent on what occurs at the electrode interface. An interesting direction to take in that regard would be to investigate the electric field responsiveness of this layering.

We mentioned above QENS and NSE experiments to investigate the scale-dependent dynamics of PILs in bulk. The local viscosity may most likely be heterogenous in these materials as well and could be probed using fluorescent molecular rotors [204]. These should have a larger affinity with specific domains in the heterogenous PIL bulk structure, thereby targeting the observation. They can also adsorb at interfaces [205] hence offering a way to probe the local viscosity of PILs in the layered region near the interface. To that aim, a collaboration was started

with E. Mirzahossein[1], M. Grzelka[2] and D. Bonn[1] which has yet to deliver results.

Finally, these considerations on interfacial viscosity and fluorescence bring us to one last point of focus which was initially expected from this work. We mentioned in Chapter 1 the quantized friction of ILs which, due to the molecular layering they exhibit, induce a dependence of the friction coefficient between two sliding planes on the thickness of the IL film. The layering we report for PILs could also lead to peculiar friction behaviour and eventually slip. Viscous polymeric materials can exhibit slip lengths several hundreds of micrometers long. We expect the layering of PILs at interfaces to enhance, or in any case affect, this slipping behaviour. This could be observed in a fluorescence photobleaching experiment in a shearing cell [206].

In essence, the present work highlights the abundance of insights a systematic study with varying side chain length such as ours can offer. The fine-tuning of local interactions explored on our PILs series impacts much more than the local structure alone. The interfacial structure is distinctly modified and viscoelastic properties hold clear signs of its influence as well. More investigation on model PIL series are required to complement the understanding of PILs across different chemical structures. These materials hold an immense potential in a wide range of applications, which is only hindered by the clouded understanding we have of them. It is still unclear whether what was put forward in the present work regarding one particular PIL series holds any kind of universality across other PILs. There is still a strong possibility the term poly(ionic liquid) may only be a chemical classification, and their own versatility might prevent us from drawing universal laws as for non-ionic polymers. Nevertheless, we hope the modest contribution of this work will motivate additional research in that regard. Not only would it provide precision tools in the targeting of applications, it might also shed light on ILs themselves and other ion containing systems, polymeric or not.

[1]Van der Waals-Zeeman Institute, Institute of Physics, University of Amsterdam, 1098, XH, Amsterdam, The Netherlands.

[2]Université Paris Saclay, Laboratoire Léon Brillouin, UMR 12 CNRS-CEA, CEA Saclay, Gif-sur-Yvette 91191, France.

Appendix 1 - X-ray reflectivity fitting parameter

n=2				
Film thickness (nm)	**Model**			
6		**SiO_2**	**SiO_2 hydrated**	**Layer 1**
	Thickness (Å)	10 (fixed)	9.30 ± 0.01	37.20 ± 0.02
	SLD (10^{-6} Å^{-2})	18.42 (fixed)	18.33 ± 0.02	7.60 ± 0.03
	Roughness (Å)	2.5 (fixed)	4.70 ± 0.02	5.80 ± 0.02
8		**SiO_2**	**SiO_2 hydrated**	**Layer 1**
	Thickness (Å)	10 (fixed)	7.50 ± 0.01	65.20 ± 0.03
	SLD (10^{-6} Å^{-2})	18.42 (fixed)	14.70 ± 0.03	11.30 ± 0.03
	Roughness (Å)	2.5 (fixed)	3.0 ± 0.01	4.80 ± 0.02
11		**SiO_2**	**SiO_2 hydrated**	**Layer 1**
	Thickness (Å)	23.16 ± 0.05	x	86.80 ± 0.02
	SLD (10^{-6} Å^{-2})	18.65 ± 0.01	x	11.08 ± 0.02
	Roughness (Å)	6.00 ± 0.01	x	4.04 ± 0.01

Table 6.1: Fitting parameter table of XRR data for **PC_2VImTFSI** thin films obtained at the last step of the fitting procedure discussed in Chapter 4 and given in Figure 4.11.

n=4			
Film thickness (nm)	**Model**		
5		**SiO_2**	**Layer 1**
	Thickness (Å)	19.11 ± 0.05	33.90 ± 0.02
	SLD (10^{-6} Å^{-2})	18.46 ± 0.01	8.92 ± 0.02
	Roughness (Å)	5.48 ± 0.01	7.07 ± 0.02
7		**SiO_2**	**Layer 1**
	Thickness (Å)	19.08 ± 0.06	51.34 ± 0.01
	SLD (10^{-6} Å^{-2})	18.93 ± 0.01	11.96 ± 0.01
	Roughness (Å)	5.39 ± 0.01	3.96 ± 0.003
9		**SiO_2**	**Layer 1**
	Thickness (Å)	16.64 ± 0.06	67.87 ± 0.01
	SLD (10^{-6} Å^{-2})	18.69 ± 0.01	11.11 ± 0.02
	Roughness (Å)	5.34 ± 0.02	3.91 ± 0.01
11		**SiO_2**	**Layer 1**
	Thickness (Å)	15.91 ± 0.07	90.85 ± 0.04
	SLD (10^{-6} Å^{-2})	18.69 ± 0.01	10.39 ± 0.02
	Roughness (Å)	6.45 ± 0.02	4.20 ± 0.01
12		**SiO_2**	**Layer 1**
	Thickness (Å)	15.21 ± 0.06	107.27 ± 0.02
	SLD (10^{-6} Å^{-2})	18.47 ± 0.01	10.93 ± 0.02
	Roughness (Å)	6.00 ± 0.02	4.04 ± 0.01

Table 6.2: Fitting parameter table of XRR data for **PC_4VImTFSI** thin films obtained at the last step of the fitting procedure discussed in Chapter 4 and given in Figure 4.11.

n=7						
Film thickness (nm)	**Model**					
5		**SiO_2**	**SiO_2 hydrated**	**Layer 1**	**Layer 2**	
	Thickness (Å)	23.45 ± 0.40	x	12.63 ± 0.29	16.95 ± 0.31	
	SLD (10^{-6} Å^{-2})	19.44 ± 0.02	x	11.63 ± 0.04	10.35 ± 0.03	
	Roughness (Å)	5 (fixed)	x	3 (fixed)	4.72 ± 0.03	
6		**SiO_2**	**SiO_2 hydrated**	**Layer 1**	**Layer 2**	
	Thickness (Å)	20.77 ± 0.04	x	19.15 ± 0.17	16.51 ± 0.17	
	SLD (10^{-6} Å^{-2})	18.42 (fixed)	x	11 (fixed)	11.5 (fixed)	
	Roughness (Å)	5 (fixed)	x	3 (fixed)	4.73 ± 0.01	
7		**SiO_2**	**SiO_2 hydrated**	**Layer 1**	**Layer 2**	**Layer 3**
	Thickness (Å)	12.56 (fixed)	7.24 (fixed)	28.03 (fixed)	6.70 (fixed)	17.65 (fixed)
	SLD (10^{-6} Å^{-2})	18.42 (fixed)	14.90 ± 0.01	9.67 ± 0.01	7.52 ± 0.01	10.30 ± 0.01
	Roughness (Å)	2.5 (fixed)	3.01 ± 0.02	3.67 (fixed)	3.88 (fixed)	4.01 ± 0.01

Table 6.3: Fitting parameter table of XRR data for **PC_7VImTFSI** thin films obtained at the last step of the fitting procedure discussed in Chapter 4 and given in Figure 4.12.

n=10						
Film thickness (nm)	**Model**					
3		**SiO_2**	**SiO_2 hydrated**	**Layer 1**		
	Thickness (A)	6.85 ± 0.35	20.90 ± 0.37	1.17 ± 0.95		
	SLD (10^{-6} $Å^{-2}$)	18.42 (fixed)	17.17 ± 0.19	29.43 ± 11.60		
	Roughness (Å)	2.5 (fixed)	4.93 ± 0.87	7.39 ± 0.79		
5		**SiO_2**	**SiO_2 hydrated**	**Layer 1**	**Layer 2**	
	Thickness (A)	10 (fixed)	11.07 ± 0.20	18.99 ± 0.24	15.22 ± 0.25	
	SLD (10^{-6} $Å^{-2}$)	18.42 (fixed)	19.32 ± 0.05	8.10 ± 0.07	8.81 ± 0.07	
	Roughness (Å)	2.5 (fixed)	6.64 ± 0.08	3 (fixed)	5.40 ± 0.05	
6		**SiO_2**	**SiO_2 hydrated**	**Layer 1**	**Layer 2**	
	Thickness (A)	10 (fixed)	14.96 ± 0.18	21.45 ± 0.18	14.78 ± 0.27	
	SLD (10^{-6} $Å^{-2}$)	18.42 (fixed)	18.4971 (fixed)	6.38 (fixed)	8.62 (fixed)	
	Roughness (Å)	3 (fixed)	6.04 ± 0.07	3.22 ± 0.08	7.12 ± 0.17	
8		**SiO_2**	**SiO_2 hydrated**	**Layer 1**	**Layer 2**	**Layer 3**
	Thickness (A)	12.56 (fixed)	7.61 ± 0.06	28.77 ± 0.29	13.03 ± 0.20	17.66 ± 0.10
	SLD (10^{-6} $Å^{-2}$)	18.42 (fixed)	15.18 ± 0.23	9.32 ± 0.08	7.27 ± 0.09	9.63 ± 0.08
	Roughness (Å)	2.5 (fixed)	3.89 ± 0.20	4 (fixed)	4 (fixed)	5.00 ± 0.04

Table 6.4: Fitting parameter table of XRR data for **PC_{10}VImTFSI** thin films obtained at the last step of the fitting procedure discussed in Chapter 4 and given in Figure 4.12.

Appendix 2 - Summary in french - Résumé en français

Les poly(liquide ionique)s (PLI) sont des macromolécules composées de liquides ioniques (LI). Ils possèdent donc des propriétés hybrides qui font d'eux des matériaux prometteurs, notamment pour des applications en tant qu'électrolyte solide. Ils héritent des LIs une nanostructure particulière qui repose sur la ségrégation de la phase apolaire qui mène chez les LI imidazolium à une structure globulaire pour les chaînes carbonnées courtes ou bicontinue en éponge pour des chaînes longues. L'ajout de ces interactions locales à un polymère ouvre la voie au développement de nouvelles fonctionnalités reposant à la fois sur leur structure et leur dynamique. Les propriétés de conduction et la morphologie locale des PLIs ont été étudiées extensivement sur ces dix dernières années dans le but d'améliorer leurs performances d'électrolytes. Des études systématiques manquent cependant pour décorréler les processus complexes qui leur confèrent leur propriétés.

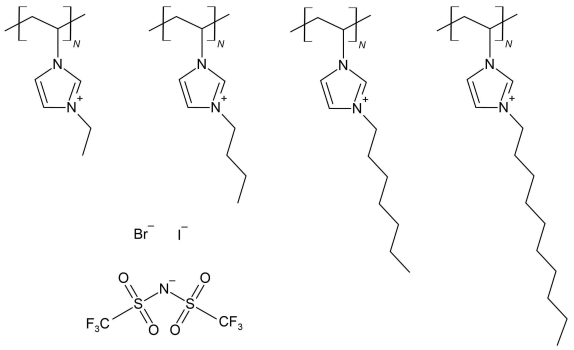

Figure 6.11: Structure chimique de la série de poly(1-vinyl-3-alkylimidazolium) (PC_nVImX) à longueur de chaîne latérale n variables ainsi que les contre ions (X) bromure, iodure et bis(trifluoromethylsulfonyl)imide (TFSI)

La présente étude est centrée sur une série de PLI imidazolium ($PC_nVImTFSI$) de longueur de chaîne latérale n variable, et par conséquent, aux interactions locales ajustables, représentée en Figure 6.11. La synthèse de cette série commence par la polymérisation de polyvinylimidazole suivie par sa quaternisation par un halogénure d'alcane de longueur de chaîne n. Par conséquent le degré de polymérisation et la polydispersité du matériau est identique pour toutes les valeurs de longueur de chaîne latérales. Afin de mieux comprendre l'influence des interactions locales sur ces matériaux, la morphologie de cette série de PLI est étudiée par des techniques de diffusion de neutrons aux petits angles (DNPA) et de rayons X aux grands angles (DXGA). Ces résultats servent de base à la compréhension des propriétés viscoélastiques de la série, étroitement liées à la structure des matériaux et étudiées par des techniques de rhéologie oscillatoire. Enfin, pour observer comment la structure en volume est affectée par la présence d'une interface, la structure de films fins de PLIs

est étudiée par une combinaison de réflectivité spéculaire de rayons X (RRX) et de diffusion de rayons X en incidence rasante (DXIR).

En utilisant la DNPA, la structure en volume est étudiée de la taille de la chaîne de PLI, sa conformation, jusqu'à son diamètre. Des signaux de diffusions donnés en Figure 6.12a, le rayon de giration de la chaîne, en d'autres termes la taille de la pelotte statistique, est extrait et représenté en Figure 6.12b. Une augmentation de R_g à grandes valeurs de n est simplement attribuée à des effets stériques entre monomères de plus en plus volumineux. Le premier régime de décroissance, plus suprenant, pour des chaînes latérales courtes est attribué à un gain de flexibilité de la chaîne principale, potentiellement affectée par des répulsions électrostatiques qui varient avec n.

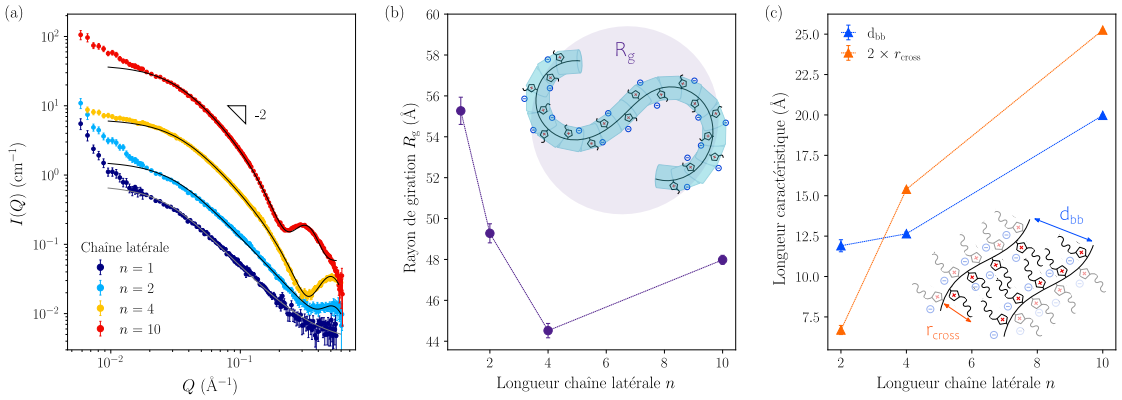

Figure 6.12: Spectres DNPA de mélanges équimassiques de PC$_n$VImTFSI hydrogénés et deutérés en fondu pour différentes longueurs de chaîne latérale n. Les traits pleins représentent les ajustements à partir desquels le rayon de giration (b) et les distances locales, diamètre de chaîne $2r_{\text{cross}}$ et distance interchaîne d_{bb} (c), sont extraits. Les schémas en (b) et (c) représentent les distances caractéristiques d'intérêt.

A l'échelle locale, la DNPA permet une comparaison directe entre le diamètre de la chaîne $2r_{\text{cross}}$ et la distance entre chaînes principales d_{bb} en Figure 6.12c. Ces deux grandeurs augmentent avec la taille du monomère. Le diamètre de la chaîne augmente cependant plus rapidement que la distance interchaîne, révélant une interpénétration des longues chaînes latérales. Cette distance interchaîne d_{bb} peut être également suivie par DXGA. Il a ainsi été montré qu'elle décroît avec une augmentation de la température, un effet donc contraire à l'expansion thermique du matériau et suggérant que la température favorise l'interpénétration des chaînes. Cependant, la conformation de la chaîne suivie en DNPA n'est pas afffectée par la température, quelque soit la longueur de la chaîne latérale.

En tant que rares exemples de polyélectrolyte en fondu, les PLIs ont des propriétés viscoelastiques surprenantes malgré leur grande densité ionique. Par des techniques de rhéologie oscillatoire et en utilisant la superposition temps-température, les réponses linéaires des PLIs de la série ont été mesurées et sont représentées en Figure 6.13a. Elles partagent une forme commune, ressemblant à celle de polymères neutres non enchevêtrés. Malgré leur ressemblance, quand la longueur de la chaîne latérale diminue, les modules et notamment le module élastique G' augmentent,

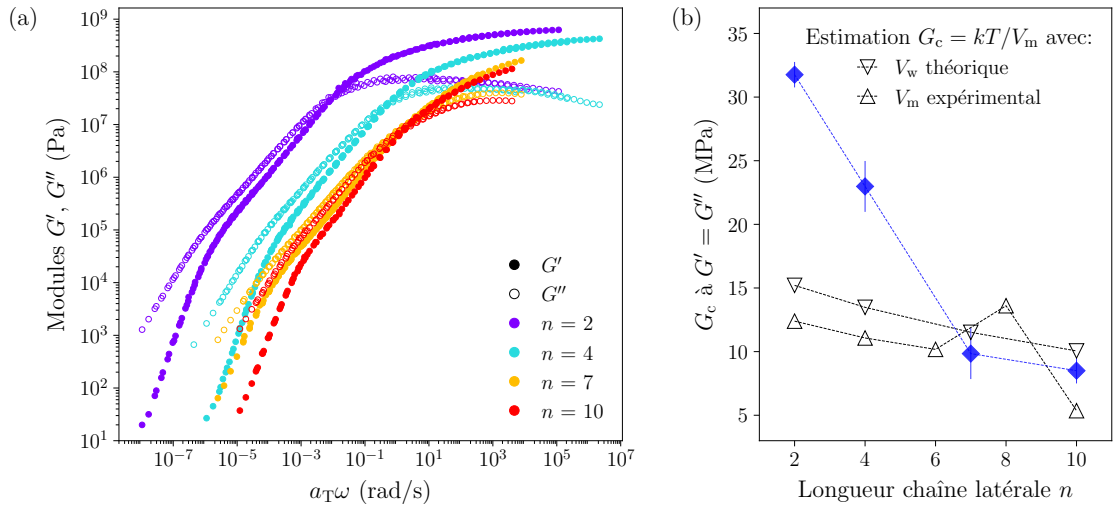

Figure 6.13: (a) Réponse viscoélastique linéaire de fondus de **PC$_n$VImTFSI** pour différentes longueurs de chaîne latérale n. La température de référence choisie est la température de transition vitreuse $T_{\text{ref}} = T_g$. (b) Valeur du module au point de croisement $G' = G''$ en fonction de n comparé à une estimation $G_c = kT/V_m$ avec V_m le volume moléculaire de l'unité de répétition.

le matériau gagne donc en cohésion, et les réponses se décalent vers les faibles fréquences, autrement dit les relaxations du matériaux sont retardées. Ces tendences sont semblables à d'autres matériaux ioniques comme les ionomères, des copolymères statistiques avec une certaine fraction de monomères chargés. Dans ces matériaux, les phases ioniques s'aggrègent et créeent autour d'elles des zones de restrictions, introduisant un nouveau temps de relaxation plus lent. En termes de réponses fréquentielles, celles des ionomères à faible associations ioniques sont semblables aux réponses observées sur ces PLIs et suivent les mêmes tendances, suggérant un effet similaire de l'augmentation de la fraction ionique et la diminution de la longueur de la chaîne latérale respectivement dans les ionomères et les PLIs. Une estimation d'un module caractéristique de kT par groupe ionique, communément utilisée pour les ionomères est donnée en Figure 6.13b et comparé au module caractéristique $G' = G''$. Cette estimation est fidèle aux observations expérimentales à grand n. Pour les chaînes latérales courtes, faibles n, le module caractéristique est sous-estimé et des processus de dissociation ionique plus complexes sont suspectés. Leur mise en évidence nécessiterait des approches complémentaires telles que la spectroscopie diélectrique.

Malgré les nombreuses applications des PLIs qui se jouent aux interfaces, telles que les application électrochimiques, et le comportement inhabituel des LIs qui s'y stratifient en couches d'ions, la structure interfaciale des PLIs est peu connue. À ce sujet, la structure de films fins obtenus par dépôt à la tournette est étudiée dans les trois directions de l'espace en utilisant à la fois la réflectivité spéculaire de rayons X (RRX) et leur diffusion en incidence rasante. La première est sensible à la densité électronique dans la direction normale au plan, la deuxième sondant la structure dans le plan près de l'interface. Les signaux de réflectivités obtenus en utilisant un diffractomètre Xeuss 2.0 pour des films fins de **PC$_4$VImTFSI**,

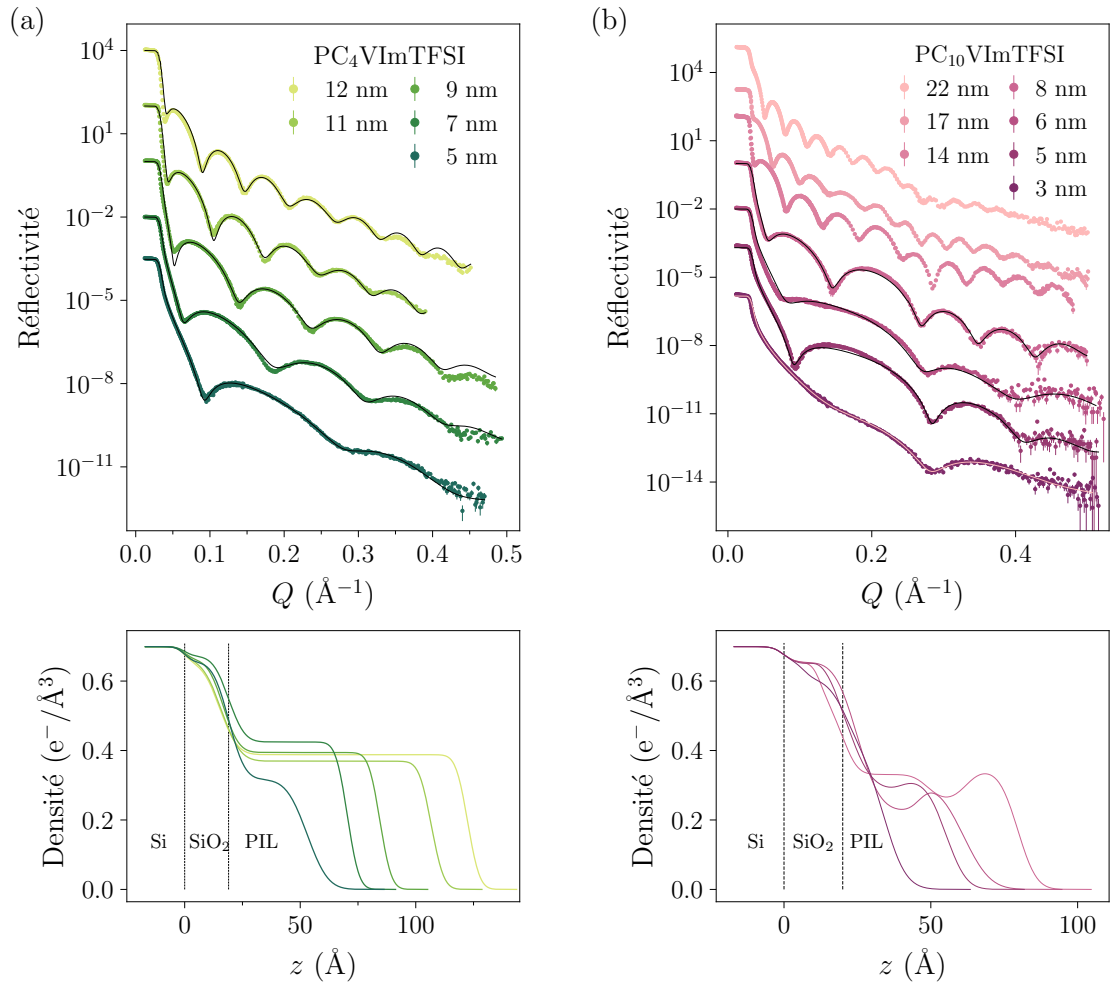

Figure 6.14: Courbes de réflectivité spéculaire pour des films fins de **PC_4VImTFSI** (a) et **PC_{10}VImTFSI** (b) pour différentes épaisseurs de film, obtenus sur un diffractomètre Xeuss 2.0 (Xenocs). Les courbes sont décalées verticalement pour une meilleure visibilité. Les traits plein représentent les ajustements correspondants aux profils de densité électroniques donnés dessous.

représentatifs des chaînes latérales courtes et de **PC_{10}VImTFSI**, pour les chaînes longues, sont donnés en Figure 6.14. Pour des chaînes latérales courtes, les films sont homogènes et les courbes de réflectivité révèlent des franges de Kiessig régulières. Pour les chaînes latérales plus longues, ces franges sont modulées par un autre signal, suggérant une structuration périodique des films.

Cette stratification apparaît clairement sur les profils de densité électroniques extraits par ajustement des signaux de réflectivité, également donnés en Figure 6.14. Cet ajustement est limité par la complexité numérique issue du grand nombre de paramètres ajustables (densité, épaisseur et rugosité des couches intermédiaires). Néanmoins le calcul de la transformée de Fourier de ces signaux, pourtant peu utilisée dans le domaine de la matière molle, permet d'accéder à la fonction d'autocorrélation du gradient de densité électronique $g(z)$. Cette fonction est notamment sensible aux interfaces, au niveau desquelles le gradient est le plus fort. Un film homogène présente deux interfaces et par conséquent la fonction $g(z)$ cor-

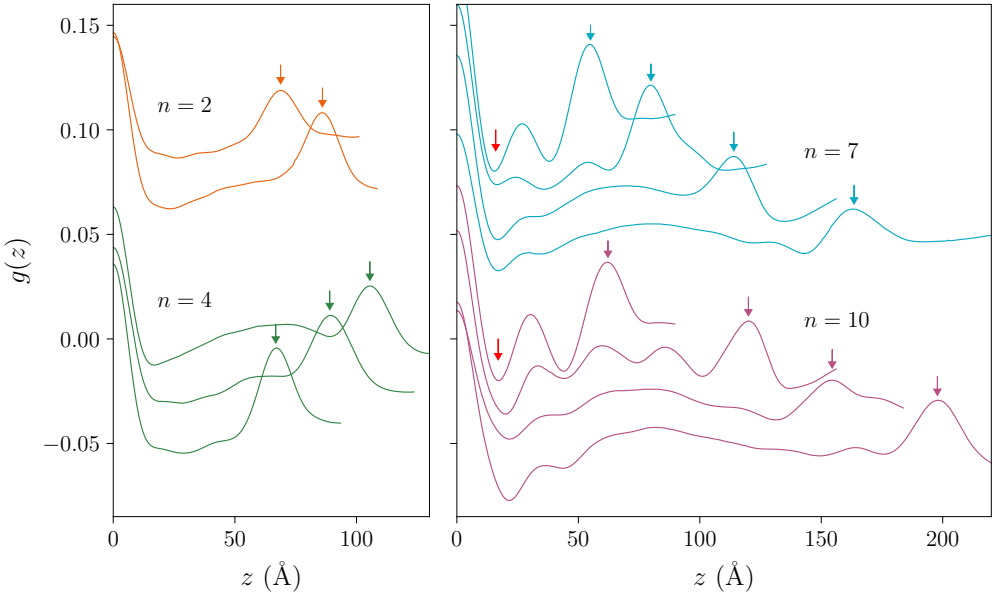

Figure 6.15: Transformée de Fourier des signaux de réflectivité spéculaires de films fins de $\mathbf{PC}_n\mathbf{VImTFSI}$ avec $n = 2$ and 4 (gauche), $n = 7$, et 10 (droite). Les flèches aux couleurs des courbes représentent le pic de l'épaisseur totale du film. La position du pic interlamellaire est indiquée par une flèche rouge. Les courbes sont décalées verticalement pour une meilleure visibilité.

respondante contient un seul pic à l'épaisseur totale du film, tels que ceux observée sur la partie gauche de la Figure 6.15. La présence de pics supplémentaires, tels qu'observés sur la partie droite de la Figure 6.15, permet de valider le modèle stratifié pour les chaînes latérales longues et d'accéder à la distance interlamellaire, indiquée par le premier pic de corrélation. Celle-ci décroît avec l'épaisseur du film comme observé en FIgure 6.16a, suggérant un effet de confinement. De plus, la DXIR donne accès à la structure dans le plan à proximité de l'interface. L'effet du confinement y est également observé avec une distance interchaîne dans le plan qui augmente pour des épaisseurs plus fines. De ces deux résultats quantitatifs émerge un mécanisme selon lequel les monomères et leur chaîne carbonnées s'alignent avec l'interface quand l'épaisseur du film diminue tel que représenté en Figure 6.16b, encombrant par conséquent le plan parallèle à l'interface, imposant une distance plus grande entre les chaînes principales (Figure 6.16c).

Si ces effets sont de grande valeur pour les applications électrochimiques des PLIs, ils ont également des répercussions dans d'autres systèmes comme les nanoparticules. Des PLIs triazolium polymérisés en dispersion génèrent des nanoparticules avec une structure interne du fait de la même ségrégation des phases apolaires. Leur étude microscopie électronique à transmission (cryo-TEM) et DXGA, repsectivement en Figures 6.17a et 6.17b, révèlent que la longueur de la chaîne carbonnée contrôle non seulement la distance caractéristique de la structure interne mais aussi la forme des particules, qui peuvent être des vésicules multilamellaires en oignon, des ellipsoïdes ou bien des cubosomes.

L'approche fondamentale de ce travail, reposant sur une série de PLIs modèle, révèle les propriétés remarquables de ces matériaux et une meilleure compréhen-

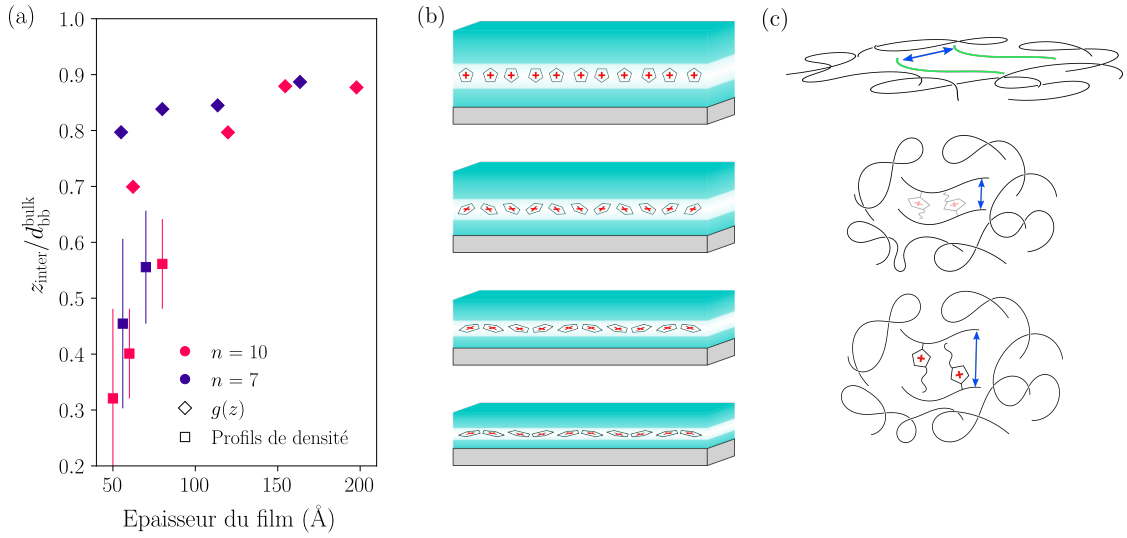

Figure 6.16: (a) Distance interlamellaire z_{inter} déterminée par la position du premier pic des transformées de Fourier des signaux de réflectivité $g(z)$ données en Figure 6.15 (◊) et à partir des profils de densité électroniques en Figure 6.14 normalisée par la distance interchaîne en bulk $d_{\text{bb}}^{\text{bulk}}$ déterminée en DNPA (Figure 6.12c) en fonction de l'épaisseur de films de **PC$_n$VImTFSI** pour $n = 7$ et 10. (b) Vue de côté schématique d'un film fin représenté en bleu. Les monomères d'une couche déplétée en contre ion sont représentés sans leur chaînes latérales. L'épaisseur du film diminue du haut vers le bas. (c) Haut : représentation du plan près de l'interface avec deux chaînes principales en vert. Milieu et bas : vue du dessus de ce même plan pour deux épaisseurs, le film du bas étant le plus fin.

sion des implications des interactions locales. La présence de deux régimes, chaînes latérales courtes ou longues, à la fois sur la morphologie en volume, celle aux interfaces, et leurs propriétés viscoélastiques suggèrent que le changement de structure, globulaire pour des chaînes courtes et bicontinue pour les plus longues, est au coeur de ces propriétés. Néanmoins, changer la longueur de la chaîne latérale influence aussi les associations ioniques et les relaxations polymériques. Des études dynamiques sur cette série de PLIs, en spectroscopie dielectrique ou en diffusion inélastique de neutrons permettraient éventuellement de décorréler ces effets et d'identifier chacune de leur contribution. Aux interfaces, il est très probable que l'application d'un champ électrique ou un changement de chimie de surface influence la structure lamellaire des films fins. L'influence de cette dernière sur des propriétés de glissement ou de conduction de ces matériaux reste à explorer.

Il reste également à démontrer si ces conclusions sont universelles à travers la diversité de structure chimiques existantes. Ceci fournirait les outils nécessaires pour tirer le meilleur parti de la versatilité de ces matériaux en variant leur architecture ou encore les conditions de température ou de confinement afin de cibler au mieux leurs applications.

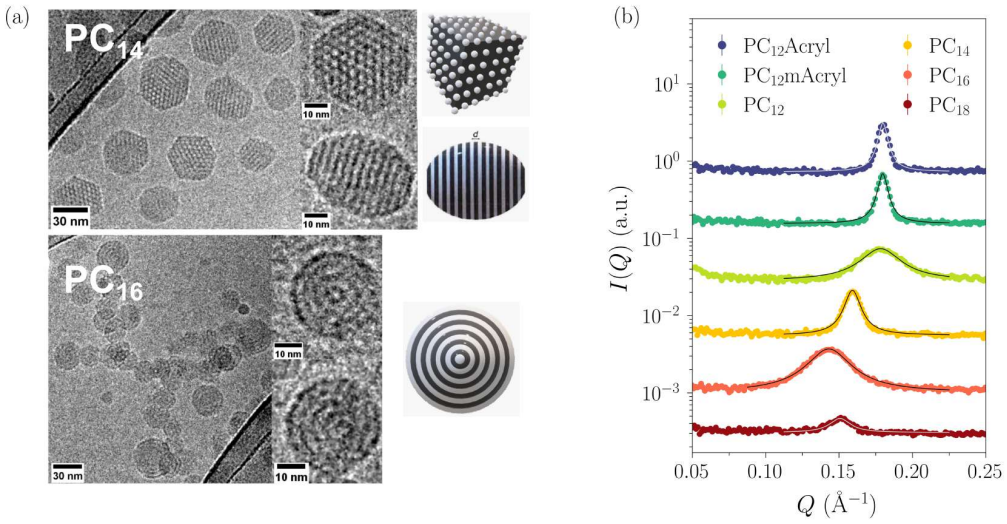

Figure 6.17: Images représentatives en cryo-MET de nanoparticles de PLIs obtenue par polymérisation en dispersion de LIs acrylamides fonctionnalisés avec des groupements triazolium à longueur de chaîne carbonnée $n = 14$ et 16 en solution aqueuse de concentration 25 mM. Les schémas de gauche sont des représentations des structures observées, à savoir un mélange d'ellipsoïdes et de cubosomes pour $n = 14$ et des vésicules multilamellaires en oignon pour $n = 16$. (b) Signaux DXGA de dispersions aqueuses de nanoparticules de PLI 1,2,3-triazolium acrylamide. L'ajustement avec un modèle Lorentzien donne la position du pic de corrélation correspondant à la distance caractéristique d en (a). Les données sont décalées verticalement pour une meilleure visibilité.

Bibliography

[1] Y.-L. Wang, B. Li, S. Sarman, F. Mocci, Z.-Y. Lu, J. Yuan, A. Laaksonen, M. D. Fayer, *Chem. Rev.* **2020**, *120*, 5798–5877.

[2] M. Rubinstein, R. H. Colby, *Polymer Physics*, Oxford Univ. Press, **2003**.

[3] P. Walden, *Bull. Acad. Imper. Sci. (St. Petersburg)* **1914**, *1800*.

[4] F. H. Hurley, T. P. WIer, *J. Electrochem. Soc.* **1951**, *98*, 203.

[5] H. L. Chum, V. R. Koch, L. L. Miller, R. A. Osteryoung, *J. Am. Chem. Soc.* **1975**, *97*, 3264–3265.

[6] G. W. Parshall, *J. Am. Chem. Soc.* **1972**, *94*, 8716–8719.

[7] W. T. Ford, R. J. Hauri, S. G. Smith, *J. Am. Chem. Soc.* **1974**, *96*, 4316–4318.

[8] R. J. Gale, B. Gilbert, R. A. Osteryoung, *Inorg. Chem.* **1978**, *17*, 2728–2729.

[9] C. L. Hussey, *Adv. molten salt chem* **1983**, *5*, Place: New York, NY Publisher: Plenum Press, 185–230.

[10] J. S. Wilkes, J. A. Levisky, R. A. Wilson, C. L. Hussey, *Inorg. Chem.* **1982**, *21*, 1263–1264.

[11] S. Tait, R. A. Osteryoung, *Inorg. Chem.* **1984**, *23*, 4352–4360.

[12] K. M. Dieter, C. J. Dymek, N. E. Heimer, J. W. Rovang, J. S. Wilkes, *J. Am. Chem. Soc.* **1988**, *110*, 2722–2726.

[13] R. G. Horn, D. F. Evans, B. W. Ninham, *J. Phys. Chem.* **1988**, *92*, 3531–3537.

[14] T. Welton, *Biophys Rev* **2018**, *10*, 691–706.

[15] G. Reynolds, C. Dymek, *Journal of Power Sources* **1985**, *15*, 109–118.

[16] M. Díaz, A. Ortiz, I. Ortiz, *Journal of Membrane Science* **2014**, *469*, 379–396.

[17] S. M. Zakeeruddin, M. Grätzel, *Adv. Funct. Mater.* **2009**, *19*, 2187–2202.

[18] A. Eftekhari, *Energy Storage Materials* **2017**, *9*, 47–69.

[19] A. E. Bradley, C. Hardacre, J. D. Holbrey, S. Johnston, S. E. J. McMath, M. Nieuwenhuyzen, *Chem. Mater.* **2002**, *14*, 629–635.

[20] C. Hardacre, S. E. J. McMath, M. Nieuwenhuyzen, D. T. Bowron, A. K. Soper, *J. Phys.: Condens. Matter* **2003**, *15*, S159–S166.

[21] J. N. A. Canongia Lopes, A. A. H. Pádua, *J. Phys. Chem. B* **2006**, *110*, 3330–3335.

[22] A. Triolo, O. Russina, H.-J. Bleif, E. Di Cola, *J. Phys. Chem. B* **2007**, *111*, 4641–4644.

[23] H. V. R. Annapureddy, H. K. Kashyap, P. M. De Biase, C. J. Margulis, *J. Phys. Chem. B* **2010**, *114*, 16838–16846.

[24] C. Ye, W. Liu, Y. Chen, L. Yu, *Chemical Communications* **2001**, *0*, Publisher: Royal Society of Chemistry, 2244–2245.

[25] D. Mecerreyes, *Progress in Polymer Science* **2011**, *36*, 1629–1648.

[26] B. P. Mudraboyina, M. M. Obadia, I. Allaoua, R. Sood, A. Serghei, E. Drockenmuller, *Chemistry of Materials* **2014**, *26*, 1720–1726.

[27] A. S. Shaplov, R. Marcilla, D. Mecerreyes, *Electrochimica Acta* **2015**, *175*, 18–34.

[28] J. Salamone, S. Israel, P. Taylor, B. Snider, *Polymer* **1973**, *14*, 639–644.

[29] R. L. Weber, Y. Ye, A. L. Schmitt, S. M. Banik, Y. A. Elabd, M. K. Mahanthappa, *Macromolecules* **2011**, *44*, 5727–5735.

[30] M. D. Green, D. Salas-de la Cruz, Y. Ye, J. M. Layman, Y. A. Elabd, K. I. Winey, T. E. Long, *Macromol. Chem. Phys.* **2011**, *212*, 2522–2528.

[31] H. Chen, J.-H. Choi, D. Salas-de la Cruz, K. I. Winey, Y. A. Elabd, *Macromolecules* **2009**, *42*, 4809–4816.

[32] D. S.-d. la Cruz, M. D. Green, Y. Ye, Y. A. Elabd, T. E. Long, K. I. Winey, *J. Polym. Sci. B Polym. Phys.* **2012**, *50*, 338–346.

[33] C. Iacob, A. Matsumoto, M. Brennan, H. Liu, S. J. Paddison, O. Urakawa, T. Inoue, J. Sangoro, J. Runt, *ACS Macro Lett.* **2017**, *6*, 941–946.

[34] H. Liu, S. J. Paddison, *Macromolecules* **2017**, *50*, 2889–2895.

[35] H. Liu, S. J. Paddison, *ACS Macro Lett.* **2016**, *5*, 537–543.

[36] J. Yuan, D. Mecerreyes, M. Antonietti, *Progress in Polymer Science* **2013**, *38*, 1009–1036.

[37] J. Yuan, M. Antonietti, *Polymer* **2011**, *52*, 1469–1482.

[38] A. Eftekhari, T. Saito, *European Polymer Journal* **2017**, *90*, 245–272.

[39] J. Zhao, X. Shen, F. Yan, L. Qiu, S. Lee, B. Sun, *Journal of Materials Chemistry* **2011**, *21*, 7326.

[40] X. Chen, J. Zhao, J. Zhang, L. Qiu, D. Xu, H. Zhang, X. Han, B. Sun, G. Fu, Y. Zhang, F. Yan, **2012**, *22*, 18018–18024.

[41] M. M. Obadia, E. Drockenmuller, *Chemical Communications* **2016**, *52*, 2433–2450.

[42] T. Y. Kim, H. W. Lee, M. Stoller, D. R. Dreyer, C. W. Bielawski, R. S. Ruoff, K. S. Suh, *ACS Nano* **2011**, *5*, 436–442.

[43] J. Yuan, S. Soll, M. Drechsler, A. H. E. Müller, M. Antonietti, *Journal of the American Chemical Society* **2011**, *133*, 17556–17559.

[44] *Ionic Liquids*, (Ed.: B. Kirchner), Springer Berlin Heidelberg, Berlin, Heidelberg, **2010**.

[45] U. Schröder, J. D. Wadhawan, R. G. Compton, F. Marken, P. A. Z. Suarez, C. S. Consorti, R. F. De Souza, J. Dupont, *New J. Chem.* **2000**, *24*, 1009–1015.

[46] S. M. Urahata, M. C. C. Ribeiro, *The Journal of Chemical Physics* **2004**, *120*, 1855–1863.

[47] Y. Wang, G. A. Voth, *J. Am. Chem. Soc.* **2005**, *127*, 12192–12193.

[48] R. Hayes, G. G. Warr, R. Atkin, *Chem. Rev.* **2015**, *115*, 6357–6426.

[49] O. Russina, A. Triolo, L. Gontrani, R. Caminiti, D. Xiao, L. G. Hines Jr, R. A. Bartsch, E. L. Quitevis, N. Pleckhova, K. R. Seddon, *J. Phys.: Condens. Matter* **2009**, *21*, 424121.

[50] A. Triolo, A. Mandanici, O. Russina, V. Rodriguez-Mora, M. Cutroni, C. Hardacre, M. Nieuwenhuyzen, H.-J. Bleif, L. Keller, M. A. Ramos, *J. Phys. Chem. B* **2006**, *110*, 21357–21364.

[51] O. Russina, A. Triolo, *Faraday Discuss.* **2012**, *154*, 97–109.

[52] H. Weiss, J. Mars, H. Li, G. Kircher, O. Ivanova, A. Feoktystov, O. Soltwedel, M. Bier, M. Mezger, *J. Phys. Chem. B* **2017**, *121*, 620–629.

[53] J. C. Araque, J. J. Hettige, C. J. Margulis, *J. Phys. Chem. B* **2015**, *119*, 12727–12740.

[54] C. Hardacre, J. D. Holbrey, C. L. Mullan, T. G. A. Youngs, D. T. Bowron, *The Journal of Chemical Physics* **2010**, *133*, 074510.

[55] R. Atkin, G. G. Warr, *J. Phys. Chem. B* **2008**, *112*, 4164–4166.

[56] G. Law, P. R. Watson, *Langmuir* **2001**, *17*, 6138–6141.

[57] M. Heres, T. Cosby, E. U. Mapesa, H. Liu, S. Berdzinski, V. Strehmel, M. Dadmun, S. J. Paddison, J. Sangoro, *Macromolecules* **2019**, *52*, 88–95.

[58] B. Doughty, A.-C. Genix, I. Popov, B. Li, S. Zhao, T. Saito, D. A. Lutterman, R. L. Sacci, B. G. Sumpter, Z. Wojnarowska, V. Bocharova, *Phys. Chem. Chem. Phys.* **2019**, *21*, 14775–14785.

[59] F. Wieland, V. Bocharova, P. Münzner, W. Hiller, R. Sakrowski, C. Sternemann, R. Böhmer, A. P. Sokolov, C. Gainaru, *J. Chem. Phys.* **2019**, *151*, 034903.

[60] A. Arbe, A.-C. Genix, J. Colmenero, D. Richter, P. Fouquet, *Soft Matter* **2008**, *4*, 1792.

[61] R. L. Miller, R. F. Boyer, J. Heijboer, *J. Polym. Sci. Polym. Phys. Ed.* **1984**, *22*, 2021–2041.

[62] M. Beiner, H. Huth, *Nature Mater* **2003**, *2*, 595–599.

[63] J. N. Israelachvili, *Intermolecular and Surface Forces*, 3rd ed., Academic Press Elsevier, **2011**.

[64] B. M. Ocko, X. Z. Wu, E. B. Sirota, S. K. Sinha, O. Gang, M. Deutsch, *Phys. Rev. E* **1997**, *55*, 3164–3182.

[65] J. A. Forrest, K. Dalnoki-Veress, *Advances in Colloid and Interface Science* **2001**, *94*, 167–195.

[66] S. Perkin, T. Albrecht, J. Klein, *Phys. Chem. Chem. Phys.* **2010**, *12*, 1243–1247.

[67] S. Perkin, L. Crowhurst, H. Niedermeyer, T. Welton, A. M. Smith, N. N. Gosvami, *Chem. Commun.* **2011**, *47*, 6572.

[68] K. Ueno, M. Kasuya, M. Watanabe, M. Mizukami, K. Kurihara, *Phys. Chem. Chem. Phys.* **2010**, *12*, 4066.

[69] I. Bou-Malham, L. Bureau, *Soft Matter* **2010**, *6*, 4062.

[70] S. Perkin, *Phys. Chem. Chem. Phys.* **2012**, *14*, 5052.

[71] M. Mezger, R. Roth, H. Schröder, P. Reichert, D. Pontoni, H. Reichert, *The Journal of Chemical Physics* **2015**, *142*, 164707.

[72] M. Mezger, H. Schroder, H. Reichert, S. Schramm, J. S. Okasinski, S. Schoder, V. Honkimaki, M. Deutsch, B. M. Ocko, J. Ralston, M. Rohwerder, M. Stratmann, H. Dosch, *Science* **2008**, *322*, 424–428.

[73] E. Sloutskin, B. M. Ocko, L. Tamam, I. Kuzmenko, T. Gog, M. Deutsch, *Journal of the American Chemical Society* **2005**, *127*, 7796–7804.

[74] M. P. Singh, R. K. Singh, S. Chandra, *Progress in Materials Science* **2014**, *64*, 73–120.

[75] C. Iacob, J. R. Sangoro, W. K. Kipnusu, R. Valiullin, J. Kärger, F. Kremer, *Soft Matter* **2012**, *8*, 289–293.

[76] S. Maruyama, I. B. H. Prastiawan, K. Toyabe, Y. Higuchi, T. Koganezawa, M. Kubo, Y. Matsumoto, *ACS Nano* **2018**, *12*, 10509–10517.

[77] Q. Zhao, P. Bennington, P. F. Nealey, S. N. Patel, C. M. Evans, *Macromolecules* **2021**, *54*, 10520–10528.

[78] C. M. Evans, G. E. Sanoja, B. C. Popere, R. A. Segalman, *Macromolecules* **2016**, *49*, 395–404.

[79] T. Kinsey, K. Glynn, T. Cosby, C. Iacob, J. Sangoro, *ACS Appl. Mater. Interfaces* **2020**, *12*, 44325–44334.

[80] M. Tarnacka, A. Chrobok, K. Matuszek, S. Golba, P. Maksym, K. Kaminski, M. Paluch, *ACS Appl. Mater. Interfaces* **2016**, *8*, 29779–29790.

[81] S. Mogurampelly, V. Ganesan, *Macromolecules* **2018**, *51*, 9471–9483.

[82] S. Mogurampelly, J. R. Keith, V. Ganesan, *J. Am. Chem. Soc.* **2017**, *139*, 9511–9514.

[83] R. Kumar, J. P. Mahalik, K. S. Silmore, Z. Wojnarowska, A. Erwin, J. F. Ankner, A. P. Sokolov, B. G. Sumpter, V. Bocharova, *Sci. Adv.* **2020**, *6*, eaba7952.

[84] Y. Ye, J.-H. Choi, K. I. Winey, Y. A. Elabd, *Macromolecules* **2012**, *45*, 7027–7035.

[85] Z. Yu, C. Fang, J. Huang, B. G. Sumpter, R. Qiao, *J. Phys. Chem. C* **2018**, *122*, 22494–22503.

[86] M. A. Gebbie, M. Valtiner, X. Banquy, E. T. Fox, W. A. Henderson, J. N. Israelachvili, *Proceedings of the National Academy of Sciences* **2013**, *110*, 9674–9679.

[87] M. A. Gebbie, A. M. Smith, H. A. Dobbs, A. A. Lee, G. G. Warr, X. Banquy, M. Valtiner, M. W. Rutland, J. N. Israelachvili, S. Perkin, R. Atkin, *Chem. Commun.* **2017**, *53*, 1214–1224.

[88] H. Tokuda, S. Tsuzuki, M. A. B. H. Susan, K. Hayamizu, M. Watanabe, *J. Phys. Chem. B* **2006**, *110*, 19593–19600.

[89] A. A. Lee, D. Vella, S. Perkin, A. Goriely, *J. Phys. Chem. Lett.* **2015**, *6*, 159–163.

[90] Y. Zhang, E. J. Maginn, *J. Phys. Chem. Lett.* **2015**, *6*, 700–705.

[91] F. Ferdeghini, Q. Berrod, J.-M. Zanotti, P. Judeinstein, V. G. Sakai, O. Czakkel, P. Fouquet, D. Constantin, *Nanoscale* **2017**, *9*, 1901–1908.

[92] Q. Berrod, F. Ferdeghini, J.-M. Zanotti, P. Judeinstein, D. Lairez, V. García Sakai, O. Czakkel, P. Fouquet, D. Constantin, *Sci Rep* **2017**, *7*, 2241.

[93] G. L. Burrell, N. F. Dunlop, F. Separovic, *Soft Matter* **2010**, *6*, 2080.

[94] N. Voeltzel, P. Vergne, N. Fillot, N. Bouscharain, L. Joly, *Tribol Lett* **2016**, *64*, 25.

[95] R. Safinejad, N. Mehdipour, H. Eslami, *Phys. Chem. Chem. Phys.* **2018**, *20*, 21544–21551.

[96] A. Piednoir, A. Steinberger, C. Cottin-Bizonne, C. Barentin, *J. Phys. Chem. B* **2020**, *124*, 2685–2690.

[97] R. Lhermerout, C. Diederichs, S. Perkin, *Lubricants* **2018**, *6*, 9.

[98] A. M. Smith, K. R. J. Lovelock, N. N. Gosvami, T. Welton, S. Perkin, *Phys. Chem. Chem. Phys.* **2013**, *15*, 15317.

[99] O. Borodin, D. L. Price, B. Aoun, M. A. González, J. B. Hooper, M. Kofu, S. Kohara, O. Yamamuro, M.-L. Saboungi, *Phys. Chem. Chem. Phys.* **2016**, *18*, 23474–23481.

[100] O. Russina, A. Triolo, L. Gontrani, R. Caminiti, *J. Phys. Chem. Lett.* **2012**, *3*, 27–33.

[101] A. M. Smith, M. A. Parkes, S. Perkin, *J. Phys. Chem. Lett.* **2014**, *5*, 4032–4037.

[102] F. Fan, W. Wang, A. P. Holt, H. Feng, D. Uhrig, X. Lu, T. Hong, Y. Wang, N.-G. Kang, J. Mays, A. P. Sokolov, *Macromolecules* **2016**, *49*, 4557–4570.

[103] J. R. Sangoro, C. Iacob, A. L. Agapov, Y. Wang, S. Berdzinski, H. Rexhausen, V. Strehmel, C. Friedrich, A. P. Sokolov, F. Kremer, *Soft Matter* **2014**, *10*, 3536–3540.

[104] F. Fan, Y. Wang, T. Hong, M. F. Heres, T. Saito, A. P. Sokolov, *Macromolecules* **2015**, *48*, 4461–4470.

[105] A. Düvel, P. Heitjans, P. Fedorov, G. Scholz, G. Cibin, A. V. Chadwick, D. M. Pickup, S. Ramos, L. W. L. Sayle, E. K. L. Sayle, T. X. T. Sayle, D. C. Sayle, *J. Am. Chem. Soc.* **2017**, *139*, 5842–5848.

[106] U. H. Choi, M. Lee, S. Wang, W. Liu, K. I. Winey, H. W. Gibson, R. H. Colby, *Macromolecules* **2012**, *45*, 3974–3985.

[107] H. Staudinger, *Helv. Chim. Acta* **1922**, *5*, 785.

[108] J. J. Berzelius, *Jahresberichte über die Fortschritte der physichen der Wissenschaften* **1833**, *12*, 63–67.

[109] N. Zheng, Y. Xu, Q. Zhao, T. Xie, *Chem. Rev.* **2021**, *121*, 1716–1745.

[110] E. Van Ruymbeke, *Journal of Rheology* **2017**, *61*, 1099–1102.

[111] X. Yu, X. Cao, Q. Chen, *Rheol Acta* **2021**, *60*, 241–249.

[112] A. Eisenberg, B. Hird, R. B. Moore, *Macromolecules* **1990**, *23*, 4098–4107.

[113] A. Eisenberg, J.-S. Kim, *Introduction to ionomers*, Wiley, New York, **1998**.

[114] M. S. Green, A. V. Tobolsky, *The Journal of Chemical Physics* **1946**, *14*, 80–92.

[115] L. Leibler, M. Rubinstein, R. H. Colby, *Macromolecules* **1991**, *24*, 4701–4707.

[116] M. Rubinstein, A. N. Semenov, *Macromolecules* **1998**, *31*, 1386–1397.

[117] A. N. Semenov, M. Rubinstein, *Macromolecules* **1998**, *31*, 1373–1385.

[118] Z. Zhang, Q. Chen, R. H. Colby, *Soft Matter* **2018**, *14*, 2961–2977.

[119] K. Nakamura, T. Saiwaki, K. Fukao, T. Inoue, *Macromolecules* **2011**, *44*, 7719–7726.

[120] G. Liu, R. G. Larson, L. Li, H. Luo, X. He, Y. Niu, G. Li, *Macromolecules* **2023**, *56*, 2719–2728.

[121] Q. Zhao, C. M. Evans, *Macromolecules* **2021**, *54*, 3395–3404.

[122] J. D. Ferry, *Viscoelastic Properties of Polymers*, John Wiley & Sons, **1980**.

[123] K. Nakamura, K. Fukao, T. Inoue, *Macromolecules* **2012**, *45*, 3850–3858.

[124] U. H. Choi, Y. Ye, D. Salas de la Cruz, W. Liu, K. I. Winey, Y. A. Elabd, J. Runt, R. H. Colby, *Macromolecules* **2014**, *47*, 777–790.

[125] U. H. Choi, A. Mittal, T. L. Price, M. Lee, H. W. Gibson, J. Runt, R. H. Colby, *Electrochimica Acta* **2015**, *175*, 55–61.

[126] W. Zhang, Z. Kochovski, Y. Lu, B. V. Schmidt, M. Antonietti, J. Yuan, *ACS Nano* **2016**, *10*, 7731–7737.

[127] A. Matsumoto, R. Yoshizawa, O. Urakawa, T. Inoue, A. Q. Shen, *Macromolecules* **2021**, *54*, 5648–5661.

[128] F. Cousin, *EPJ Web of Conferences* **2015**, *104*, (Eds.: M. Ceretti, W. Paulus, M.-H. Mathon, C. Ritter), 01004.

[129] A. Brûlet, D. Lairez, A. Lapp, J.-P. Cotton, *Journal of Applied Crystallography* **2007**, *40*, 165–177.

[130] P.-G. de Gennes, *Scaling Concepts in Polymer Physics*, Cornell University Press, Cornell University Press, **1979**.

[131] P. J. Flory, *Principles of Polymer Chemistry*, Cornell University Press, **1953**.

[132] B. Hammouda in *Polymer Characteristics*, *Vol. 106*, Springer-Verlag, Berlin/Heidelberg, **1993**, pp. 87–133.

[133] H. Benoit, *Comptes Rendus* **1957**, *245*, 2244–2247.

[134] B. Hammouda, M.-H. Kim, *Journal of Molecular Liquids* **2017**, *247*, 434–440.

[135] J. P. Cotton, D. Decker, H. Benoit, B. Farnoux, J. Higgins, G. Jannink, R. Ober, C. Picot, J. Des Cloizeaux, *Macromolecules* **1974**, *7*, 863–872.

[136] P. Debye, *The Journal of Physical and Colloid Chemistry* **1947**, *51*, 18–32.

[137] W.-R. Chen, P. D. Butler, L. J. Magid, *Langmuir* **2006**, *22*, 6539–6548.

[138] G. Jerke, J. S. Pedersen, S. U. Egelhaaf, P. Schurtenberger, *Langmuir* **1998**, *14*, 6013–6024.

[139] J. Combet, *EPJ Web of Conferences* **2018**, *188*, (Eds.: M. Wolff, F. Cousin), 03001.

[140] J. Combet, P. Lorchat, M. Rawiso, *The European Physical Journal Special Topics* **2012**, *213*, 243–265.

[141] P. De Gennes, P. Pincus, R. Velasco, F. Brochard, *J. Phys. France* **1976**, *37*, 1461–1473.

[142] G. S. Manning, *The Journal of Chemical Physics* **1969**, *51*, 924–933.

[143] J. A. Widegren, A. Laesecke, J. W. Magee, *Chemical Communications* **2005**, 1610.

[144] Wiley, *Characterization and Analysis of Polymers*, John Wiley & Sons, **2008**.

[145] M. Heres, T. Cosby, E. U. Mapesa, J. Sangoro, *ACS Macro Lett.* **2016**, *5*, 1065–1069.

[146] A. Guinier, G. Fournet, *Small-angle Scattering of X-rays*, Wiley, **1955**.

[147] V. Delhorbe, D. Bresser, H. Mendil-Jakani, P. Rannou, L. Bernard, T. Gutel, S. Lyonnard, L. Picard, *Macromolecules* **2017**, *50*, 4309–4321.

[148] D. W. Schubert, T. Dunkel, *Materials Research Innovations* **2003**, *7*, 314–321.

[149] R. M. A. Azzam, *Ellipsometry and polarized light*, North-Holland Pub. Co., **1977**.

[150] A. Gibaud, S. Hazra, *SURFACE CHARACTERIZATION* **2000**, *78*, 11.

[151] M. Tolan, *X-Ray Scattering from Soft-Matter Thin Films*, Springer Berlin, Heidelberg, **1999**.

[152] L. G. Parratt, *Phys. Rev.* **1954**, *95*, 359–369.

[153] F. Cousin, A. Chennevière, *EPJ Web of Conferences* **2018**, *188*, 04001.

[154] W. H. Steel, *Interferometry*, Cambridge Univ. Press, **1985**.

[155] G. Vignaud, A. Gibaud, *J Appl Crystallogr* **2019**, *52*, 201–213.

[156] A. Glavic, M. Björck, *J Appl Crystallogr* **2022**, *55*, 1063–1071.

[157] A. R. J. Nelson, S. W. Prescott, *J Appl Crystallogr* **2019**, *52*, 193–200.

[158] I. W. Hamley, J. S. Pedersen, *J Appl Crystallogr* **1994**, *27*, 29–35.

[159] F. Bridou, B. Pardo, *Journal of X-Ray Science and Technology* **1994**, *4*, 200–216.

[160] O. H. Seeck, I. D. Kaendler, M. Tolan, K. Shin, M. H. Rafailovich, J. Sokolov, R. Kolb, *Appl. Phys. Lett.* **2000**, *76*, 2713–2715.

[161] A. Gibaud, G. Vignaud, S. K. Sinha, *Acta Crystallographica Section A Foundations of Crystallography* **1993**, *49*, 642–648.

[162] G. Renaud, R. Lazzari, F. Leroy, *Surface Science Reports* **2009**, *64*, 255–380.

[163] P. Fontaine, G. Ciatto, N. Aubert, M. Goldmann, *Science of Advanced Materials* **2014**, *6*, 2312–2316.

[164] R. Singh Payal, S. Balasubramanian, *ChemPhysChem* **2012**, *13*, 1764–1771.

[165] M. Mezger, B. M. Ocko, H. Reichert, M. Deutsch, *Proceedings of the National Academy of Sciences* **2013**, *110*, 3733–3737.

[166] E. Sloutskin, B. M. Ocko, L. Tamam, I. Kuzmenko, T. Gog, M. Deutsch, *J. Am. Chem. Soc.* **2005**, *127*, 7796–7804.

[167] T. Outerelo Corvo, A. Jourdain, S. O'Brien, F. Restagno, E. Drockenmuller, A. Chennevière, *Macromolecules* **2022**, *55*, 4111–4118.

[168] B. Schrode, S. Pachmajer, M. Dohr, C. Röthel, J. Domke, T. Fritz, R. Resel, O. Werzer, *J Appl Cryst* **2019**, *52*, Number: 3 Publisher: International Union of Crystallography, 683–689.

[169] Y. Yoneda, *Phys. Rev.* **1963**, *131*, 2010–2013.

[170] S. Baldelli, *Acc. Chem. Res.* **2008**, *41*, 421–431.

[171] D. Richter, M. Kruteva, *Soft Matter* **2019**, *15*, 7316–7349.

[172] J. Siirilä, S. Häkkinen, H. Tenhu, *Polym. Chem.* **2019**, *10*, 766–775.

[173] E. J. Foster, E. B. Berda, E. W. Meijer, *J. Am. Chem. Soc.* **2009**, *131*, 6964–6966.

[174] N. J. W. Penfold, J. Yeow, C. Boyer, S. P. Armes, *ACS Macro Lett.* **2019**, *8*, 1029–1054.

[175] Y.-I. Jeong, J.-B. Cheon, S.-H. Kim, J.-W. Nah, Y.-M. Lee, Y.-K. Sung, T. Akaike, C.-S. Cho, *Journal of Controlled Release* **1998**.

[176] J. Shim, H. Seokkang, W. Park, S. Han, J. Kim, I. Chang, *Journal of Controlled Release* **2004**, *97*, 477–484.

[177] W. Zhang, Z. Kochovski, B. V. Schmidt, M. Antonietti, J. Yuan, *Polymer* **2016**, *107*, 509–516.

[178] K. Manojkumar, D. Mecerreyes, D. Taton, Y. Gnanou, K. Vijayakrishna, *Polym. Chem.* **2017**, *8*, 3497–3503.

[179] C. W. Macosko, *Rheology: principles, measurements, and applications*, VCH, New York, **1994**.

[180] W. Kuhn, *Kolloid-Zeitschrift* **1934**, *68*, 2–15.

[181] B. H. Zimm, W. H. Stockmayer, *The Journal of Chemical Physics* **1949**, *17*, 1301–1314.

[182] P. E. Rouse, *The Journal of Chemical Physics* **1953**, *21*, 1272–1280.

[183] B. H. Zimm, *The Journal of Chemical Physics* **1956**, *24*, 269–278.

[184] S. Onogi, T. Masuda, K. Kitagawa, *Macromolecules* **1970**, *3*, 109–116.

[185] T. C. B. McLeish, *Advances in Physics* **2002**, *51*, 1379–1527.

[186] S. F. Edwards, *Proceedings of the Physical Society* **1965**, *85*, 613.

[187] S. F. Edwards, *Proc. Phys. Soc.* **1967**, *92*, 9–16.

[188] P. de Gennes, *The Journal of Chemical Physics* **1971**, *55*, 572–579.

[189] M. Doi, S. F. Edwards, *J. Chem. Soc. Faraday Trans. 2* **1978**, *74*, 1818–1832.

[190] A. K. Doolittle, *Journal of Applied Physics* **1951**, *22*, 1471–1475.

[191] M. L. Williams, R. F. Landel, J. D. Ferry, *Journal of the American Chemical Society* **1955**, *77*, 3701–3707.

[192] R. H. Colby, X. Zheng, M. H. Rafailovich, J. Sokolov, D. G. Peiffer, S. A. Schwarz, Y. Strzhemechny, D. Nguyen, *Phys. Rev. Lett.* **1998**, *81*, 3876–3879.

[193] L. G. Baxandall, *Macromolecules* **1989**, *22*, 1982–1988.

[194] Q. Chen, G. J. Tudryn, R. H. Colby, *Journal of Rheology* **2013**, *57*, 1441–1462.

[195] V. A. H. Boudara, D. J. Read, J. Ramírez, *Journal of Rheology* **2020**, *64*, 709–722.

[196] T. Li, H. Li, H. Wang, W. Lu, M. Osa, Y. Wang, J. Mays, K. Hong, *Polymer* **2021**, *213*, 123207.

[197] C. Huang, C. Wang, Q. Chen, R. H. Colby, R. A. Weiss, *Macromolecules* **2016**, *49*, 3936–3947.

[198] C. Huang, Q. Chen, R. A. Weiss, *Macromolecules* **2017**, *50*, 424–431.

[199] Y. Yu, Y. Chen, *ACS Omega* **2021**, *6*, 14869–14874.

[200] Z. Zhang, C. Liu, X. Cao, L. Gao, Q. Chen, *Macromolecules* **2016**, *49*, 9192–9202.

[201] I. A. Nyrkova, A. R. Khokhlov, M. Doi, *Macromolecules* **1993**, *26*, 3601–3610.

[202] Y. Biswas, P. Banerjee, T. K. Mandal, *Macromolecules* **2019**, *52*, 945–958.

[203] K. Sinha, J. K. Maranas, *Macromolecules* **2011**, *44*, 5381–5391.

[204] M. R. Bittermann, M. Grzelka, S. Woutersen, A. M. Brouwer, D. Bonn, *J. Phys. Chem. Lett.* **2021**, *12*, 3182–3186.

[205] E. Mirzahossein, M. Grzelka, F. Guerton, D. Bonn, R. Brown, *Sci Rep* **2022**, *12*, 22197.

[206] M. Hénot, A. Chennevière, E. Drockenmuller, L. Léger, F. Restagno, *Macromolecules* **2017**, *50*, 5592–5598.